Cavity-enhanced spectroscopies for applications of remote sensing, chemical kinetics and detection of radical species

Thesis by

Thinh Quoc Bui

In partial fulfillment of the requirements

For the Degree of
Doctor of Philosophy

California Institute of Technology
Pasadena, California
2015
(Defended May 22, 2015)

Acknowledgements

I would like to first acknowledge my advisors, professor Mitchio Okumura at Caltech and Dr. Pin Chen at JPL. Their guidance and support have profoundly shaped my adult life. I also acknowledge professor Jun Ye at the University of Colorado/JILA, Boulder for his mentorship on a collaborative project. I also thank Dr. Joseph Hodges and Dr. David Long at NIST, Gaithersburg for their assistance in setting up the spectrometers used in this work. I also acknowledge my committee members, professors Rudy Marcus, Geoff Blake, Ken Libbrecht, and Long Cai for their insights and guidance.

I have also had the opportunities with work with many other invaluable staff members at Caltech. Our machinists Mike Roy and Steve Olson were responsible for putting the CAD drawings on paper into reality, as well as fix many of the components that we break. Rick Gerhart, our glassblower, made all of the glass/quartz cells used in this work. I also acknowledge guidance from Rich Abbott (LIGO) in building practical circuit components. I also appreciate help and guidance from JPL scientists and staff during my time there: Dr. Stan Sander, Dr. Brian Drouin, Dr. Keeyoon Sung, Dr. Linda Brown, Dr. Lance Christensen and Tim Crawford.

Finally, I would like to thank my peers, both graduate and undergraduate, who have worked with me or guided me over these years. I have worked with three great undergraduates, Daniel Hogan, Jared Forte, and Josh Fromm and have befriended many others: Geoff Beck, Heather Widgren, Marissa Weichman, and Matthew Voss. In the Okumura group, I have enjoyed working with many graduate students and post-docs: Leah Dodson, Laura Mertens, Linhan Shen, Matthew Smarte, Elizabeth Lunny, Elle

Chimiak, Kathryn Perez, Hannah Allen, Kana Takematsu, Matthew Sprague, Laurence Yeung, David Long, Kathleen Spencer, Aileen Hui, Sigrid Barklund, Nathan Honsowetz, Dr. Nathan Eddingsaas, Dr. Priyanka (Milinda) Rupasinghe, Dr. Luis Gomez, and Dr. Damien Amedro. While I was at the JILA/University of Colorado in Professor Jun Ye's group, I was very fortunate to have worked with graduate students Bryce Bjork and Brian Changala, and Dr. A.J. Fleisher. I also thank Dr. Ralph H. Page for his support and guidance early in my graduate career. Finally, I also have had the privilege to meet Dr. Allan Nishimura (Westmont College) who was on a sabbatical with our group for a summer.

This thesis is for my family, who made all of this possible.

Abstract

This thesis describes applications of cavity enhanced spectroscopy towards applications of remote sensing, chemical kinetics and detection of transient radical molecular species. Both direct absorption spectroscopy and cavity ring-down spectroscopy are used in this work. Frequency-stabilized cavity ring-down spectroscopy (FS-CRDS) was utilized for measurements of spectral lineshapes of O_2 and CO_2 for obtaining laboratory reference data in support of NASA's OCO-2 mission. FS-CRDS is highly sensitive (> 10 km absorption path length) and precise (> 10000:1 SNR), making it ideal to study subtle non-Voigt lineshape effects. In addition, these advantages of FS-CRDS were further extended for measuring kinetic isotope effects: A dual-wavelength variation of FS-CRDS was used for measuring precise D/H and $^{13}C/^{12}C$ methane isotope ratios (σ>0.026%) for the purpose of measuring the temperature dependent kinetic isotope effects of methane oxidation with $O(^1D)$ and OH radicals. Finally, direct absorption spectroscopic detection of the *trans*-DOCO radical via a frequency combs spectrometer was conducted in collaboration with professor Jun Ye at JILA/University of Colorado. Dr. A.J. Fleisher at JILA led the investigation.

Table of Contents

List of Figures

List of Tables

Summary

The work outlined in this thesis covers broad subjects of remote sensing, chemical kinetics and spectroscopy of transient radicals. The first chapter reviews the relevant topics necessary for cavity-enhanced spectroscopy, which is used for all the projects in this thesis. This chapter also covers the details for the cavity ring-down instrumentation used in Chapters 1—5. The cavity-enhanced spectroscopy in Chapter 6 uses the traditional cavity-enhanced direct absorption method but with novel applications of a frequency combs laser.

Chapter 2-3 discusses progress and results towards high-precision spectroscopy relevant to remote sensing, mainly for NASA's OCO-2 mission. The OCO-2 satellite measures the global distribution of CO_2 on Earth by measuring Fourier-transform spectra of CO_2 near 1.6 μm and 2.06 μm and O_2 A-band near 0.760 μm. The objective of the work is to provide lineshape parameters for CO_2 near 2.06 μm and O_2 near 0.760 μm beyond the Voigt lineshape approximation: Dicke narrowing, speed dependence, line mixing and collisional-induced absorption (CIA). For the O_2 A-band, the largest errors originate from uncertainties from line mixing and CIA. Photoacoustic spectroscopy is implemented to measure unsaturated lineshapes of air-broadened O_2 A-band from 0.2-4 atm to study line mixing and CIA. The CO_2 near 2.06 μm, the proper lineshape to incorporate both Dicke narrowing and speed dependence is studied.

Chapter 4-5 discusses two separate experiments with the goal of measuring the temperature kinetic isotope effect of methane oxidation by $O(^1D)$ and OH. The first experiment in chapter 4 is to develop a dual-wavelength cavity ring-down spectroscopic

technique to measure methane isotopologues simultaneously. By using two lasers in the dual-wavelength scheme, $^{13}CH_4/^{12}CH_4$ and $^{12}CH_3D/^{12}CH_4$ isotope ratios are measured with precisions better than 0.026%. Chapter 5 discusses the new temperature dependent results for the kinetic isotope effects of methane oxidation by $O(^1D)$ and OH. Pulsed photolysis experiments are performed to measure methane isotopologue depletions in order to determine KIE from 177—293 K. The temperature dependent trends for $OH+CH_4$ show qualitative and quantitative differences with literature values extrapolated from warmer temperatures.

Chapter 6 introduces a new method using a frequency combs spectrometer to measure broadband spectra of transient radical species. This project was led by Dr. A.J. Fleisher as JILA. The performance of this novel frequency comb spectrometer was tested by detecting the broadband (65 cm^{-1}) absorption spectrum of *trans*-DOCO radical with a 1/*e* lifetime of ~100 μs from the photolysis of the deuterated acrylic acid precursor. This avenue of broadband, time-resolved molecular detection allows us to move towards the study of complex chemical reactions that produce multiple intermediates and products, such as the important OH+CO reaction.

Chapter 1: High-finesse cavity and frequency-stabilized cavity ring-down spectroscopy (FS-CRDS) background

1.1 Introduction to High-Finesse Cavities

1.1.1 Cavity Transmission

This example is the case of a Fabry-Perot type cavity, which has two mirrors spaced by distance *d*. Cavities used in our work usually involves two concave mirrors with reflectivity *R* and radius of curvature $\Re$. Note that the reflectivity *R* is the square of the amplitude of the reflection coefficient. For estimating realistic scenarios, we will use *R*=0.99995 and *d*=75 cm whenever these quantities appear. The transmission and reflection functions for a Fabry-Perot cavity derived by Yariv and Yeh[1] are expressed in eqs. 1-2. δ is the round-trip phase shift.

$$\frac{I_T}{I_0} = \frac{(1-R)^2}{(1-R)^2 + 4R\sin^2(\delta/2)} \quad \text{(eq. 1)}$$

$$\frac{I_R}{I_0} = \frac{4R\sin^2(\delta/2)}{(1-R)^2 + 4R\sin^2(\delta/2)} \quad \text{(eq. 2)}$$

The cavity transmission and reflection functions are plotted as a function of phase shift, δ, for three different values of mirror reflectivity (*R* =0.8, 0.9, 0.99). The results are shown in Figures 1.1A and 1.1B for transmission and reflection, respectively. The cavity modes/resonances are denoted by ν_q and form a comb spectrum spanning the bandwidth of the high-reflectivity mirrors. Neglecting any additional losses, I_R=1-I_T and is the mirror image of the transmission function. As reflectivity increases, the cavity modes become increasingly narrow, as we will see in the next few paragraphs. In order to couple laser light into and out of these cavities, the laser wavelengths have to be resonant with these cavity modes. One can observe these resonances on an oscilloscope by modulating a

piezoelectric transducer (PZT) mounted on a cavity mirror or modulating the laser wavelength (e.g. current modulation).

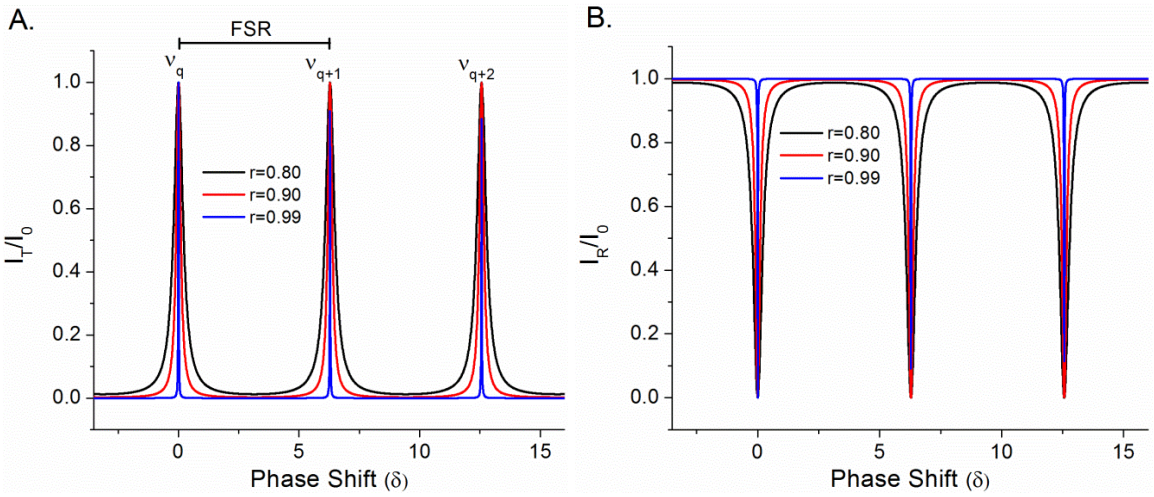

Figure 1.1: A) Cavity transmission B) Cavity reflection at different mirror reflectivity, *R*. The highest reflectivity (*R* =0.99, blue) exhibits the narrowest cavity mode linewidth. The FSR is the frequency spacing between cavity modes.

The first evident feature from Figure 1.1 is the cavity free spectral range, *FSR*, which is the frequency spacing between resonant cavity modes (ν_q). The *FSR* is calculated from the speed of light, *c*, and the mirror spacing distance, *d*. The *FSR* dependence on refractive index, *n*, is also important since *n* is affected by the content within the cavity, e.g., a gas.

$$FSR = \frac{c}{2nd} \quad \text{eq. 3}$$

The phase shift, δ, from eqs. 1-2 can be written in terms of frequency detuning ($\Delta\nu = \nu - \nu_q$) from cavity modes, ν_q (Figure 1A).[2] The phase shift, δ, is expressed in eq. 4. Here, the *q* subscript is an integer denoting the mode number, *n* is the refractive index, and *c* is the speed of light.

$$\delta = \frac{4\pi nd(\nu_q + \Delta\nu_q)}{c} = 2q\pi + \frac{2\pi\Delta\nu_q}{FSR} \quad \text{eq. 4}$$

When inserting eq. 4 into eqs. 1-2, the $sin^2(2q\pi)$ component is equal to zero for any q. This results in eq. 5. Eq. 5 presents a more intuitive picture that the transmission function is maximum when the detuning $\Delta\nu$ frequency is equal to the *FSR*, which would make the denominator term $4Rsin^2(\pi)=0$.

$$\frac{I_T}{I_0} = \frac{(1-R)^2}{(1-R)^2 + 4R\sin^2\left(\frac{\pi\Delta\nu_q}{FSR}\right)} \quad \text{eq. 5}$$

1.1.2 High-Finesse Cavity Design Parameters

Designing a high-finesse cavity requires knowledge of a few key design features based on one's needs and applications. Note that many of these quantities and formulas can be found in standard optics references like Nagourney[3], Yariv & Yeh[1], Demtröder[4], etc. First, the cavity stability criterion must be met. A stable cavity means that the cavity field (Gaussian beam) replicates itself after one round trip. Dimensionless parameters g_1 and g_2 are defined to describe the cavity geometry (eq. 6). $\Re$ is the radius of curvature of the concave cavity mirrors.

$$g_1 \equiv 1 - \frac{d}{\Re_1} \qquad g_2 \equiv 1 - \frac{d}{\Re_2} \quad \text{eq. 6}$$

The stability criterion is given simply by:

$$0 \le g_1 g_2 \le 1 \quad \text{eq. 7}$$

Outside of this range, the cavity is unstable and Gaussian beam solutions are no longer permitted. Note that the stability criterion established in eq. 7 is derived from the ABCD matrix law (Section 1.2.3) for paraxial rays confined inside a resonator with mirrors of radius of curvature $\Re$ separated by distance *d*.

A useful quantity to describe an optical cavity with high reflectivity mirrors is *finesse*. The finesse is given by eq. 8 where *R* is the mirror reflectivity. For R=0.99995, the *finesse* is 1.26×10^5. *Finesse* is useful for determining the effective optical path length for absorption, L_{eff} (eq. 9). It should make sense that the physical path length, *d*, is enhanced by this *finesse* factor. For a *d*=75 cm cavity and *R*=0.99995, L_{eff} =60 km.

$$Finesse = \frac{\pi (R_1 R_2)^{1/4}}{1 - \sqrt{R_1 R_2}} \quad \text{eq. 8}$$

$$L_{eff} = \frac{2}{\pi} Finesse \times d \quad \text{eq. 9}$$

A resonator is also characterized by the *Q* factor (eq. 10), which describes a resonator's bandwidth relative to its center frequency. In the case of optical cavities, the optical wavelength, λ_0, is needed to define the *Q* factor. For a laser centered at λ_0=1650 nm, the $Q=1.14 \times 10^{11}$. $\Delta\nu_{\text{FWHM}}$ is the cavity mode linewidth (eq. 11) calculated from the *FSR* and the *finesse*. It should be noted that the cavity linewidth is an important design parameter when one considers coupling light into the cavity. The narrower the cavity linewidth, the more difficult it is to couple light from a laser with a much larger

bandwidth. Linewidths of commercial lasers are typically at least a factor of 10 larger than cavity linewidths. In this example scenario, $\Delta\nu_{\mathrm{FWHM}}$=1.59 kHz. The best commercial external cavity diode lasers typically have 100 kHz linewidths.

$$Q = \frac{v}{\Delta v_{FWHM}} = \frac{2d}{\lambda} \times Finesse \quad \text{eq. 10}$$

$$\Delta v_{FWHM} = \frac{FSR}{Finesse} \quad \text{eq. 11}$$

Finally, an optical resonator can be described by its effectiveness in trapping light within the resonator, represented by the photon lifetime. The photon lifetime is related to the *Q* factor and the optical frequency, f_{opt} (eq. 12).

$$t_{ph} = \frac{Q}{2\pi f_{opt}} \quad \text{eq. 12}$$

1.1.3 Gaussian Beams

In order to effectively couple a laser Gaussian beam into a high-finesse cavity, some basic properties of Gaussian beam are needed. The complex beam parameter, *q*, is commonly used to describe properties and propagation of Gaussian beams. The complex *q* parameter originates as a Gaussian beam solution to the wave equation, which is not derived here because it can be found in most optics references. Note that the *q* parameter does not include the phase contribution to the wave equation solution.

$$\frac{1}{q} = \frac{1}{\Re} - i\frac{\lambda}{n\pi\omega^2} \quad \text{eq. 13}$$

$\Re$ is the radius of curvature of the mirror, λ_0 is the laser wavelength, n is an integer, and ω is the beam waist radius. The beam waist is also referred to as the spot size in some references. At the minimum beam waist, ω_0, $\Re = \infty$, and q becomes purely imaginary.

$$q \equiv q_0 = i\frac{n\pi\omega_0^{\,2}}{\lambda} \quad \text{eq. 14}$$

At any arbitrary distance z, $q(z)$ is given by,

$$q(z) = q_0 + z \quad \text{eq. 15}$$

where q_0 is given by eq. 14. Eqs. 13 and 15 can be used to derive the waist and curvature as a function of distance z:

$$\omega(z) = \omega_0\left[1+\left(\frac{\lambda z}{n\pi\omega_0^{\,2}}\right)^2\right]^{1/2}$$
$$\Re(z) = z\left[1+\left(\frac{n\pi\omega_0^{\,2}}{\lambda z}\right)^2\right] \quad \text{eq. 16}$$

A final useful quantity is the Rayleigh length, z_R, which is the distance from the minimum beam waist to the position where the waist radius increases by $\sqrt{2}$ (eq. 17). z_R and ω_0 are shown in Figure 1.2.

$$z_R = \frac{\pi\omega_0^{\,2}}{\lambda} \quad \text{eq. 17}$$

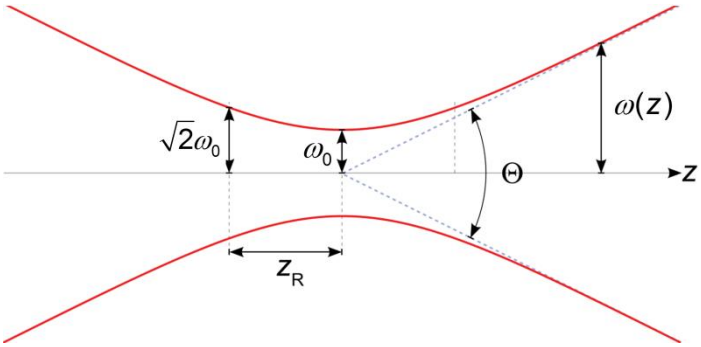

Figure 1.2: Gaussian beam profile with waist, ω_0, and Rayleigh length, z_R. The distance from the beam waist, ω_0, to the position where the waist radius increases by a factor of $\sqrt{2}$ is the Rayleigh length.

1.2 Mode Matching

1.2.1 Laser and cavity beam waist and radius of curvature

The quantities from eqs. 1-17 allow us to calculate properties of Gaussian beams propagating in free-space and within a spherical resonator cavity. Now we want to mode match our laser to this cavity to ensure optimal light coupling and maximize transmission. It is important to emphasize that without proper mode matching, the coupling efficiency of a CW laser to a high-finesse cavity can be very poor, resulting in no observed light in transmission. This can be the case even if the cavity is perfectly aligned. Mode matching is an exercise to shape the *laser* Gaussian beam TEM_{00} mode waist and curvature to match the location and size of the *cavity* beam waist and curvature. This assumes that the laser beam has a Gaussian-like mode structure, which is usually not the case for diode lasers (usually elliptical). One can use either anamorphic prism pairs or a cylindrical lens to shape the elliptical diode laser beam to be more Gaussian-like.

The first step in mode matching is to determine the cavity minimum beam waist position and curvature. The schematic in Figure 1.3 depicts this scenario.

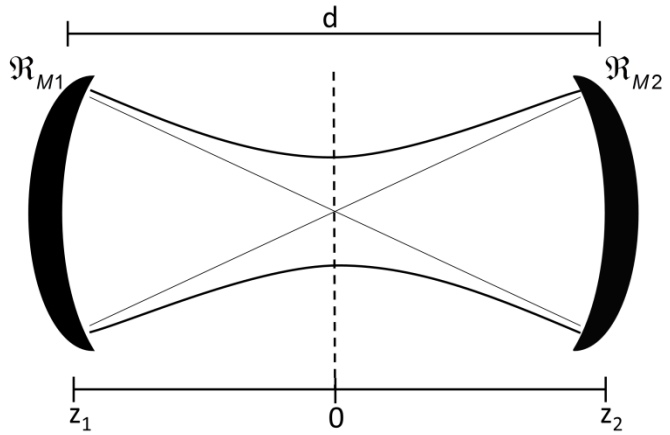

Figure 1.3: Resonator cavity formed by two concave mirrors with radius of curvature $\Re_1$ and $\Re_2$ separated by distance *d*.

Assume that the cavity is formed by two mirrors with radius of curvature $\Re_1$ and $\Re_2$ separated by distance d and that the cavity beam waist minimum is located at position z=0. z_1 and z_2 are distances with respect to this z=0 reference point. We first define:

$$z_2 = z_1 + d \quad \text{eq. 18}$$

For mode matching, we want to match the laser beam radius of curvature, $\Re_L$, and the mirror curvatures, $\Re_{M1}$ and $\Re_{M2}$. If the laser beam radius of curvature and cavity mirror curvatures are matched, i.e., $\Re_L(z_1) = \Re_{M1}$ *and* $\Re_L(z_2) = \Re_{M2}$, then we have equations 19 and 20:

$$\Re_L(z_1) = z_1 + z_R^{\,2} / z_1 = \Re_{M1} \quad \text{eq. 19}$$

$$\Re_L(z_2) = z_2 + z_R^{\,2} / z_2 = -\Re_{M2} \quad \text{eq. 20}$$

Eqs. 19 and 20 are obtained by making use of eqs. 16 and 17. The negative sign from eq. 20 is from the definition that the curvature is positive for z>0 and negative for z<0. Isolating z_1 and z_R from eqs. 18-20, we obtain the useful quantities expressed in eqs. 21-22.

$$z_1 = \frac{-d(\Re_{M2} + d)}{\Re_{M1} + \Re_{M2} + 2d} \quad \text{eq. 21}$$

$$z_R^{\,2} = \frac{-d(\Re_{M1} + d)(\Re_{M2} + d)(\Re_{M1} + \Re_{M2} + d)}{(\Re_{M1} + \Re_{M2} + 2d)^2} \quad \text{eq. 22}$$

Eqs. 18, 21, and 22 allow us to predict everything about the Gaussian beam propagating inside the resonator cavity, such as the location of the cavity beam waist and curvature. For example, the minimum beam waist of the resonator cavity can be calculated by using eq. 22 with eq. 17:

$$\omega_0 = \left(\lambda z_R / \pi\right)^{1/2} \quad \text{eq. 23}$$

The second step of mode matching is to shape the input laser beam waist and curvature by using either 1 or 2 lenses to match that of the cavity Gaussian beam parameters determined from the previous section. This means the laser beam profile must be measured at two different locations: at minimum spot size and some distance, *z*, away. With knowledge of ω_0, the beam size at distance *z* allows us to calculate z_R. There are two main ways to measure the beam profile, which are described in the next two sections.

1.2.2 Razor blade method

The laser beam waist can be measured either with a beam profiler or a razor blade and a power meter. As an example, the razor blade method was used to measure the beam waist from a Velocity ECDL (external cavity diode laser). A razor blade was placed on a 100 μm resolution translation stage between the laser and a power meter. The power measured as the blade is translated across the laser beam in direction *x* (perpendicular to laser propagation) is shown in Figure 1.4 as black circles. P_0 and $P(x)$ are the input and measured powers, respectively. The data was fitted to a complementary error function, *erfc*, shown in eq. 24.[5] and the fit result is plotted as a red line. In this case, the beam waist size obtained from the fit was ω=826 μm.

$$P(x) = \frac{P_0}{2} erfc\left(\frac{\sqrt{2}(x - x_0)}{\omega}\right) \quad \text{eq. 24}$$

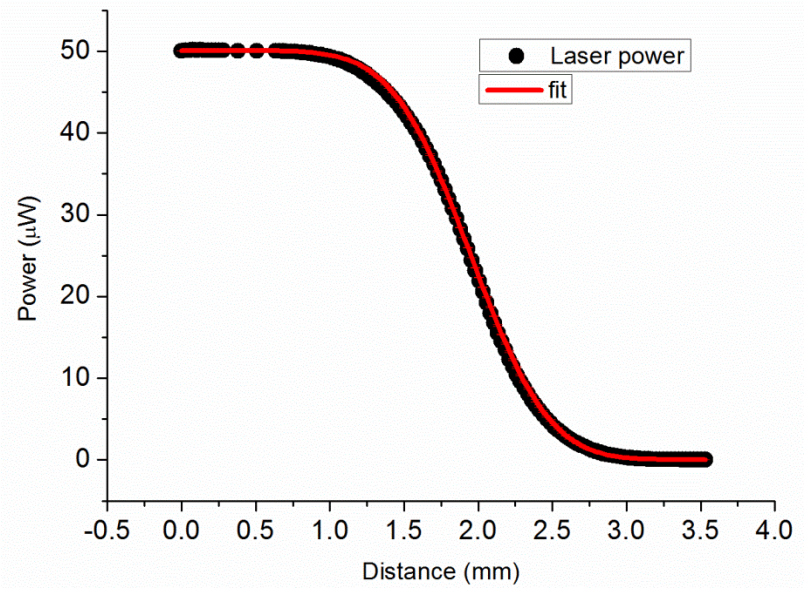

Figure 1.4: Beam waist measured using a razor blade method. The laser power was measured as the razor blade translates in a single axis perpendicular to the propagation direction. The fit to the data using a complementary error function is shown in red.

1.2.3 Beam profiler method

Another much simpler approach to measure a beam shape is with a commercial beam profiler. A nice benefit of a beam profiler is the ability to image the beam in real time. Moreover, the same razor blade method via a fast chopper is used to measure the beam waist, and the program from the beam profiler nicely displays it out on the screen. We used a beam profiler model Ophir-Spiricon Pyrocam III to measure the DBR laser beam profile after the AOM, which we have observed the 1st order diffraction beam to be distorted from the input beam. The measured the beam profile of the DBR laser after the 2nd pass through the AOM is displayed in Figure 1.5. The top and bottom images are the 2D (XY) and 3D (XYZ) beam profile images, respectively. The Z dimension is the beam intensity. From the top 2D image, the beam profile is an ellipse and has a beam diameter

dimensions (X,Y)=(1.47 mm,1.77 mm), which exhibits obvious deviations from a circular 2D Gaussian beam profile.

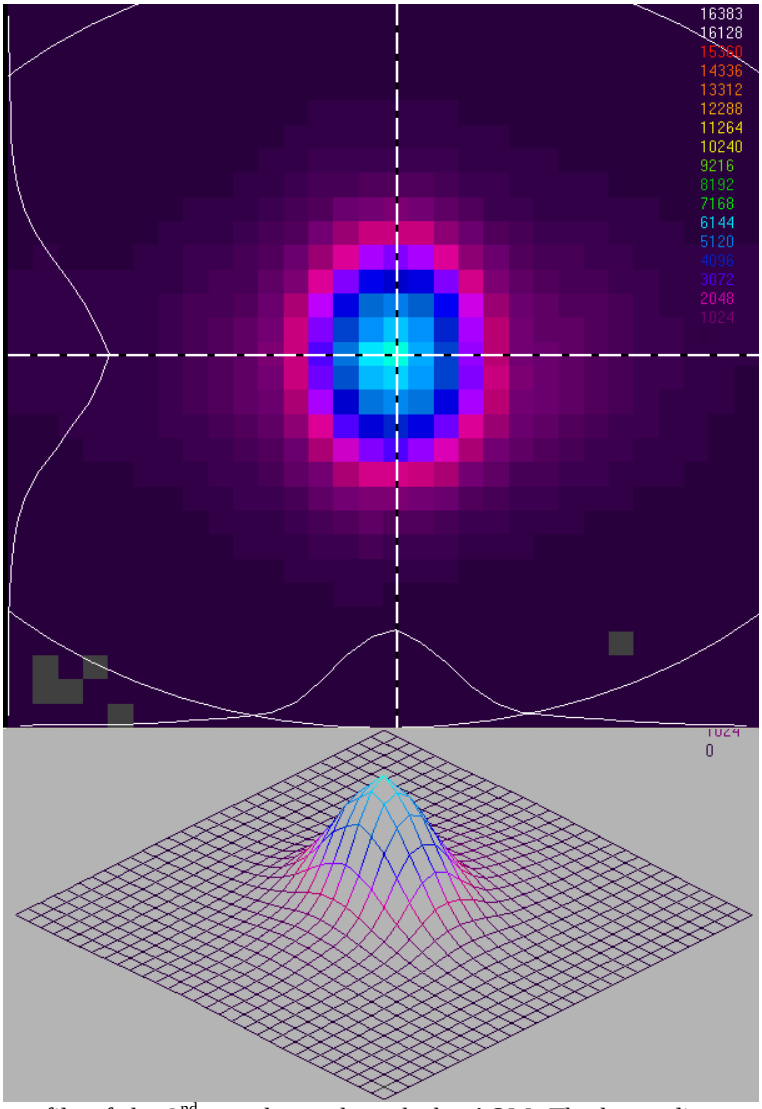

Figure 1.5: Beam profile of the 2nd pass beam through the AOM. The beam diameters in the X and Y dimensions are 1.44 mm and 1.77 mm, respectively.

It is well known that single mode fiber optics are nearly ideal spatial mode filters. By injecting the elliptical beam from Figure 1.5 into a 10 m length single mode fiber optic, the propagating beam mode quality was significantly improved at the expense of power loss through the process of fiber optic coupling. The resulting beam profile is

shown in Figure 1.6. The resulting beam dimensions were (X,Y)=(2.03 mm, 2.05 mm), which were very Gaussian-like mode qualities.

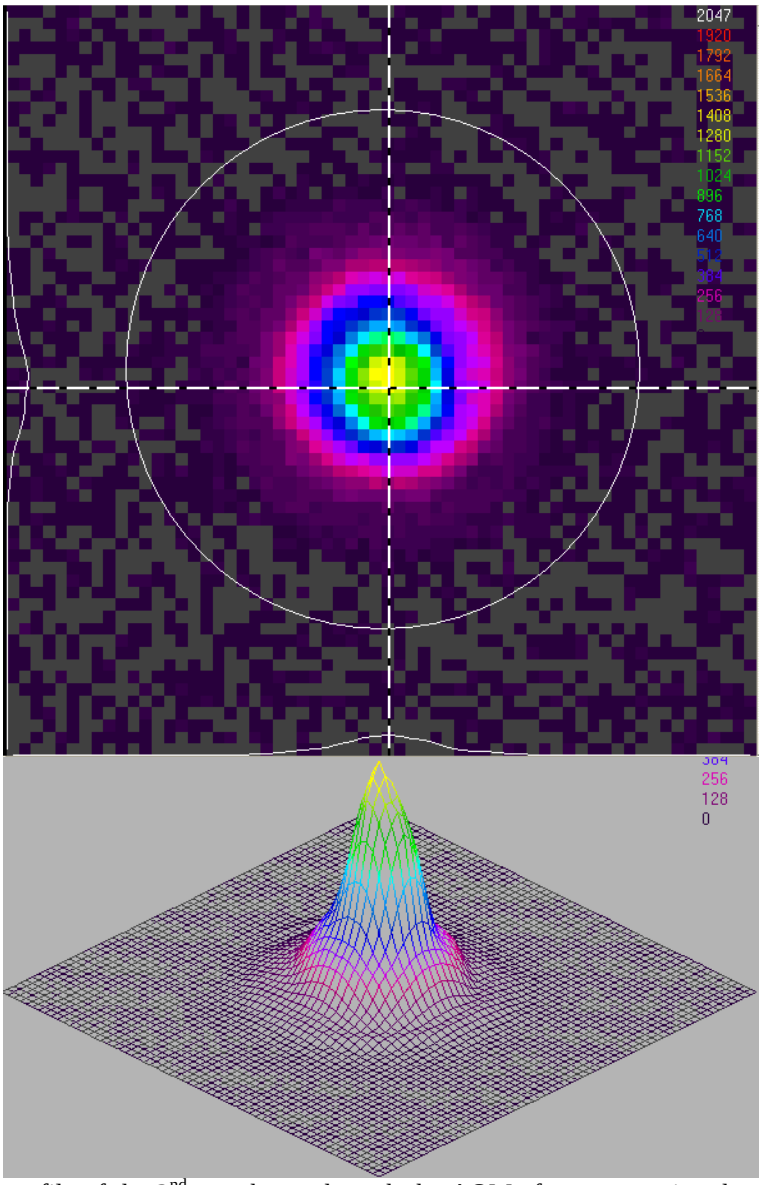

Figure 1.6: Beam profile of the 2nd pass beam through the AOM after propagating through a 10 m single mode fiber optic cable. The beam diameters in the X and Y dimensions are 2.03 mm and 2.05 mm, respectively.

1.2.4 ABCD Law for mode matching

After the laser beam profile characterization, we can now proceed to mode match to the cavity. Using a single lens is often sufficient, but two lenses (telescope) provide more flexibility. Figure 1.7 display a typical condition for mode matching with two lenses of focal length f_1 and f_2.

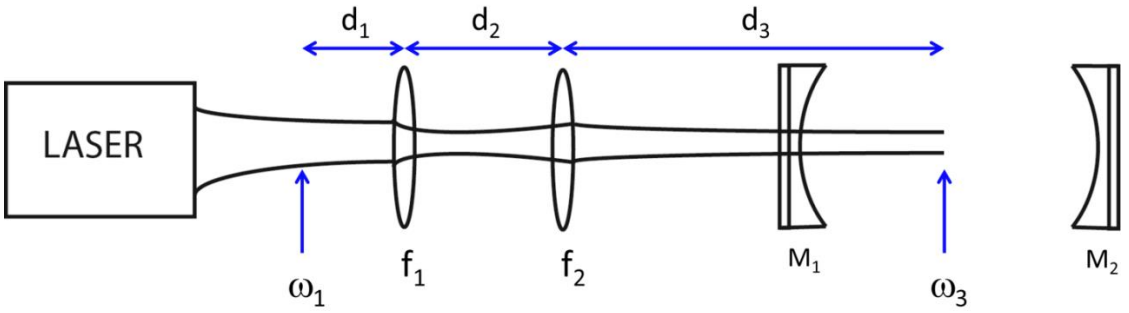

Figure 1.7: Laser mode matching scheme using two lenses with focal length f_1 and f_2. The beam waists, ω, of the laser and cavity and the positions of the lens, d, are used in the ABCD matrix for propagating a Gaussian beam. The high-finesse cavity is formed from two high-reflectivity mirrors M_1 and M_2.

In general, ABCD matrices are used to facilitate Gaussian beam propagation through optical components (eq. 25). The goal is to achieve a laser beam waist ω_3 that matches the cavity spot size.

$$\begin{pmatrix} A & B \\ C & D \end{pmatrix} = \begin{pmatrix} 1 & d_3 \\ 0 & 1 \end{pmatrix} \begin{pmatrix} 1 & 0 \\ -1/f_2 & 1 \end{pmatrix} \begin{pmatrix} 1 & d_2 \\ 0 & 1 \end{pmatrix} \begin{pmatrix} 1 & 0 \\ -1/f_1 & 1 \end{pmatrix} \begin{pmatrix} 1 & d_1 \\ 0 & 1 \end{pmatrix} \quad \text{eq. 25}$$

In eq. 25, the individual matrices are ray matrices for describing beam translation and focusing through lenses for each step depicted in Figure 1.7. Multiplying these matrices in order gives eq. 26.

$$\begin{pmatrix} A & B \\ C & D \end{pmatrix} = \begin{pmatrix} \frac{d_2(d_3-d_2)+f_1f_2-d_3(f_1+f_2)}{f_1f_2} & \frac{f_1(d_2(d_3-f_2)+f_1f_2-d_3(f_1+f_2))}{f_1f_2} - \frac{d_2d_3}{f_2} + d_2 + d_3 \\ \frac{f_1+f_2-d_2}{f_1f_2} & \frac{d_2(d_2-f_1+f_2)+f_2(f_2-d_2)}{f_1f_2} \end{pmatrix} \quad \text{eq. 26}$$

This results in a q_3 parameter at beam waist ω_3 as a function of the input beam q_1 parameter:

$$q_3 = \frac{Aq_1 + B}{Cq_1 + D} \quad \text{eq. 27}$$

The true utility of the *ABCD* law is given in eq. 27, which allows for transformation of Gaussian beams via the q parameter. Applying eq. 13 with eq. 27 gives all the desired results for Gaussian beam propagation through optical elements.

The goal of the following exercise is to apply eq. 27 to the scenario in Figure 1.7 to find the location d_3 and spot size ω_3 at that location. First, we know that at the focus, i.e., $\omega = \omega_0$, the radius of curvature is infinite ($\Re = \infty$). Assuming that ω_1 and ω_3 from Figure 1.7 are at the focus, then

$$\frac{1}{q_1} = \frac{1}{\Re_1} - i\frac{\lambda}{n\pi\omega_1^2} = -i\frac{\lambda}{n\pi\omega_1^2} = \frac{1}{iz_1} \quad \text{eq. 28}$$

$$\frac{1}{q_3} = \frac{1}{\Re_3} - i\frac{\lambda}{n\pi\omega_3^2} = -i\frac{\lambda}{n\pi\omega_3^2} = \frac{1}{iz_3} \quad \text{eq. 29}$$

From the ABCD law, eq. 27, we have

$$iz_3 = \frac{Aiz_1 + B}{Ciz_1 + D} = \frac{(Aiz_1 + B)(-Ciz_1 + D)}{C^2z_1^2 + D^2} = \frac{ACz_1^2 + BD}{C^2z_1^2 + D^2} + \frac{iz_1}{C^2z_1^2 + D^2} \quad \text{eq. 30}$$

Since *A, B, C, D*, z_1 and z_2 are all real values, the first quantity in the right hand side of eq. 31 must be equal to zero:

$$ACz_1^2 + BD = 0 \quad \text{eq. 31}$$

As a result,

$$z_3 = \frac{z_1}{C^2 z_1^{\,2} + D^2} \quad \text{eq. 32}$$

Isolating $z_1^{\,2}$ from eq. 31 and plugging into eq. 32 gives,

$$z_3 = \frac{z_1}{C^2\left(-\frac{BD}{AC}\right) + D^2} = \frac{z_1 AC}{DC(AD - BC)} = \frac{A}{D} z_1 \quad \text{eq. 33}$$

The last quantity of eq. 33 is a result of the fact that ABCD matrices are unimodular, which means that *AD-BC=1*. From eq. 28 and eq. 29, $z_1=\pi\omega_1^{\,2}/\lambda$ and $z_3=\pi\omega_3^{\,2}/\lambda$. Inserting these quantities into eq. 33 gives the desired ω_3 as a function of input ω_1.

$$\omega_3^{\,2} = \frac{A}{D}\omega_1^{\,2} \quad \text{eq. 34}$$

The ω_3 location, z_3, can be found from eq. 30 by plugging in values for *A, B, C, D* from eq. 26 and isolating d_3, which is not done here.

Finally, there a multiple solutions for f_1 and f_2 that will satisfy a designed ω_3 at d_3. Therefore, it is ideal to pick out lenses that are commercially available and adjust d_1, d_2 and d_3 to achieve the desired beam spot size at the cavity. Another approach is to apply a MATLAB genetic algorithm tool to search for suitable values for d_1, d_2 and d_3 from specified f_1 and f_2. This method has been applied by Mike Thorpe in his thesis with the MATLAB code provided in Appendix A.[6]

1.3 Measuring the cavity length

Accurate and absolute quantification of molecular densities using absorption spectroscopy is dependent on knowledge of the absorption path length. If only low

precision (> 1%) is required, one can use a ruler to estimate the physical separation *d* of the mirrors and factor in *finesse* to calculate the path length of a high-finesse cavity. For high-precision measurements, this approach will be plagued by uncertainties associated with using imprecise meter sticks, measuring tape, etc. An approach that is used with the FS-CRDS cavity ring-down system is to measure the cavity *FSR* (eq. 9) directly to determine the optical path length *d*. Unfortunately, the *FSR* is also a function of the refractive index, *n*, which means the vacuum *FSR* measurement will give a different value than atmospheric pressure, despite the same physical *d*. This problem can be addressed by measuring the *FSR* at a few working pressures to map out *n* (usually linear with pressure) to correctly determine *d*.

The procedure to measure the cavity *FSR* is based on Lisak and Hodges.[7] First, the cavity is locked to a HeNe reference laser. Then the probe laser is tuned to jump successive cavity modes, ν_q, while measuring the laser wavelength with a Bristol 621 wavemeter at each ν_q. A LabVIEW program was used to automate this measurement. Figure 1.8 shows the result from an experiment to measure the vacuum (200 μtorr) *FSR* to determine the mirror spacing *d*. The laser frequency ("amplitude") is plotted as a function of ν_q mode number and the fitted slope gives the *FSR*=199.22(5) MHz. The residuals from the fit are in the bottom panel. With the measured *FSR* and *n*~1, eq. 3 gives a very precise *d*=75.2935(2) cm. With *d* known, the effective absorption path length, L_{eff}, can be calculated from eqs. 7 and 8.

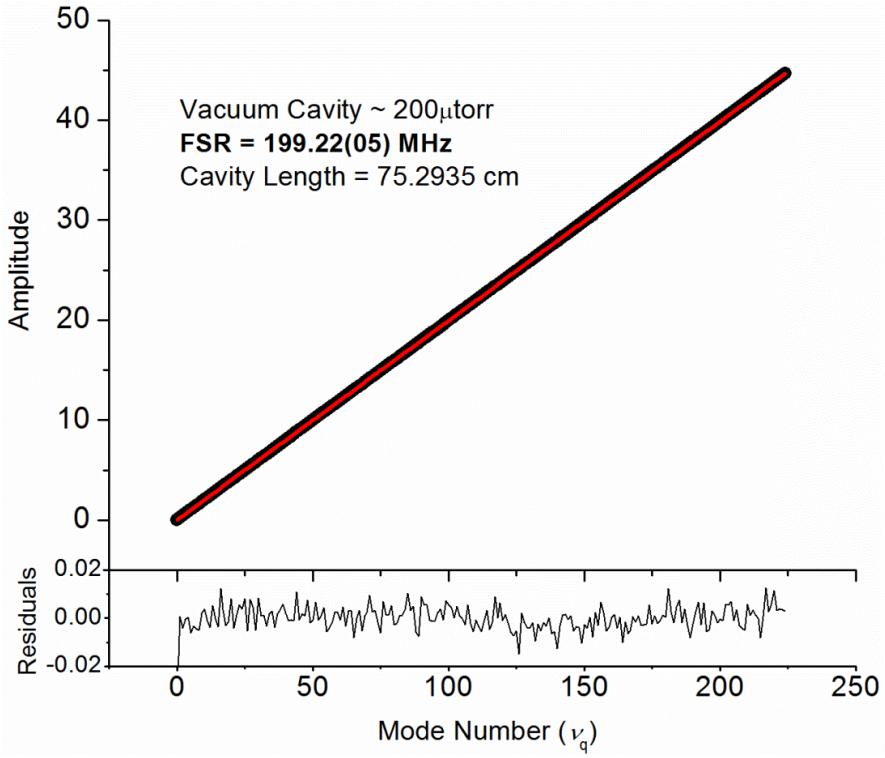

Figure 1.8: Cavity FSR measurement. Laser frequency as a function of cavity mode number (ν_q) from a cavity locked to a frequency-stabilized HeNe reference laser (Micro-g LaCoste ML-1). The slope of the fit to the data is the *FSR*. The residuals from the fit are shown on the bottom panel.

1.4 Locking Cavity to Reference 633 nm Laser

1.4.1 Heterodyne beat note - DBR & frequency stabilized HeNe laser

Why do we need to lock the cavity length? Common sense suggests that if we do not move it, the length should stay the same. The problem lies within the high frequency stability of <1 MHz desired for spectroscopy. Consequently, we want to anchor the cavity-comb spectrum, which will serve as the stable frequency axis for scanning a probe laser. Small changes of the cavity optical path length *d* of the order $\lambda_{probe}/2$ can introduce large shifts in the cavity resonances with respect to the cavity FSR. In this precise regime, laboratory room temperature fluctuations can cause sufficient material

expansion/contraction to make this uncertainty >> 1 MHz. We can gauge this impact with an example. A probe laser at wavelength λ_{probe}=1650 nm corresponds to a probe laser frequency of ν_{probe} = 1.8x10^{14} Hz. To achieve a frequency uncertainty of $\Delta\nu$ =1 MHz, then we need a stability of $\Delta\nu/\nu_{probe}$ = 5.5x10^{-9}. From the cavity *FSR* (eq. 3), one can show that $\Delta d/d=\alpha\Delta T$, where the uncertainty in the cavity mirror spacing, Δd, is proportional to the uncertainty in the room temperature multiplied by the linear thermal expansion coefficients, α, of the metal that the mirror is mounted on. For stainless steel material, $\alpha \approx$1.1x10^{-5} K^{-1}. Therefore, $\Delta d/d$ =1.1x10^{-6} for ΔT=0.1 K, which is a very stable room temperature. With respect to $\Delta\nu/\nu_{probe}$, this corresponds to a frequency uncertainty of 200 MHz. Therefore, a cavity length *d* in free drift at room temperature can experience large shifts in resonance frequencies with respect to the probe laser frequency.

A stable reference laser at 633nm serves as the frequency anchor to lock the cavity length. A commercial frequency-stabilized HeNe laser is a convenient choice. Micro-g LaCoste sells a polarization locked ML-1 model that has a quoted frequency drift of 500 kHz/24 Hr. The only limitation is that the output power of the ML-1 is less than 1 mW. Recently, a quoted 1 MHz linewidth 633nm DBR laser with high power (14 mW) was reported by Blume et al. [8] The DBR laser has recently been commercialized by Eagleyard Photonics. To compare the stability of this laser with the Micro-g Lacoste ML-1 HeNe, we performed a heterodyne beat note experiment as depicted in Figure 1.9. The DBR laser (SN#00011) was driven by the ILX LDX-3620B current driver and the SRS LDC500 TEC controller.

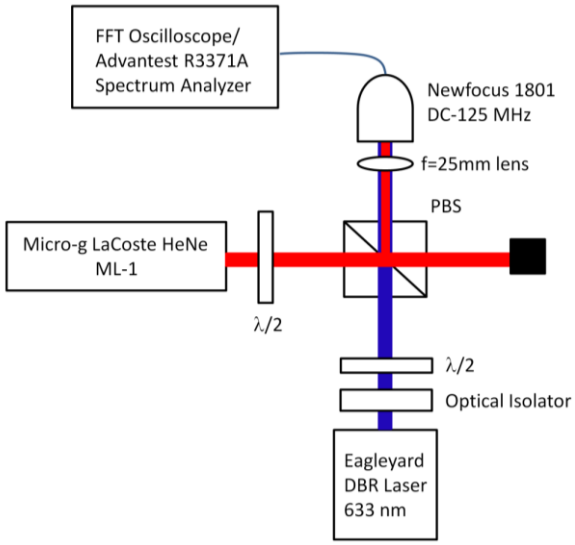

Figure 1.9: Schematic for a heterodyne beat note between the HeNe laser and the DBR laser. The lasers are spatially overlapped by a PBS cube and focused into a 125 MHz detector. The DBR laser was tuned to the fix frequency of the HeNe laser. The output from the detector is sent to both a FFT oscilloscope and a spectrum analyzer.

To conduct a heterodyne beat note experiment, the two lasers have to 1) be spatially overlapped at the photodetector and 2) the laser frequencies have to be sufficiently close to one another so that their note beat frequency falls within the detector bandwidth. Heterodyning refers to mixing of two different frequencies to produce the sum and difference frequencies, i.e., taking the product of sine/cosine waves:

$$\sin(2\pi f_{HeNe}t)\sin(2\pi f_{DBR}t) = \tfrac{1}{2}\left[\cos(2\pi[f_{HeNe} - f_{DBR}]t] - \cos(2\pi[f_{HeNe} + f_{DBR}]t)\right] \quad \text{eq. 35}$$

Since the frequency sum of $f_{\mathrm{HeNe}}+f_{\mathrm{DBR}}$ is still an optical frequency, $\approx 10^{14}$ Hz, it is not detectable within the detector bandwidth. The difference frequency, however, can by tuned to be within the detector bandwidth. The HeNe laser wavelength was measured to be 632.9908 nm. It is much easier to tune the DBR laser to the HeNe wavelength, rather than vice versa. To tune the DBR to near λ_0=632.9908 nm (15798.01792 cm^{-1}) of the HeNe, the diode temperature and current setting was set to 4.15 °C and 88.92 mA. The

HeNe and DBR lasers were spatially overlapped by using a polarizing beam splitter cube (PBS). The λ/2 waveplates rotated the laser polarizations to send both lasers through the same path after the PBS. Finally the co-propagating lasers were focused into a 125 MHz detector (Newfocus 1801) by a 25 mm lens. The output of the detector is sent to both a FFT oscilloscope (Tektronix TDS2024) and a spectrum analyzer (Advantest R3371A). 10 beat notes were recorded and averaged to obtain Figure 1.10. The data was fitted to a Lorentzian profile given by eq. 36. G is an arbitrary gain factor, y_0 is the baseline offset, ν_0 is the center frequency, ν is the detuning frequency, and $\Delta\nu$ is the linewidth full-width at half maximum (FWHM).

$$L(\nu) = G \times \frac{\Delta\nu/2\pi}{(\nu-\nu_0)^2 + (\Delta\nu/2)^2} + y_0 \quad \text{eq. 36}$$

The retrieved linewidth From the Lorentzian fit was $\Delta\nu$=4.27 MHz. Unfortunately, the observed linewidth from Figure 1.10 is a convolution of both lasers, and it is not possible to determine the linewidth of one without knowledge of the other.

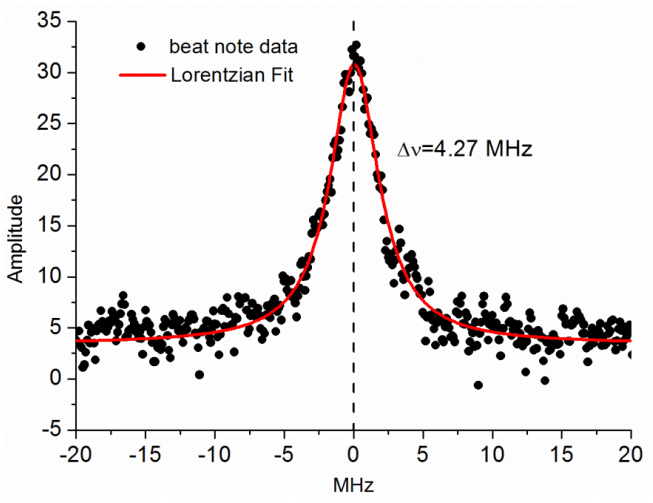

Figure 1.10: Average of 10 beat notes. The data was fitted to a Lorentzian profile (eq. 36) to obtain a linewidth HWHM $\Delta\nu$=4.27 MHz. The observed beat note is a convolution of linewidth of both the DBR laser and the HeNe laser. Therefore, one must know the linewidth of one laser to resolve the other.

The linewidth of the HeNe is approximated to be less than 1 MHz. Therefore, the DBR linewidth is estimated to be 2-3 MHz for this measurement. This measured linewidth is higher than that reported by Blume et al.[8], but that can be a consequence of using different TEC and current drivers. Further investigations are required on this matter.

1.4.2 Locking the cavity length to the 633nm DBR laser - Background

The *FSR* is a function of the cavity length *d*. As a result, the goal of this experiment is to lock the cavity length to the stable 633 nm DBR laser frequency to provide a stable frequency axis for spectroscopy. Locking requires some type of discriminator signal, serving as an error signal to feedback on the system under control (e.g., cavity PZT). A well-known way to generate this discriminator signal is to perform laser frequency modulation, use the cavity modes at 633nm as a reference, and perform phase-sensitive (lock-in) detection to obtain the discriminator signal. Note that the cavity mirrors have R=0.95 high-reflectivity coatings at 633 nm to produce the narrow cavity modes. The first step is to modulate the laser frequency directly using a function generator set at a fixed frequency, f_{mod}. One can modulate the laser frequency by modulating the laser current directly, or by the use of an AOM or EOM. Laser frequency modulation results in a laser intensity ($I_T(\nu)$) that is modulated around the center laser frequency, ν_0, as expressed in eq. 37.

$$I_T(\nu) = I_T[\nu_0 + \delta\nu \sin(f_{\text{mod}}\, t)] \quad \text{eq. 37}$$

The $\delta\nu$ is the maximum deviation of the laser frequency from modulation and is also called the modulation depth. This modulation frequency, f_{mod}, is chosen so that it is

smaller than the cavity mode linewidth, $f_{mod} < \Delta\nu_{FWHM}$, for which a Taylor expansion of the function provides the transmitted intensity as a function of frequency (eq. 38).

$$I_T(\nu) = I_T(\nu_0) + \sum_n \frac{(\delta\nu)^n}{n!} \sin^n(f_{mod}\, t)\left(\frac{d^n I_T}{d\nu^n}\right) = I_T(\nu_0) + \delta\nu \sin(f_{mod}\, t)\left(\frac{dI_T}{d\nu}\right) + \ldots \quad \text{eq. 38}$$

According to eq. 38, the modulated laser intensity has a DC term, $I_T(\nu_0)$, and a second term that is proportional to the first derivative of intensity ($dI_T/d\nu$). By using phase-sensitive detector like a lock-in amplifier to detect at f_{mod}, we retrieved the first derivative signal (the discriminator signal). The cavity mode transmission signals and the corresponding discriminator curves plotted for both a 1 MHz and 5 MHz cavity linewidth are displayed in Figure 1.11.

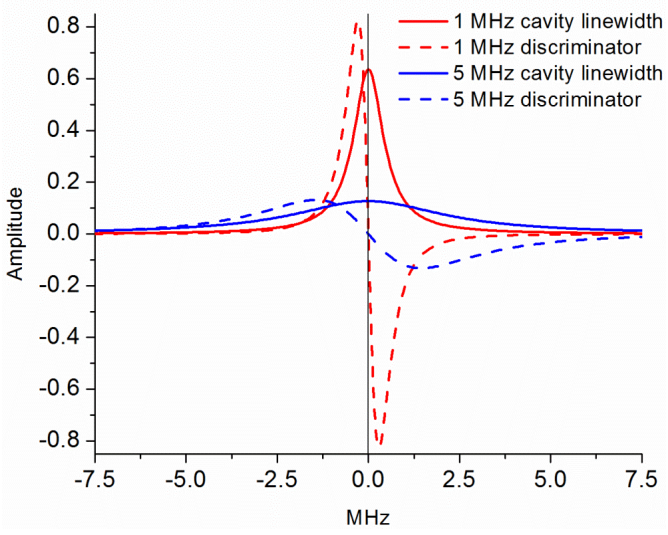

Figure 1.11: Red and blue solid lines show the Lorentzian cavity modes with linewidths of 1 and 5 MHz, respectively. The corresponding first derivative signals (discriminator curves) for 1 MHz (red) and 5 MHz (blue) cavity linewidth are plotted as dashed lines. A black vertical line at zero detuning is included as reference for peak centers.

It should be more obvious from Figure 1.11 for how one can use this signal as feedback to lock the cavity length to the laser. The useful locking component of the discriminator

is the linear region around the zero amplitude crossing near the center. If the laser frequency is on the left side of the cavity mode, a positive voltage (amplitude) is fed back to the cavity to shift it back to center. If the laser frequency is on the right side of the cavity mode, a negative voltage is used as feedback. Finally, if the cavity is locked to the laser, then the laser frequency coincides with the peak of the cavity mode, and the discriminator (error) signal would be zero. Consequently, this locking scheme is called a peak lock. Also displayed on Figure 1.11 are the differences between locking to a narrow (1 MHz, red) and larger (5 MHz, blue) cavity linewidth. The feedback signal is significantly larger around a smaller frequency deviation about zero for the 1 MHz than the 5 MHz linewidth. Therefore, better frequency stability of the *FSR* is achieved by locking to a 1 MHz cavity linewidth compared to 5 MHz.

1.4.3 Locking the cavity length to the 633nm DBR laser – Instrumentation

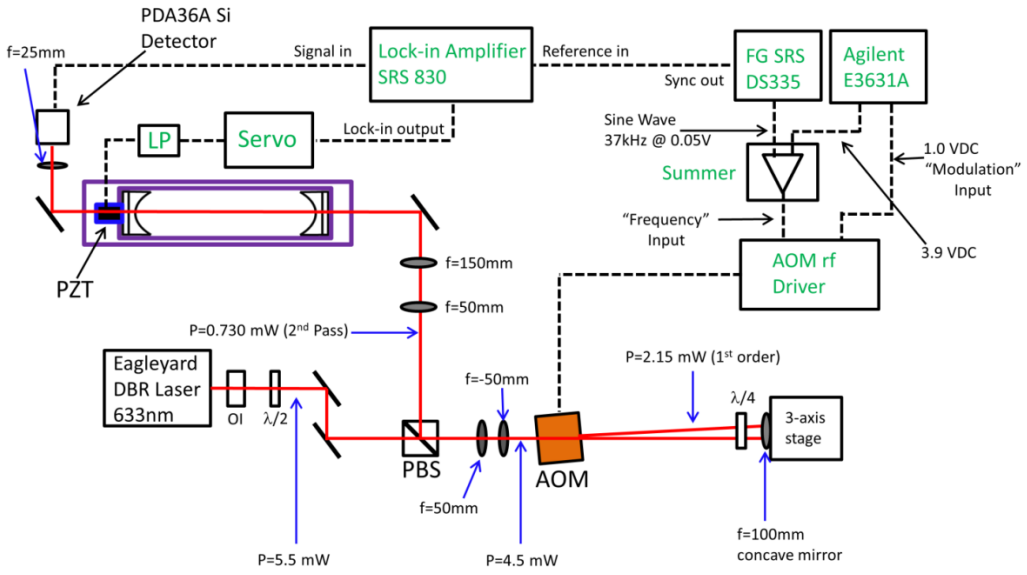

Figure 1.12: Schematic of instrumentation for locking the cavity to a stable DBR 633nm laser. The 633 nm DBR laser light is sent through a double pass AOM configuration to produce the FM beam for producing the discriminator signal. The laser is coupled to a cavity with high-finesse cavity (purple) with a PZT mirror mount on one side. Output from the Si detector is sent to a lock-in amplifier for obtaining the discriminator curve. The discriminator curve is the error signal that after servo filtering is sent to the PZT to control lock the cavity length.

The instrumentation to generate the discriminator curve and locking are shown in Figure 1.12 and is based on the design by Hodges et al.[9] The free-space 633nm DBR laser is mounted on an ILX butterfly mount (LDM-4980). The laser output passes through an optical isolator (OI, Thorlabs IO-3D-633) and a λ/2 waveplate prior to coupling to a polarizing beam splitter cube (PBS). In this experiment, the frequency modulation (FM) of the DBR laser is achieved by an acousto-optic modulator (AOM). The light is focused by a pair of telescoping lenses (f=50 mm and f=-50 mm) lenses prior to coupling into a Brimrose AOM (TEF-400-100-0.633). The AOM is turned on by a fixed 1 VDC signal supplied by the Agilent E3631 DC supply via the AOM rf driver's "modulation" input. A sinusoidal waveform output from a SRS function generator (DS335) modulates the laser (via the AOM rf driver's "frequency" input) at a frequency of 37 kHz and modulation depth of 0.04 V (≈1.1 MHz excursion). A common problem with using an AOM is the fact that the diffracted beam is deflected at an angle compared to the input beam. In this case, the addition FM on the 1st order diffracted beam induces a sinusoidal modulation of the beam pointing direction, which can prevent cavity coupling. As a result, the 1st order diffracted beam (≈48% diffraction efficiency) is sent through a double pass configuration to overcome this problem.[10] This is achieved by sending the first order through a $\lambda/4$ waveplate to a concave mirror (f=100 mm), which sends the back reflected light through the AOM for a second diffraction (≈28% efficiency). The two passes through a $\lambda/4$ waveplate result in an effective rotation of the input beam polarization by 90°. By conservation of momentum, the second diffraction beam retraces the original input beam and compensates for the initial 1st order beam deflection. This analysis was previously done by Donley et al.[10]. This double pass configuration results in

a favorable scenario that the beam pointing position is immune to any FM signal imposed on it. Finally, this 2nd diffraction beam retraces the input path and passes through the PBS cube, which sends the beam in the direction orthogonal to the DBR laser input beam.

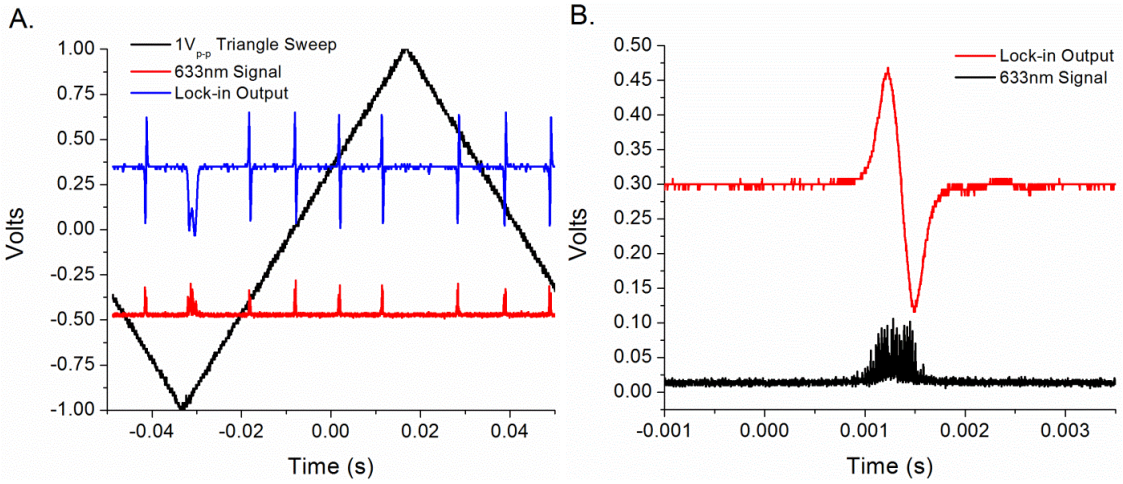

Figure 1.13: A) Output of the Si detector (red) and the lock-in amplifier (blue) as the cavity PZT is modulated by a triangle waveform (black) at 10 Hz. B. Zoomed-in image of A to a single cavity resonance. The peak of the cavity mode corresponds to the zero crossing point of the first derivative signal, consistent with Figure 1.10.

The 2nd pass beam is mode matched to the cavity by a telescopic lens system to reduce the input beam waist to match the cavity waist. The transmitted beam is focused into a Thorlabs Si detector (PDA36A). The output of the detector is sent to the signal input of a SRS lock-in amplifier (SR830). The reference input required for phase sensitive detection is the Sync output of the function generator (SRS DS335). The output of the lock-in amplifier (blue) with the corresponding cavity modes (red) are shown in Figure 1.13 as the cavity PZT is modulated by a triangle wave (black) at 10 Hz (1 V_{p-p}). The signal from Figure 1.13B is the experimental version of Figure 1.11. Figure 1.13A shows the four cavity FSRs that are swept across by a 1 V_{p-p} triangle waveform. Figure 1.13B is a zoomed-in image of 1.13A to show the cavity mode and the first derivative

signal form the lock-in amplifier. Once again, the peak of the cavity mode is centered at the center (zero crossing) of the discriminator curve. It should be mentioned that the error signal should be maximized to obtain the highest signal-to-noise. This can be done by changing the detection phase on the lock-in amplifier. A general procedure that works well is first to manual adjust the phase so that the first derivative signal goes to zero, then add a 90° phase shift to obtain the maximum amplitude. The error signal is subsequently filtered and shaped by an electronic servo (Vescent Photonics D2-125, Newport LB1005), then fed back into the cavity PZT to lock the cavity length to the 633 nm DBR laser. It is also safe practice to install a passive low pass (LP) filter (≈1 kHz) between the servo and the cavity PZT. This protects the PZT from any large amplitude, high-frequency signal that is resonant with the PZT's resonance frequency (typically f_{res} ≈10-20 kHz) for Piezomechanik mounted PZT).

A servo, also called a loop filter, is an electronic device that shapes the error signal prior to feedback on the cavity PZT actuator. The practice of servoing for laser locking requires sufficient understanding of control theory and circuitry. A quick introduction to topics of generating error signals and locking can be found in Nagourney's text in Chapters 11-12.[3] In general, it is important to consider the frequency responses of the system under control (e.g., lasers, cavity PZT, etc.) so that one can shape the gain and frequency/phase response transfer functions of the error signal using the loop filter. There are additional considerations of lock loop stabilities that are outside the scope of this thesis. A very useful reference for more details about laser-cavity lock stabilities is from a book chapter by Fox et al.[11]

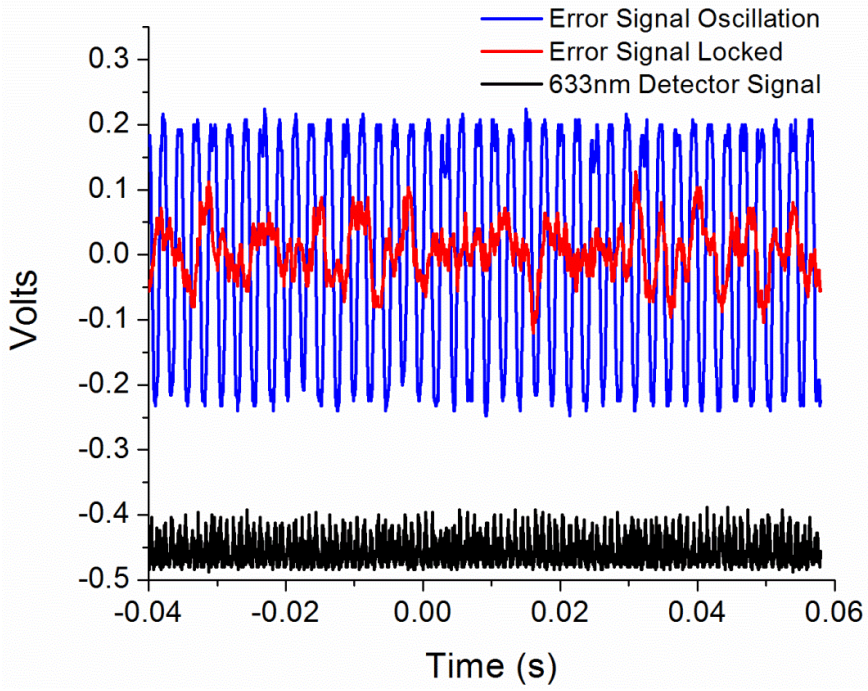

Figure 1.14: Oscilloscope signals to indicate a successful cavity lock. All traces were DC coupled. Black trace: Si detector signal. A locked transmission signal should have a DC offset from zero and remain at that level as long as the lock is engaged. Red trace: error signal indicating a successful lock. The error signal amplitude fluctuates around zero volts. Blue trace: error signal oscillation, indicating that further servo tuning (gain, low pass frequency, etc.) is needed.

After the servo and low pass filter, the error signal is sent to actuate the cavity PZT. The servo low pass filter frequency setting should be set to 1 KHz or less since the locking bandwidth is limited by the PZT bandwidth. The Si detector signal and the error signal output from the servo should be connected to an oscilloscope for observing a cavity lock. Example oscilloscope traces are shown in Figure 1.14. Make sure to DC couple oscilloscope traces for both the Si detector signal and the error signal since we are measuring changes in DC signals. First, the PZT voltage should be manually tuned so that the cavity length becomes resonant with the 633nm DBR laser frequency. The Si detector signal (black trace) should jump around when near resonance, indicating transient cavity coupling and transmission. After tuning to near resonance, the servo

output should be turned on to observe the lock. The error signal (red trace) should fluctuate around zero volts on the scope, indicating a successful lock. This should be intuitive from Figure 1.11: When the cavity mode center frequency is resonant with the laser frequency, the error signal has zero amplitude. Another indication of a successful lock is the signal from the Si detector. If DC coupled, the transmission should increase to and stay at some DC value (black trace). The large variance in the black trace is due to the 633nm laser amplitude noise. As the name suggests, the fluctuation in the output laser intensity causes the same observed behavior in the transmission intensity. A successful lock can be feeble causing a loss of lock after a short period of time or external perturbation to the cavity. A common cause for a weak lock is a noisy error signal. One should take extra measures to maximize the signal to noise ratio of the error signal by changing the settings on the lock-in amplifier. In addition, non-optimal gain and bandwidth settings on the servo can result in a weak lock.

If cavity lock was not successful, there are a few reasons. First, if the lock is unstable due to incorrect servo settings, then an oscillation of the error signal will be observed, similar to the blue trace. A second common mistake is setting servo gain and/or low pass filter too high so that the lock loop becomes unstable. Third, the cavity alignment is not good enough to suppress nearby higher-ordered TEM modes such that the lock jumps cavity modes. Finally, if lock was not successful after tuning on the servo, this could be an indication that the error signal phase is 180° out of phase: positive feedback is occurring rather than negative feedback. This can be easily tested by changing the error signal phase from the lock-in amplifier by 180°.

1.5 Frequency-stabilized cavity ring-down of near-IR and IR.

1.5.1 Cavity ring-down background

Cavity ring-down spectroscopy (CRDS) with pulsed or continuous-wave (CW) lasers is a well-known cavity-enhanced spectroscopic method that can provide precise and absolute quantitative measurements.[9, 12-14] In spectroscopy, one desires to determine the absorption coefficient, α, from measuring light absorption as expressed in eq. 39.

$$I(t) = I_0 e^{-\alpha L_{eff}} \quad \text{eq. 39}$$

I(t) is the time dependent light intensity, I_0 is the input light intensity, and L_{eff} is the absorption path length. α is the product of the absorption cross section, σ, and the number density, N: $\alpha = \sigma \times N$. In a cavity ring-down experiment, the exponential decay of the input light intensity at characteristic time τ is measured (eq. 40).

$$I(t) = I_0 e^{-t/\tau} \quad \text{eq. 40}$$

Eqs. 39-40 have similar forms, differing only in the exponential term. Therefore, if τ could be equated to αL_{eff}, we could determine α from an experimental ring-down measurement. In fact, a simple algebraic derivation leads to the central cavity ring-down relationship between α and τ as expressed in eq. 41. d is the mirror spacing distance and c is the speed of light.

$$\alpha = \frac{d}{cL_{eff}}\left(\frac{1}{\tau_{abs}} - \frac{1}{\tau_{vac}}\right) \quad \text{eq. 41}$$

Here, τ_{vac} (eq. 42) and τ_{abs} (eq. 43) correspond to the laser ring-down times in vacuum and with absorber, respectively. *R* is the mirror reflectivity.

$$\tau_{vac} = \frac{d}{c(1-R)} \quad \text{eq. 42}$$

$$\tau_{abs} = \frac{d}{c((1-R)+\alpha L_{eff})} \quad \text{eq. 43}$$

It is important to note that since α is determined without directly measuring the light intensities, $I(t)$ and I_0, CRDS is essentially immune to laser intensity noise. Also, since L_{eff} is in the denominator, α becomes increasingly small (higher sensitivity) as the cavity *finesse* (i.e., mirror reflectivity) is increased.

Now we want to determine how the uncertainty in the measured τ propagates to the uncertainty in determining α. By taking partial derivatives with respect to τ_{vac} and τ_{abs} from eq. 41, the following relationship is established between the uncertainties in α, $\delta\alpha$, and τ, $\delta\tau$:

$$\delta\alpha = \frac{d}{cL_{eff}}\left[\frac{\left(\tau_{vac}^{\,2} - \tau_{abs}^{\,2}\right)}{\left(\tau_{abs}^{\,2}\tau_{vac}^{\,2}\right)}\right]\delta\tau \quad \text{eq. 44}$$

Following the analysis by Demtröder[15], we define an averaged $\tau_{avg} = (\tau_{vac} + \tau_{abs})/2$. With the assumption that $\tau_{vac} - \tau_{abs} << \tau_{avg}$, we can show that eq. 44 becomes

$$\delta\alpha \approx \frac{d}{cL_{eff}}\left[\frac{2\left(\tau_{vac} - \tau_{abs}\right)}{\left(\tau_{avg}\right)^3}\delta\tau\right] \quad \text{eq. 45}$$

It is apparent from eq. 45 that the highest sensitivity is achieved when τ_{avg} is longest, which means that the mirror reflectivity should be as high as possible.

1.5.2 Frequency-stabilized cavity ring-down spectroscopy

The cw-CRDS experiments in our group started with a collaboration with Dr. Joseph Hodges at NIST in Gaithersburg, MD. His group first implemented the frequency stabilization in cw-CRDS for molecular spectroscopy.[9, 16] Details of this experiment are described in detail from PhD theses by David Long[17] and David Robichaud[18] for the experiments performed at NIST. We have implemented this technique for spectroscopy of methane isotopes near 1.65 μm and CO_2 lineshapes studies near 2.06 μm. The instrumentation for the probe laser side is shown in Figure 1.15.

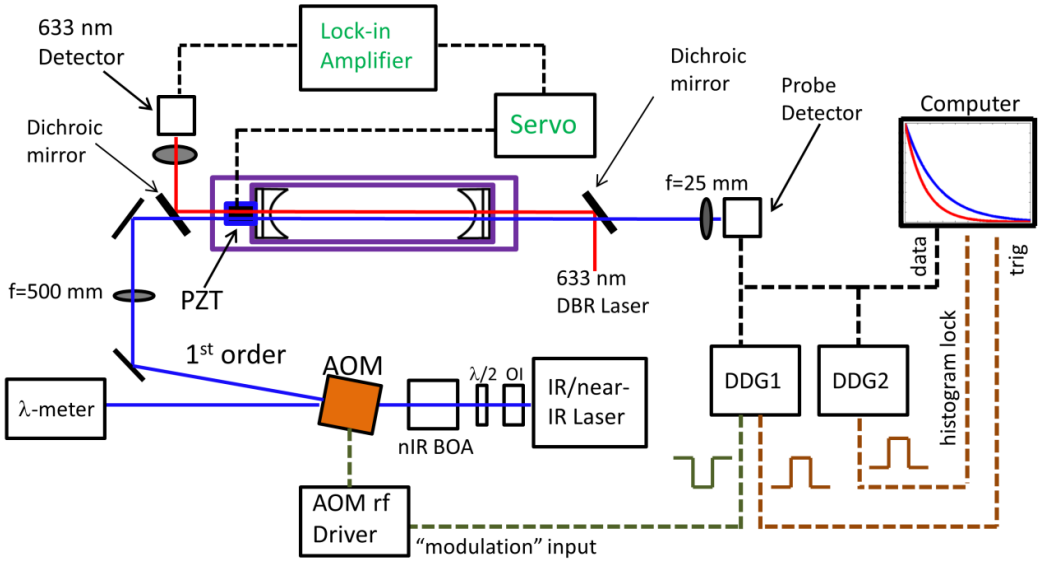

Figure 1.15: Schematic of instrumentation FS-CRDS. Details are in the text. The near-IR lasers are amplified by a booster optical amplifier (BOA). Output of the amplifier is fiber coupled into an AOM. The 1st order beam is mode matched into the ring-down cavity by a single lens. The transmitted beam is detected by a photodetector, which sends out a voltage signal to trigger DDG1 and DDG2. The detector signal is also sent to a digitizer card for ring-down decay measurement.

Note that this figure complements Figure 1.12, which show the components for the cavity lock to the 633 nm DBR laser. Also, only components that are unique to our system are described since the methods of operation is already published by David Long[17] and David Robichaud[18].

The cavity lock components (Figure 1.12) have been condensed to the 633 nm DBR laser, lock-in amplifier and servo. The probe laser (near-IR or IR) output is shown in blue. For near-IR wavelengths, we have two DFB lasers (1.45-1.65 μm) and one ECDL laser (Newfocus Velocity 6330, 1.55-1.63 μm). The near-IR lasers are amplified by the booster optical amplifier (Thorlabs BOA1080P) mounted on a Thorlabs butterfly mount (LM14S2). Output of the near-IR laser is sent to a fiber-coupled AOM (Brimrose model MM55-8-70-1600-3FP+). The 0^{th} order output is used for measuring the wavelength (Bristol 621). The 1^{st} order output is coupled into the ring-down cavity via dichroic mirrors. These dichroic mirrors were custom coated by CVI Melles Griot to reflect 633 nm and transmit 1550-1660 nm. The purchased model code was: LWP-45-RS633-TP1550-1650-PW1-1. The transmitted near-IR beam is mode matched to the cavity by a single f=500 mm lens. The output beam is measured by a 10 MHz photodetector (Newfocus 2053-FS). The signal from the photodetector is split three ways: DDG1, DDG2 and "data" channel of the Gage Digitizer card (OSCAR-14, CSE4327, 14 Bit, 100 MS/s, 1GS) on the computer. After being triggered by the near-IR detector signal, DDG1 (SRS DG535) sends out a -4 V pulsed signal to shut off the AOM and a +4 V pulsed signal to trigger the Gage digitizer. With the AOM off, the cavity light decay is measured with the "data" channel. The same detector signal is also used to trigger second DDG2 (BNC model 575), which sends out a burst of pulses to serve as part of the

"histogram" locking described in Hodges and Ciuryło[16] and David Robichaud's thesis[18]. In general, the histogram lock is a slow bandwidth lock to keep the probe laser near cavity resonance. With this approach, we have achieved up to acquisition rates of 300 Hz for ring-down acquisition. Note that this is still a very small duty cycle. The ring-down time constant for a cavity with R=0.99995 mirrors is τ=50 μs. Allowing for a total duration of 1.5τ for the ring-up time and 6τ for the ring-down time, the theoretical acquisition rate achievable is $(7.5\tau)^{-1}$ or ≈2.7 kHz. A maximum 300 Hz acquisition rate corresponds to an 11% duty cycle. Finally, the IR system (λ=4.3-4.5 μm) differs only in the type of cavity mirrors, dichroic mirrors (RMI, part number: RT1012C0634204), detector (VIGO PVI-4TE-5), and common other optical elements like lenses and mirrors. All other electronic components remain the same.

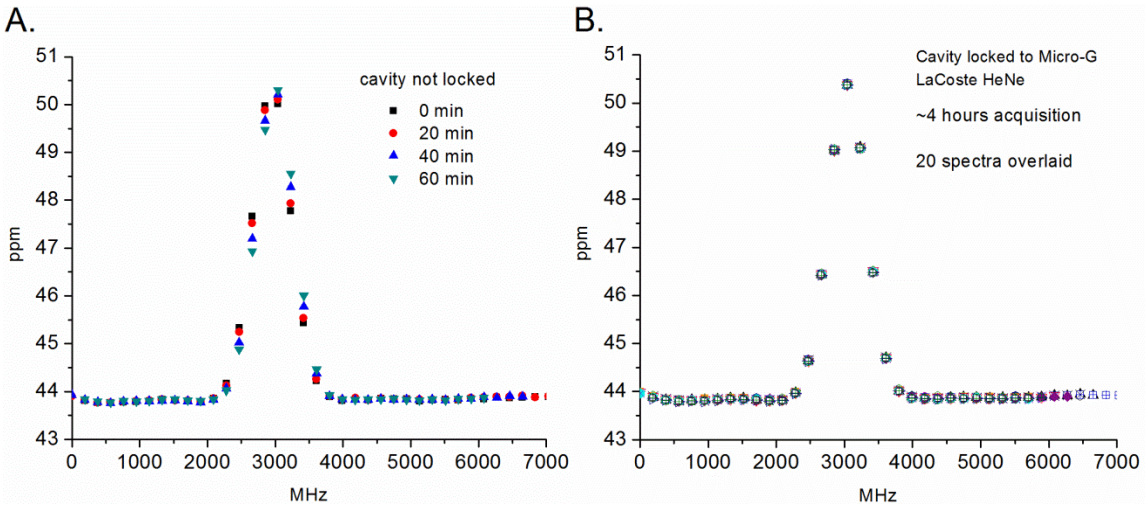

Figure 1.16: A. Spectra collected over 1 hour with cavity in free drift. B. Spectra collected over > 4 hours with cavity locked. In both cases, the same $^{12}CH_3D$ transition near 6457.0327 cm^{-1} is acquired.

To compare performances of conventional cavity ring-down spectroscopy with FS-CRDS, we measured time-lapsed spectra ($^{12}CH_3D$, 6457.0327 cm^{-1}) with the cavity in free drift (Figure 1.16A) and locked to a Micro-g LaCoste HeNe (Figure 1.16B). Figure 1.16A show the frequency drift of the discrete spectral points over a period of one hour,

which is a result of the natural drift of the cavity FSR. From the frequency to amplitude conversion on the left side of the spectra near 47 ppm, we can estimate that the frequency drift is ~ 50 MHz within one hour for an unlocked cavity. On the other hand, Figure 1.16B show the 20 overlaid spectra acquired over >4 hours with the cavity locked to a stabilized HeNe laser. Here, the frequency drift is too small to quantify because the standard deviation for the discrete point near 46 ppm for the 20 spectra is within instrumental noise (~ 0.013 ppm).

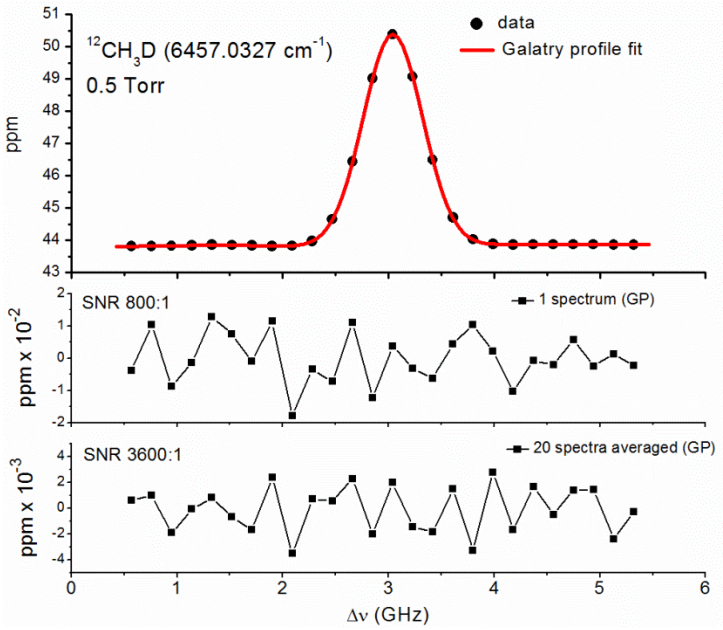

Figure 1.17: Spectra fit results using the Galatry line profile for single spectrum and 20 averaged spectra for data in Figure 1.16B. The fitted SNR improves by a factor >4.

Since the discrete points in Figure 1.16A cannot be averaged without introducing distortion into the spectrum, conventional CRDS is limited by natural drifts over long time scales. The advantage of FS-CRDS is displayed in Figure 1.17, which compares the single spectrum and 20 averaged spectra fit results using the Galatry line profile for data in Figure 1.16B. The fitted signal to noise ratio for the 20 averaged spectra improved by a factor of >4 over the single spectrum case.

1.6 References

1. Yariv, A. and P. Yeh, *Photonics: Optical Electronics in Modern Communications*. 6th ed. 2006: Oxford University Press. 848.

2. Foltynowicz, A., *Fiber-laser-based Noise-Immune Cavity-Enhanced Optical Heterodyne Molecular Spectroscopy*, in *Physics*. 2009, Umea University: Sweden.

3. Nagourney, W., *Quantum Electronics for Atomic Physics*. 2010: Oxford University Press. 381.

4. Demtröder, W., *Laser Spectroscopy, Vol. 1: Basic Principles*. Fourth ed. Vol. 1. 2008: Springer.

5. Yoshida, Y. and T. Asakura, *A simple technique for quickly measuring the spot size of Gaussian laser beams.* Optics & Laser Technology, 1976. **8**(6): p. 273-274.

6. Thorpe, M., *Cavity-enhanced direct frequency comb spectroscopy*, in *Physics*. 2009, University of Colorado. p. 200.

7. Lisak, D. and J.T. Hodges, Appl. Phys. B, 2007. **88**(2): p. 317-325.

8. Blume, G., et al., *Narrow Linewidth of 633-nm DBR Ridge-Waveguide Lasers.* Ieee Photonics Technology Letters, 2013. **25**(6): p. 550-552.

9. Hodges, J.T., et al., Rev. Sci. Instrum., 2004. **75**(4): p. 849-863.

10. Donley, E.A., et al., *Double-pass acousto-optic modulator system.* Review of Scientific Instruments, 2005. **76**(6): p. 6.

11. Fox, R.W., C.W. Oates, and L.W. Hollberg, *Stabilizing Diode Lasers to High-finesse Cavities*, in *Experimental Methods in the Physical Sciences: Cavity-Enhanced Spectroscopies*. 2001.

12. Okeefe, A. and D.A.G. Deacon, *CAVITY RING-DOWN OPTICAL SPECTROMETER FOR ABSORPTION-MEASUREMENTS USING PULSED LASER SOURCES.* Review of Scientific Instruments, 1988. **59**(12): p. 2544-2551.

13. Zalicki, P. and R.N. Zare, *CAVITY RING-DOWN SPECTROSCOPY FOR QUANTITATIVE ABSORPTION-MEASUREMENTS.* Journal of Chemical Physics, 1995. **102**(7): p. 2708-2717.

14. Romanini, D., et al., *CW cavity ring down spectroscopy.* Chemical Physics Letters, 1997. **264**(3-4): p. 316-322.

15. Demtröder, W., *Laser Spectroscopy, Vol. 2: Experimental Techniques*. Fourth ed. Vol. 2. 2008: Springer.

16. Hodges, J.T. and R. Ciuryło, Rev. Sci. Instrum., 2005. **76**: p. 023112.

17. Long, D.A., *Frequency-Stabilized Cavity Ring-Down Spectroscopy of O2 and CO2 to Support Atmospheric Remote Sensing*, in *Chemistry*. 2012, California Institute of Technology: Pasadena, CA. p. 167.

18. Robichaud, D.J., *High-Resolution Study of the O2 A-Band using Frequency Stabilized Cavity Ring-Down Spectroscopy*, in *Chemistry*. 2008, California Institute of Technology: Pasadena, CA. p. 174.

1.7 Appendix—CAD drawings

A. NIR Cavity Mount

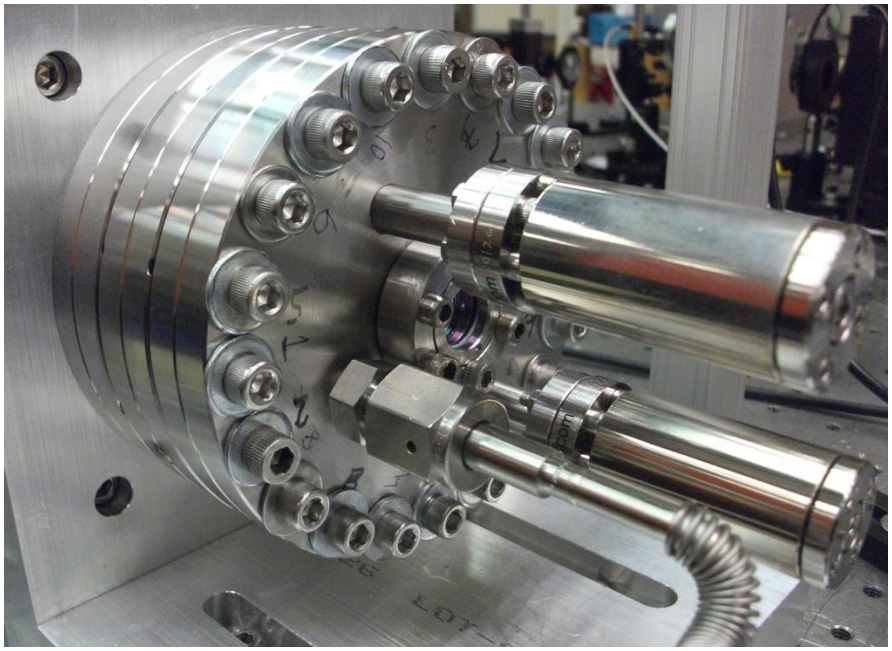

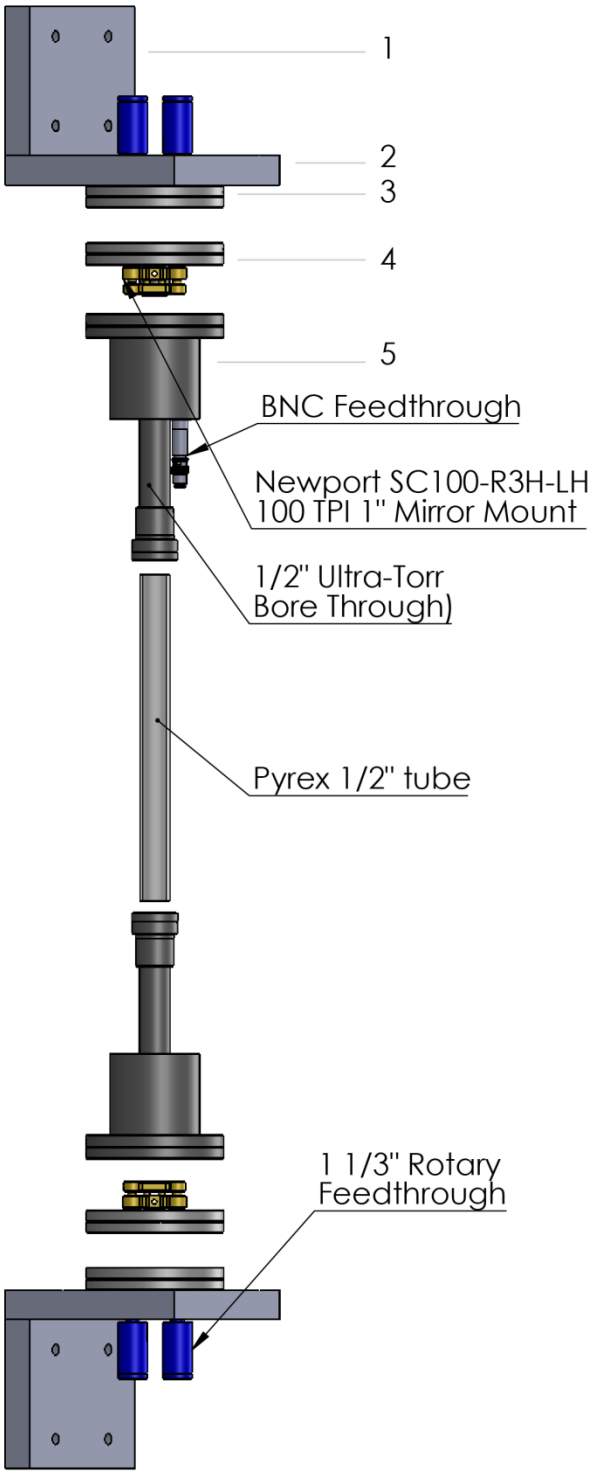
1
2
3
4
5
BNC Feedthrough
Newport SC100-R3H-LH
100 TPI 1" Mirror Mount
1/2" Ultra-Torr
Bore Through)
Pyrex 1/2" tube
1 1/3" Rotary
Feedthrough

A.1 Aluminum table mount

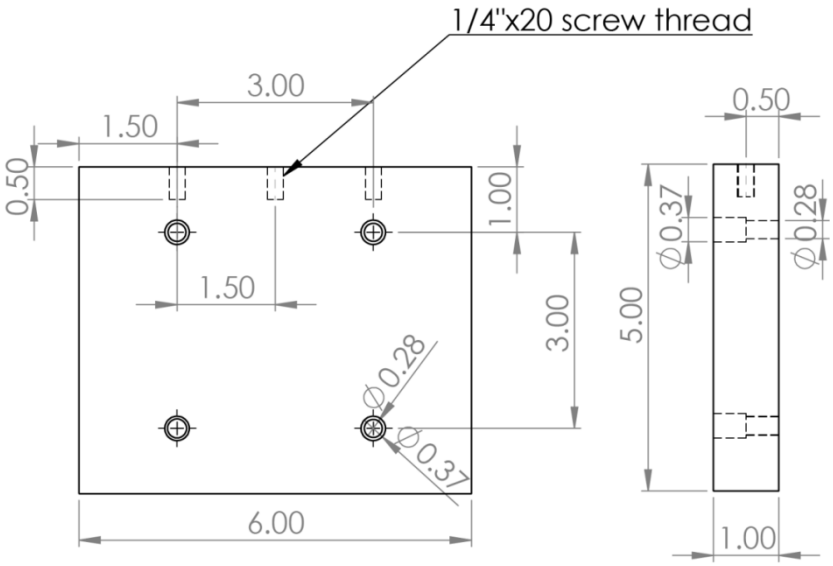

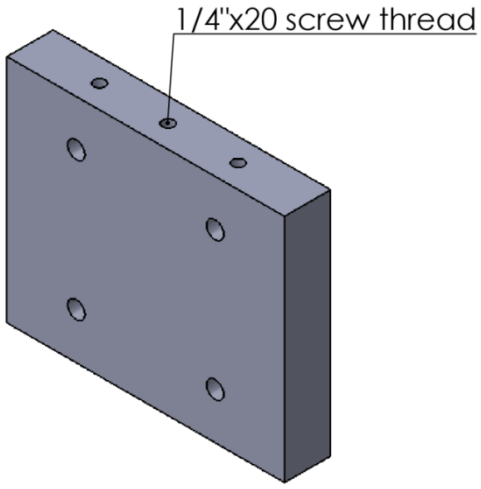

A.2 Aluminum cavity mount

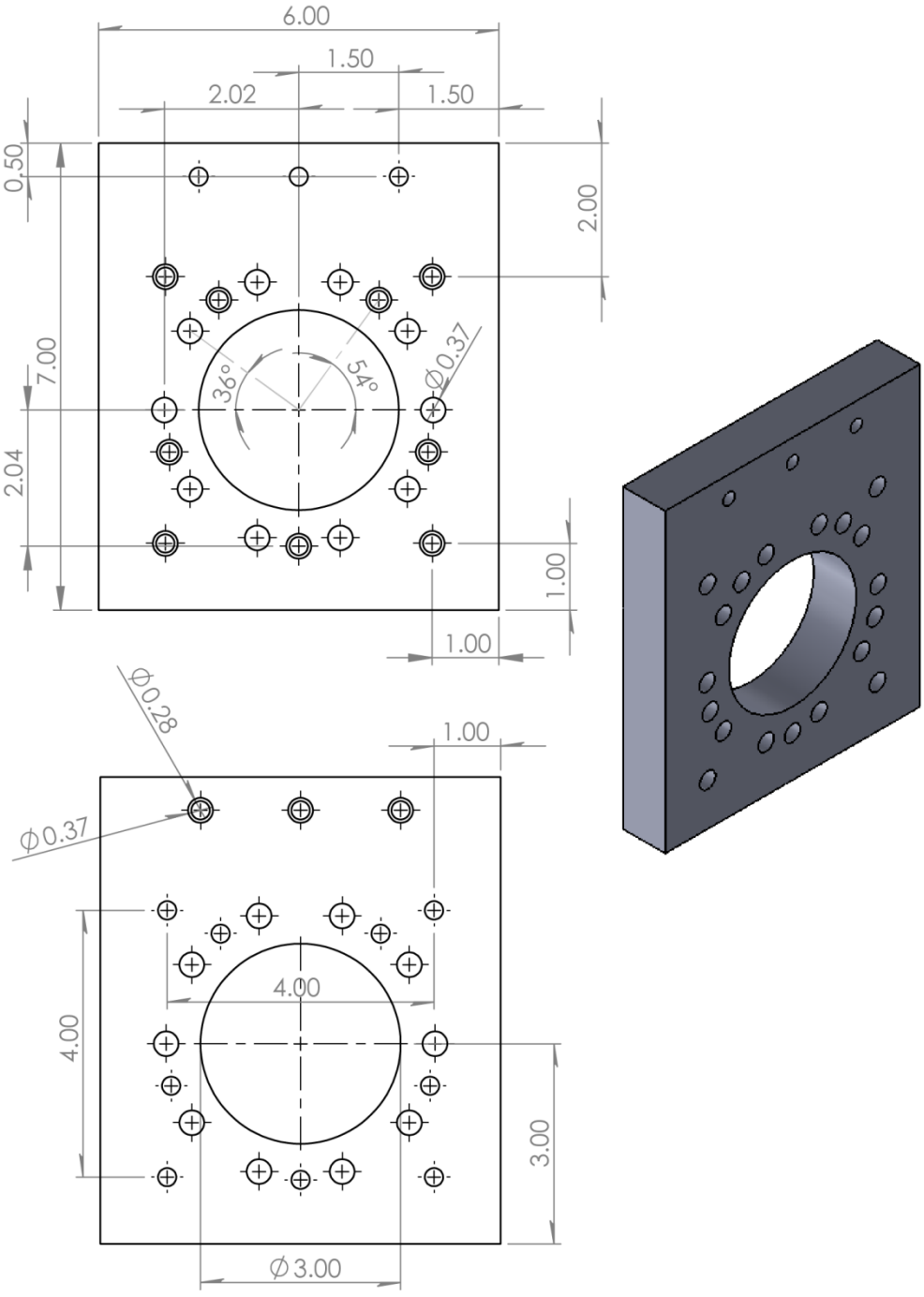

A.3 Window 4 5/8” CF flange

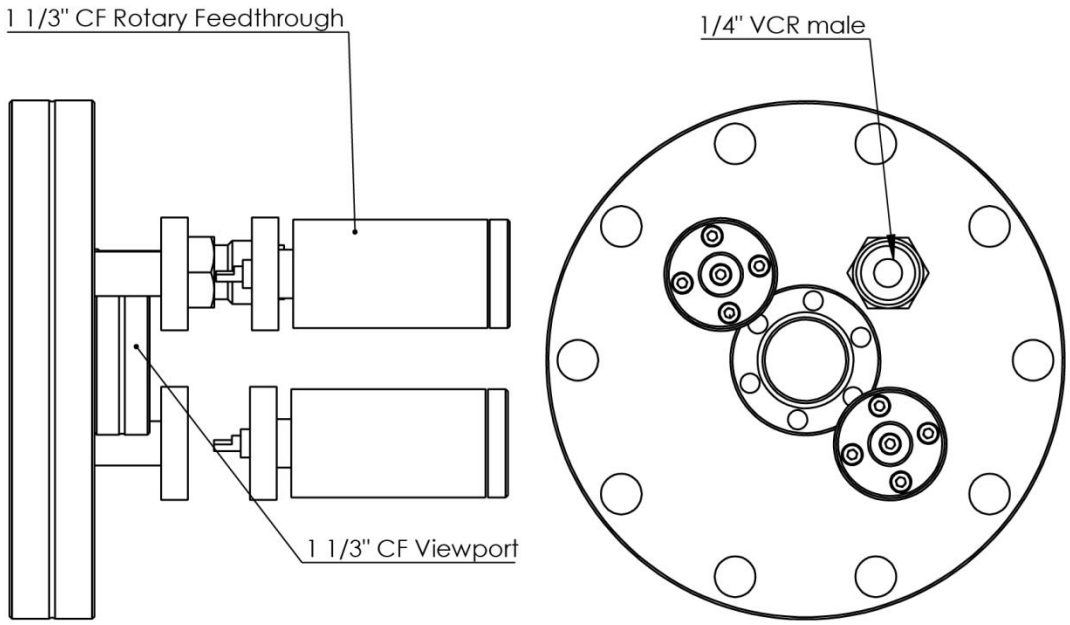

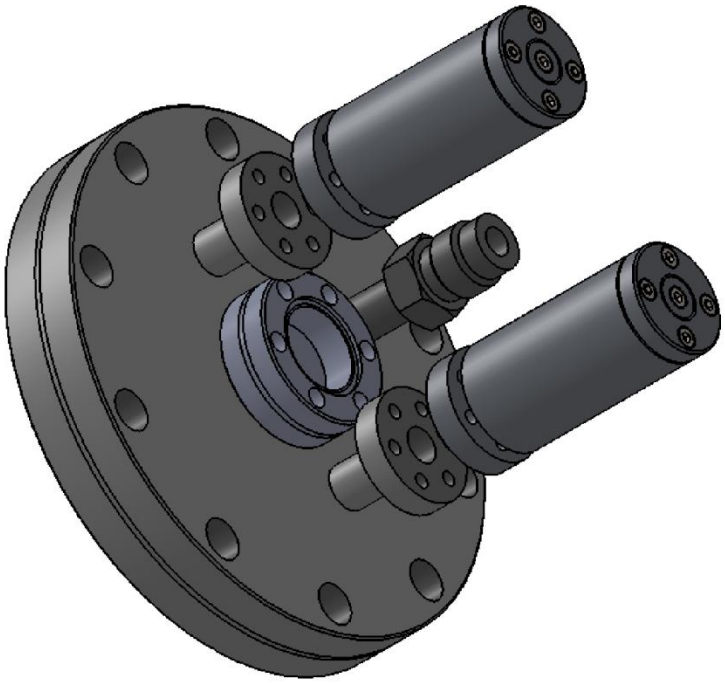

A.4 Mirror 4 5/8” CF flange

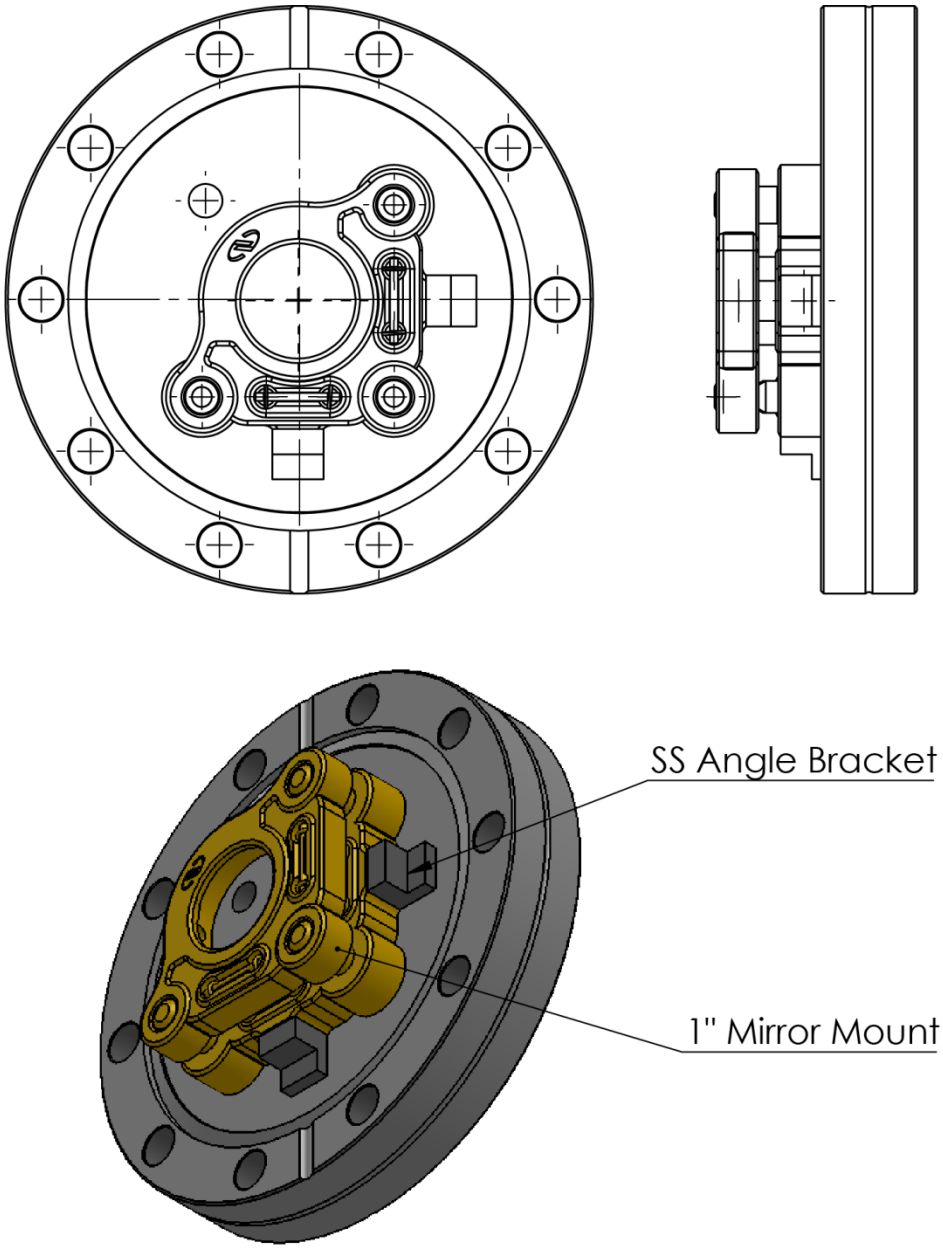

A.5 4 5/8” CF Ultra-Torr Flange

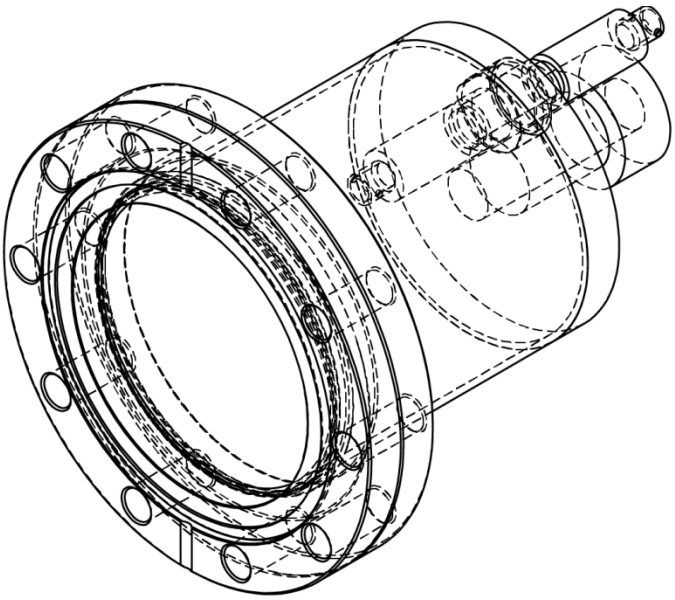

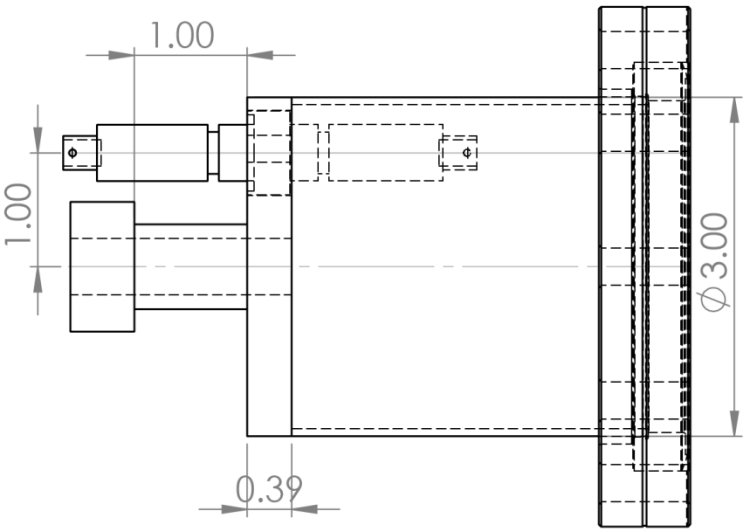

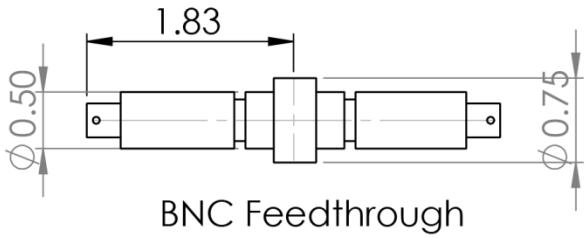

BNC Feedthrough

A.6 Window 4 5/8” CF Flange details

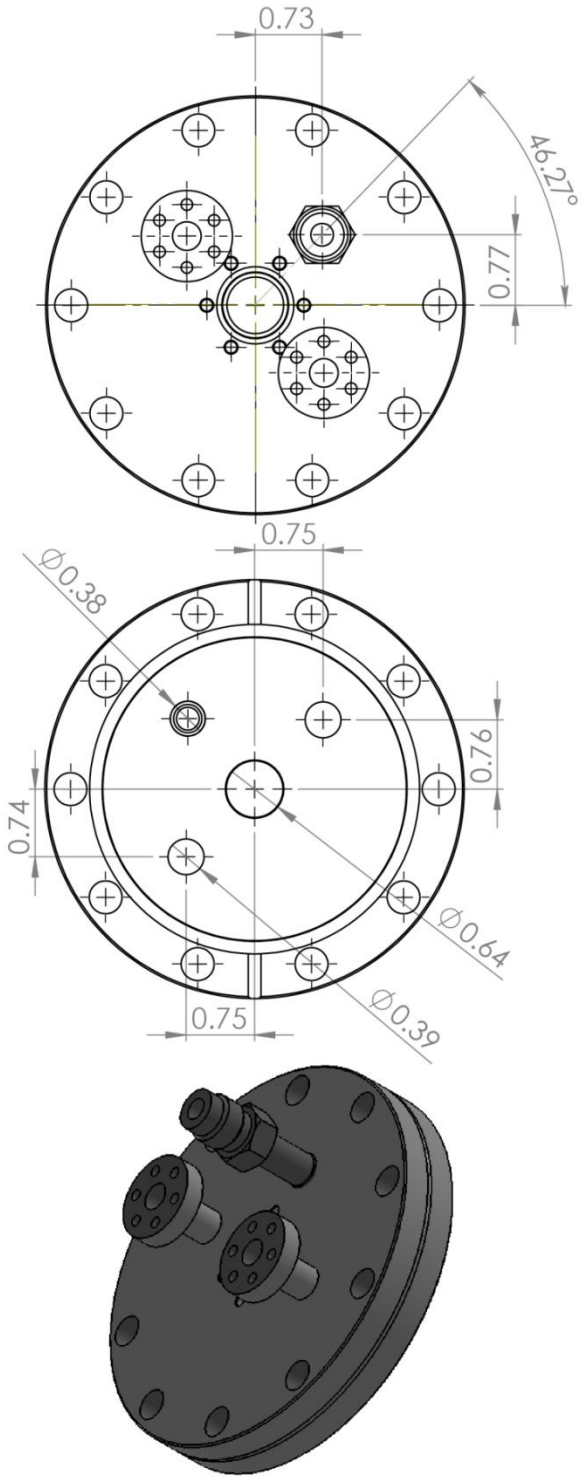

A.7 Mirror 4 5/8” CF flange details

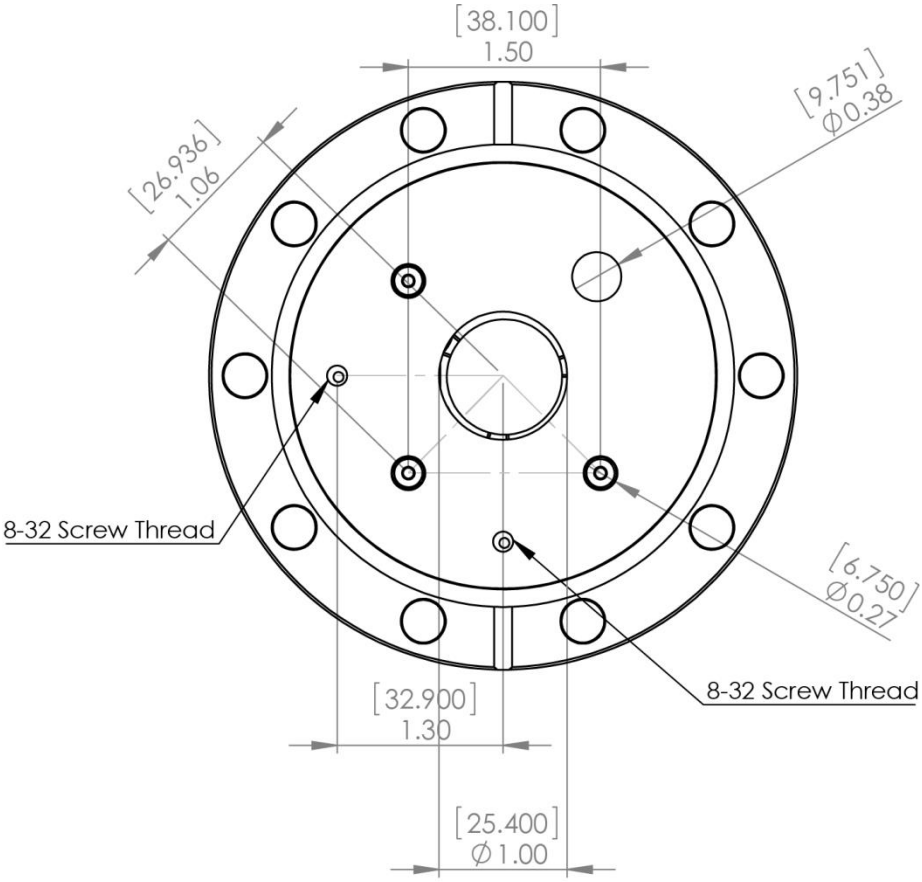

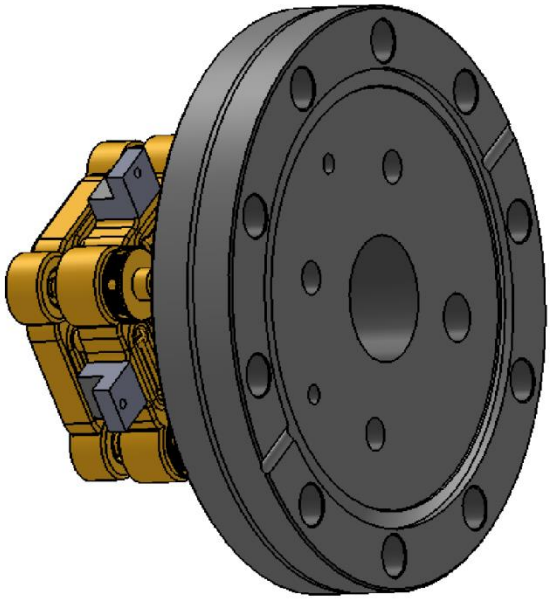

A.8 Angle Bracket for mirror mount to CF flange

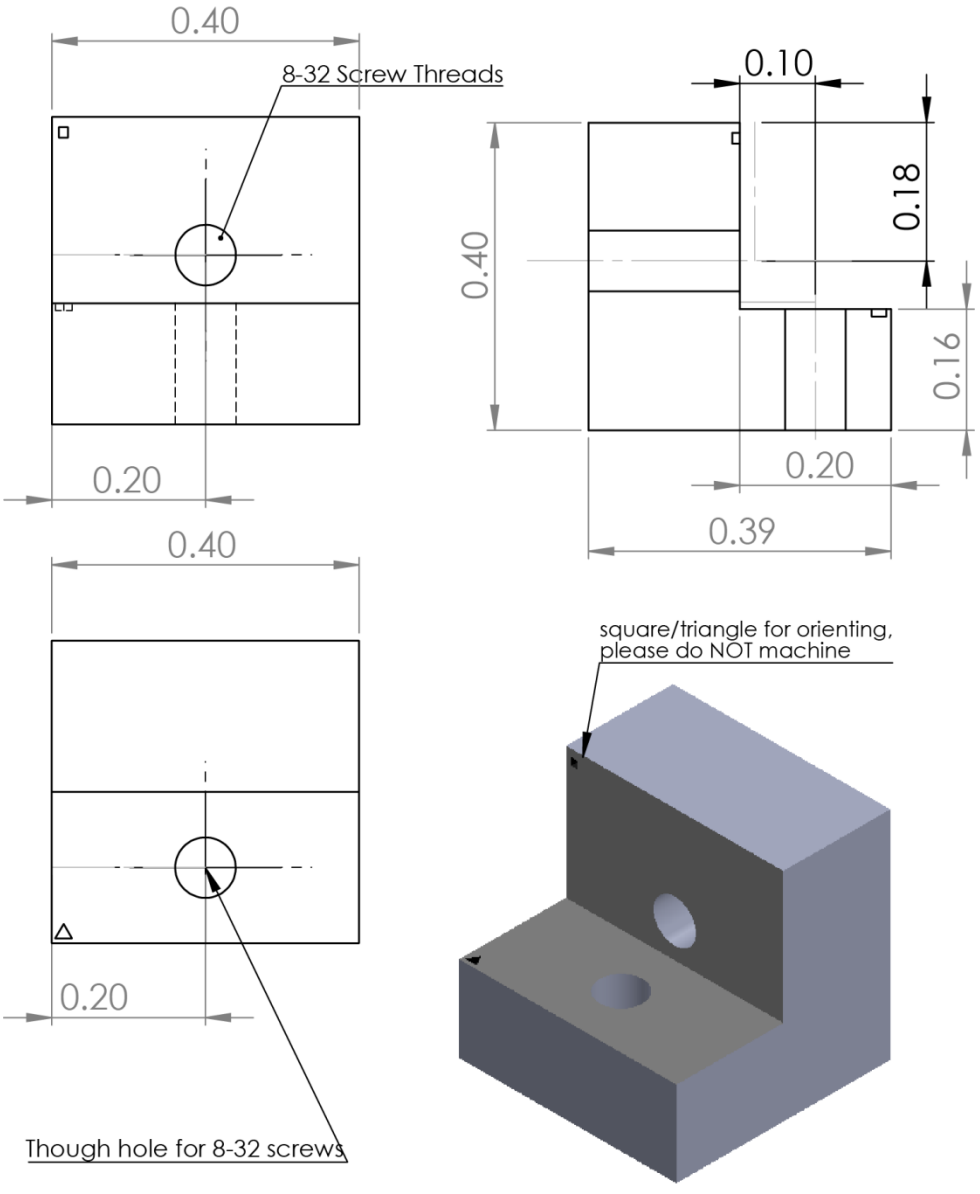

A.9 1 1/3” CF flange for rotary feedthrough

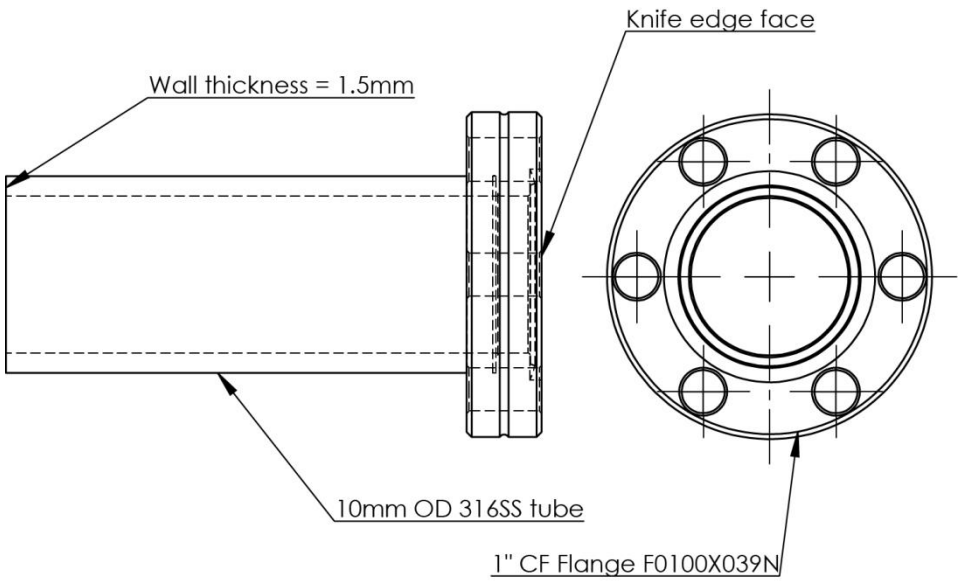

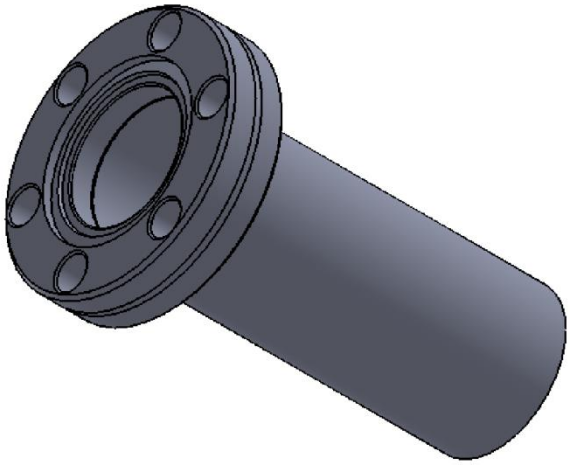

B. MIR Cavity Mount

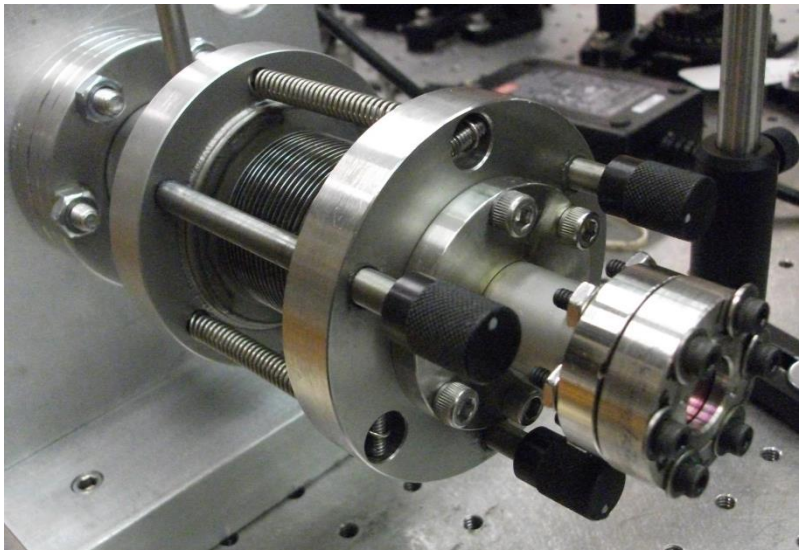

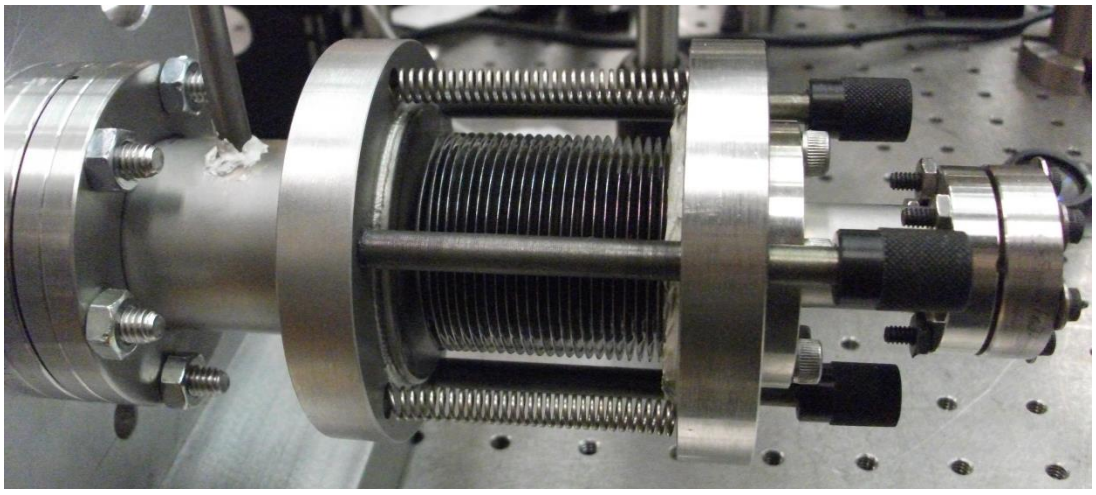

B.1 Mirror Mount Assembly

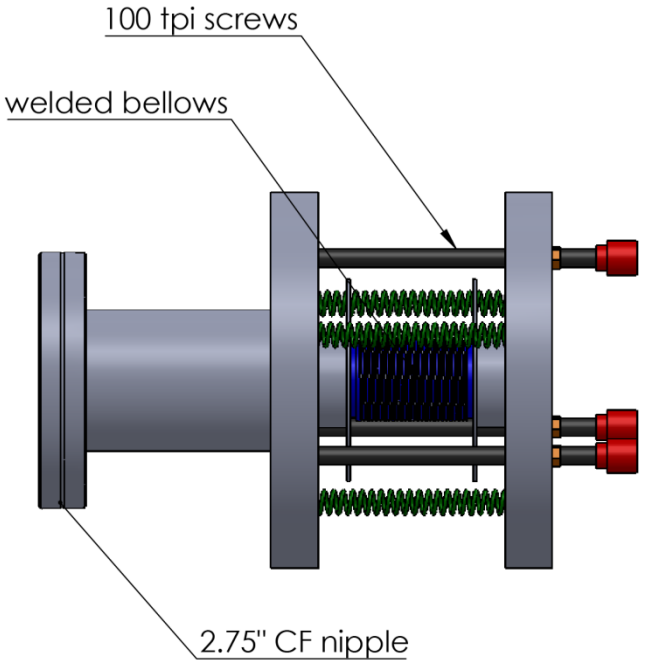

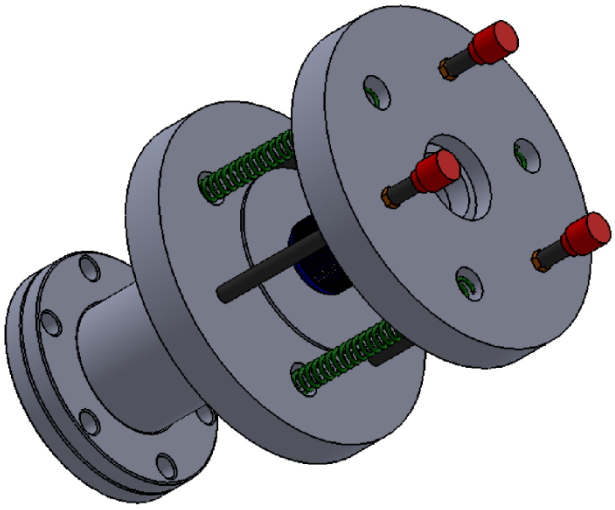

B.2 Mirror mount inner flange

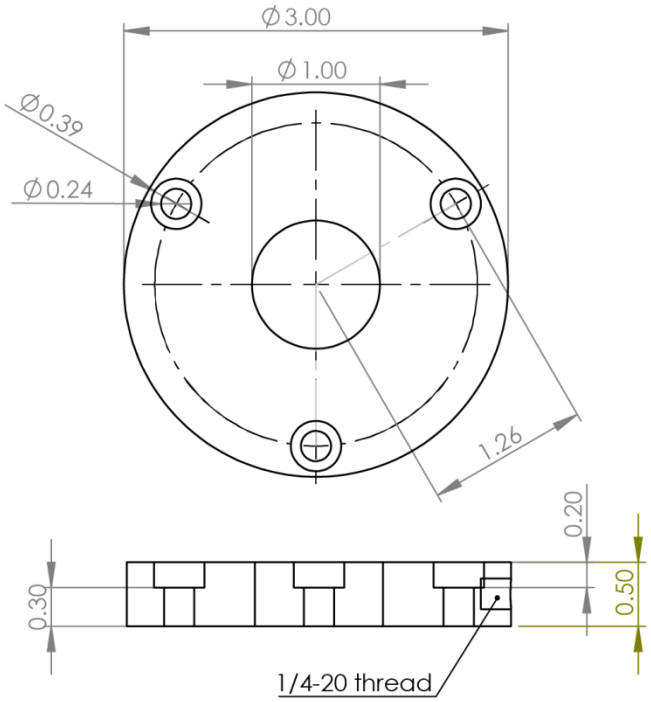

B.3 Mirror mount outer flange

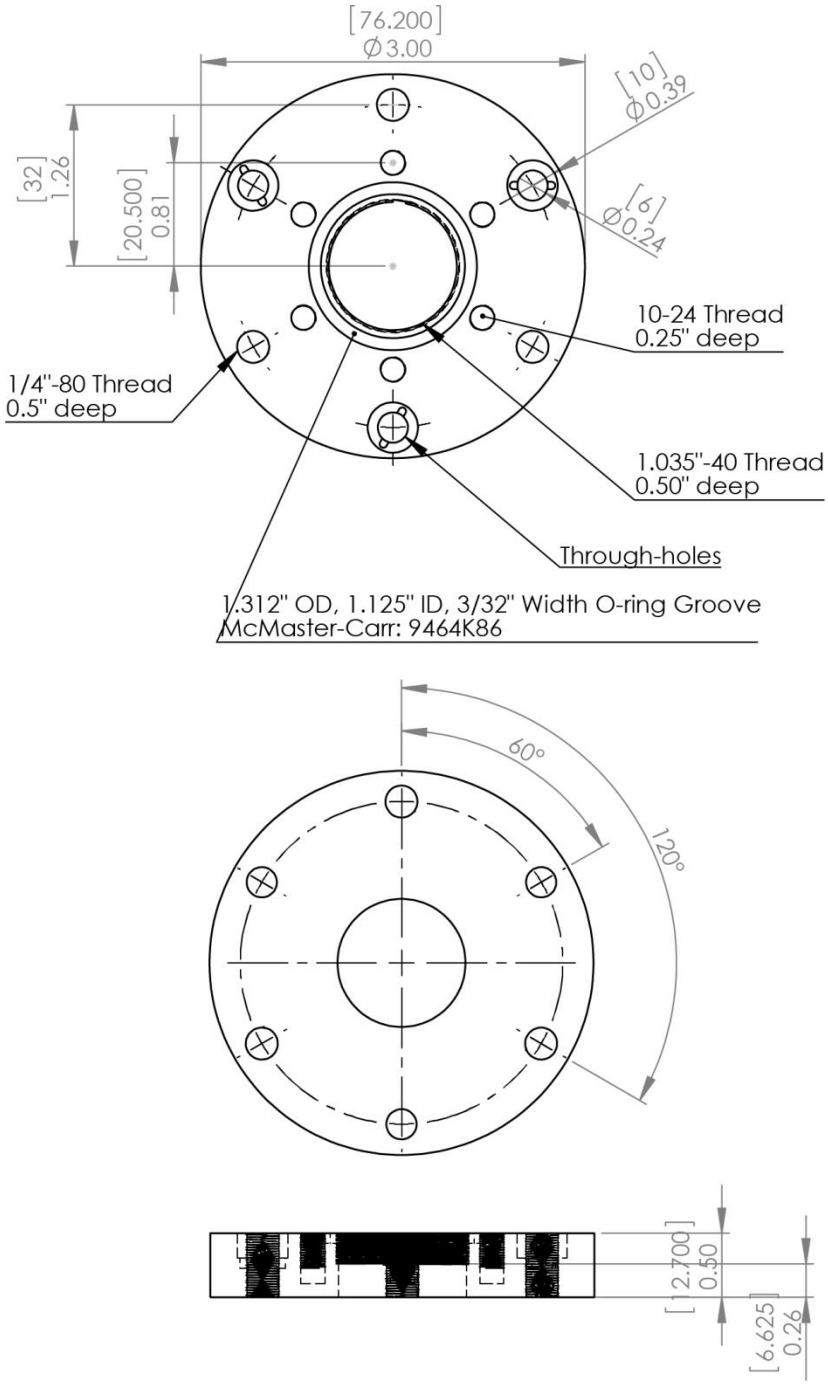

Chapter 2: Laboratory measurements of O_2 A-band in support of OCO-2

2.1 Abstract/Motivation for Laboratory Spectroscopy in Support of OCO-2

To achieve NASA's strategic scientific mission of monitoring global atmospheric CO_2 [NASA's Climate Architecture, 2010] at an unprecedented precision of 0.25%, we perform laser based laboratory measurements and lineshape studies of the O_2 A-band at 0.760μm and CO_2 at 2.06μm to meet the requirements of current (ACOS/GOSAT/TCCON) and future (OCO-2/OCO-3/ASCENDS) remote sensing applications. We utilize a high-precision (<0.01% uncertainty) photoacoustic spectrometer (PAS), at high spectral resolution and a large dynamic range, to provide unique measurements of unsaturated lineshapes of the O_2 A-band and frequency-stabilized cavity ring-down spectroscopy (FS-CRDS) for OCO-2's target CO_2 band at 2.06 μm (<0.003% uncertainty). These spectroscopic measurements and lineshape studies will target non-Voigt features (speed dependence, Dicke narrowing, line mixing, collisional-induced absorption) that introduce large baseline residuals, and if not properly accounted for, will compromise the precision requirements for current and future NASA's satellite remote sensing missions.

2.2 Introduction—OCO-2

CO_2, a natural component of the Earth's atmosphere, has recently drawn much attention due to its status as a primary man-made greenhouse gas and increasing role in radiative forcing—its concentration has steadily increased from 280ppm to 388ppm since

the industrial era 150 years ago.[19] Moreover, the specific nature, geographic distribution, and temporal variability of CO_2 sinks are still inadequately understood, which limits accurate predictions of their future impact on climate change.[20] OCO-2's space-based remote sensing of the temporal and spatial variations of CO_2 can reduce these uncertainties within the carbon sources/sinks by measuring the column-averaged CO_2 dry air mole fraction, X_{CO2}, with high precisions of 1 ppm (0.25%). OCO-2's strategy aims to retrieve X_{CO2} from a simultaneous fit of the near-infrared O_2 A-band spectrum at 0.760 μm and the CO_2 bands at 1.61 μm and 2.06 μm as measured by the OCO-2 satellite. *Therefore, this retrieval procedure for X_{CO2} requires precise and accurate knowledge of the line parameters for 1) the O_2 A-band, which is currently hindered by the poorly understood contributions of line mixing (LM) effects at higher pressures relevant to remote sensing, and 2) the CO_2 band at 2.06μm, for which the current lineshape data lacks the necessary precision (>>0.25%) and is not comprehensive for all non-Voigt effects (speed dependence, Dicke narrowing, line mixing, collisional induced absorption). These uncertainties in the lineshape parameters inherently imposes biases >>0.25% leading to spurious results in the remote sensing observational data.* As an example, Figure 2.1 shows the evolution of the O_2 A-band lineshapes as a function of pressure and the contributions from line mixing, which is currently not adequately treated at the 0.25% level.

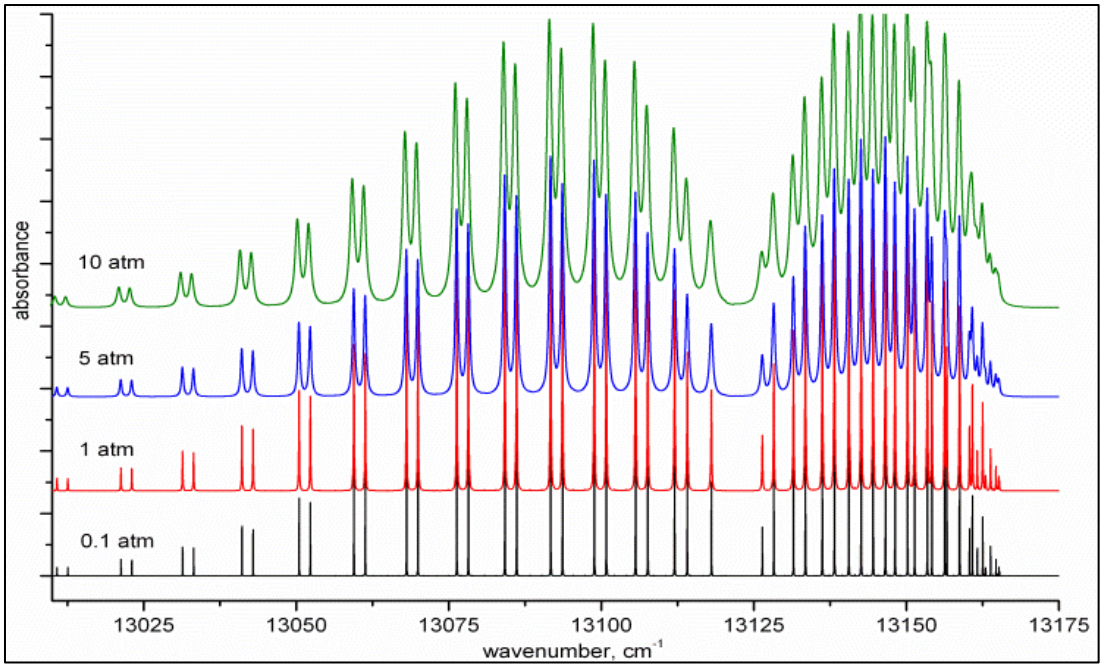

Figure 2.1: Simulation of air-broadened O_2 A-band spectra as a function of pressure using values from HITRAN 2012[21]. At higher pressures, the wings between the line centers experience line mixing effects (begin to overlap) that are not included in any current line profiles.

2.3 Background–O_2 A-band

For fifty years the O_2 *A*-band [$b^1\Sigma_g^+ \leftarrow X^3\Sigma_g^-(0,0)$] has been an important target for atmospheric remote sensing. The *A*-band has been utilized by satellite missions such as the Orbiting Carbon Observatory (OCO, OCO-2)[19, 22], Scanning Imaging Absorption Spectrometer of Atmospheric Cartography (SCIAMACHY)[23], Global Ozone Monitoring Experiment (GOME)[24], and Greenhouse gases Observing Satellite (GOSAT)[25]. Also, the *A*-band has been applied to remote measurements of cloud-top heights, cloud optical properties, surface pressure, and aerosol optical properties.[26-28] This band is ideal for these remote sensing applications for several reasons: O_2 in the atmosphere is uniformly distributed with a well-known mixing ratio, many relatively weak *A*-band transitions are

not saturated for long path lengths, and the band is centered at 0.762 μm in a window region largely free of spectral interferences.

For OCO-2, high-resolution measurements have aimed to determine surface pressure to 0.1% and CO_2 concentration to 0.25%.[19] These increasingly precise remote sensing measurements, however, have shown that the present uncertainty in O_2 spectroscopic reference data ultimately limits the accuracy of the resulting retrievals.[29, 30] In addition, we were motivated by previous studies on the effects of chosen lineshape profile and line mixing for data retrieval.[31-34] To address the high demands of OCO-2 and remote sensing, our group has utilized frequency-stabilized cavity ring-down spectroscopy (FS-CRDS) to measure low-pressure (<0.1atm) lineshape parameters for many O_2 A-band transitions up to $J' = 60$ in the *P*-branch and $J' = 42$ in the R-branch.[26, 27] Transition line shapes were fit using Galatry line profiles, resulting in line intensity relative uncertainties of ~0.1%-0.5%. Even though Galatry lines profiles are highly successful at modeling O_2 A-band spectral lines precisely from our FS-CRDS measurements at low pressure (<0.1 atm), the Dicke narrowing contributions of the Galatry are most dominant near the line center, whereas the wings of the lines are less affected. Unfortunately, spectral features change drastically when the pressure increases. Common line profiles like the Voigt and Galatry, which are sufficient for describing spectrally isolated individual rovibrational transitions, fail in the high pressure regime.[35, 36] In addition to the rotationally resolved transitions, the broad collision-induced absorption (CIA) features and line mixing effects (LM) are also present that are not effectively captured by modeling with individual line profiles, e.g., Voigt, Galatry, etc. O_2 CIA absorption bands and line mixing effects have been the subject of a number of

studies [35-41]. These contributions to the observed lineshape demands high resolution studies of the O_2 A-band at a range of pressures in order to observe the transition of collisional effects that dominate at low pressures (Dicke narrowing, Doppler broadening) to high pressures (line mixing (LM)[35, 36, 42] and CIA[35, 36]). Most importantly, more comprehensive measurements and lineshape studies to incorporate LM and CIA for the O_2 A-band are necessary. Recently modeling work by Long et al.[28] observed that the most significant sources of bias for modeling atmospheric spectra are due to uncertainties in the following spectral parameters listed in increasing order of importance: Dicke narrowing, LM and CIA.

2.4 Background - 2.06 μm CO_2

Since NASA's remote sensing missions have set unprecedented precision targets for CO_2 concentration measurements as demanding as 0.25%, a detailed and thorough understanding of the spectral line shapes of CO_2 over a range of atmospherically relevant temperatures and pressures is required.[19] Our group, NIST and JPL collaborators have devoted much effort in studying higher-order effects such as collisional narrowing, speed-dependent effects and line mixing which are yet to be incorporated into the vast majority of atmospheric retrievals. These effects will play an even greater role in active sensing missions (such as NASA's Active Sensing of CO_2 Emissions over Nights Days and Seasons, ASCENDS) where individual transitions in the near-infrared spectral region will be utilized, rather than entire band.[43]

While infrared CO_2 transitions have been extensively studied only recently have non-Voigt line profiles begun to be employed. In a recent Fourier-transform spectroscopy (FTS) study, unambiguous evidence of line narrowing was observed, and further it was found that the use of the Voigt profile (which does not incorporate this effect) limited the accuracy of the measured spectroscopic parameters to ~1%.[44] A recent FTS study by Hartmann et al. 2009 [45] reported the importance of line mixing effects for the OCO-2 target CO_2 band at 2.06μm. This was expected for two main reasons: 1) the line intensities are stronger (wider lines) in this spectral region, especially for atmospheric retrieval from remote sensing and 2) CO_2 at 2.06μm is composed of four overlapping bands, for which complex line mixing processes can occur (intra vs inter-band mixing). Figure 2.2 (left) shows Hartmann et al.'s [45] results using a Voigt line profile with line mixing corrections, with which they were only able to reduce the residuals down to ~2%. Using FS-CRDS, our group more recently showed that not only line mixing was important for CO_2, but other non-Voigt effects including Dicke narrowing and speed dependence contributions were important. Figure 2.2 (right) from Long et al. 2011 [43] shows that fitting 1.6 μm CO_2 spectral lines with pure Voigt profiles (black squares) resulted in pressure-dependent systematic uncertainties of the spectrum area to >2%. Moreover, spectral fitting with other with other lineshape profiles (Galatry, Nelkin-Ghatak, etc.) that included non-Voigt effects systematically gave better results to <1% precision.

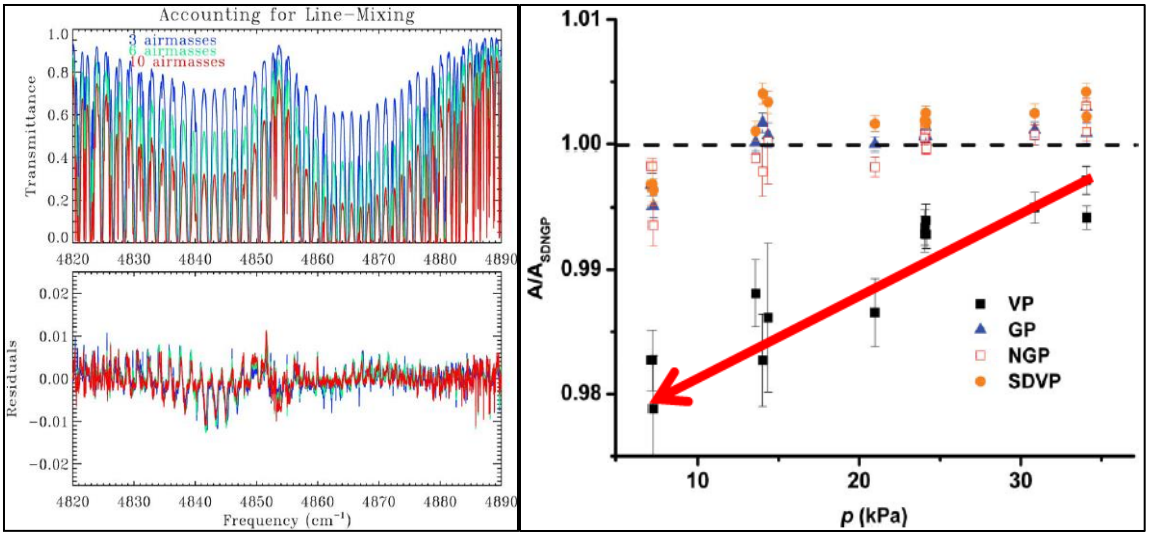

Figure 2.2: (Left) from Hartmann & Toon 2009[27]—2.06μm CO_2 Voigt profile with LM contribution. Peak to peak residuals are >2%. (Right) from Long et al. 2011[22] - Pressure dependence of the ratio of the spectrum area for CO_2 concentration retrieval obtained by fitting various line profiles (Voigt profile, Galatry profile, Nelkin-Ghatak profile, speed-dependent Voigt profile) to that obtained with the speed-dependent Nelkin Ghatak profile. Fitting spectra with the Voigt profile systematically underestimates the spectrum area up to 2%

Finally, a recent laser direct absorption method reported low-pressure (<5 kPa) measurements of self-broadened CO_2 line shapes for 9 R-branch lines near 5,000 cm^{-1} (2.006 nm).[46] Unlike previous FTS studies of CO_2 line shapes, they were able to clearly distinguish various line profiles because of the relatively high signal-to-noise ratio (~10,000:1) and spectral resolution (~1 MHz) of the measurements. However, they experience difficulty describing the observed line shapes with the Voigt, Galatry, Nelkin-Ghatak, speed-dependent Voigt, correlated Galatry or correlated Nelkin-Ghatak profiles. Notably, none of these theoretical profiles incorporated both collisional narrowing and speed-dependent effects [43], and more studies are required for this important spectral region.

2.5 Objective 1: Line Mixing (LM) and Collisional Induced Absorption (CIA) Effects in the O_2 A-band near 0.760 μm

From Boesch et al. 2006[47], surface pressures deduced from SCIAMACHY and ground-based FT spectra are systematically higher than that measured locally by a pressure transducer, and that fitting purely Voigt lineshapes underestimate the absorption by O_2 at 760nm [30]. Tran et al. 2006[35] performed FTS measurements of the O_2 A-band at pressures 20-200 atm at low spectral resolution (0.5 cm^{-1}) and demonstrated that corrections for line-mixing (LM) and collisional induced absorption (CIA) effects that broaden spectral lines are needed. Even in such high pressure regimes, Tran & Hartmann 2008[36] noted that both Voigt and purely Lorentzian lineshapes are inadequate for accurately determining the "photon path escape factors" – for scaling the O_2 volume mixing ratio – and surface pressure without inclusion of LM effects. More recently, Spiering et al. 2010[48, 49] used a pulsed cavity ringdown to study LM of the A-band at 0.760 μm for pressures 1-5 bar. Spiering et al.[48, 49] had to measure absorption at the troughs since their CRDS instrument saturated at the line center at high pressures. This shortcoming complicates line analysis since it was previously shown by Tran et al. 2006 [35] that that ignoring line mixing underestimates absorption at the peaks, but Spiering et al. 2010 [48] were unable to experimentally measure both the peak and wings simultaneously. Also, their data agreed with Tran et al. 2006[35] to only within 5%. Spiering et al.[48] concluded that the current LM model is limited and is a source of systematic errors and more complete data sets are needed. Finally, most recent measurements from Long et al.[50] used FS-CRDS [9, 51] to report LM and CIA for the O_2 A-band P-branch up to 1 atm pressure. Due to the same dynamic range limitations, their peaks were also truncated due

to saturation. Most importantly, LM and CIA data from FS-CRDS displayed quantitative and qualitative discrepancies exceeding 1% when compared to values reported from Tran et al.[35] and Spiering et al.[48].

Spectral analysis of individual rovibrational transitions is inadequate for treating CIA and LM effects: LM effects involve inelastic collisions that couple multiple transitions and CIA produces large, unstructured absorption features that affect the baseline continuum of the full A-band. For LM, a well-known "relaxation" matrix[35, 52] has been used to introduce coupling between spectral transitions. The diagonal elements contain the traditional pressure-broadening shifts and widths, and the off-diagonal elements account for interferences among lines. Tran and Hartmann[36], and Tran et al.[35] have treated LM by applying a model derived from the Energy Corrected Sudden (ECS) approximation to fit their high pressure spectra (20-200 atm). They used the fitted values for the off-diagonal relaxation matrix to compute a model spectrum with LM, and the difference between that with the experimental spectra is the empirically determined CIA contribution. Since Dicke narrowing and speed dependence negligibly affected the line wings, both effects were neglected at the high pressures used in their experiment. We seek to improve upon these measurements by collecting and analyzing spectra for air and self-broadened O_2 A-band from 0.2 to 4 atm. This pressure range is ideal for capturing the transition from a spectrally-isolated regime to onset of LM and CIA. Spectral analysis will be achieved by multispectrum analysis formulated by Benner et al.[53]

2.5.1 O_2 A-band instrumentation & experiments

The photoacoustic spectrometer is based on the design of Gillis et al.[54] Figure 2.3 shows a schematic of the instrumental apparatus.

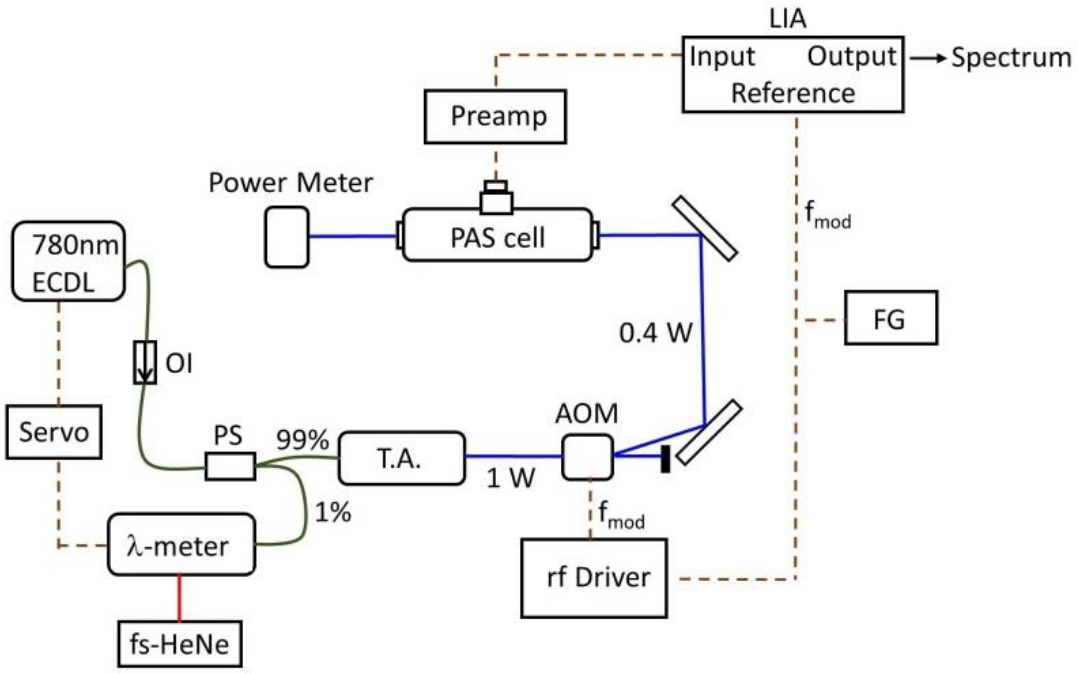

Figure 2.3: Photoacoustic spectrometer for measuring high pressure O_2 A-band. A 780 nm ECDL passes through an optical isolator (OI) before being inserted into a fiber-coupled power splitter (PS). 1% of the light is sent to a high accuracy wavelength meter and 99% is sent to the tapered-amplifier (T.A.). About 1 W of the amplified light is intensity modulated by an AOM at f_{mod}. The 1st order diffracted beam is coupled into a photoacoustic cell (PAS cell) and the absorption signal is picked up by a microphone. By lock-in detection with an lock-in amplifier (LIA), an absorption spectrum is acquired. The transmitted laser beam power is measured by a power meter at the output end of the PAS cell.

An external cavity diode laser (Sacher Lasertechnik ECDL) with tuning range from 760-780nm (~40 mW) was fiber coupled into a power splitter. 99% of the light is directed into a tapered-amplifier (Newfocus TA-7600) and 1% to a wavelength meter (HighFinesse/Ångstrom WSU-2) with high absolute accuracy of ~ 2 MHz. The high accuracy wavelength meter is continuously referenced to a frequency-stabilized HeNe

(Micro-g LaCoste ML-1, ~100 kHz/8 hrs drift). By taking advantage of the high acquisition rate of the wavelength meter (<500 Hz), we implemented a slow servo (~100 Hz) to correct for the long term drift of the laser through correction of the laser current. This was achieved by a simple proportional-integral control code via LabVIEW. The amplified light (~1 W) is intensity modulated at f_{mod} by an acousto-optic modulator (AOM, Brimrose) with the diffracted beam (~ 400 mW) sent into the PAS cell. Signal output from the microphone (Knowles, MD6052USZ-1) is sent to a preamplifier (SRS SR560), which serves as bandpass filter at f_{mod} prior to the lock-in amplifier. Lock-in detection with a lock-in amplifier (SRS SR830) at f_{mod} resulted in the absorption spectrum that is recorded by LabVIEW code from a computer. A calibrated power meter (Newport 918D-SL) was used to measure the transmitted laser power through the PAS cell. The purpose of the power measurement is for normalization of the absorption signal.

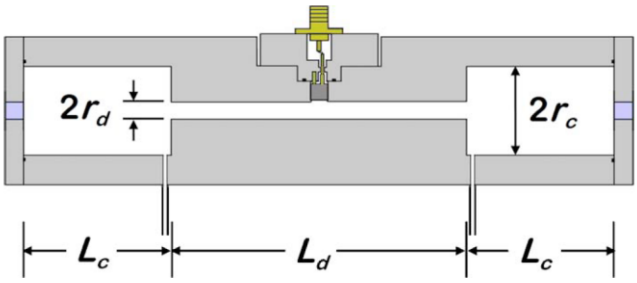

Figure 2.4: Acoustic resonator design taken from Gillis et al.[54]. The central duct with length L_{d} is the acoustic half-wave resonator. The chambers with length L_{c} serve as buffers to reduce background signals from window absorption and gas flow ports.

The PAS resonator cell is taken from Gillis et al.[54] and shown in Figure 2.4. The cell is enclosed by optical windows with antireflective coatings for the O_2 A-band wavelengths. The microphone is situated at the center of the small duct that spans the length L_{d}. This central duct behaves as a half-wave resonator with open ends: the

longitudinal modes occur as $n\lambda/2=L_d$, where n is an integer and λ is the laser wavelength. The purpose of the larger chambers (length L_c) at either end of the central duct is to serve as buffers to reduce signals from background absorption from windows and perturbations from gas flow ports.

The frequency response of the PAS resonator was measured to determine the laser f_{mod} for optimal photoacoustic coupling. First, the ECDL wavelength tuned to the peak of an arbitrary O_2 absorption line. Then the output of the lock-in amplifier is recorded as f_{mod} is tuned from f_{mod} =0-6 kHz via the function generator's GPIB port. The result of the measurement is displayed in Figure 2.5. There are two main acoustic resonances at ≈1.6 kHz and ≈4.9 kHz. Laser coupling is much more efficient at the former, so f_{mod} near 1.6 kHz was chosen. A fit to a resonance response function given by eq. 18 from Gillis et al.[54] gave a center frequency of 1.623 kHz with a halfwidth, g, of 42.8 Hz. For a FWHM of $2g$=85.6 Hz, the resonator Q factor, $Q=f_{res}/2g\approx19$.

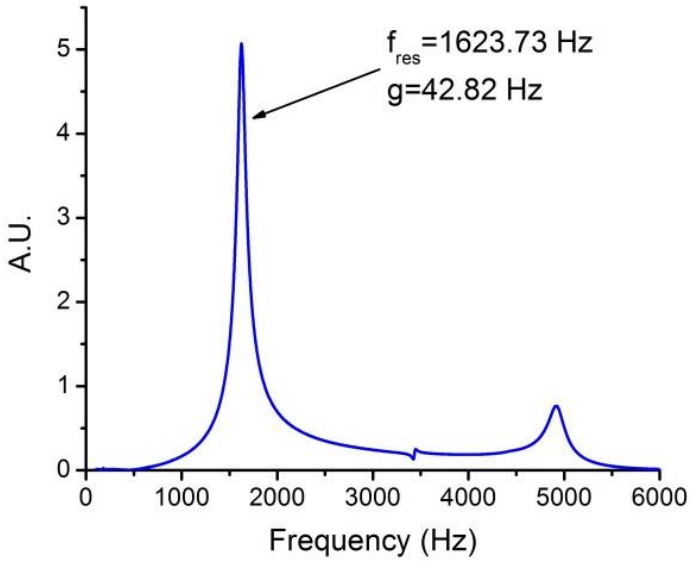

Figure 2.5: Photoacoustic signal as a function of f_{mod}. Sharp resonances near 1.6 kHz and 4.9 kHz indicate laser-resonator photoacoustic coupling. The largest response occurs when f_{res}=1.623 kHz. The fitted halfwidth, g, is 42.82 Hz.

An Allan variance for the photoacoustic spectrometer was obtained at a single wavelength in vacuum and plotted in Figure 2.6. A single wavelength acquisition can be averaged for about 1200 s (20 minutes) before the variance increases. A fitted slope of ≈0.5 suggests that data averaging is white noise limited until about 1200 s.

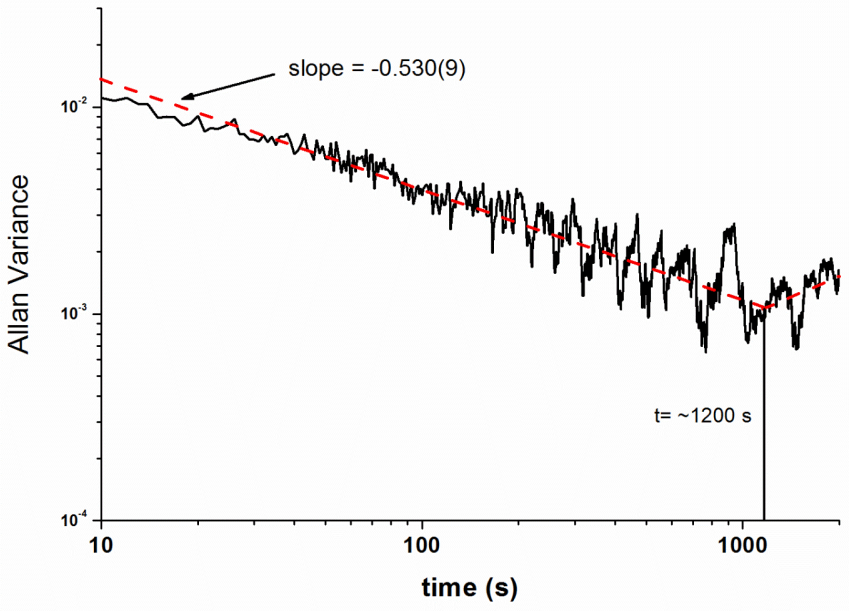

Figure 2.6: Allan variance at a single wavelength in vacuum for PAS. The variance averages down to 1200s before long-term drifts take over. A slope of approximately -0.5 suggests white noise dominated performance.

2.5.2 High pressure air-broadened O_2 A-band Data

O_2 A-band spectra were recorded at only10 s integration time per wavelength step to speed up the acquisition of the full A-band spectrum spanning greater than 160 cm^{-1} at high spectral resolution steps of 0.005cm^{-1}. For high pressure measurements of O_2 in air, we first tested the dynamic range of the PAS spectrometer. A P-branch doublet pair (P9P9 and P9Q8 transitions) of O_2 in air was measured for pressures 38-411 kPa (285 – 3080 Torr). The spectra are shown in Figure 2.7A. The signal-to-noise ratio (SNR) of the

spectra exceeded 10000:1. The five spectra were fitted with a Galatry[55] line profile and the total integrated area for both transitions are plotted in 2.7B. The high linearity of the integrated area with respect to pressure suggests that the spectrometer is still within the linear regime and have not reached saturation. Deviations from linearity at the two highest pressures (253.3 and 410.6 kPa) were the result of the improper line profiles used in the fit to treat collisional line mixing: our line profile model only considered nearest neighbor line mixing, which was inadequate at these high pressures.

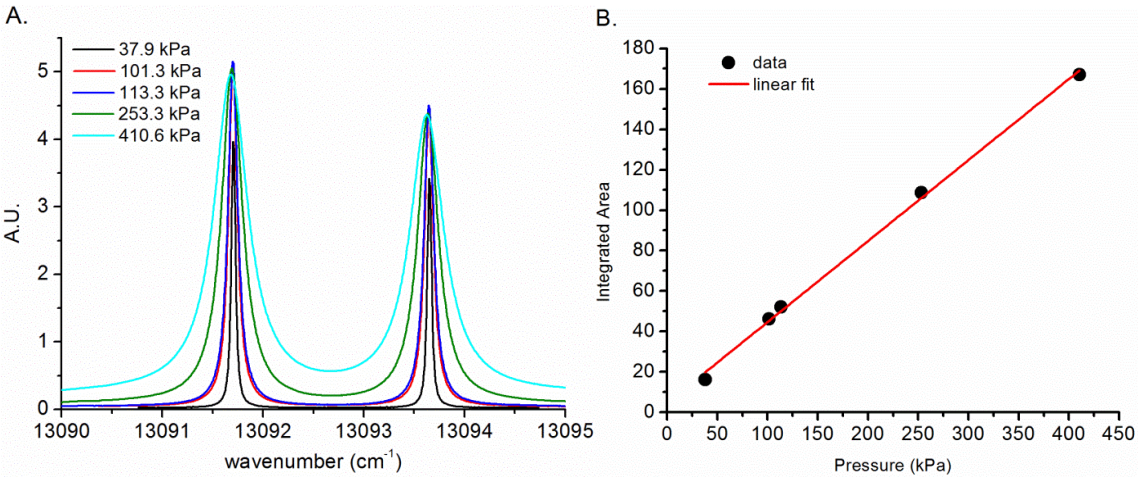

Figure 2.7: A) P-branch doublet pair (P9P9 and P9Q8 transitions) was measured at 5 different pressures between 38 and 411 kPa. B) Integrated area as a function of pressure plot obtained from fitting the doublet to a Galatry line profile. The linearity of the result suggests that the spectrometer is still behavior linearly and have not reached saturation.

With sufficient dynamic range to measure up to 410.6 kPa (3080 Torr) of air, we acquired full O_2 A-band spectra from 13000 – 13170 cm^{-1} at three different pressures: 113.3, 253.3 and 410.6 kPa. The full spectrum required about one week of acquisition time to achieve, mostly due to mode hopping of the ECDL laser. The spectra are displayed in Figure 2.8. The air spectra at 410.6 kPa displayed unusual rise near 13000 cm^{-1}, which was not apparent in the other two pressures. The baseline oscillation in the

background is present in all three pressures. We also have acquired a pure O_2 spectra at 410.6 kPa (Figure 2.9) for testing CIA contributions.

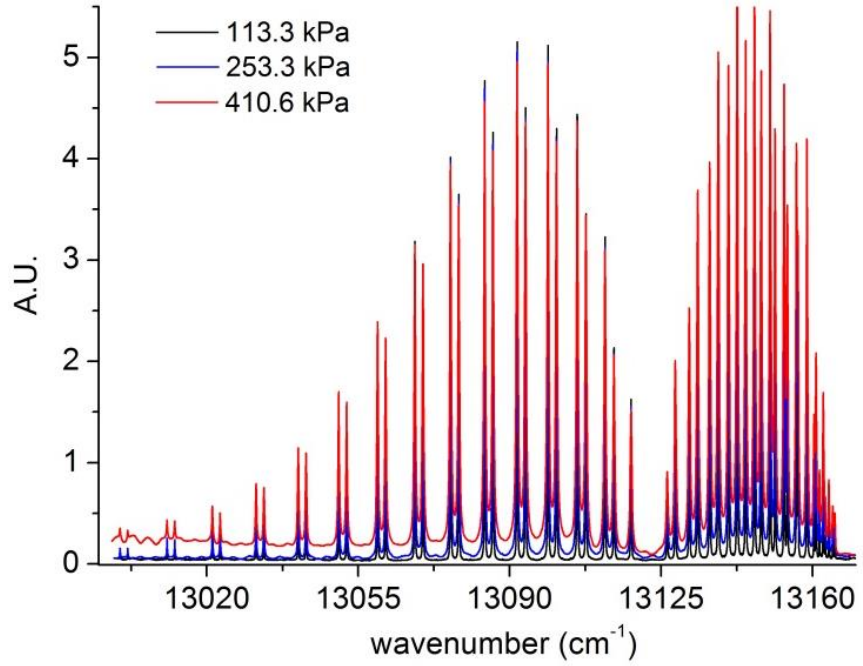

Figure 2.8: Air-broadened O_2 A-band spectrum at pressures of 113.3 kPa, 253.3 kPa and 410.6 kPa. The 410.6 kPa displayed an unexpected rise in the baseline continuum near 13000 cm^{-1}.

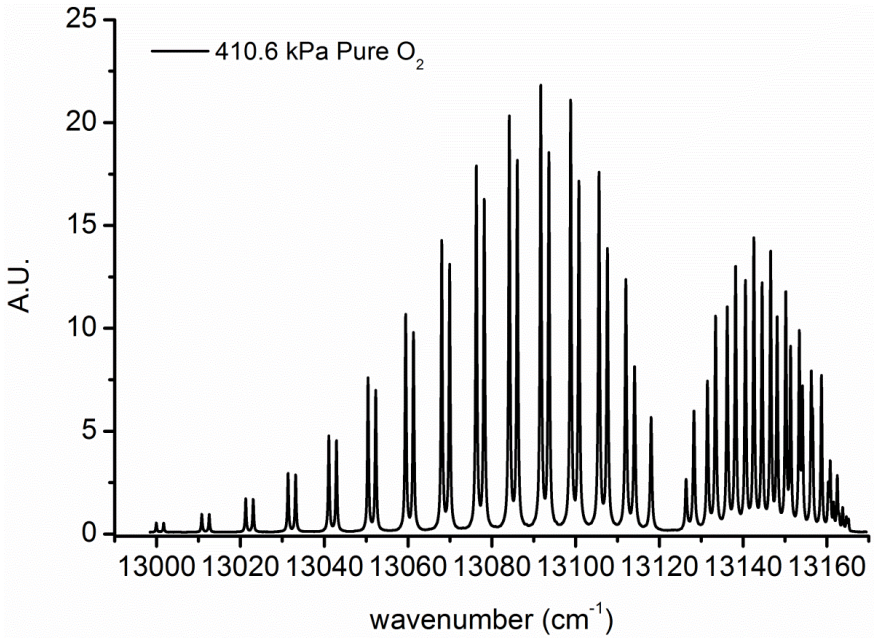

Figure 2.9: Pure O_2 A-band spectrum at 410.6 kPa.

2.5.3 Preliminary Spectra Fitting Results

Preliminary spectral analyses using a Galatry line profile with nearest neighbor line mixing approximation are shown in Figure 2.10. The three fitted spectra are the P9P9 and P9Q8 doublet transitions at pressure 113.3, 253.3 kPa and 410.6 kPa. The upper and lower panels show the fit and the residuals, respectively. From the residual at the lowest pressure, 113.3 kPa, the baseline noise is $\sigma_{baseline}$<0.001, giving spectral SNR > 10000:1.

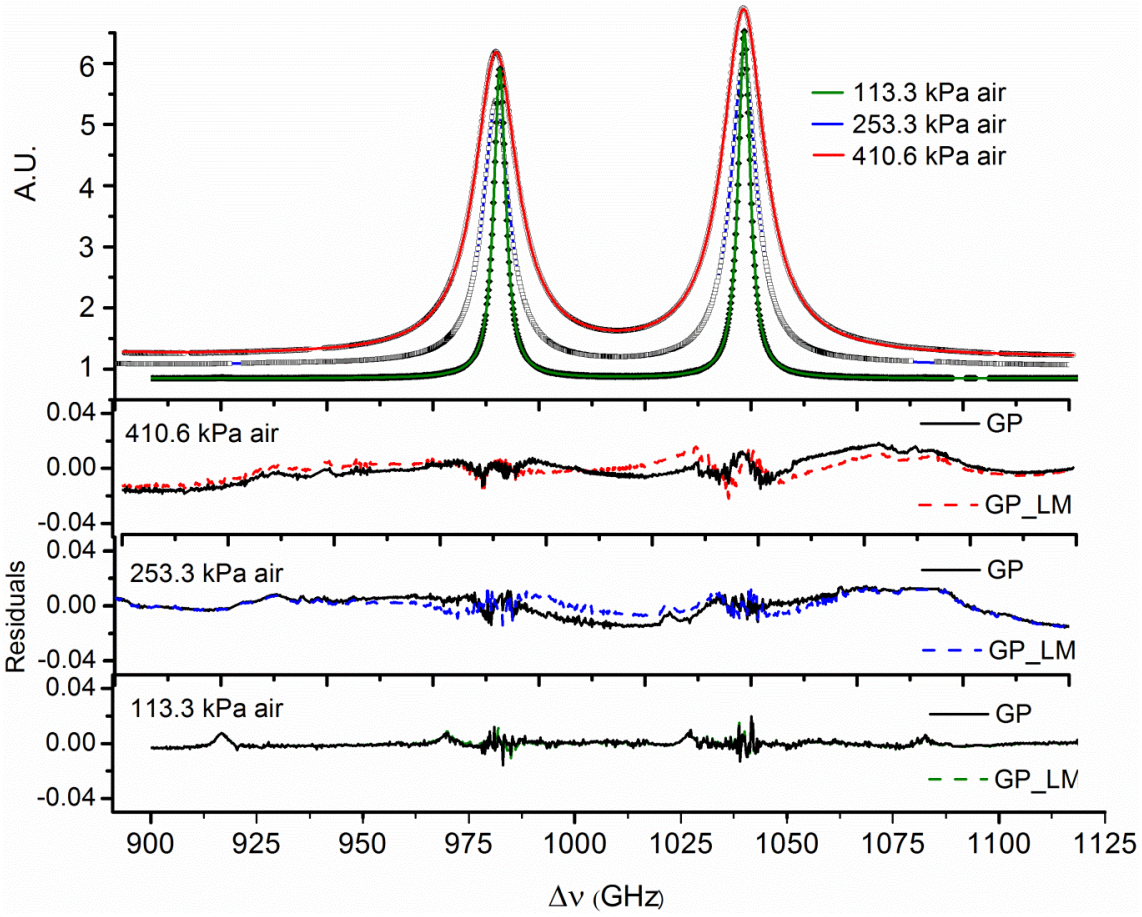

Figure 2.10: Spectral fits using the Galatry line profile with nearest neighbor line mixing for air-broadened O_2 at 113.3, 253.3 and 410.6 kPa.

The residuals at the two highest pressures show persistent curvature between and outside the doublet at the wings. This is a clear indication of line mixing effects that are not effectively captured by the Galatry line profile with nearest neighbor line mixing

approximation. The lowest pressure display minimal baseline curvature, which suggests that the spectral are still sufficiently isolated. Further investigations with full A-band multispectrum fits incorporating the full relaxation matrix are currently underway.

2.6 Objective 2: Spectral lineshape studies of CO_2 at 2.06 μm

Due to the inconsistency between experiment and theory from Casa et al.[46] and a recent report from Hartmann et al.[45] concerning line mixing effects for 2.06μm CO_2, we set out to improve on the laboratory measurements to determine the proper lineshape for OCO-2's target CO_2 band at 2.06μm. More accurate, precise, and comprehensive measurements of CO_2 2.06μm band are required as current data do not achieve the required precision <0.25% necessary for NASA's OCO-2 remote sensing applications. As previously demonstrated in our group, the sensitivity and spectral fidelity (high stability) of frequency-stabilized cavity ring-down spectroscopy (FS-CRDS) make it an ideal technique for detailed study of subtle line shape effects with high precision.[51] Furthermore, the use of the multi-spectrum fitting method[53, 56], which simultaneously fits spectra across a wide pressure range, can enable the collisional narrowing and speed-dependent effects to be separated and quantified. A detailed lineshape study of this band is the main subject of the next chapter in this thesis.

2.7 References

1. C. E. Miller, D. Crisp, P. L. DeCola, S. C. Olsen, J. T. Randerson, A. M. Michalak, A. Alkhaled, P. Rayner, D. J. Jacob, P. Suntharalingam, D. B. A. Jones, A. S. Denning, M. E. Nicholls, S. C. Doney, S. Pawson, H. Boesch, B. J. Connor, I. Y. Fung, D. O'Brien, R. J. Salawitch, S. P. Sander, B. Sen, P. Tans, G. C. Toon, P. O. Wennberg, S. C. Wofsy, Y. L. Yung and R. M. Law, J. Geophys. Res., [Atmos.] **112** (D10), D10314 (2007).

2. H. Boesch, D. Baker, B. Connor, D. Crisp and C. Miller, Remote Sensing **3** (2), 270-304 (2011).

3. L. S. Rothman, I. E. Gordon, Y. Babikov, A. Barbe, D. C. Benner, P. F. Bernath, M. Birk, L. Bizzocchi, V. Boudon, L. R. Brown, A. Campargue, K. Chance, E. A. Cohen, L. H. Coudert, V. M. Devi, B. J. Drouin, A. Fayt, J. M. Flaud, R. R. Gamache, J. J. Harrison, J. M. Hartmann, C. Hill, J. T. Hodges, D. Jacquemart, A. Jolly, J. Lamouroux, R. J. Le Roy, G. Li, D. A. Long, O. M. Lyulin, C. J. Mackie, S. T. Massie, S. Mikhailenko, H. S. P. Muller, O. V. Naumenko, A. V. Nikitin, J. Orphal, V. Perevalov, A. Perrin, E. R. Polovtseva, C. Richard, M. A. H. Smith, E. Starikova, K. Sung, S. Tashkun, J. Tennyson, G. C. Toon, V. G. Tyuterev and G. Wagner, J. Quant. Spectrosc. Radiat. Transf. **130**, 4-50 (2013).

4. D. Crisp, B. M. Fisher, C. O'Dell, C. Frankenberg, R. Basilio, H. Bosch, L. R. Brown, R. Castano, B. Connor, N. M. Deutscher, A. Eldering, D. Griffith, M. Gunson, A. Kuze, L. Mandrake, J. McDuffie, J. Messerschmidt, C. E. Miller, I. Morino, V. Natraj, J. Notholt, D. M. O'Brien, F. Oyafuso, I. Polonsky, J. Robinson, R. Salawitch, V. Sherlock, M. Smyth, H. Suto, T. E. Taylor, D. R. Thompson, P. O. Wennberg, D. Wunch and Y. L. Yung, Atmospheric Measurement Techniques **5** (4), 687-707 (2012).

5. J. P. Burrows, E. Holzle, A. P. H. Goede, H. Visser and W. Fricke, Acta Astronautica **35** (7), 445-451 (1995).

6. R. B. A. Koelemeijer, P. Stammes, J. W. Hovenier and J. F. de Haan, Journal of Geophysical Research-Atmospheres **106** (D4), 3475-3490 (2001).

7. Y. Yoshida, Y. Ota, N. Eguchi, N. Kikuchi, K. Nobuta, H. Tran, I. Morino and T. Yokota, Atmospheric Measurement Techniques **4** (4), 717-734 (2011).

8. D. A. Long, D. K. Havey, M. Okumura, C. E. Miller and J. T. Hodges, Journal of Quantitative Spectroscopy & Radiative Transfer **111** (14), 2021-2036 (2010).

9. D. J. Robichaud, L. Y. Yeung, D. A. Long, M. Okumura, D. K. Havey, J. T. Hodges, C. E. Miller and L. R. Brown, Journal of Physical Chemistry A **113** (47), 13089-13099 (2009).

10. D. A. Long and J. T. Hodges, Journal of Geophysical Research-Atmospheres **117**, 6 (2012).

11. D. M. O'Brien, R. M. Mitchell, S. A. English and G. A. Da Costa, Journal of Atmospheric and Oceanic Technology **15** (6), 1272-1286 (1998).

12. Z. Yang, P. O. Wennberg, R. P. Cageao, T. J. Pongetti, G. C. Toon and S. P. Sander, Journal of Quantitative Spectroscopy & Radiative Transfer **90** (3-4), 309-321 (2005).

13. R. Schermaul and R. C. M. Learner, Journal of Quantitative Spectroscopy & Radiative Transfer **61** (6), 781-794 (1999).

14. R. Herman and R. F. Wallis, Journal of Chemical Physics **23** (4), 637-646 (1955).

15. A. Predoi-Cross, C. Holladay, H. Heung, J.-P. Bouanich, G. C. Mellau, R. Keller and D. R. Hurtmans, Journal of Molecular Spectroscopy **251** (1-2), 159-175 (2008).

16. L. R. Brown and C. Plymate, Journal of Molecular Spectroscopy **199** (2), 166-179 (2000).

17. H. Tran, C. Boulet and J. M. Hartmann, Journal of Geophysical Research-Atmospheres **111** (D15), 14 (2006).

18. H. Tran and J. M. Hartmann, Journal of Geophysical Research-Atmospheres **113** (D18) (2008).

19. G. C. Tabisz, E. J. Allin and H. L. Welsh, Can. J. Phys. **47**, 2859-2871 (1969).

20. G. D. Greenblatt, J. J. Orlando, J. B. Burkholder and A. R. Ravishankara, J. Geophys. Res. **95**, 18577-18582 (1990).

21. H. Tran, C. Boulet and J. M. Hartmann, J. Geophys. Res. **111**, 6869-6882 (2006).

22. D. A. Long, D. J. Robichaud and J. T. Hodges, J. Chem. Phys **137**, 014307 (2012).

23. R. Thalman and R. Volkamer, Phys. Chem. Chem. Phys. **15** (15371) (2013).

24. A. Lévy, N. Lacome and C. Chackerian Jr., in *Spectroscopy of the Earth Atmosphere and Interstellar Medium* (Elsevier, New York, 1992), pp. 261-337.

25. D. A. Long, K. Bielska, D. Lisak, D. K. Havey, M. Okumura, C. E. Miller and J. T. Hodges, J. Chem. Phys **135** (6), 064308 (2011).

26. R. A. Toth, L. R. Brown, C. E. Miller, V. M. Devi and D. C. Benner, J. Quant. Spectrosc. Radiat. Transf. **109** (6), 906-921 (2008).

27. J. M. Hartmann, H. Tran and G. C. Toon, Atmospheric Chemistry and Physics **9** (19), 7303-7312 (2009).

28. G. Casa, R. Wehr, A. Castrillo, E. Fasci and L. Gianfrani, J. Chem. Phys **130** (18), 184306 (2009).

29. H. Boesch, G. C. Toon, B. Sen, R. A. Washenfelder, P. O. Wennberg, M. Buchwitz, R. de Beek, J. P. Burrows, D. Crisp, M. Christi, B. J. Connor, V. Natraj and Y. L. Yung, Journal of Geophysical Research-Atmospheres **111** (D23) (2006).

30. F. R. Spiering, M. B. Kiseleva, N. N. Filippov, H. Naus, B. van Lieshout, C. Weijenborg and W. J. van der Zande, Journal of Chemical Physics **133** (11), 9 (2010).

31. F. R. Spiering, M. B. Kiseleva, N. N. Filippov, B. van Lieshout, A. M. H. van der Veen and W. J. van der Zande, Molecular Physics **109** (4), 535-542 (2011).

32. D. A. Long, D. J. Robichaud and J. T. Hodges, Journal of Chemical Physics **137** (1) (2012).

33. J. T. Hodges, H. P. Layer, W. W. Miller and G. E. Scace, Rev. Sci. Instrum. **75** (4), 849-863 (2004).

34. D. A. Long, A. Cygan, R. D. van Zee, M. Okumura, C. E. Miller, D. Lisak and J. T. Hodges, Chem. Phys. Lett. **536**, 1-8 (2012).

35. A. S. Pine, J. Quant. Spectrosc. Radiat. Transf. **57** (2), 145-155 (1997).

36. D. C. Benner, C. P. Rinsland, V. M. Devi, M. A. H. Smith and D. Atkins, J. Quant. Spectrosc. Radiat. Transf. **53** (6), 705-721 (1995).

37. K. A. Gillis, D. K. Havey and J. T. Hodges, Review of Scientific Instruments **81** (6), 13 (2010).

38. L. Galatry, Phys. Rev. **122** (4), 1218 (1961).

39. D. Lisak, P. Masłowski, A. Cygan, K. Bielska, S. Wojtewicz, M. Piwiński, J. T. Hodges, R. S. Trawiński and R. Ciuryło, Phys. Rev. A **81** (4) (2010).

Chapter 3: Laboratory measurements of 2.06 μm CO_2 in support of OCO-2: Observations of Dicke narrowing and speed dependence in air-broadened CO_2 lineshapes near 2.06 μm

This chapter was published as:

T.Q. Bui, D.A. Long, A. Cygan, V.T. Sironneau, D.W. Hogan, P.M. Rupasinghe, R. Ciuryło, D. Lisak and M. Okumura. *J. Chem. Phys.*, 141, 174301 (2014).

3.1 Abstract

Frequency-stabilized cavity ring-down spectroscopy (FS-CRDS) was used to study CO_2 lineshapes in the (20013)←(00001) band centered near 2.06 μm. Two rovibrational transitions were chosen for this study to measure non-Voigt collisional effects for air-broadened lines over the pressure range of 7 kPa to 28 kPa. Lineshape analysis for both lines revealed evidence of simultaneous Dicke (collisional) narrowing and speed-dependent effects that would introduce biases exceeding 2% in the retrieved air-broadening parameters if not incorporated in the modeling of CO_2 lineshapes. Additionally, correlations between velocity- and phase/state-changing collisions greatly reduced the observed Dicke narrowing effect. As a result, it was concluded that the most appropriate line profile for modeling CO_2 lineshapes near 2.06 μm was the correlated speed-dependent Nelkin-Ghatak profile, which includes all of the physical effects mentioned above and leads to a consistent set of line shape parameters that are linear with gas pressure.

3.2 Introduction

Current and upcoming remote sensing missions (including NASA's OCO-2 and ASCENDS) have necessitated high-precision studies to retrieve accurate lineshape parameters in the $4\nu_2+\nu_3$ band [(20013)←(00001)] centered at 2.06 μm.[19, 57, 58] The (20013)←(00001) band, along with two other bands, (20012)←(00001) and (20011)←(00001), form the Fermi triad of CO_2 bands spanning 4700–5200 cm^{-1}. Since these missions have set a target precision of 0.25%, we studied non-Voigt lineshape

effects to achieve a reduction in uncertainties of the retrieved spectroscopic parameters to below the 1% limit of the Voigt profile.[44]

It is well established from high-resolution molecular spectroscopy that the Voigt profile is inadequate to properly describe high-precision measurements of CO_2 lineshapes.[43, 46, 59-65] Recently, Casa et al. used laser absorption spectroscopy to measure CO_2 lineshapes of the $\nu_1+2\nu_2+\nu_3$ band [(20012)←(00001)] at 2.0 μm.[46] By recording spectra with high resolution (≈1 MHz) and high signal-to-noise ratios (≈10000:1), they were able to resolve non-Voigt features. However, the line profiles employed in their analysis—Voigt, Galatry, Nelkin-Ghatak, speed-dependent Voigt, correlated Galatry and Nelkin-Ghatak profiles—could not completely model their spectra. More recently, Long et al. measured the *R*(16) line from a tetrad CO_2 band [(30012)←(00001)] near 1.6 μm and observed that both collisional narrowing and speed-dependent effects are necessary to describe the lineshape and reduce the fit residuals to the measurement noise level.[43] This necessity for simultaneous collisional narrowing and speed-dependent effects was first demonstrated by Duggan et al.[66] for CO transitions. Similar observations were subsequently made for many other systems, including HF+Ar,[67] H_2+Ar,[68] H_2O+Xe,[69] C_2H_2+Xe,[70] H_2O+N_2,[71] and more recently O_2+O_2.[72] This suggests a possible limitation in the analysis by Casa et al.[46] We extend this analysis to the 2.06 μm CO_2 band region to reconcile these observations.

3.3 Spectrum analysis

The purpose of this experiment is to quantify the physical effects governing the lineshapes of CO_2 in the (20013)←(00001) vibrational band centered at 2.06 μm. The simplest profile considered here is the Voigt profile (VP), which is the convolution of Gaussian (Doppler-broadened) and Lorentzian (pressure-broadened) profiles. Moreover, the complex Voigt profile (I_{VP}) has been defined previously.[73, 74] When collisions with a perturber gas occur, other non-Voigt phenomena can arise. The first effect is Dicke (collisional) narrowing, which arises from velocity-changing collisions that effectively reduce the Doppler broadening contribution.[75] Rautian and Sobelman[76] incorporated Dicke narrowing by treating velocity-changing collisions as a combination of soft and hard collisions. Furthermore, assuming limiting cases that collisions are either soft or hard gives rise to the Galatry[55] (GP) and Nelkin-Ghatak[77] (NGP) profiles, respectively. The soft-collision model treats absorber motion as a diffusional process, whereas the hard collision model assumes a complete loss of velocity memory of the absorber after collisions. Although this assumption from the latter is non-physical, it results in the following convenient analytic form of the NGP in terms of the VP given by [76, 77]

$$I_{\mathrm{NGP}}(u) = \frac{I_{\mathrm{VP}}^{*}(u)}{1 - \pi z I_{\mathrm{VP}}^{*}(u)}, \quad (1)$$

where $u=(\omega-\omega_0)/\omega_D$ is the reduced frequency, $z=\nu_{opt}/\omega_D$ is the reduced effective frequency of the velocity-changing collisions, ν_{opt}, and I_{VP}* is I_{VP} with the Lorentzian frequency halfwidth Γ (half-width at half-maximum—HWHM) expressed by a reduced variable $g=\Gamma/\omega_D$ replaced by $g+z$, following the notation from Ref. [23]. ω_D is related to

the Doppler frequency halfwidth, Γ_D (HWHM), by the equation $\Gamma_D = \omega_D\sqrt{\ln 2}$. In both the GP and NGP profiles, the relevant variable for fitting is the collisional narrowing parameter, β, which is a function of pressure, p, in terms of the collisional narrowing frequency ν_{opt}: $\beta(p)=\nu_{opt}/p$. It is important to note that both the GP and NGP profiles assume uncorrelated collisional perturbations (i.e., the collisions affect either molecular dephasing or velocity changes, but not both simultaneously).[78, 79]

In addition to collisional narrowing (which causes symmetric changes in the lineshape if correlations between dephasing and velocity-changing collisions are neglected), collision time asymmetry[80-82] (which occurs when collisions are not treated as instantaneous) and line mixing[83, 84] can introduce dispersion asymmetry in the lineshape center and near wings.[85] Finally, one must also consider the influence of speed dependence of collisional broadening and line shifting on the resulting lineshape.[86-88] This effect generally causes a narrowing of the pressure-broadened line profile in addition to line asymmetry caused by speed dependence of line shifting. When such speed-dependent effects are considered, either the speed-dependent Voigt[86] (SDVP, eq. 2), speed-dependent Galatry (SDGP)[89] or speed-dependent Nelkin-Ghatak[90] (SDNGP, eq. 3) profiles are commonly used. Importantly, the SDGP and SDNGP include collisional narrowing, whereas the SDVP does not. The SDVP and SDNGP are given by,[91]

$$I_{SDVP}(u) = \frac{2}{\pi^{3/2}} \int_{-\infty}^{\infty} dx e^{-x^2} x(\arctan[\frac{u - dB_S(x) + x}{gB_W(x)}] + \frac{i}{2}\ln\{1+[\frac{u - dB_S(x) + x}{gB_W(x)}]^2\}), \quad (2)$$

and

$$I_{\mathrm{SDNGP}}(u) = \frac{I_{\mathrm{SDVP}}{}^{*}(u)}{1-\pi z I_{\mathrm{SDVP}}{}^{*}(u)} \quad .(3)$$

In eq. (2) $d=\Delta/\omega_{\mathrm{D}}$ is the reduced collisional shift, Δ, and $B_{\mathrm{S}}(x)$ and $B_{\mathrm{W}}(x)$ are dimensionless functions for the reduced speed-dependent shifts and widths, respectively, and x is the reduced absorber speed (the ratio of the actual to the most probable speed). It was previously shown that if the interaction potential for the absorber-perturber pair is given by an inverse power relationship, C/r^{q}, the expressions for $B_{\mathrm{S}}(x)$ and $B_{\mathrm{W}}(x)$ can be written in terms of confluent hypergeometric functions.[86, 87] A common quadratic approximation is used to simplify these reduced speed-dependent functions with respect to the speed-dependent width and shift parameters (a_{W} and a_{S}, respectively, which are also used as fitted parameters),[92, 93] shown more explicitly as:

$$\begin{aligned} B_{\mathrm{W}}(x) &= \frac{\Gamma(v_{\mathrm{A}})}{\Gamma} = 1 + a_{\mathrm{W}}\left(x^{2} - \frac{3}{2}\right) \\ B_{\mathrm{S}}(x) &= \frac{\Delta(v_{\mathrm{A}})}{\Delta} = 1 + a_{\mathrm{S}}\left(x^{2} - \frac{3}{2}\right) \end{aligned} \qquad (4)$$

Here, $\Gamma(v_{\mathrm{A}})$ and $\Delta(v_{\mathrm{A}})$ are the collisional widths and shifts as a function of absorber velocity, v_{A}. One may easily show that for systems containing more than one perturber, total reduced speed-dependent functions $B_{\mathrm{W}}(x)$ and $B_{\mathrm{S}}(x)$ are also given in the quadratic form. In this case, the a_{W} and a_{S} parameters for a gas mixture are weighted averages of the corresponding parameters for individual perturbing gases.[94]

Finally, when correlations between velocity-changing and dephasing collisions[76] are important, a partially correlated speed-dependent profile (pCSDNGP), introduced by Pine[67] can be used. This profile, $I_{\mathrm{pCSDNGP}}(u)$, is expressed in the same way as eq. (3),[95] but

differs in the definition of the complex narrowing parameter, ν_{opt}.[76, 78, 96-98] In the $I_{pCSDNGP}(u)$, ν_{opt} is given by $\nu_{opt} = \nu_{diff} - \eta_\Gamma\Gamma - i\eta_\Delta\Delta = \mathrm{Re}(\nu_{opt}) + i\mathrm{Im}(\nu_{opt})$, where the velocity dependence of Γ and Δ parameters was neglected.[78] ν_{diff} is the frequency of velocity-changing collisions calculated from the mass diffusion coefficient. The real and imaginary part of ν_{opt} is designated as $\mathrm{Re}(\nu_{opt})$ and $\mathrm{Im}(\nu_{opt})$, respectively. The correlation parameters, η_Γ and η_Δ, correspond to collisional broadening and shifting, respectively. In the case of no correlation, η_Γ and η_Δ parameters are equal to zero and $\nu_{opt} = \nu_{diff}$.

For the CO_2-air system probed in this experiment, the ratios of the perturber (O_2 and N_2) to absorber (CO_2) mass are m_{O2}/m_{CO2}=0.73 and m_{N2}/m_{CO2}=0.64; therefore, the absorber is only slightly heavier. Using the diffusion coefficient of CO_2 in air D=0.159 cm^2s^{-1} (p=101.325 kPa, T=296 K),[99] the mean-free-path of CO_2 can be calculated as $l_{mfp}=3D/\bar{\upsilon}$, where $\bar{\upsilon}$ is the relative mean velocity of the perturber-absorber pair. For T=296 K, p=26.7 kPa, the mean-free-path of CO_2 is calculated to be l_{mfp}=0.341 μm, which is much smaller than the optical wavelength of 2.06 μm. This suggests that collisional narrowing must also be considered. To facilitate studies of isolated lineshapes, measurements were made at sufficiently low pressures (i.e., 7 kPa to 28 kPa) such that line mixing effects could be neglected. Nevertheless, all other stated effects are accessible in this pressure range.

3.4 Experiment

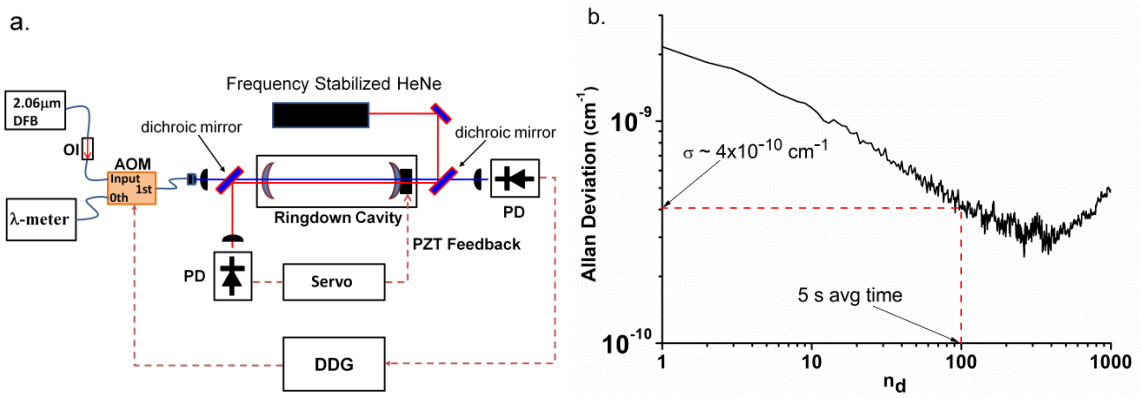

Figure 3.1: a. Schematic of the 2.06 μm frequency-stabilized cavity ring-down spectrometer. OI=optical isolator, PD=photodiode, AOM=acousto-optic modulator, DDG=digital delay generator. 2.06 μm light is injected into a fiber-coupled AOM and subsequently free-space coupled into the ring-down cavity. Once the transmitted light intensity reaches a threshold, a DDG shuts off the light to initiate the ring-down. Light from a frequency-stabilized HeNe laser is counter-propagated through the cavity and is used to stabilize the cavity's length. b. Allan deviation plot for the 2.06 μm FS-CRDS spectrometer. The *x*-axis displays the number of ring-down traces (acquired at an acquisition rate of ≈20 Hz), n_d, at a given frequency. The *y*-axis gives the Allan deviation corresponding to the baseline losses. For typical experimental conditions, 100 ring-down traces were acquired, corresponding to a minimum detectable absorption of $\approx 4\times10^{-10}$ cm^{-1}.

Measurements were performed using a 2.06 μm frequency-stabilized cavity ring-down spectrometer (FS-CRDS) located at the California Institute of Technology (see Fig. 1A). The spectrometer is based on the design of Hodges et al.[9, 16, 51]. Briefly, the ring-down cavity was actively locked to a temperature-stabilized HeNe laser with an optical frequency stability of 100 kHz (8 h). The probe laser was a distributed-feedback diode laser (≈3 mW power) centered at 2.055 μm. The fiber-pigtailed output was sent through a fiber-optic isolator and then into a fiber-coupled acousto-optic modulator (AOM). The 1st order output from the AOM was free-space coupled via a single focusing lens (*f*=500 mm) into the ring-down cavity. The 0th-order output was free-space coupled into a wavelength meter with a standard uncertainty of 30 MHz. Light exiting the ring-down

cavity was focused onto an adjustable-gain, extended InGaAs detector with a maximum bandwidth of 1 MHz.

For these experiments, the ring-down mirrors had dichroic coatings: reflectivity $R \approx 99.99\%$ at 2.06 μm, corresponding to a vacuum finesse of ≈31000, and $R \approx 95\%$ at 0.633 μm. One hundred ring-down traces of $\tau \approx 26\mu s$ were acquired using a fast fitting algorithm[100] at a rate of 20 Hz to 30 Hz and averaged at each wavelength, corresponding to a minimum detectable absorption coefficient of $\approx 4\times10^{-10}$ cm^{-1} (see Fig. 1B). The cavity's free spectral range (FSR) was measured by the method of Lisak and Hodges[7] to be 203.890(82) MHz. This pressure-corrected value sets the frequency spacing between the spectrum data points.

The gas sample was composed of CO_2 in air with a mixing ratio of ≈90 □mol mol^{-1} at pressures of 7 kPa to 27 kPa as measured by a capacitance manometer (full-scale range of 133.32(13) kPa). The air content contained 20.9% oxygen with the remainder being nitrogen. The cavity temperature was monitored by a 2.252 kΩ thermistor and displayed short-term (i.e., the time required to record a single spectral line) fluctuations less than 100 mK. All measurements were performed within the temperature range of 295.4 K to 296.1 K. Since this value is close to the HITRAN reference temperature of T_{ref}=296 K,[21] the uncertainties in the temperature corrections to the air-broadening coefficients were negligible compared to the fit uncertainties.

3.5 Results and Discussion

In this section we present the results from a thorough lineshape analysis for two selected air-broadened lines from the (20013)←(00001) CO_2 band centered near 2.06 μm, specifically the *R*(24) line at 4871.791 cm^{-1} and the *R*(30) line at 4875.749 cm^{-1}. The CO_2-air mixture pressure range was 48.1 - 210 Torr (6.5 - 28 kPa) for the *R*(24) line and 48.1 - 180.3 Torr (6.5 -24 kPa) for the *R*(30) line. The *R*(30) line was chosen because it is a potential target for the ASCENDS[58] mission, while the *R*(24) line is more ideal for lineshape analysis because of its isolation from isotopic interferences. The two selected lines are shown in Fig. 2. Note that for the *R*(30) line at 4875.749 cm^{-1}, a $^{13}CO_2$ isotopologue in the right wing presents the main interference with a line intensity that is 6.2% of the main isotopologue transitions.[21]

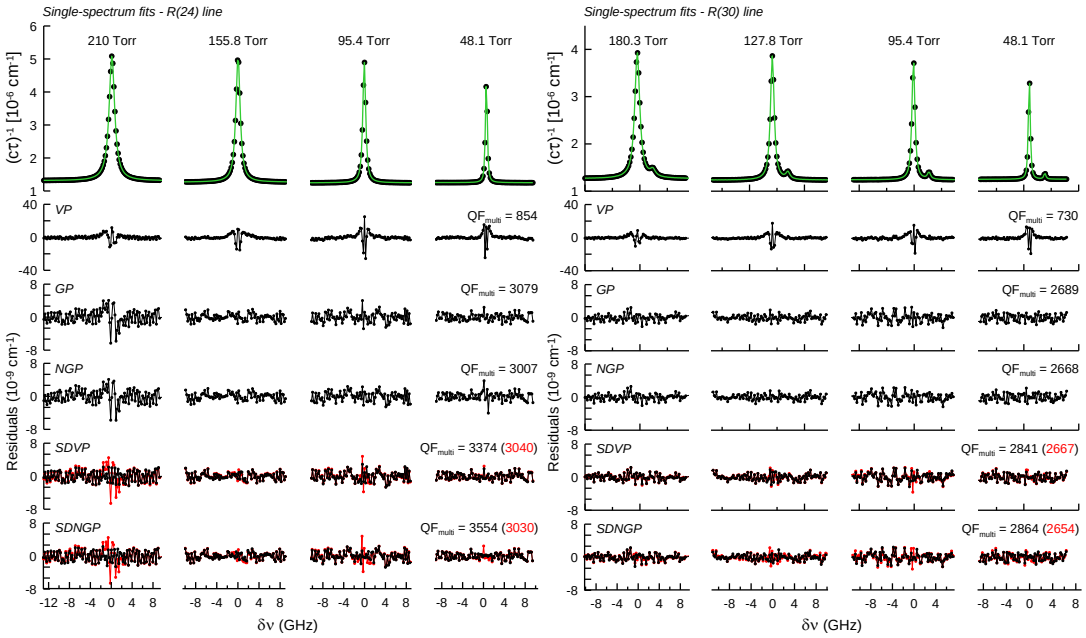

Figure 3.2: Four representative single spectrum fits for the *R*(24) and *R*(30) transitions using a variety of line profiles. The upper panel shows the measurement and the corresponding single-spectrum fit using the SDNGP. The bottom five panels show the fit residuals for the VP, GP, NGP, SDVP and SDNGP, respectively. The black and red residuals presented for the SDVP and SDNGP fits are with ($a_S \neq 0$) and without ($a_S=0$) the speed dependence of collisional shifts, respectively. $\delta\nu$ on the x-axis corresponds to the frequency detuning from line centers in GHz.

Beyond the normally used Voigt profile, we have incorporated into our lineshape analysis more advanced profiles that take into account line narrowing effects as well as lineshape asymmetries. For each of the fits, the Doppler widths were calculated from the known temperature around 296 K and were held fixed. In addition, the collisional shifts were set to the HITRAN2012[21] values found in Table 1.

Line	ν_0 (cm^{-1}) HITRAN	Δ/p (cm^{-1}/atm) HITRAN	$2\Gamma/p$ (cm^{-1}/atm)	Re(ν_{opt})/p (cm^{-1}/atm)	Im(ν_{opt})/p (cm^{-1}/atm)	a_W	a_S
R(24)	4871.791674	-0.005683	0.074682(33)	0.00134(60)	0.00290(40)	0.0799(21)	0.2080(170)
R(30)	4875.748732	-0.005859	0.073129(33)	0.00248(18)	-0.00010(30)	0.0786(13)	0.0750(140)

Table 3.1: Lineshape parameters for the R(24) and R(30) lines obtained from the pCSDNGP multi-spectrum fit analysis at T_{avg} = 295.72 K. Line positions, ν_0, and collisional shift coefficients, Δ/p, used in the data analysis are taken from measured values by Toth et al.[101, 102], which are found in the HITRAN database. The stated uncertainties of the lineshape parameters arise from the uncertainty in the fit. The correlation parameters, η_Γ and η_Δ, obtained from the pCSDNGP profile are stated in the text.

Residuals from the single-spectrum fit analysis for the different lineshape models are presented in Fig. 2 for four intermediate pressures. The VP gives the worst fit with the residuals exhibiting a large systematic feature indicative of line narrowing. Upon including Dicke narrowing (i.e., the GP and NGP fits), the large residuals observed with the VP disappear. Similar results were obtained for the SDVP fit which uses a different mechanism of line narrowing, namely the speed dependence of collisional broadening. For a better comparison of the fit results provided by the different lineshape models, we introduced a quality of fit factor for multi-spectrum fits,[72] QF_{multi}, defined as the ratio of the peak absorption signal for the spectrum having the highest absorption, $\text{Max}_j\{\alpha_{\text{max},j}-\alpha_{\text{min},j}\}$, to the standard deviation $\tilde{S}_{R_{\text{multi}}}$ of the fit residuals calculated from all of the spectra included in the multi-spectrum fit:

$$QF_{\text{multi}} = \frac{\text{Max}_j\{\alpha_{\text{max},j} - \alpha_{\text{min},j}\}}{\tilde{S}_{R_{\text{multi}}}}. \qquad (5)$$

In the above expression, $\alpha_{\text{max},j}$ is the maximum absorption coefficient and $\alpha_{\text{min},j}$ is the baseline level of the absorption spectrum for the $j_{\underline{\text{th}}}$ spectrum. $\tilde{S}_{R_{\text{multi}}}$ is the standard deviation of the fit residuals calculated from the formula

$$\tilde{S}_{R_{\text{multi}}} = \sqrt{\frac{1}{\sum_{j=1}^{N} M_j - k} \sum_{j=1}^{N} \sum_{i=1}^{M_j} \left[\alpha_{\text{exp}}\left(\nu_{ji}\right) - \alpha_{\text{fit}}\left(\nu_{ji}\right)\right]^2}, \quad (6)$$

where N is the number of spectra taken included in the multi-spectrum fit, M_j is the number of points in the j_{th} spectrum *(j = 1, ..., N)* and $\sum_{j=1}^{N} M_j - k$ is the total number of degrees of freedom with k lineshape parameters fitted in the multi-spectrum fit procedure. The terms $\alpha_{\text{exp}}(\nu_{ji})$ and $\alpha_{\text{fit}}(\nu_{ji})$ are experimental and fitted absorption coefficients, respectively, for the i_{th} measurement point in the j_{th} spectrum.

Based upon the residuals from single-spectrum fits, we observed that Dicke narrowing and speed-dependent effects describe the narrowing mechanism of the CO_2 lineshapes equally well. In addition, under conditions of low and intermediate ratios of the collisional width, Γ, to the Doppler width, Γ_{D}, the lineshape affected by the speed dependence of collisional broadening can often be well modeled by the Dicke narrowed profile.[92, 103] Unfortunately, this treatment leads to a nonlinear pressure dependence of the narrowing parameter $Re(\nu_{\text{opt}})$[66, 104, 105] in this intermediate case (i.e., $1<\Gamma/\Gamma_{\text{D}}<5$). This nonphysical result can be seen in the $R(24)$ NGP fit shown in Fig. 3A.

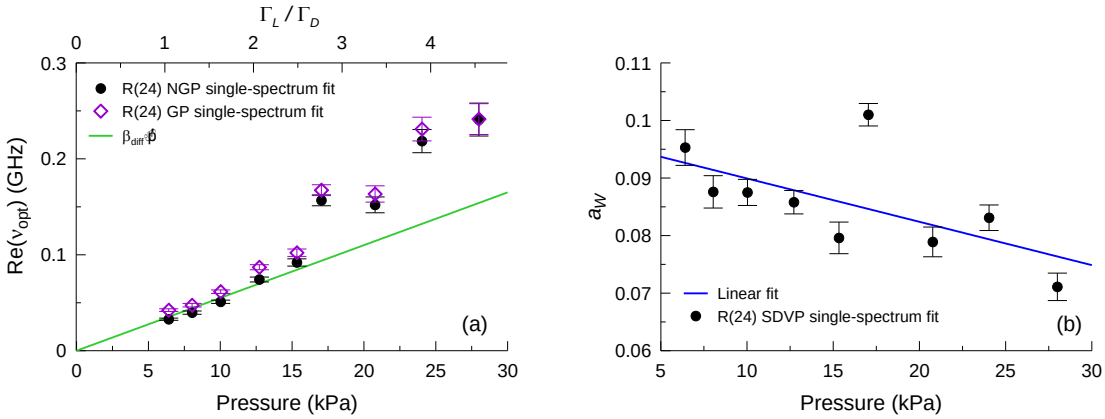

Figure 3.3: Pressure dependence of the frequency of optical collisions, Re(ν_{opt}), and speed-dependence parameter, a_W, parameter obtained for the *R*(24) line from the NGP, GP, and SDVP single-spectrum fits, respectively. The green line is the frequency of optical collisions, ν_{diff}, calculated from the mass diffusion coefficient. The blue line is a linear fit to data. Note that the given error bars arise only from the uncertainty in the fit, and that the additional scatter in the data is from instrumental effects.

On the other hand, a reduction of the observed a_W parameter with pressure in the SDVP fits, presented in Fig. 3B, suggests that Dicke narrowing also contributes to the shape of both the *R*(24) and *R*(30) lines. Consequently, the data were also analyzed with the SDNGP, which includes both of these narrowing effects. Residuals from this single-spectrum fit analysis with the SDNGP are presented in Fig. 2, and are similar to those obtained when using the GP, NGP and SDVP. Moreover, we noticed that the incorporation of the speed dependence of collisional shifting (which describes lineshape asymmetry) into the fits with the SDNGP and SDVP led to a further improvement of the residuals.

It should be noted, however, that flat residuals obtained from these single-spectrum fits do not guarantee proper interpretation of the lineshape effects in the measured spectra. Systematic instrumental errors may affect the shape of the investigated lines and can be well masked by nonlinear pressure dependencies of the fitted lineshape parameters as well as lineshape asymmetries. Also in the case of relatively complex

profiles like the SDNGP, numerical correlations between the different lineshape parameters can become important and lead to a large scatter in the obtained results. It will be shown later that a multi-spectrum fit analysis[53] helps to overcome these problems.[106, 107]

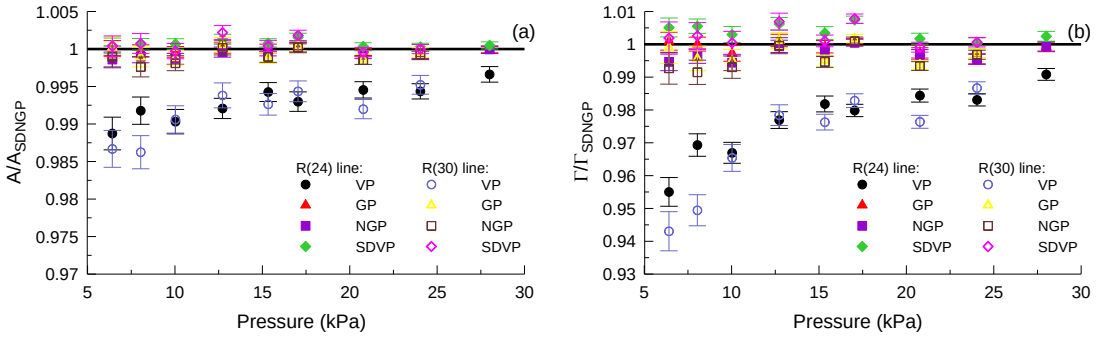

Figure 3.4: Pressure-dependent integrated area and air-broadened collisional width ratios of the VP, GP, NGP and SDVP to the SDNGP, denoted as A/A_{SDNGP} and Γ/Γ_{SDNGP}, respectively. Both the $R(24)$ and $R(30)$ lines are shown. The error bars arise from the uncertainty in the fit.

We note that the choice of line profile not only affects the fit residuals but also has a strong effect upon the resulting fitted parameters. In Fig. 4 deviations in the collisional widths and areas obtained for the $R(24)$ and $R(30)$ lines from the single-spectrum fit analysis with the VP, GP, NGP, and SDVP relative to the SDNGP are shown. The VP fit differs by as much as 5% and 1.2% from the SDNGP for the collisional width and area, respectively. The maximum deviations of the GP, NGP, and SDVP from the SDNGP for the collisional widths and areas are of the order of 0.7% and 0.2%, respectively. Moreover, the VP fit results do not converge with the other profiles even at high pressures, which indicates that the VP is not suitable for high accuracy measurements. This finding is consistent with previous observations by Long et al.[43] for CO_2 lines near 1.6 μm as well as for other systems.[68, 71, 105, 106, 108, 109]

As shown in Fig. 2, the single-spectrum fit analysis with the SDNGP can reproduce the investigated spectra down to the instrument noise level. However, the large scatter in the fitted values for the Re(ν_{opt}) and a_W parameters presented in Fig. 6 indicate that they may be correlated. This competition of speed dependence of collisional broadening with collisional narrowing, particularly at low pressures, has been reported in a number of previous studies.[43, 69-71, 92, 103]

A solution to remove correlation between the Re(ν_{opt}) and a_W parameters is to incorporate a multi-spectrum fit procedure[53] into the lineshape analysis.[95, 106, 107, 110, 111] Therefore, we performed simultaneous fits to the nine spectra from 6.5 - 28 kPa for the *R*(24) line and eight spectra from 6.5 - 24 kPa for the *R*(30) line with a few necessary constraints. First, the collisional widths and frequencies of optical collisions were constrained to be linear with pressure according to the relations $\Gamma(p)=\gamma p$ and $\nu_{opt}(p)=\beta p$, where γ and β are the collisional broadening and collisional narrowing coefficients, respectively, fitted in the multi-spectrum analysis. Moreover, in the case of the speed-dependent profiles, singular values for the a_W and a_S parameters were fitted for all pressures to assure their pressure independences. Due to the small fluctuations of CO_2 concentration in the CO_2-air mixture, the spectral areas were fitted individually for each pressure.

Figure 5 shows the representative residuals from the multi-spectrum fit analyses for the *R*(24) and *R*(30) lines. Similar to the single-spectrum fit analysis, the VP gave the worst results. However, contrary to the single-spectrum analysis, the fits residuals for the profiles which describe different mechanisms of line narrowing are now distinguishable.

Comparing the QF_{multi} for the GP and NGP, it appears that the soft collision model better describes the line narrowing effect for both investigated lines. On the other hand, the large improvements in the QF_{multi} for the SDVP without the speed dependence of collisional shifting (a_S=0) by as much as 12% and 8% for the *R*(24) and *R*(30) lines, respectively, when compared to the corresponding results with the GP suggest that the speed dependence of collisional broadening is the dominant contribution to the total narrowing of these lines. It was also observed that the incorporation of Dicke narrowing improves the QF_{multi} compared to the SDVP (with a_S=0). In addition, the incorporation of the speed dependence of collisional shifting in the SDVP and SDNGP analysis improved the residuals and led to a further increase of the QF_{multi}. However, the contribution of speed-dependent asymmetry into the shape of the *R*(24) and *R*(30) lines appears to be weaker for the multi-spectrum fits than for the single-spectrum ones.

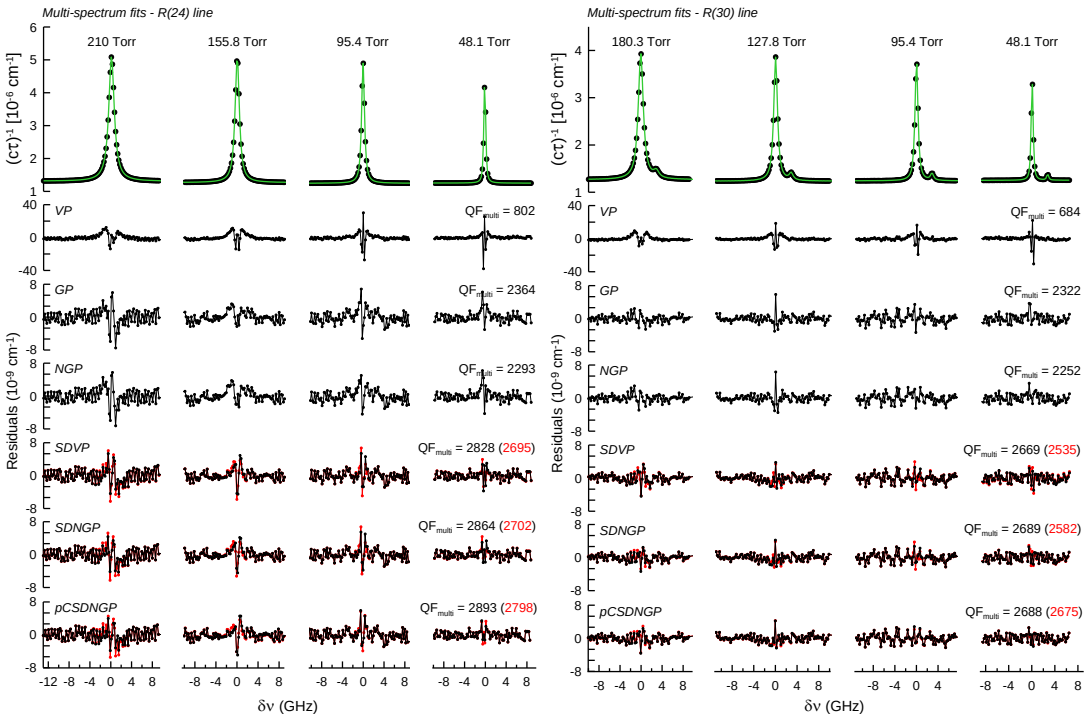

Figure 3.5: Four representative multi-spectrum fits for the *R*(24) and *R*(30) transitions using a variety of line profiles. The upper panel shows the measurement and the corresponding fit using the pCSDNGP. The bottom six panels show the fit residuals for the VP, GP, NGP, SDVP, SDNGP and pCSDNGP, respectively. The black and red residuals presented for SDVP, SDNGP and pCSDNGP fits are with ($a_S \neq 0$) and without ($a_S = 0$) the speed dependence of collisional shifts, respectively. $\delta\nu$ on the x-axis corresponds to the frequency detuning from line centers in GHz.

A comparison of the differences between the QF_{multi} improvements obtained from SDNGP fits with ($a_S \neq 0$) and without ($a_S = 0$) speed-dependent asymmetry in the case of the single- and multi-spectrum fit analysis gave the following results: 15% and 7% for the *R*(24) line and 7% and 4% for the *R*(30) line, respectively. These differences suggest that the observed lineshape asymmetry is caused partially by instrumental effects and is integrally simulated by the speed-dependent asymmetry in the single-spectrum fit analysis. Note also that the asymmetry differences between single- and multi-spectrum fits are larger for the *R*(24) line, which are attributed to a larger contribution of instrumental errors to the total line shape.

As previously shown by Lisak et al.,[110] the utility of multi-spectrum fitting in advanced lineshape analysis can be demonstrated from a simple test of the fitted parameters. From Fig. 6, the large pressure variations of the Re(ν_{opt}) and a_W parameters for the *R*(24) line are suggestive of strong numerical correlations between them. The black points correspond to the parameters obtained from the SDNGP single-spectrum fits with Re(ν_{opt}) and a_W both fitted. The straight dashed lines are the Re(ν_{opt}) and a_W values obtained from the SDNGP multi-spectrum fit. The blue diamonds in Fig. 6B correspond to single-spectrum fits of the SDNGP in which the Re(ν_{opt}) was constrained to the value from the multi-spectrum fit and a_W was fitted individually for each pressure. Consequently, the fitted a_W is expected and observed to be nearly pressure independent. Moreover, the large scatter in the fitted values of a_W and their uncertainties are significantly reduced. Therefore, the additional constraints provided by the multi-spectrum fitting procedure was necessary to properly treat the correlations between the Re(ν_{opt}) and a_W parameters.

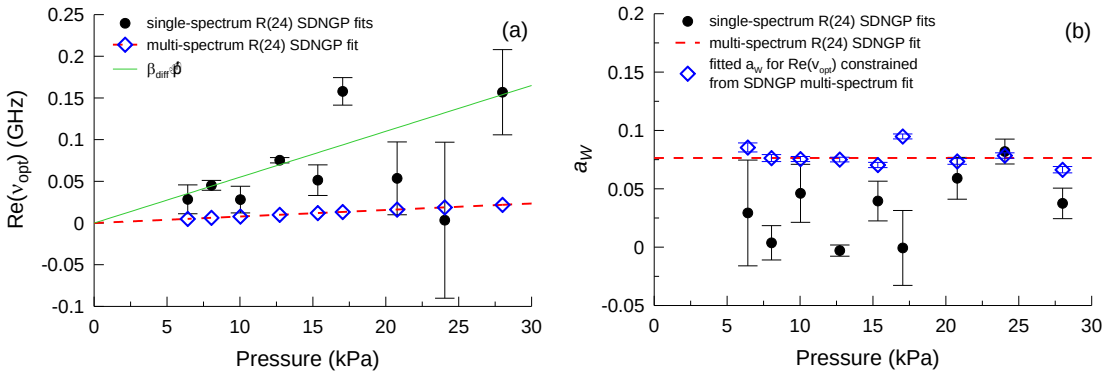

Figure 3.6: A test of the multi-spectrum fit parameters for Re(ν_{opt}) and a_W. The black points represent the parameter values obtained from the SDNGP single-spectrum fit analysis. Numerical correlations between Re(ν_{opt}) and a_W parameters are evident from the large scatter. The red dashed lines are the Re(ν_{opt}) and a_W values yielded by the SDNGP multi-spectrum fit. The blue diamonds in graph (a) correspond to Re(ν_{opt}) from the SDNGP multi-spectrum fit. The blue diamonds in graph (b) correspond to a_W parameters fitted individually for each pressure in the SDNGP single-spectrum fit analysis when Re(ν_{opt}) is constrained to the value from the SDNGP multi-spectrum fit. The green solid line is the frequency of optical collisions ν_{diff} calculated from the mass diffusion coefficient[99].

The green solid lines plotted in Figs. 3A and 6A correspond to the frequency of velocity-changing collisions calculated from the mass diffusion coefficient[99] (ν_{diff} = 5.5 kHz/Pa). By comparing the ν_{diff} and Re(ν_{opt}) values, one may estimate the contribution of correlation between velocity- and phase-changing collisions (v-p correlations) into the lineshapes of the investigated CO_2 lines. In Fig. 3A, the Re(ν_{opt}) values obtained from NGP single-spectrum fits agree with ν_{diff} for pressures up to 12 kPa. This incidental agreement can suggest that there is no need for inclusion of v-p correlations or speed dependence of collisional broadening for the *R*(24) line. However, such conclusion can be incorrect as first shown by Duggan et al.[108] for CO lines. We have already shown that the NGP is inadequate for modeling the data, and that the speed dependence of collisional broadening has a much greater contribution to the total narrowing of lineshapes than the Dicke narrowing effect. Moreover, the retrieved value of the Re(ν_{opt}) from the SDNGP multi-spectrum fit, presented in Fig. 6A as the red dashed line, is almost one order of magnitude smaller than ν_{diff}. This is indicative of v-p correlations for the *R*(24) line. Similar conclusions were drawn for the *R*(30) line.

Correlations between phase- and velocity-changing collisions (v-p correlations) are another source of lineshape asymmetry and cannot be ignored when asymmetry has been observed. To properly account for v-p correlations, we performed the multi-spectrum fit analysis with the partially correlated SDNGP (pCSDNGP) for both investigated lines. The residuals and QF_{multi} values from the pCSDNGP fits are presented in Fig. 6 and are observed to be similar to those obtained from the SDNGP analysis. It should be noted that both mechanisms of lineshape asymmetry, namely the speed

dependence of collisional shifting and v-p correlations, were considered in the presented fits. A comparison of the QF_{multi} factors for the pCSDNGP with ($a_S \neq 0$) and without ($a_S = 0$) speed-dependent asymmetry shows that the speed-dependent asymmetry can be well simulated by the v-p correlation asymmetry. To quantify the contribution of the v-p correlations into the total narrowing and asymmetry, we calculated the correlation parameters, η_Γ and η_Δ, based on the ν_{diff} value and pCSDNGP multi-spectrum parameters of Re(ν_{opt}), Im(ν_{opt}), Γ and Δ. The results are η_Γ = (0.231±0.008), η_Δ = (0.51±0.12) for the *R*(24) line and η_Γ = (0.2202±0.0024), η_Δ = (-0.024±0.051) for the R(30) line. The small relative uncertainties of the η_Γ parameters of about 3% and 1% for the *R*(24) and *R*(30) lines, respectively, confirm the occurrence of v-p correlations in the shape of investigated CO_2 lines. Moreover, a small value for η_Δ obtained for the *R*(30) line suggests that there is minimal v-p correlation asymmetry for this line. This is also confirmed by a relatively small difference between QF_{multi} obtained from the pCSDNGP analysis with ($a_S \neq 0$) and without ($a_S = 0$) speed-dependent asymmetry. On the other hand, the η_Δ value for the *R*(24) line is surprisingly high. However, the slightly worse residuals obtained for the *R*(24) line indicate that additional lineshape asymmetry may be introduced by instrumental errors. It should be noted that the collisional shift, Δ, is a much smaller effect than collisional broadening Γ; therefore, a quantitative analysis of Im(ν_{opt}) and a_S is more challenging experimentally than analysis of Re(ν_{opt}) and a_W.

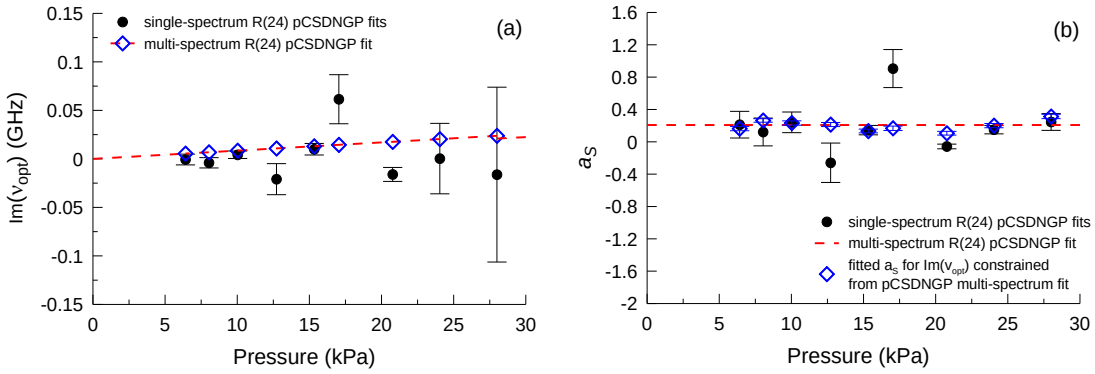

Figure 3.7: A test of the multi-spectrum fit parameters Im(ν_{opt}) and a_S. The black points are the parameters obtained from the pCSDNGP single-spectrum fit analysis. Numerical correlations between the Im(ν_{opt}) and a_S parameters in the single-spectrum fits are evident from the large scatter. The red dashed lines are the Im(ν_{opt}) and a_S values yielded by the pCSDNGP multi-spectrum fit. The blue diamonds in graph (a) correspond to Im(ν_{opt}) from the pCSDNGP multi-spectrum fit. The blue diamonds in graph (b) correspond to the a_S parameters fitted individually for each pressure in the pCSDNGP single-spectrum fit analysis where Im(ν_{opt}) is constrained to the value from the pCSDNGP multi-spectrum fit.

A test of the multi-spectrum fit parameters of Im(ν_{opt}) and a_S describing v-p correlations and speed-dependent asymmetries, respectively, is demonstrated in Fig. 7. The black points show the fitted Im(ν_{opt}) and a_S values obtained from the pCSDNGP single-spectrum fits. The large scatter suggests that they are correlated. The red dashed lines are the Im(ν_{opt}) and a_S values obtained from the pCSDNGP multi-spectrum fit. The blue diamonds in Fig. 7B correspond to single-spectrum fits of the pCSDNGP in which the Im(ν_{opt}) was constrained to the value from the pCSDNGP multi-spectrum fit, and a_S was fitted for each pressure. In addition, we constrained the pressure dependence of Re(ν_{opt}) and the pressure independence of a_W, and we fixed their values to those obtained from the pCSDNGP multi-spectrum fit. As observed before, the fitted a_S are nearly independent on pressure and the scatter in the fitted values of a_S is greatly reduced when Im(ν_{opt}) is constrained to the value from the multi-spectrum fit. The recommended parameters describing the shape of the $R(24)$ and $R(30)$ lines, obtained from the pCSDNGP multi-spectrum fits, are assembled in Table 1.

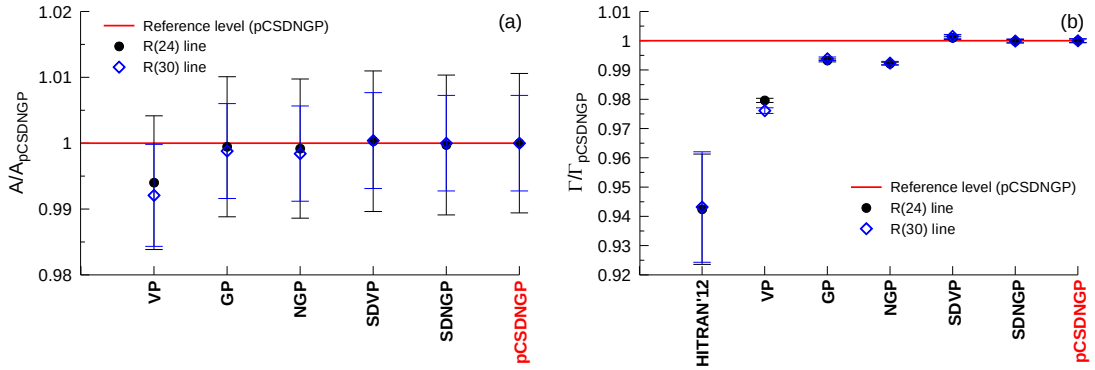

Figure 3.8: A comparison of the fitted line areas per unit pressure (a) and collisional air-broadening coefficients (b) retrieved from the multi-spectrum fit analysis with the use of different lineshape models in relation to the pCSDNGP. Both the *R*(24) and *R*(30) lines are shown. In case of the collisional broadening coefficient, differences between the recommended pCSDNGP and HITRAN2012 values are also presented. The shown uncertainties are the fit uncertainties.

Comparisons of the integrated line areas per unit pressure and the collisional air-broadening coefficients retrieved from the multi-spectrum fit analysis with the use of different lineshape models in relation to the pCSDNGP are presented in Fig. 8. The VP differs from the pCSDNGP by 0.6% and 2% for the line area and collisional broadening coefficient, respectively. The GP, NGP and SDVP differ from the pCSDNGP by less than 0.1% for the line area. However, for the Γ values, the GP and NGP results differ by more than 0.6% from the pCSDNGP, whereas for the SDVP the difference is only about 0.1%. The areas and collisional broadening coefficients obtained from the SDNGP are very close to those retrieved from the pCSDNGP. It should be noted that collisional air-broadening coefficients given in the HITRAN2012 database are systematically lower by almost 6% and 2% compared to values obtained from pCSDNGP and VP fits, respectively. Note that the error bars presented in Fig. 8 arise from the uncertainty in the fit. Moreover, the large error bars of $\Gamma/\Gamma_{\mathrm{pCSDNGP}}$ for the HITRAN2012 case correspond to a reported 2% relative uncertainty of the collisional air-broadening coefficient. Finally, observed fluctuations of the CO_2 concentration in the CO_2-air mixture measurements are

responsible for the large uncertainty of area per unit pressure coefficient and also for the large error bars of $A/A_{pCSDNGP}$ for all of the investigated lineshape models.

3.6 Conclusions

A lineshape analysis of two air-broadened rovibrational CO_2 transitions near 2.06 μm was performed with spectra recorded with a frequency-stabilized cavity ring-down spectrometer. Two dominant line narrowing mechanisms–velocity-changing collisions and the speed dependence of collisional broadening–were identified in the total lineshape. To quantify the individual contribution from both narrowing effects and remove their correlation, the multi-spectrum fit technique was incorporated into the SDNGP lineshape analysis. In addition, a noticeably smaller value of the frequency of optical collisions was retrieved from the SDNGP multi-spectrum fit compared to the value calculated from the mass diffusion coefficient, thus providing evidence of correlations between the phase- and velocity-changing collisions for both the *R*(24) and *R*(30) transitions. Moreover, small asymmetries in the lineshapes were also observed. However, this asymmetry can be equally well ascribed to either the speed dependence of collisional shifting or to the correlations between phase- and velocity-changing collisions. Consequently, we concluded that the partially correlated SDNGP (pCSDNGP)[67] profile is the most appropriate model considered here to reproduce the experimental lineshapes at a high quality level. Experimental tests of pCSDNGP have also recently been reported for O_2[95] and H_2O.[112] Furthermore, efficient algorithms for calculating the pCSDNGP line profile have been developed[79, 113, 114] and its use has been strongly recommended for modeling

lineshapes in the spectrally isolated regime.[115] We note that an alternative nomenclature in the literature for the same pCSDNGP profile used here is the partially correlated speed-dependent hard-collision profile.[112] In the case of quadratic speed-dependence, the following names were used as well: partially correlated quadratic-speed-dependent hard-collision profile (pCqSDHCP),[79, 113-115] partially correlated quadratic-speed-dependent Nelkin-Ghatak profile[94] and Hartmann-Tran profile (HTP).[115]

Experimental data were also fitted with the commonly used Voigt profile (VP). However, we showed that it is not sufficient for modeling CO_2 transitions with the accuracy and precision demanded in remote sensing applications. We noticed 2% and 4% biases introduced by the VP in the retrieved air-broadening parameters compared to the values obtained from the recommended pCSDNGP and HITRAN2012 database. Moreover, it is interesting and remarkable that lineshape models incorporating only the Dicke narrowing effect (GP, NGP) provide systematically lower values of collisional air-broadening coefficients by about 0.6% compared to pCSDNGP. Finally, we acknowledge the necessity of more comprehensive lineshape models that incorporate collisional line-mixing at higher pressures for utility of the broader remote sensing community.

3.7 Acknowledgements

This work was supported by the Orbiting Carbon Observatory –2 (OCO-2) project at the Jet Propulsion Laboratory under contract with the National Aeronautics and Space Administration (NASA) through the NASA grant NAS7-03001. T. Q. B. was supported by a NASA Earth and Space Sciences Fellowship and the NASA Mars Fundamental Research Grant NNX12AI01G. D.W.H. was supported by the Jack and Edith Roberts Summer Undergraduate Research Fellowship. Support for D. A. L. and V. T. S. was provided by the NIST Greenhouse Gas Measurements and Climate Research Program. A. C., D. L., R. C. were partially supported by the Foundation for Polish Science TEAM Project co-financed by the EU European Regional Development Fund, the National Science Centre, Projects DEC-2011/01/B/ST2/00491 and UMO-2013/11/D/ST2/02663, and is part of the program of the national laboratory FAMO in Toruń, Poland. A. C. was further supported by the Foundation for Polish Science START Project.

3.8 References

1. C. E. Miller, D. Crisp, P. L. DeCola, S. C. Olsen, J. T. Randerson, A. M. Michalak, A. Alkhaled, P. Rayner, D. J. Jacob, P. Suntharalingam, D. B. A. Jones, A. S. Denning, M. E. Nicholls, S. C. Doney, S. Pawson, H. Boesch, B. J. Connor, I. Y. Fung, D. O'Brien, R. J. Salawitch, S. P. Sander, B. Sen, P. Tans, G. C. Toon, P. O. Wennberg, S. C. Wofsy, Y. L. Yung and R. M. Law, J. Geophys. Res., [Atmos.] **112** (D10), D10314 (2007).

2. D. Crisp, R. M. Atlas, F. M. Breon, L. R. Brown, J. P. Burrows, P. Ciais, B. J. Connor, S. C. Doney, I. Y. Fung, D. J. Jacob, C. E. Miller, D. O'Brien, S. Pawson, J. T. Randerson, P. Rayner, R. J. Salawitch, S. P. Sander, B. Sen, G. L. Stephens, P. P. Tans, G. C. Toon, P. O. Wennberg, S. C. Wofsy, Y. L. Yung, Z. M. Kuang, B. Chudasama, G. Sprague, B. Weiss, R. Pollock, D. Kenyon and S. Schroll, in *Trace Constituents in the Troposphere and Lower Stratosphere*, edited by J. P. Burrows and A. M. Thompson (Pergamon-Elsevier Science Ltd, Kidlington, 2004), Vol. 34, pp. 700-709.

3. G. D. Spiers, R. T. Menzies, J. Jacob, L. E. Christensen, M. W. Phillips, Y. H. Choi and E. V. Browell, Appl. Opt. **50** (14), 2098-2111 (2011).

4. R. A. Toth, L. R. Brown, C. E. Miller, V. M. Devi and D. C. Benner, J. Quant. Spectrosc. Radiat. Transf. **109** (6), 906-921 (2008).

5. V. M. Devi, D. C. Benner, L. R. Brown, C. E. Miller and R. A. Toth, J. Mol. Spectrosc. **245** (1), 52-80 (2007).

6. V. M. Devi, D. C. Benner, L. R. Brown, C. E. Miller and R. A. Toth, J. Mol. Spectrosc. **242** (2), 90-117 (2007).

7. A. Predoi-Cross, W. Liu, C. Holladay, A. V. Unni, I. Schofield, A. R. W. McKellar and D. Hurtmans, J. Mol. Spectrosc. **246** (1), 98-112 (2007).

8. T. Hikida, K. M. T. Yamada, M. Fukabori, T. Aoki and T. Watanabe, J. Mol. Spectrosc. **232** (2), 202-212 (2005).

9. T. Hikida and K. M. T. Yamada, J. Mol. Spectrosc. **239** (2), 154-159 (2006).

10. G. Casa, R. Wehr, A. Castrillo, E. Fasci and L. Gianfrani, J. Chem. Phys **130** (18), 184306 (2009).

11. D. A. Long, K. Bielska, D. Lisak, D. K. Havey, M. Okumura, C. E. Miller and J. T. Hodges, J. Chem. Phys **135** (6), 064308 (2011).

12. L. Joly, F. Gibert, B. Grouiez, A. Grossel, B. Parvitte, G. Durry and V. Zeninari, J. Quant. Spectrosc. Radiat. Transf. **109** (3), 426 (2008).

13. A. Predoi-Cross, A. R. W. McKellar, D. C. Benner, V. M. Devi, R. Gamache, C. E. Miller, R. A. Toth and L. R. Brown, Can. J. Phys. **87** (5), 517-535 (2009).

14. P. Duggan, P. M. Sinclair, A. D. May and J. R. Drummond, Phys. Rev. A **51**, 218 (1995).

15. A. S. Pine, J. Quant. Spectrosc. Radiat. Transf. **62**, 397 (1999).

16. F. Chaussard, R. Saint-Loup, H. Berger, P. Joubert, X. Bruet, J. Bonamy and D. Robert, J. Chem. Phys. **113**, 4951 (2000).

17. D. Lisak, G. Rusciano and A. Sasso, J. Mol. Spectrosc. **227**, 162 (2004).

18. D. Lisak, G. Rusciano and A. Sasso, Phys. Rev. A **72** (1), 012503 (2005).

19. D. Lisak, J. T. Hodges and R. Ciuryło, Phys. Rev. A **73**, 012507 (2006).

20. A. Cygan, D. Lisak, S. Wójtewicz, J. Domysławska, J. T. Hodges, R. S. Trawiński and R. Ciuryło, Phys. Rev. A. **85**, 022508 (2012).

21. P. L. Varghese and R. K. Hanson, Appl. Opt. **23** (14), 2376-2385 (1984).

22. F. Schreier, J. Quant. Spectrosc. Radiat. Transf. **48**, 743-762 (1992).

23. R. H. Dicke, Phys. Rev. **89** (2), 472-473 (1953).

24. S. G. Rautian and I. I. Sobelman, Sov. Phys. Usp. **9** (5), 701 (1967).

25. L. Galatry, Phys. Rev. **122** (4), 1218 (1961).

26. M. Nelkin and A. Ghatak, Phys. Rev. A **135** (1A), A4 (1964).

27. R. Ciuryło, A. S. Pine and J. Szudy, J. Quant. Spectrosc. Radiat. Transf. **68** (3), 257-271 (2001).

28. N. H. Ngo, D. Lisak, H. Tran and J. M. Hartmann, J. Quant. Spectrosc. Radiat. Transf. **129**, 89-100 (2013).

29. P. W. Anderson, Phys. Rev. **86**, 809–809 (1952).

30. J. Szudy and W. E. Baylis, J. Quant. Spectrosc. Radiat. Transfer **15**, 641-668 (1975).

31. A. Bielski, R. Ciuryło, J. Domysławska, D. Lisak, R. S. Trawiński and J. Szudy, Phys. Rev. A **62** (3), 032511 (2000).

32. M. Baranger, Phys. Rev. **111**, 494 (1958).

33. P. W. Rosenkranz, IEEE Trans. Antennas Propag. **23**, 498–506 (1975).

34. R. Ciuryło and J. Szudy, Phys. Rev. A **63**, 042714 (2001).

35. P. R. Berman, J. Quant. Spectrosc. Radiat. Transf. **12** (9), 1331 (1972).

36. J. Ward, J. Cooper and E. W. Smith, J. Quant. Spectrosc. Radiat. Transfer **14** (7), 555–590 (1974).

37. H. M. Pickett, J. Chem. Phys **73** (12), 6090-6094 (1980).

38. R. Ciuryło and J. Szudy, J. Quant. Spectrosc. Radiat. Transf. **57**, 411 (1997).

39. B. Lance, G. Blanquet, J. Walrand and J. P. Bouanich, J. Mol. Spectrosc. **185** (2), 262-271 (1997).

40. R. Ciuryło, Phys. Rev. A. **58** (2), 1029-1039 (1998).

41. D. Priem, F. Rohart, J. M. Colmont, G. Wlodarczak and J. P. Bouanich, J. Mol. Struct. **517**, 435-454 (2000).

42. R. Ciuryło, R. Jaworski, J. Jurkowski, A. S. Pine and J. Szudy, Phys. Rev. A **63**, 032507 (2001).

43. D. Lisak, A. Cygan, P. Wcisło and R. Ciuryło, J. Quant. Spectrosc. Radiat. Transf. **151**, 43 (2015).

44. J. Domysławska, S. Wójtewicz, A. Cygan, K. Bielska, D. Lisak, P. Masłowski, R. S. Trawiński and R. Ciuryło, J. Chem. Phys. **139**, 194312 (2013).

45. L. Demeio, S. Green and L. Monchick, J. Chem. Phys. **102**, 9160 (1995).

46. A. S. Pine, J. Chem. Phys. **101**, 3444 (1994).

47. P. Joubert, J. Bonamy, D. Robert, J. Domenech and D. Bermejo, J. Quant. Spectrosc. Radiat. Transf. **61**, 519 (1999).

48. W. J. Massman, Atmospheric Environment **32** (6), 1111-1127 (1998).

49. J. T. Hodges, H. P. Layer, W. W. Miller and G. E. Scace, Rev. Sci. Instrum. **75** (4), 849-863 (2004).

50. D. A. Long, A. Cygan, R. D. van Zee, M. Okumura, C. E. Miller, D. Lisak and J. T. Hodges, Chem. Phys. Lett. **536**, 1-8 (2012).

51. J. T. Hodges and R. Ciuryło, Rev. Sci. Instrum. **76**, 023112 (2005).

52. D. Halmer, G. von Basum, P. Hering and M. Mürtz, Rev. Sci. Instrum. **75**, 2187 (2004).

53. D. Lisak and J. T. Hodges, Appl. Phys. B **88** (2), 317-325 (2007).

54. L. S. Rothman, I. E. Gordon, Y. Babikov, A. Barbe, D. C. Benner, P. F. Bernath, M. Birk, L. Bizzocchi, V. Boudon, L. R. Brown, A. Campargue, K. Chance, E. A. Cohen, L. H. Coudert, V. M. Devi, B. J. Drouin, A. Fayt, J. M. Flaud, R. R. Gamache, J. J. Harrison, J. M. Hartmann, C. Hill, J. T. Hodges, D. Jacquemart, A. Jolly, J. Lamouroux, R. J. Le Roy, G. Li, D. A. Long, O. M. Lyulin, C. J. Mackie, S. T. Massie, S. Mikhailenko, H. S. P. Muller, O. V. Naumenko, A. V. Nikitin, J. Orphal, V. Perevalov, A. Perrin, E. R. Polovtseva, C. Richard, M. A. H. Smith, E. Starikova, K. Sung, S.

Tashkun, J. Tennyson, G. C. Toon, V. G. Tyuterev and G. Wagner, J. Quant. Spectrosc. Radiat. Transf. **130**, 4-50 (2013).

55. R. A. Toth, C. E. Miller, L. R. Brown, V. M. Devi and D. C. Benner, J. Mol. Spectrosc. **243**, 43-61 (2007).

56. R. A. Toth, C. E. Miller, V. M. Devi, D. C. Benner and L. R. Brown, J. Mol. Spectrosc. **246** (2), 133-157 (2007).

57. D. Priem, J. M. Colmont, F. Rohart, G. Wlodarczak and R. Gamache, J. Mol. Spectrosc. **204** (204) (2000).

58. J. F. D'Eu, B. Lemoine and F. Rohart, J. Mol. Spectrosc. **212**, 96 (2002).

59. F. Rohart, G. Wlodarczak, J. M. Colmont, G. Cazzoli, L. Dore and C. Puzzarini, J. Mol. Spectrosc. **251**, 282 (2008).

60. D. C. Benner, C. P. Rinsland, V. M. Devi, M. A. H. Smith and D. Atkins, J. Quant. Spectrosc. Radiat. Transf. **53** (6), 705-721 (1995).

61. A. S. Pine and R. Ciuryło, J. Mol. Spectrosc. **208**, 180 (2001).

62. A. S. Pine and T. Gabard, J. Quant. Spectrosc. Radiat. Transf. **66**, 69 (2000).

63. P. Duggan, P. M. Sinclair, R. Berman, A. D. May and J. R. Drummond, J. Mol. Spectrosc. **186** (1), 90-98 (1997).

64. M. D. De Vizia, F. Rohart, A. Castrillo, E. Fasci, L. Moretti and L. Gianfrani, Phys. Rev. A **83**, 052506 (2011).

65. D. Lisak, D. K. Havey and J. T. Hodges, Phys. Rev. A **79** (5), 052507 (2009).

66. P. Amodio, L. Moretti, A. Castrillo and L. Gianfrani, J. Chem. Phys. **140**, 044310 (2014).

67. M. D. De Vizia, A. Castrillo, E. Fasci, P. Amodio, L. Moretti and L. Gianfrani, Phys. Rev. A **90**, 022503 (2014).

68. N. H. Ngo, D. Lisak, H. Tran and J. M. Hartmann, J. Quant. Spectrosc. Radiat. Transf. **134**, 105 (2014).

69. H. Tran, N. H. Ngo and J. M. Hartmann, J. Quant. Spectrosc. Radiat. Transf. **129**, 199 (2013).

70. J. Tennyson, P. F. Bernath, A. Campargue, A. G. Csaszar, L. Daumont, R. R. Gamache, J. T. Hodges, D. Lisak, O. V. Naumenko, L. S. Rothman, H. Tran, N. F. Zobov, J. Buldyreva, C. D. Boone, M. D. De Vizia, L. Gianfrani, J. M. Hartmann, R. McPheat, D. Weidmann, J. Murray, N. H. Ngo and O. L. Polyansky, Pure Appl. Chem., in press (2014).

Chapter 4: Dual-wavelength cavity ring-down spectroscopy for methane isotope ratio measurement

4.1 Abstract

We demonstrate a frequency-stabilized cavity ring-down spectrometer capable of measuring simultaneously isotopologues of methane $^{12}CH_4$, $^{13}CH_4$, $^{12}CH_3D$ with precisions of δD~0.286‰ and $\delta^{13}C$~0.11‰. Two orthogonally polarized continuous-wave (CW) lasers are coupled into an optical ring-down cavity for spectral measurements over the full wavelength range of 1.45-1.65μm. The stability of our instrument allows long-term averaging (>7 hours) for improving the precision in our methane isotope ratio measurement. In addition, we discuss the necessity of modeling methane lineshapes with the Galatry profile to achieve the highest precision.

4.2 Introduction

High-precision methane isotope ratio measurements are critical in the field of chemical physics for understanding important equilibrium fractionation and kinetic isotope effects. Isotope ratio measurements have been traditionally done using mass spectrometry, e.g., isotope ratio mass spectrometer (IRMS), since detection sensitivity is only limited by counting statistics. Despite this advantage, isobaric issues, such as complex fragmentation after ionization,[116] contaminant gases, or isotopologues with the same cardinal masses, often present challenges to accurate isotope measurements. This difficulty can be overcome by performing treatment of the samples, but isotope fractionation during these procedures can introduce additional errors. Altogether, many challenges are present for making *in situ* measurements of isotope ratios with mass spectrometry.

Infrared spectroscopy for isotope measurements presents a useful alternative with a number of demonstrations showing good precisions for a wide variety of molecular species, e.g., H_2O, CO_2, CH_4, N_2O and CO. Furthermore, spectroscopic measurements of methane isotope ratios have been reported with spectrometers that operate from near-IR to mid-IR regions.[117-124] The highest precisions for pure/pre-concentrated samples were achieved by Yamamoto and Yoshida[119] for δD of ±0.7‰ and $\delta^{13}C$ of ±0.027‰ using a modified Herriot-type cell, and by Bergamaschi et al.[120] for δD of ±5.1‰ and $\delta^{13}C$ of ±0.44‰ using tunable diode laser absorption spectroscopy (TDLS). For ambient air samples, Chen et al.[124] demonstrated precisions for $\delta^{13}C$ of ±1.7‰ for 1.9ppmv of CH_4 using cavity ring-down spectroscopy.

Infrared spectroscopic determinations of isotope ratios are not without their complications. Common challenges to measuring precise stable isotope ratios include demandingly high sensitivity and stability. Moreover, temperature uncertainties present a significant challenge especially when transitions with significantly different lower-state energies (E") are chosen.[120] One proposed solution is to use two cells[120, 125], which presents further technical challenges to ensure that both are stabilized (vibration, temperature, pressure, optical absorption path lengths) to a high degree and requires non-trivial calibration methods to achieve accurate results.[126]

Rather than using a two cell approach, we present a method to inject two different lasers into a single cell and use cavity ring-down spectroscopy for isotope ratio measurements. While the two wavelength spectrometers in a single multi-pass cells has been proposed previously[127, 128], our method combines the advantages of cavity ring-down spectroscopy and wavelength duplexing. We measure a transition of different

methane isotopologues using each laser and calculate the integrated area of the line to determine the desired isotope ratios ($^{13}C/^{12}C$, D/H). This spectrometer is a modified from FS-CRDS[9, 51], which has the necessary high spectral resolution, long term stability, and sensitivity needed for high-precision measurements. Finally, we also ensure that the proper line profile is used to model our spectra, as suggested by Long et al.[129] for CO_2 isotope ratio measurements.

4.3 Experimental Methods

We modeled the spectrometer design by Hodges et al.[9] but modified to enable a dual-wavelength acquisition scheme. A schematic is shown in Figure 4.1A. A combination of either distributed feedback (DFB) lasers or a DFB and an external cavity diode laser (ECDL) laser was used for the isotope ratio measurements. The polarizations of the lasers are set by manually-adjusted fiber-coupled polarization controllers for the DFB lasers and *λ/2* waveplates for the ECDL. With one source *s* polarized and the other *p* polarized, the light is coupled into a polarization-maintaining (PM) fiber coupled AOM. The first-order AOM output, containing both polarizations lasers, is injected into a stainless-steel ring-down cavity (RDC) using a single mode-matching lens (F=50cm). The reflectivity of the cavity mirrors is measured to be R>99.995%, yielding a vacuum finesse of F>63,000 and effective path length of L>47 km at the peak reflectivity of the mirrors. A Wollaston prism separates light coupled out from the cavity by polarization, and photodiodes monitor light intensity of each polarization. The signals from the photodiodes are sent to a TTL-controlled RF switch (μs response time), which outputs to

a digital digitizer. A computer-controlled RF switch is used to alternate between two photodiodes so that the ring-down decays from each laser can be measured in quick succession. By switching between the two lasers, we are able to measure rotational lines with similar ground state energies and collect their spectra simultaneously. Finally, we monitor the temperature of the cavity using a NIST calibrated 2.3kΩ thermistor using the 4-wire configuration. The thermistor has a calibrated absolute temperature uncertainty of 2 mK. The cavity is placed inside an acrylic enclosure as passive thermal isolation from air currents, but no active temperature control is performed.

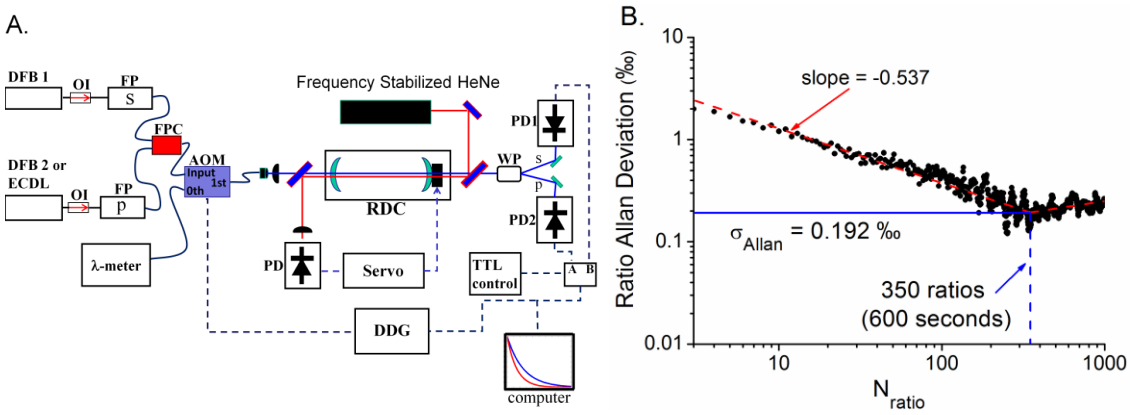

Figure 4.1: **A.** Dual-wavelength acquisition scheme for methane isotope ratio measurements. Two fiber-coupled distributed feedback (DFB) or external cavity diode laser (ECDL) lasers are orthogonally polarized ("*s*" and "*p*") by fiber polarizers (FP) and injected into a fiber-coupled AOM via a fiber power combiner (FPC). A single beam containing both polarized lasers beams are injected into a ring-down cavity (RDC) using a single lens. Light exiting the cavity is separated by polarization through a Wollaston prism (WP) and sent to separate photodiodes. Outputs from the photodiodes are connected to an RF switch. Computer control allows alternation between the two photodiodes to measure ring-down decays from each laser. **B.** Allan deviation plot for the ratio of the dual laser (λ_1=1.660μm, λ_2=1.548μm) ring-down acquisitions for vacuum baseline losses at a single wavelength. The acquisition rate for a ratio is ~ 0.5 Hz.

The Allan deviation plot shown in Figure 4.1B demonstrates the precision of our dual wavelength acquisition scheme for at a single wavelength. 1000 ratio acquisitions (N_{ratio}) of vacuum baseline losses at a single wavelength for 1.660 μm and 1.548 μm lasers were acquired at a rate of ~ 0.5 Hz/ratio. The Allan deviation displays a power-law

relationship with respect to the number of ratio acqusitions n_r, $\sigma_{\text{Allan}} = \sigma(1)N_{\text{ratio}}{}^{\beta}$, where the fitted slope (red dashed line) is $\beta = -0.537$, corresponding to a white noise dominated system up to 350 ratios (~600 s). At this maximum integration time, the best ratio precision achieved at a single wavelength is $\sigma_{\text{min}} \sim 0.192‰$.

4.4 Lineshape Modeling

For the most accurate line intensity measurements, integrated intensities yield more robust concentration values compared to peak heights, whose quantitative interpretation depends on the choice of line profiles to model spectral lineshapes.[71, 129] In particular, it has become increasingly apparent from high resolution spectroscopy that the Voigt profile is insufficient for modeling methane spectra.[130, 131] Moreover, Dicke (collisional) narrowing[75] has been previously shown to be important to methane lineshapes.[130] As a result, we have performed lineshape studies at two different pressures below 50 torr for methane isotopes and determined that an optimal line profile is the Galatry[55] profile, which incorporates the Dicke narrowing effect. Since the Galatry profile describes the effects of collisions in a diffusional regime, we can test the model's validity by comparing the fitted collisional narrowing coefficient to the theoretical value calculated from the mass diffusion coefficient[99] of methane in air.[132] This narrowing coefficient, η, can be estimated from the mass diffusion coefficient D and absorber mass m_a at a given pressure (p) and temperature (T): $\eta = k_B T / (2\pi m_a D p)$. Figure 4.2 shows an example comparing fits using the traditional Voigt profile and the Galatry profile for low pressure methane in the spectrally isolated regime. From the Galatry profile fits, we

extracted experimental collisional narrowing values η_e=7.73(09) kHz/Pa and η_e=7.88(26) kHz/Pa, which agrees with the theoretical values η_t=10.77 kHz/Pa and η_t=10.01 kHz/Pa to within 23.8% and 32.9% for $^{12}CH_4$ and $^{13}CH_4$, respectively. This agreement suggests that the physical effects governing the lineshape of methane (Doppler broadening, Lorentzian broadening, and Dicke narrowing) are properly modeled.

In the low pressure regime, the mean free path, l_{mfp}, is given by $l_{mfp} = 3D/\bar{\upsilon}$, where D is the mass diffusion coefficient (D=0.1952 cm^2s^{-1} for methane in air at p=101.325 kPa, T=296 K) and $\bar{\upsilon}$ is the relative mean velocity of the perturber-absorber pair. This calculation yields $l_{mfp} \sim$ 6.62 μm for $^{12}CH_4$ at 1.33 kPa and 1350 μm for $^{13}CH_4$ at0.00667 kPa. These values are much larger than the near-IR probe wavelength λ_{probe}~1.65 μm. While this calculation would suggest that the contribution of Dicke narrowing to be small, the high signal-to-noise ratio of our measurements indicate that it is not negligible. Therefore, Dicke narrowing is necessary to properly model the lineshape at high precision, even in this low pressure regime. Finally, we did not observe speed dependence effects to be necessary in modeling methane spectra, as was previously shown for the lineshapes of CO_2[129, 133].

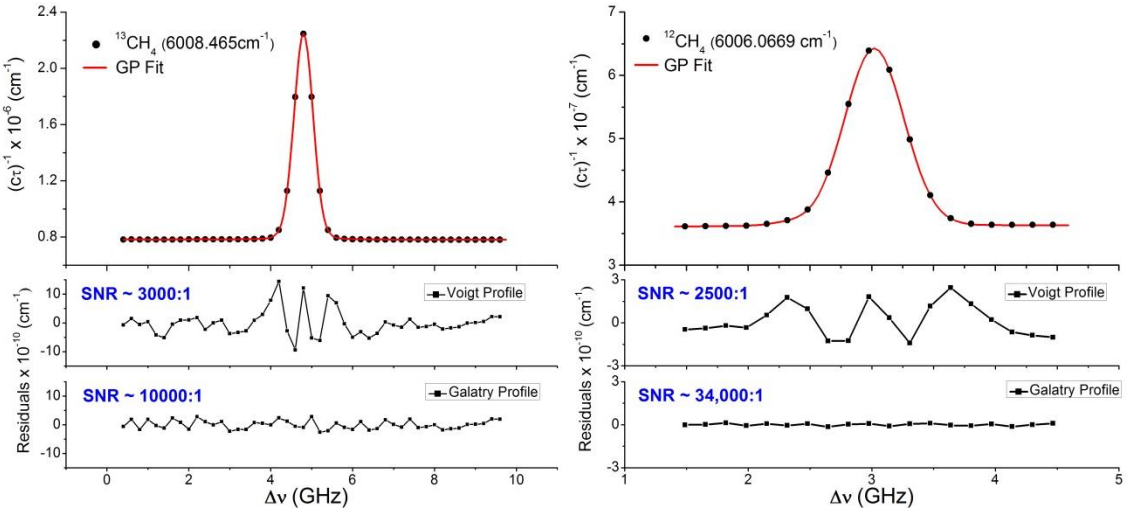

Figure 4.2: A comparison of the Voigt profile (VP) versus Galatry profile (GP) model for methane spectra near 1.65μm at a total pressure of ~50 mTorr (0.00667 kPa) for $^{13}CH_4$ and ~10 torr (1.33 kPa) for $^{12}CH_4$. In the upper panel, the measured data are shown as black points and the GP fit is the red solid line. In the bottom two panels are the residuals for the VP and GP. The signal-to-noise ratio of the fit (SNR) is defined as the peak absorption divided by the RMS of the residuals. The GP improves the fit by a factors of >3.

4.5 Discussion

Our data acquisition scheme is shown in Figure 4.3. Figure 4.3A shows a raw spectrum, a composite of two overlaid spectral regions with every other data point coming from one laser. Consequently, parsing the overlaid spectrum results in two independent spectrum, as shown in Figure 4.3B. The total wavelength coverage using our acquisition scheme is 1.54-1.67μm, which covers $^{12}CH_4$, $^{12}CH_3D$ and $^{13}CH_4$ isotopes.

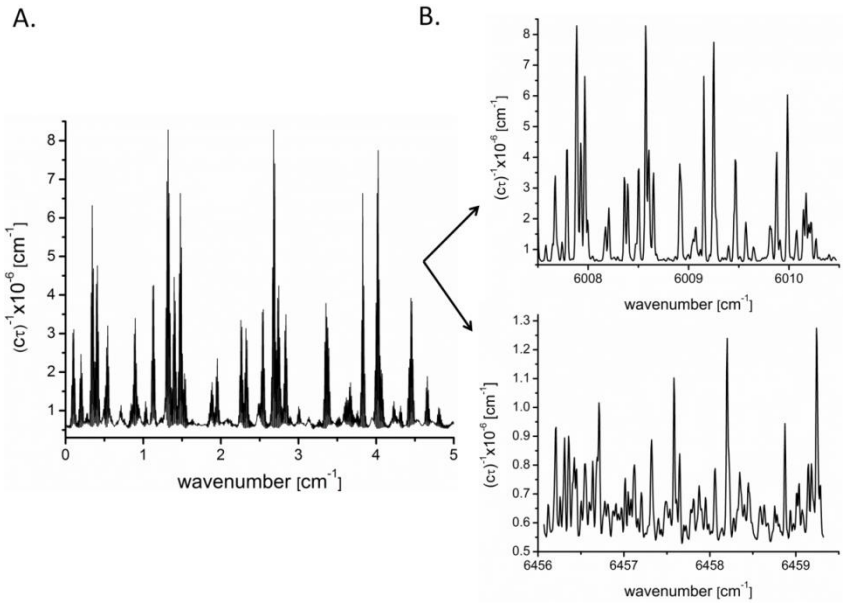

Figure 4.3: **A.** Spectrum collected from our dual-acquisition scheme. The spectrum is composed of two spectra from two independent lasers overlaid. **B.** The spectrum for the two regions (~1.66μm and ~1.54μm) after parsing the data. With this approach, we can access distant regions of the methane spectrum simultaneously for our isotope ratio measurement (limited only by the cavity mirror reflectivity curve, which was measured to have R>99.995% from 1.54-1.67μm).

This acquisition scheme allows us to acquire high signal-to-noise spectra, scan over a broad wavelength range nearly simultaneously, and automate the process to reduce user intervention. A critical factor for precise spectroscopic isotope ratio measurements is the ability to choose rotational lines with similar ground state energies and measure them simultaneously. To this end, we chose the pairs of lines to measure $^{12}CH_3D/^{12}CH_4$ (red), $^{13}CH_4/^{12}CH_4$ (blue) isotope ratios shown in Table 4.1. The samples were enriched for $^{13}CH_4$ and $^{12}CH_3D$ (composition denoted in Figure 4.4 caption) due to dynamic range limitations. The positions, intensity and ground state energies are obtained from the HITRAN 2012[21] database. These choices were made based on optimal ground state energies (to minimize temperature dependence), and minimal spectral interference in our spectral region. The last column shows the spectrometer's detection sensitivity in parts

per-billion (ppb) (101.325 kPa and 298 K) for a SNR = 1:1 for the selected methane isotopes transitions in natural abundance (0.0156% D, 1.1% ^{13}C content).

Isotopologue	Position (cm^{-1})	HITRAN Line Intensity (cm/molec.)	E" (cm^{-1})	Number Density ($molec./cm^3$)	Projected Sensitivity (ppb)*
$^{12}CH_4$	6006.06590	$6.060x10^{-24}$	293.154	$9.05x10^{14}$	12
$^{12}CH_3D$	6457.03268	$8.149x10^{-27}$	46.554	$1.89x10^{14}$	16,373
$^{12}CH_4$	6004.86265	$3.245x10^{-22}$	10.482	$4.78x10^{13}$	0.6
$^{13}CH_4$	6008.46523	$5.793x10^{-24}$	10.482	$2.04x10^{13}$	25

Table 4.1: Selected methane isotopologues for δD and δ13C measurements. The position, line intensity and ground state energies (E") are found in the HITRAN 2012[21] database. The number densities for the measured transitions were calculated from the fitted spectral areas and the HITRAN line intensities. *The last column shows the spectrometer's projected sensitivity at 101.325 kPa (1 atm) in parts-per-billion for these transitions at natural abundance (0.0156% $^{12}CH_3D$, 1.1% $^{13}CH_4$ content).

Single-line fits are shown in Figures 4.4A and 4.4B. The fitted SNR using the Galatry profile for these spectra ranged from 2000:1-5000:1. Spectral interferences limit the fitted precision to below that shown for the isolated $^{12}CH_4$, $^{13}CH_4$ spectral fits in Figure 4.2. For all cases, spectral fits were constrained with fixed Doppler widths calculated from measured temperature and pressure-broadening parameters (self and N_2) reported in HITRAN 2012.[21]

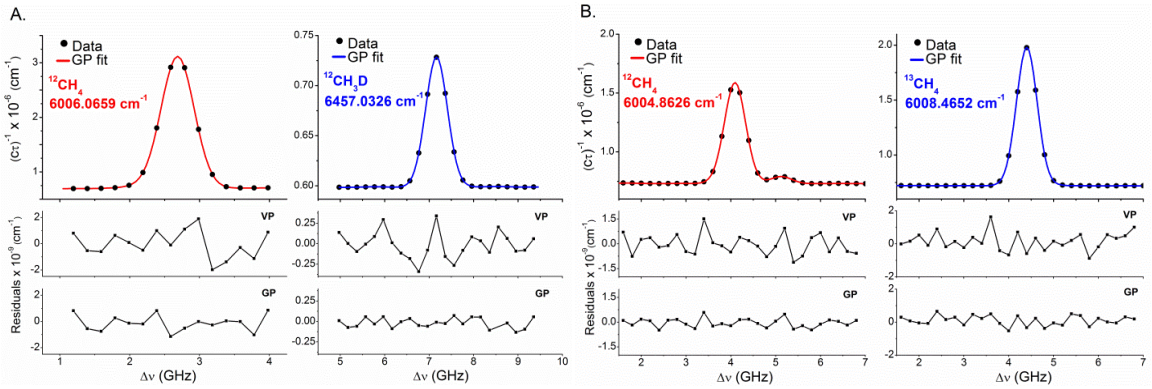

Figure 4.4: **A.** The spectra and VP/GP fits for the selected D/H isotope ratio pair are presented. The samples composed of an enriched composition of $^{12}CH_3D$:$^{12}CH_4$ (10:1) mixture with a total pressure of 100 mTorr (0.0133 kPa) **B.** The spectra and VP/GP fits for the selected $^{13}C/^{12}C$ isotope ratio pair are presented. The $^{13}CH_4$ transition is centered at 6004.8626 cm^{-1} and the $^{12}CH_4$ transition is at 6008.4652 cm^{-1}.The sample composed of N_2:$^{13}CH_4$:$^{12}CH_4$ (100:1:1) mixture with a total pressure of 100 mTorr (0.0133 kPa). The pressures ensure lines were well isolated to facilitate spectral fitting. On average, the spectra fitted SNR, defined as the peak absorption divided by the RMS of the residuals, ranged from 2000-4000:1 and 3000-5000:1 for the D/H and $^{13}C/^{12}C$ ratios, respectively.

The isotope ratio precision of our method was tested by 14 consecutive acquisitions of D/H and $^{13}C/^{12}C$ isotope ratios. Each ratio pair ($^{13}C/^{12}C$ or D/H) acquisitions requires 1500-1800 seconds for 300 ring-down averages, 200 MHz frequency steps, for a total acquisition time of >7 hours for the ensemble. In both cases, an isotope ratio is determined from a ratio of the integrated areas for each isotopologue, with values of the Doppler width, Lorentzian width, and narrowing parameter computed and fixed for all of the fits. During the acquisition period of one isotope ratio pair, the average standard deviation of the cavity temperature was measured to be 30 mK, which was used to propagate temperature uncertainties of the measured line intensities. Figure 4.5 shows the modified Allan deviation (defined below) for a representative measured ensemble expressed in terms of the δ notation in units of per mil (‰).

$$\delta X = \left(\frac{R_{\text{sample}}}{R_{\text{standard}}} - 1\right) \times 10^3 \qquad \text{(eq. 1)}$$

Here X is the minor isotopologue of interest, and R_{sample} is the sample isotope ratio of the rare isotope to the abundant, and $R_{standard}$ is the similar isotope ratio of a conventional standard (Vienna Pee Dee Belemnite for ^{13}C and Vienna Standard Mean Ocean Water for deuterium).

To quantify our measurement of precision, we define the quantity of the modified Allan deviation, σ_{Allan}, in terms of the isotope ratio acquisition number n:

$$\sigma_{Allan}(n) = \sqrt{\frac{1}{2(N-1)}\sum_{i}\left[\langle n\rangle_{i+1} - \langle n\rangle_{i}\right]^2} \qquad \text{(eq. 2)}$$

Here, N bin size and $\langle n\rangle_i$ is the average value of the measurements in bin i. The results of the Allan deviation with respect to the bin size N is shown in Figure 4.5.

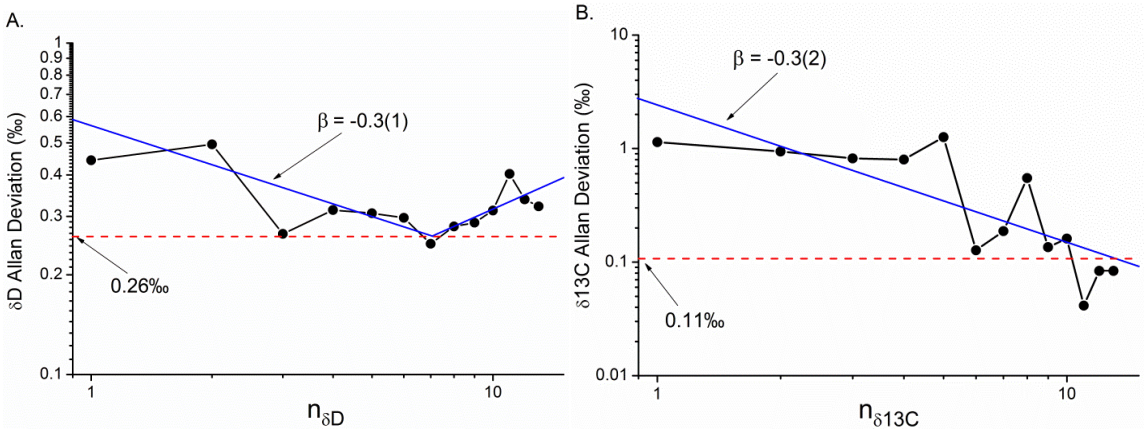

Figure 4.5: **A.** The Allan deviation for the ensemble of δ values measured for D/H isotope ratio. **B.** The Allan deviation for $^{13}C/^{12}C$ isotope ratios. For the D/H case, the Allan deviation for the acquired δ is minimized for 7 acquisitions (~3 hours); for $^{13}C/^{12}C$, 14 acquisitions (~ 7 hours).

In the case of the δD precision, the Allan deviation reaches a minimum value of ~0.26‰ with a slope of β=-0.3(1). For the $\delta^{13}C$, the minimum Allan deviation is ~0.11‰ with a slope of β=-0.3(2). While white noise limited measurements follow the power-law

relationship with a slope β=-0.5, our measurement precisions for both δD and $\delta^{13}C$ show β<-0.5 indicating that our spectrometer suffers from other noise sources that introduce long-term drifts. This is especially for true for δD, whose fitted uncertainty lies outside β=-0.5. The most common source of long-term drift in measuring spectroscopic line intensity is due to temperature. Bergamaschi et al.[120] gives the uncertainty in the δ value for isotope X, $\sigma_{\delta X}$ (in units of ‰), arising from the uncertainty in the temperature, σ_T, as,

$$\frac{\sigma_{\delta X}}{\sigma_T} = \frac{\Delta E''}{kT^2} \times 1000 \qquad \text{(eq. 3)}$$

where $\Delta E''$ is the difference in the ground state energies between the two measured transitions, k is the Boltzmann constant, and T is the gas temperature.. Accordingly, $\sigma_{\delta D} / \sigma_T$, is ~ 4 ‰/K while $\sigma_{\delta 13C} / \sigma_T = 0$ ‰/K, since $\Delta E''=0$ for the $^{13}CH_4$ and $^{12}CH_4$ transitions. Therefore, it is expected that temperature drifts will limit the averaging noise floor of δD, but not that of $\delta^{13}C$. We attribute this increase in the Allan deviation after 8-9 ratio acquisitions (3-4 hours) largely to these temperature effects. Moreover, it is important to note that a $\sigma_{\delta D}$ ~ 0.26‰ uncertainty corresponds to a σ_T ~ 65mK, which is reasonable compared to the measured cavity temperature drifts. When the uncertainty of the temperature measurement is added in quadrature with the spectroscopic uncertainty, the total measurement precisions are: δD ~ 0.286‰ and $\delta^{13}C$ ~ 0.11‰. From these studies, we observed that the dual-wavelength spectrometer displays long-term stability, especially over periods of greater than 7 hours of averaging for $\delta^{13}C$ that do not display large temperature dependencies.

4.6 Conclusion

In this report, we introduced a dual-wavelength cavity ring-down spectroscopic technique for measuring precise isotope ratios ($^{13}C/^{12}C$ and D/H) of methane in the wavelength region 1.54-1.67μm. This method takes advantage of using two lasers to simultaneously acquire spectra of two methane isotopes at arbitrary spectral regions in a single optical cavity. We are able to select low-energy rotational states of methane with similar ground state energies to minimize temperature uncertainties, as well as ensure that there is no absolute temperature difference between the measured transitions. With these advantages, we achieved high measurement precisions of 0.119‰ for $\delta^{13}C$ and 0.286‰ for δD with long-term stability.

In the future, we plan to improve the dynamic range of this spectrometer by extending the dichroic coating range of the high-finesse mirrors with mid-IR wavelengths. For example, a high-reflectivity dichroic mirror coating of ~4μm (ν_2, $^{12}CH_3D$) and 1.66μm ($2\nu_2$, $^{12}CH_4$) allows access to the $^{12}CH_3D/^{12}CH_4$ spectral lines with comparable line intensity in methane samples at natural abundance. Similarly, a dual coating at 3.3μm and 1.66μm will provide similar access to $^{13}CH_4/^{12}CH_4$ pairs.

4.7 Acknowledgements

This project was supported by NASA's Mars Fundamental Research Grant NNX12AI01G. T. Q. B. and L.S. were supported by NASA's Earth and Space Science Fellowships and the NASA Mars Fundamental Research Grant NNX12AI01G. D.W.H. was supported by the Jack and Edith Roberts Summer Undergraduate Research Fellowship.

4.8 References

1. M. Brass and T. Rockmann, Atmos. Meas. Tech. Discuss. **3**, 2433-2476 (2010).

2. A. A. Kosterev, R. F. Curl, F. K. Tittel, C. Gmachl, F. Capasso, D. L. Sivco, J. N. Baillargeon, A. L. Hutchinson and A. Y. Cho, Opt. Lett. **24**, 1762-1764 (1999).

3. H. Dahnke, D. Kleine, W. Urban, P. Hering and M. Murtz, Appl. Phys. B. **72**, 121-125 (2001).

4. K. Yamamoto and N. Yoshida, Spectrochim. Acta. A **58**, 2699-2707 (2002).

5. P. Bergamaschi, M. Schupp and G. W. Harris, Applied Optics **33** (33), 7704-7716 (1994).

6. P. Bergamaschi, M. Braunlich, T. Marik and C. Brenninkmeijer, J. Geophys. Res. **105D**, 14531-14546 (2000).

7. K. P. Petrov, S. Waltman, E. J. Dlugokencky, M. Arbore, M. M. Fejer, F. K. Tittel and L. W. Hollberg, Appl. Phys. B. **64**, 567-572 (1997).

8. M. E. Trudeau, P. Chen, G. de Andrade Garcia, L. W. Hollberg and P. P. Tans, Applied Optics **45** (17), 4136-4141 (2006).

9. Y. Chen, K. K. Lehmann, J. Kessler, B. S. Lollar, G. L. Couloume and T. C. Onstott, Anal. Chem. **85**, 11250-11257 (2013).

10. D. Richter, B. P. Wert, A. Fried, P. Weibring, J. G. Walega, J. W. C. White, B. H. Vaughn and F. K. Tittel, Opt. Lett. **34** (2), 172-174 (2009).

11. E. Kerstel and L. Gianfrani, Appl. Phys. B. **92** (3), 439-449 (2008).

12. K. Uehara, K. Yamamoto, T. Kikugawa and N. Yoshida, Sensor Actuat. B **74**, 173-178 (2001).

13. L. Gianfrani, G. Gagliardi, M. v. Burgel and E. Kerstel, Opt. Express **11**, 1566 (2003).

14. J. T. Hodges, H. P. Layer, W. W. Miller and G. E. Scace, Rev. Sci. Instrum. **75** (4), 849-863 (2004).

15. D. A. Long, A. Cygan, R. D. van Zee, M. Okumura, C. E. Miller, D. Lisak and J. T. Hodges, Chem. Phys. Lett. **536**, 1-8 (2012).

16. D. A. Long, M. Okumura, C. E. Miller and J. T. Hodges, Appl. Phys. B **105**, 471-477 (2011).

17. D. Lisak, J. T. Hodges and R. Ciuryło, Phys. Rev. A **73**, 012507 (2006).

18. G. Dufour, D. Hurtmans, A. Henry, A. Valentin and M. Lepere, J. Mol. Spectrosc. **221**, 80-92 (2003).

19. R. G. Hubbert and G. J. Troup, Phys. Lett. A **61** (1), 33-34 (1977).

20. R. H. Dicke, Phys. Rev. **89** (2), 472-473 (1953).

21. L. Galatry, Phys. Rev. **122** (4), 1218 (1961).

22. W. J. Massman, Atmospheric Environment **32** (6), 1111-1127 (1998).

23. D. Lisak, A. Bielski, R. Ciuryło, J. Domysławska, R. S. Trawiński and J. Szudy, J. Phys. B: At. Mol. Opt. Phys. **36**, 3985 (2003).

24. T. Q. Bui, D. A. Long, A. Cygan, V. T. Sironneau, D. W. Hogan, P. M. Rupasinghe, R. Ciurylo, D. Lisak and M. Okumura, J. Chem. Phys. **141** (17), 10 (2014).

25. L. S. Rothman, I. E. Gordon, Y. Babikov, A. Barbe, D. C. Benner, P. F. Bernath, M. Birk, L. Bizzocchi, V. Boudon, L. R. Brown, A. Campargue, K. Chance, E. A. Cohen, L. H. Coudert, V. M. Devi, B. J. Drouin, A. Fayt, J. M. Flaud, R. R. Gamache, J. J. Harrison, J. M. Hartmann, C. Hill, J. T. Hodges, D. Jacquemart, A. Jolly, J. Lamouroux, R. J. Le Roy, G. Li, D. A. Long, O. M. Lyulin, C. J. Mackie, S. T. Massie, S. Mikhailenko, H. S. P. Muller, O. V. Naumenko, A. V. Nikitin, J. Orphal, V. Perevalov, A. Perrin, E. R. Polovtseva, C. Richard, M. A. H. Smith, E. Starikova, K. Sung, S. Tashkun, J. Tennyson, G. C. Toon, V. G. Tyuterev and G. Wagner, J. Quant. Spectrosc. Radiat. Transf. **130**, 4-50 (2013).

Chapter 5: Temperature Dependent Kinetic Isotope Effects of Methane Oxidation by $O(^1D)$ and OH Radicals

5.1 Abstract

^{13}C and deuterium kinetic isotope effects (KIE) have been measured for methane oxidation by both $O(^1D)$ and OH radicals using a pulse photolysis experiment. N_2O photolysis was used as the $O(^1D)$ source and $O(^1D)+H_2$ as the OH source. The methane depletion measurements for KIE determination were performed by a precise spectroscopic method, dual-wavelength FS-CRDS, at temperatures 177-293 K. We observed quantitative differences with literature values for $O(^1D)+CH_4$ for ^{13}C and D KIEs. For $OH+CH_4$, our results differ in the temperature dependence behavior with published literature reports. We discuss both the experimental and theoretical comparisons for the both ^{13}C and deuterium KIEs of methane oxidation by $O(^1D)$ and OH.

5.2 Introduction

Recent *in situ* detection of methane on Mars by NASA's Curiosity rover has prompted important questions about the sources and sink of Martian methane.[1] Sources of methane can either be biological (methanogens)[2,3] or geological[3]. With source information, the understandings of sink processes are needed to map out the global carbon budget. In the atmosphere, a majority of methane loss is due to reactions with radicals ($O(^1D)$, OH, Cl, etc.).

The main oxidation pathways of gas phase methane by $O(^1D)$ and OH radicals are important sinks of methane for Earth and Martian atmospheres.

$$O(^1D)+CH_4 \rightarrow \text{products} \quad \text{(eq. 1)}$$

$$OH+CH_4 \rightarrow H_2O+CH_3 \quad \text{(eq. 2)}$$

Mars's atmosphere is thin (< 7 mbar) and cold (140 – 220 K).[4] Reactions 1 and 2 are relevant on Earth's troposphere and stratosphere where the temperature ranges from 200-273 K.[5] On Earth's troposphere, the OH reactivity constitute >94% of methane loss.[6] In the stratosphere, reactions with $O(^1D)$ and Cl contribute to both methane depletion and production of OH radicals. Isotopic signatures provide a means to constrain sources and sinks of atmospheric methane to unravel these interlinked processes. Isotopic ratios of $^{13}CH_4$ and CH_3D to CH_4 are different for different sources, e.g., biogenic, anthropogenic, natural gas emission.[7-9] The lifetime of each isotopic species is dependents on its reactivity with OH and $O(^1D)$. This necessitates knowledge of the rate constants of methane isotopologues with OH and $O(^1D)$ very accurately, i.e., their kinetic isotope effects.

In addition to being atmospherically relevant for Earth and Martian atmospheres, temperature dependent kinetic isotope effects of $OH+CH_4$ provide an important test for subtle differences in the theoretically constructed reaction potential energy surface upon isotopic substitution. These tests are significant at cold temperatures in which quantum tunneling dominates because reactants have lower translational energies to overcome the ≈7 kcal/mol reaction barrier.

There are experimental data in the literature for $O(^1D)$ and $OH+CH_4$ KIEs at T>296 K, but very limited at colder temperatures. Rust and Stevens[10] first reported a room temperature $^{13C}KIE_{OH}$ of 1.003. Later, Davidson et al.[11] used an arc lamp O_3/H_2O continuous photolysis system and measured a $^{13C}KIE_{OH}$ value of 1.010(7) and $^{13C}KIE_{O(1D)}$

of 1.001. Isotopic analysis was achieved by combustion of CH_4 to CO_2 and mass spectrometry. Methane depletions were monitored with gas chromatography and FTIR spectroscopy. Cantrell et al.[12] used similar methods to Davidson et al.[11] and determined a temperature independent $^{13C}KIE_{OH}$ of 1.0054(9) from 273-353 K. DeMore[13] used photolysis of O_3/H_2O and FTIR to measure the temperature dependent (298-360 K) for $^{D}KIE_{OH}$ and reported a value of 1.16(7) at 298 K. Gierczak et al.[14] used OH decay kinetics from pulsed photolysis to report the only cold $^{D}KIE_{OH}$ measurement over the temperature range of 250-420 K. They obtained $^{D}KIE_{OH}$ value at 298 K of 1.25(18). Most recently, Saueressig et al.[15] performed measurements of ^{13}C and D KIEs for both $O(^1D)$ and OH using arc lamp continuous photolysis and IR absorption/mass spectrometry detection. Room temperature (296 K) ^{13}C and D KIEs for $OH+CH_4$ were measured to be $^{13C}KIE_{OH}$ =1.0039(4) and $^{D}KIE_{OH}$=1.294(18). ^{13}C and D KIEs for $O(^1D)+CH_4$ were also investigated and found to be temperature independent from 223-295 K: $^{13C}KIE_{O(1D)}$ =1.013 and $^{D}KIE_{O(1D)}$ =1.06.[15]

Despite the number of experimental investigations, there are no reports of ^{13C}KIE for $OH+CH_4$ at T < 273 K and ^{D}KIE for $OH+CH_4$ for T < 250 K, which are temperatures relevant to Martian atmosphere and Earth's upper troposphere. The average Martian atmospheric temperatures range from 140-200 K and pressures < 7 mbar. In this experiment we performed laboratory measurements of temperature dependent KIEs for both $O(^1D)$ and OH reactions with methane isotopologues, $^{12}CH_4$, $^{13}CH_4$, and $^{12}CH3D$, from 177-293 K. ^{13}C and D KIEs at these cold temperatures provide missing sink fractionations by OH that are useful for constraining the atmospheric methane budget for both Earth and Mars.

5.3 Experimental Methods

Kinetic isotope effects are determined by measuring methane depletions by O(^{1}D) and OH.[11-13,15] This method differs from Gierczak et al.[14] who measured the decay of OH by laser induced fluorescence. First, we write down the rate equations for the reactions of methane isotopologues with OH/O(^{1}D) (Eqs. 3a & 3b). In this case, the example is for the deuterium KIE with OH:

$$^{12}CH_4 + OH \xrightarrow{k_H} \text{products} \quad \textbf{(}\text{Eq. 3a)}$$

$$^{12}CH_3D + OH \xrightarrow{k_D} \text{products} \quad \textbf{(}\text{Eq. 3b)}$$

By making the assumption that CH_4 loss is only due to reactivity with OH, integrating and taking the ratio gives the final form to obtain the KIE ($\equiv k_H/k_D$, eq. 4)

$$\frac{\ln([^{12}CH_4]_t/[^{12}CH_4]_0)}{\ln([^{12}CH_3D]_t/[^{12}CH_3D]_0)} = \frac{k_H}{k_D} = \text{KIE} \quad \textbf{(}\text{Eq. 4)}$$

Therefore, KIE is determined from measuring the absolute number density of the four quantities in eq. 2, which includes the two isotopologues before ($[^{12}CH_4]_0$ and $[^{12}CH_3D]_0$) and after ($[^{12}CH_4]_t$ and $[^{12}CH_3D]_t$) reactions. Plotting $\ln([^{12}CH_3D]_t/[^{12}CH_3D]_0)$ versus $\ln([^{12}CH_4]_t/[^{12}CH_4]_0)$ yields a slope that is the KIE.

The cavity ring-down (CRDS) spectroscopic method used for this experiment has been reported previously[16]. Briefly, two lasers covering range of 1540-1665 nm are used to measure rovibrational transitions of methane isotopologues ($^{13}C/^{12}C$, D/H) with low and similar ground state energies to minimize temperature uncertainties. The KIE experiment required the use of two quartz cells (reference & photochemistry cell) that are subsequently expanded into a ring-down cavity for spectroscopic measurement. The

small difference in the volumes of the two cells was determined with spectroscopy. Multiple premix gas cylinders containing a mixture of methane, N_2O and He/H_2 for isolating $O(^1D)+CH_4$ and $OH+CH_4$ experiments were prepared to fill two cells simultaneously to ensure the same mixing ratios and total pressure throughout a KIE measurement. Quantitative analyses to retrieve number densities are achieved by spectral fitting with the Galatry[17] line profile and calculating integrated areas, from which we have achieved a fitted SNR of 34,000:1 using our spectrometer[16]. This two cell approach allows us to measure absolute concentrations of methane isotopologues before and after photochemistry, and obtain the necessary isotope ratio for determining the kinetic isotope effects.

	$O(^1D) + CH_4$				**$OH+CH_4$**			
	$^{12}CH_4$	E"	$^{13}CH_4$	E"	$^{12}CH_4$	E"	$^{13}CH_4$	E"
^{13}C KIE	6006.066	293.1542	6008.465	10.4821	6009.8086	219.9452	6008.465	10.4821
	$^{12}CH_4$	E"	$^{12}CH_3D$	E"	$^{12}CH_4$	E"	$^{12}CH_3D$	E"
D KIE	6009.809	219.9452	6458.327	47.9239	6009.8086	219.9452	6458.327	47.9239

Table 5.1: Selected near-IR ($2\nu_3$) rovibrational transitions of methane isotopologues and ground state energies (E") in wavenumber (cm^{-1}) for ^{D}KIE and ^{13C}KIE of both $O(^1D)+CH_4$ and $OH+CH_4$ reactions. The ground state energies for D/H and $^{13}C/^{12}C$ are chosen to be similar for minimize temperature dependent intensity uncertainties.

The gas mixtures are enriched for $^{12}CH_3D$ and $^{13}CH_4$ for ^{D}KIE and ^{13C}KIE experiments, respectively, due to the weak line intensities in the near IR overtone region. Furthermore, specific transitions were selected to minimize differences in ground state energies (minimize temperature dependence) and to ensure maximum SNR. The transitions for the $O(^1D)$ and OH experiments are listed in Table 5.1. Since the isotopic transitions can be distant in wavelength, it was advantages to use our dual-wavelength technique for simultaneous acquisitions. Finally, number densities were obtained from

integrated areas from spectral fitting with the Galatry[17] line profile. Using this approach, precisions of 0.026% and 0.011% have been achieved for enriched methane D/H and $^{13}C/^{12}C$ isotope ratios, respectively.[17]

The temperature dependent photochemistry experiments were performed with a cylindrical quartz cell (diameter=3.8 cm, length=25 cm) positioned inside a vacuum chamber (Figure 5.1). A copper jacket encloses the quartz cell and liquid nitrogen is used to cool the cell down to <100 K. The equilibrated cell temperature is measured by a calibrated platinum resistor thermometer (Lakeshore PT-103). The temperature measurement uncertainty in this experiment is approximately 2 K from calibration with calibrated temperature sensors.193 nm light (≈ 100 mJ/pulse, 1 Hz repetition rate) from an ArF_2 excimer was sent through MgF_2 windows (>90% transmission) of the chamber to the quartz cell. A 193nm mirror was placed at the opposite end of the chamber for a 2nd pass to increase the radical concentration per pulse. Each measurement was conducted with different numbers of excimer pulses to map out the KIE curve.

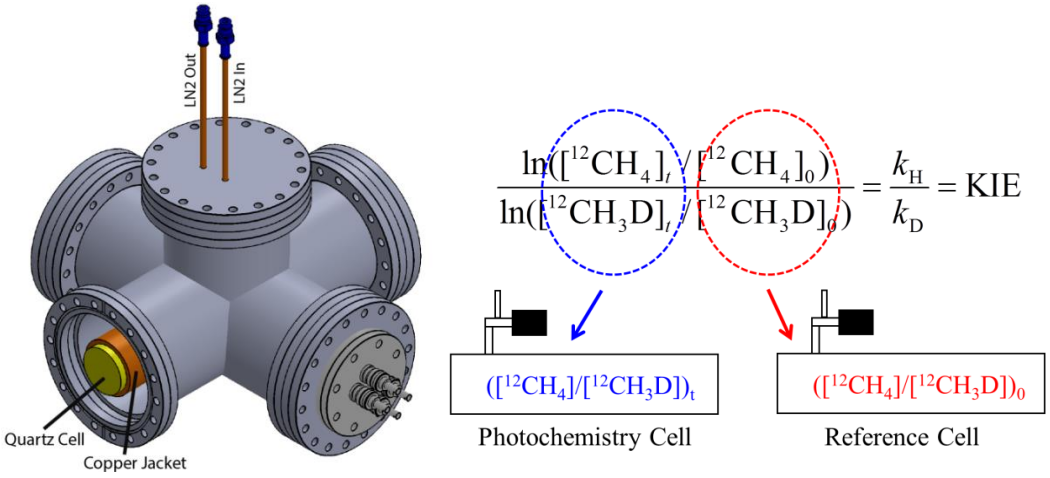

Figure 5.1: Experimental apparatus for measuring temperature dependent KIE. The reactions gas mixtures are contained in a quartz cell placed inside of a vacuum chamber. A LN_2 cooled copper jacket encloses the quartz cell to reach cryogenic temperatures <100 K, which is measured by a calibrated platinum resistor element. Excimer laser light propagates down the axis of the quartz tube to initiate the chemistry.

In this experiment, the KIE's for both $O(^1D)$ and OH + CH_4 were measured at four different temperatures: 293 K, 273 K, 227 K, and 177 K Since OH + CH_4 become increasingly sluggish as temperature decreases (a factor of ≈50 slower at 177 K compared to 293 K), limited signal to noise ratio (SNR) sets a low end of the reaction temperature at 177 K. After the desired number of excimer pulses, the content from the quartz cell is directly expanded into an evacuated ring-down cavity about five times the volume of the quartz cell for measuring methane isotopes. We confirmed that with equilibration times of 2-3 minutes, the transfer procedure results in minimal fractionation for D/H (1.93‰) and $^{13}C/^{12}C$ (1.64‰). Also, the total number of molecules transferred to the cavity also is reproducible to <1‰ level, which is needed to determine the absolute depletion for KIE measurements. Finally, the commercial program *Kintecus*[18] was used for all kinetics modeling.

5.4 Results and Discussion

For initiating the methane oxidation reactions with $O(^1D)$ and OH, N_2O was chosen as the photolytic precursor (eq. 5) for its advantage as a clean $O(^1D)$ source despite its low absorption cross-section (≈ $9x10^{-20}$ cm^2) at 193 nm. To generate the OH radical, excess H_2 was added with N_2O (eq. 6). Since $O(^1D)$ also reacts with CH_4, this approach to produce OH requires optimal conditions in order to isolate $O(^1D)$ from OH reactive channels.

$$N_2O \xrightarrow{193nm} O(^1D)+N_2 \quad \text{(eq. 5)}$$

$$O(^1D)+H_2 \rightarrow OH+H \quad \text{(eq. 6)}$$

Moreover, this work is to be distinguished from previous reported measurements in that we aim to keep the methane depletion low (<5% for $O(^1D)+CH_4$, <1% for $OH+CH_4$) by limiting the number of excimer pulses. While more challenging to measure, low depletions ensure that primary reactions dominate by minimizing secondary reactions, which facilitates kinetics modeling. Previous authors measured KIEs after significant methane depletions by continuous photolysis. For example, Saueressig et al.[15] measured KIEs after 11- 47% methane depletion, Davidson et al.[11] after 31-92%, and Cantrell et al.[12] after 30-95% depletions. We chose the pulsed photolysis rather than the continuous photolysis in order to ensure that major radical reactions are completed before initiating new photochemistry. First, we performed experiments to test our understanding of the chemistry and optimize conditions for KIE measurements.

5.4.1 Constraining kinetics model

	N_2O (molec cm^{-3})	CH_4 (molec cm^{-3})	He (molec cm^{-3})	H_2 (molec cm^{-3})	Total Pressure (Torr)
1	$1.71x10^{17}$	$1.93x10^{16}$	$1.43x10^{18}$	0	50
2	$3.27x10^{16}$	$3.27x10^{16}$	$2.59x10^{17}$	0	10
3	$4.73x10^{15}$	$4.63x10^{16}$	$2.08x10^{17}$	0	8
4	$4.60x10^{15}$	$4.64x10^{16}$	0	$2.08x10^{17}$	8

Table 5.2: Experimental conditions for constraining kinetics model: 1) 10:1:100 N_2O:CH_4:He, 2) 1:1:10 N_2O:CH_4:He, 3)1:10:50 N_2O:CH_4:He, 4) 1:10:50 N_2O:CH_4:H_2. These conditions were prepared in four premix cylinders to measure methane and N_2O depletions as a function of excimer pulses.

In order to constrain the chemical kinetics model, we performed a series of photochemical experiments (Table 5.2) to confirm our understanding of the chemistry. The first experiment was to estimate the 193nm fluence that interacts with the gas mixture in the quartz cell. 10 torr of pure N_2O was photolyzed, and the depletion was monitored as a function of laser pulses. Here, the N_2O depletions arise from both photolysis and reactivity (e.g. $O(^1D)+N_2O$). A MATLAB code was used to implement

repetitive photolysis kinetics modeling with the Kintecus[18] software. The data and the kinetics model are shown in Figure 5.2A.

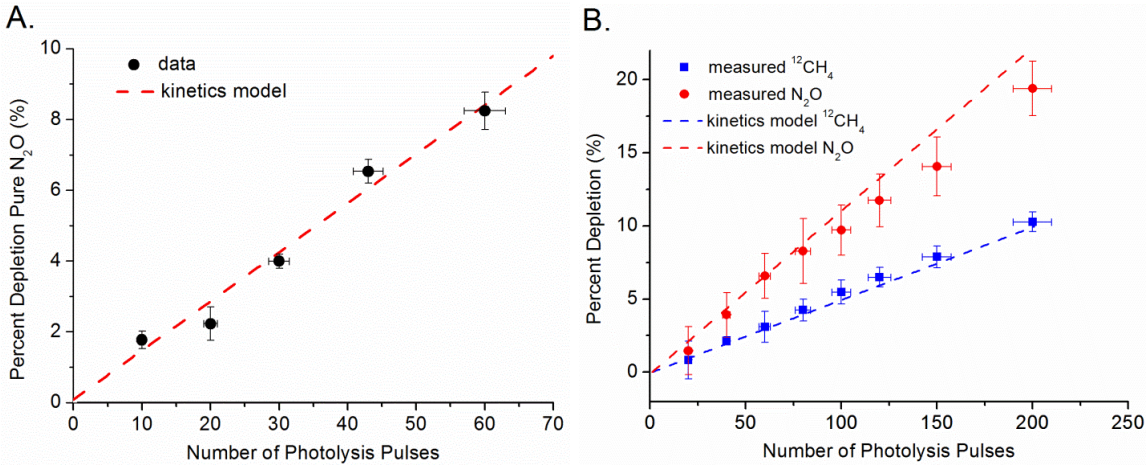

Figure 5.2: A) Measured N_2O depletion as a function of excimer pulses. A kinetics model was used to simulate N2O depletion from photolysis and chemical reactions. The pulse energy was the only fitted variable (68 mJ/pulse). B) Measured N2O and CH4 depletion using condition #1 from Table 2. The same kinetics model from A) was used, and a fitted pulse energy of 69 mJ/pulse gave good agreement at low pulse number <100 pulses. The deviation at higher pulse number arises from secondary reactions that are difficult to model.

The error bars on the x-axis are from the per pulse fluctuations in the excimer energy. The fitted pulse energy of ~68 mJ/pulse provided the best agreement with the data. Next, CH_4 was added into a mixture with N_2O and He (experiment 1 in Table 5.2). In this case, both N_2O and CH_4 depletions were measured (Figure 5.2B). All the reaction rates in the kinetics model are taken from literature and fixed. The only fitted variable was the pulse energy, which sets the initial concentration of the reactive species $O(^1D)$. A kinetics model with 69 mJ/pulse energy reproduced the data and agreed with the pulse energy from the pure N_2O experiments. We also observed that the model and the data deviated at higher pulse number, which is a signature of secondary chemistry that is not properly modeled. With these two experiments, we confirmed the validity of our kinetics model and extracted the excimer pulse energy interacting with the gas in the quartz cell.

Experiments in the following sections utilize the same kinetics model, with all reactions and kinetic rates fixed.

We attempted to quantify contributions from secondary chemistry for $O(^1D)+CH_4$ and $OH+CH_4$. In general, we chose conditions (Table 5.2) so that we can tune the contributions from $O(^1D)$ and OH to CH_4 depletions. These experiments not only aid in choosing optimal conditions to isolate $O(^1D)$ from OH, but also help constrain our chemical kinetics model. The mixing ratios 1-4 are listed in increasing OH contributions to CH_4 depletion. Figure 5.3 shows the measured CH_4 depletion for the four conditions with the corresponding kinetics modeling results. Here, the excimer pulse energies were adjusted within 5% of the 69 mJ/pulse, which is well within the uncertainty from the pulse energy fluctuations and joule meter measurement, to achieve the best agreement. The good agreement for all four conditions confirms the validity of our kinetics model. Since condition 1 is dominated by $O(^1D)$ and 4 is dominated by OH, they were chosen for KIE measurements.

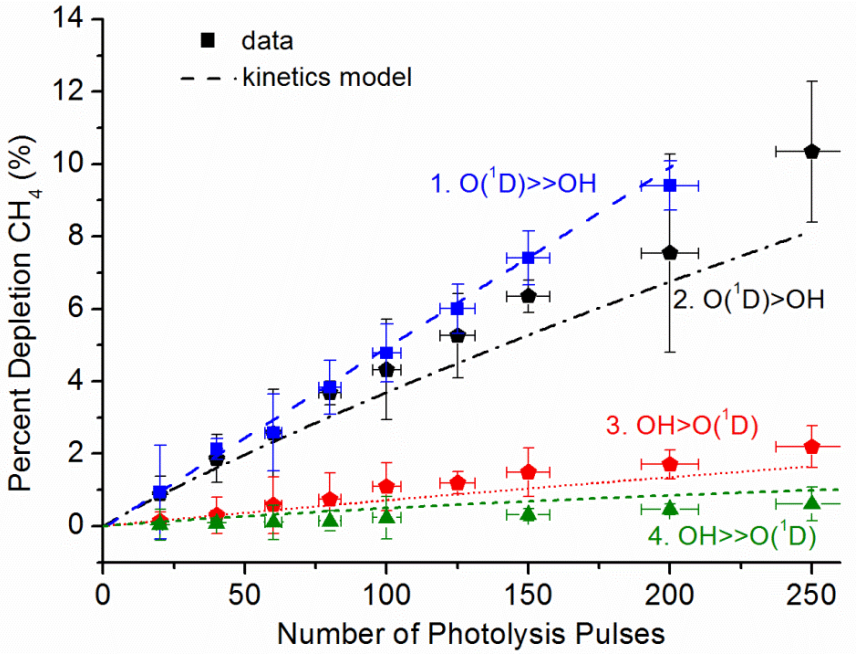

Figure 5.3: Measured methane percent depletion as a function of excimer pulses for conditions #1-4 from Table 5.2. The conditions were tuned by increasing OH contribution from 1 to 4 such that $O(^1D)+CH_4$ dominates and 1 and $OH+CH_4$ dominates in 4. The dashed lines show the kinetics model simulation of the observed behavior. Only the excimer pulse energy variable is floated to within 5% of the 69 mJ/pulse determined from the experiment in Figure 5.2 to obtain good agreement at low pulse energy. The disagreements at higher pulses are expected due to secondary reactions.

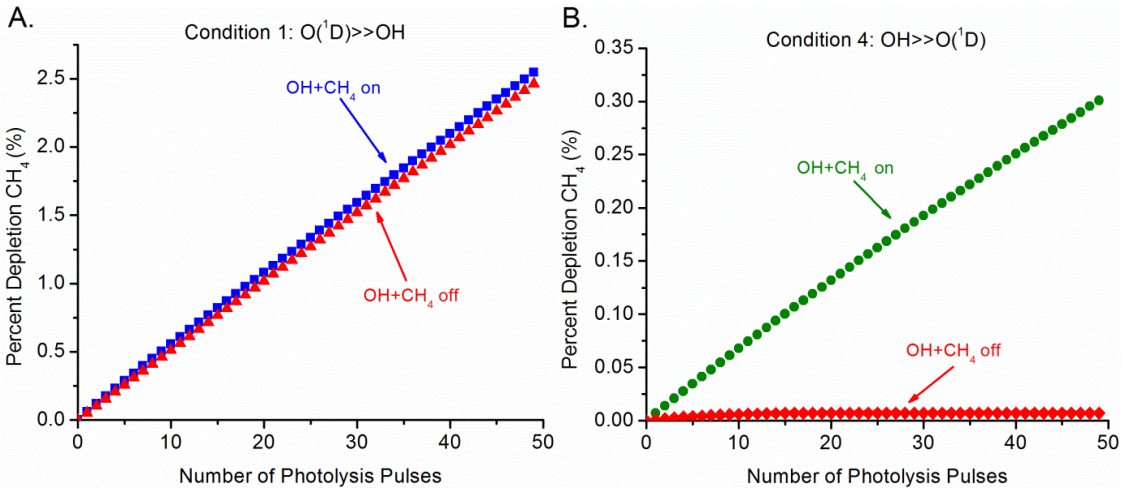

Figure 5.4: Kinetics model to estimate the contributions from OH and $O(^1D)$ for conditions 1 and 4. A) Kinetics model of methane percent depletion for condition 1 ($O(^1D)+CH_4$ dominant) when the $OH+CH_4$ channel is turned off in the model. The differences in the integrated areas from the two curves (4.5%) provides an estimate for $OH+CH_4$ contribution interfering with $O(^1D)+CH_4$. B) Kinetics model for condition 4 ($OH+CH_4$ dominant) when the $OH+CH_4$ channel is turned off in the model. From the differences in the integrated areas from the two curves, 1.5% of the methane depletion is from $O(^1D)+CH_4$.

Finally, by kinetics modeling, we can estimate contributions from secondary OH and $O(^1D)$ reactions for both $O(^1D)$ and $OH+CH_4$ channels. This was achieved by artificially "turning off" chemical reactions within the kinetics model. Figure 5.4A shows the percent depletion of CH_4 for condition 1 ($O(^1D)+CH_4$) as $OH+CH_4$ reaction is turned off. The small drop in the percent depletion per pulse is the contribution from $OH+CH_4$. The differences in depletions were estimated from integrating under the curve. Similarly, Figure 5.4B shows the percent depletion of CH_4 for condition 4 ($OH+CH_4$) with and without $OH+CH_4$. From modeling we estimate a ≈4.5% OH contribution to the $O(^1D)+CH_4$ and ≈1.5% $O(^1D)$ contribution to the $OH+CH_4$ channel. These values are used to correct the observed KIEs to the actual KIEs through eq. 7:

$$KIE_{observed} = \alpha KIE_{O1D} + (1-\alpha) KIE_{OH} \quad \text{(eq. 7)}$$

5.4.2 KIE Measurements

KIE measurement conditions for both ^{13}C and D for $O(^1D)$ and OH reactions are outlined in Table 5.3. Conditions similar to 1 and 4 from Table 5.2 are used for isolating $O(^1D)$ and OH KIEs, respectively. To achieve the highest SNR in our spectroscopic measurement, the mixing ratios are enriched in ^{13}C and D. These four conditions were prepared in premix cylinders to ensure a constant mixing ratio for each photolysis experiments.

System	$^{12}CH_4$	$^{13}CH_4$	$^{12}CH_3D$	N_2O	He	H_2	Total Pressure (Torr)
^{13}C KIE O(^{1}D)	$1.29x10^{16}$	$3.13x10^{14}$	0	$1.25x10^{17}$	$1.16x10^{18}$	0	40.0
D KIE O(^{1}D)	$1.08x10^{16}$	0	$2.64x10^{15}$	$1.25x10^{17}$	$1.32x10^{18}$	0	45.0
^{13}C KIE OH	$1.05x10^{16}$	$5.79x10^{14}$	0	$1.61x10^{15}$	0	$5.21x10^{16}$	2.0
D KIE OH	$1.33x10^{16}$	0	$2.14x10^{15}$	$1.51x10^{15}$	0	$6.19x10^{16}$	2.5

Table 5.3: The number densities of CH_4 isotopologues, N_2O, He, and H_2 (in molecules cm^{-3}) and total pressures used for ^{13C}KIE and ^{D}KIE measurements. The O(^{1}D)+CH_4 and OH+CH_4 systems use similar mixing ratios to condition #1 and #4, respectively, from Table 2.

5.4.2.1 Kinetic Isotope Effects of O(^{1}D) + CH_4

The O(^{1}D)+CH_4 experiments were performed at ~ 40 Torr of total pressure. Photolysis of N_2O at 193 nm (148 kcal/mol) produces O(^{1}D) with about 27 kcal/mol of translational energy.[19] Previously, Chen et al.[20] experimentally determined that about 10 collisions with helium gas is sufficient for complete thermalization of translationally hot O(^{1}D) while avoiding O(^{1}D)→O(^{3}P) electronic quenching. For O(^{1}D) + CH_4, The N_2O:CH_4 ratio is kept high to suppress OH side chemistry: O(^{1}D) reacts with CH_4 to generate OH products, a interfering contaminant. A high N_2O concentration favors the reaction of O(^{1}D) + N_2O, which produces two NO molecules that act as scavengers for OH through HONO formation ($k \approx 7.8x10^{-13}$ cm^3 $molec^{-1}$ s^{-1} at 40 Torr).

O(^{1}D)+CH_4 is exothermic and barrierless (insertion) reaction with a fast rate constant of $k_{O(1D)+CH4}=1.75x10^{-10}$ cm^3 $molec^{-1}$ s^{-1}. O(^{1}D)+CH_4 forms the excited methanol complex, CH_3OH*, which promptly dissociates to produce CH_3+OH radicals with 75% yield. The rest is distributed to the CH_2OH+H and H_2CO+H_2 product channels. Since $k_{O(1D)} > k_{OH}$ by 10^4 at 298 K, the small OH contribution is estimated by kinetics modeling

from Figure 5.4A - 4.5% from $OH+CH_4$. Each excimer pulse depletes ≈0.05% of methane. With the spectrometer sensitive to about 0.1% depletion, 10-100 pulses were needed to achieve measurable depletions for mapping the full KIE plot. This translates to a maximum of 5% depletion in this experiment. Keeping the pulse number low reduces contributions from secondary chemistry, which is attributed to the non-linearity of the data at high excimer pulses in Figure 5.3. After photolysis, content from the quartz cell is expanded into the CRDS cavity for measurement of methane isotopologue number densities. Figure 5.5A and 5.6C display the results of the ^{13}C KIE and D KIE experiments, respectively, from the computed quantity of eq. 2 using the obtained number densities from spectroscopy. Deviations from the dash-line with unity slope are the KIEs.

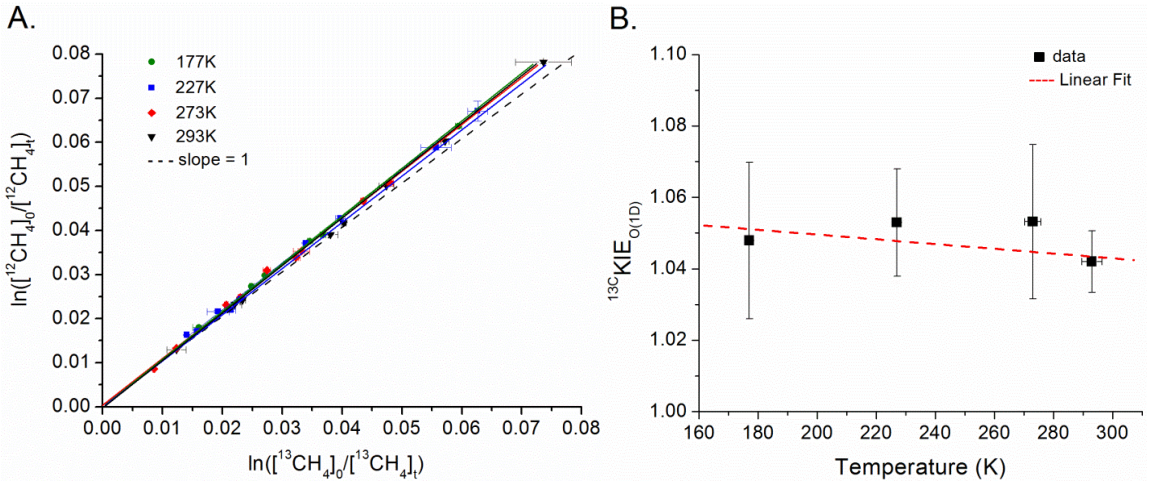

Figure 5.5: ^{13C} KIE data for $O(^1D)+CH_4$ at 177, 227, 273, 293 K. The quantities in both the *x* and *y* axes are determined from spectroscopic measurement of the two isotopologues before and after excimer pulses and computing eq. 4 B) Plot of the ^{13}C KIE as a function of temperature. No temperature dependences were observed within 2σ uncertainty.

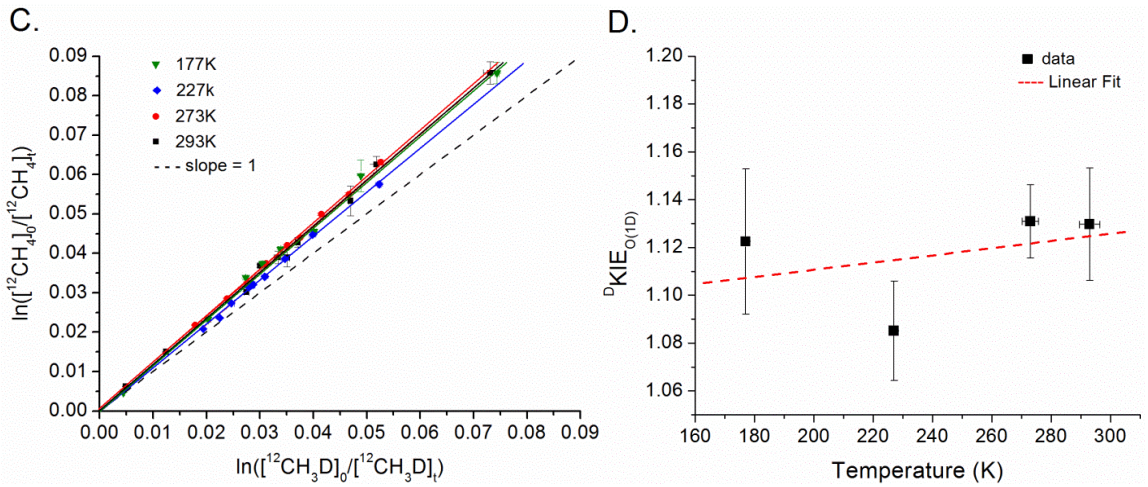

Figure 5.6: A: ^{D}KIE data for O(^{1}D)+CH_4 at 177, 227, 273, 293 K. B) Plot of the ^{D}KIE as a function of temperature. No temperature dependences were observed within 2σ uncertainty.

Plots of the measured KIEs as a function of temperature for O(^{1}D)+CH_4 are displayed in Figures 5.5B and 5.6D. No temperature dependences were observed within error, which is consistent with measurements by Saueressig et al.[15] The determined KIE with 2σ uncertainty is $^{13C}KIE_{O(1D)}$=1.042(18) and $^{D}KIE_{O(1D)}$=1.129(51) at 298 K. The large uncertainty are from measuring very small depletions (<5%) of methane isotopologues. On the low end 2σ limit, our measured values for $^{13C}KIE_{O(1D)}$ and $^{D}KIE_{O(1D)}$ are 200% and 25% larger than that reported by Saueressig et al.[15] of 1.013 and 1.06, respectively. However, these values from Saueressig et al.[15] were obtained after correction for OH+CH_4 contributions using kinetics simulations. The original measured values were 1.0115(6) and 1.101(11) for $^{13C}KIE_{O(1D)}$ and $^{D}KIE_{O(1D)}$, respectively. They also reported 20-30% error for corrections by kinetics simulations, which was due in part to OH (from O(^{1}D)+CH_4) reactivity, a problem only encountered when the extent of the chemistry is pushed to reach 11-47% methane depletion. Saueressig et al.[15] did not provide any quantitative analysis how errors from kinetics simulation propagates through

the KIE determination process. Davidson et al.[11] reported the only other $O(^1D)+CH_4$ KIE value for $^{13C}KIE_{O(1D)}$ of 1.001.

5.4.2.2 Kinetic Isotope Effects of OH + CH_4

$OH+CH_4$ is an exothermic abstraction reaction with a small entrance barrier (~7 kcal/mol). $OH+CH_4$ is slow with a bimolecular rate constant at 298 K of $k_{OH+CH4}=6.3x10^{-15}$ cm^3 $molec^{-1}$ s^{-1}. This reaction was introduced by adding excess H_2 to the mixture of CH_4 and N_2O to reach a total pressure of 2 Torr. Here, the reaction $O(^1D)+H_2$ (eq. 2) serves as the main OH radical source ($[OH]\approx3x10^{12}$ molec cm^{-3}). The condition used from Table 5.2 for isolating $OH+CH_4$ results in methane per pulse depletion of only 0.0025%. The full KIE plot necessitated 10-200 excimer pulses, which depletes a maximum of 0.5% of the initial methane. In the next few paragraphs, we analyze the relevant chemistry and dynamics that may impact KIE measurements.

From $O(_1D)+H_2$, H atoms are generated at a large quantity ($[H]\approx1x10^{12}$ molec cm^{-3}) at approximately 1 μs of reaction time. The diffusion coefficient, *D,* for H atoms in H_2 gas - H_2 comprises 80% of the gas mixture - is $D=2.1x10^{-4}$ atm m^2 s^{-1}.[21] For our reaction pressure of 2 torr, the diffusion time of H atoms to diffuse to the wall of the quartz cell x~2 cm from the center is $t=x^2/2D$ ≈4 ms. Since the H atom abstraction of CH_4 at low temperatures and pressures is quite slow with $k_{H+CH4}<<10^{-20}$ cm^3 $molec^{-1}$ s^{-1}, most of H atoms are either quenched by the walls or react with other radicals, which are discussed in the next section. Finally, H atoms can also react with N_2O to produce OH and N_2, but the reported reaction rate is slow, with $k_{H+N2O}\approx4x10^{-18}$ cm^3 $molec^{-1}$ s^{-1}.[22]

The major products from $OH+CH_4$ are H_2O+CH_3. The CH_3 radical ($<10^{11}$ molec cm^{-3}) either can recombine with itself to form C_2H_6 or with H atoms to regenerate CH_4. The former reaction, $k_{CH3+CH3}\approx 4.8x10^{-11}$ cm^3 $molec^{-1}$ s^{-1} at low pressures,[23] is innocuous, but the latter may impact the measured methane isotope ratio by fractionating isotopes during regeneration. The rate constant for CH_4 regeneration is calculated from k_0 and k_∞ values reported by Brouard et al.[24] using the JPL kinetics evaluation[25] equation for termolecular rates constants. At 2 torr, $k_{H+CH3}\approx 1.9x10^{-12}$ cm^3 $molec^{-1}$ s^{-1}. With $[CH_3]<10^{11}$ molec cm^{-3}, the decay rate of H atoms from $H+CH_3$ is 0.19 s^{-1}, which is significantly slower than quenching by the walls, especially at colder temperatures.

The dynamics of the reaction $O(^1D)+H_2$ as an OH source is also considered. It has been previously shown that $O(^1D)+H_2$ produces vibrationally excited OH(v=1-4).[26] We are prevented from adding a buffer gas to vibrationally quench OH radicals because any species other than He gas will also efficiently quench $O(^1D)$ to $O(^3P)$. Cheskis et al.[27] first reported rate constants for the vibrational relaxation for $OH(v=1-3)+CH_4$. Yamasaki et al.[28] measured rate constants for both the vibrational relaxation and reactive removal of $OH(v=1-4)+CH_4$ using laser induced fluorescence. Reactions with H_2, the dominant species in the $OH+CH_4$ mixture, also quench vibrationally excited OH. Light and Matsumoto[29] have also reported an upper limit vibrational quenching rate constant for $OH(v=1)+H_2$ of $k\approx 6x10^{-13}$ cm^3 $molec^{-1}$ s^{-1}. With inclusion of reported vibrational quenching rates for vibrationally excited OH by both CH_4 and H_2, kinetics simulations were used to estimate the contribution of $OH(v=0,1,2,3)+CH_4$ at our conditions. The simulation suggests that after 100 μs, the branching fraction for $OH(v=0):OH(v=1):OH(v=2)$ was $\approx 1:2x10^{-3}:3x10^{-3}$. Since the decay rate of $OH+CH_4$ at

our OH number density of $\approx 10^{13}$ molecules cm^{-3} is on the millisecond to seconds timescale, ground state OH(v=0) dominates CH_4 depletion. These important contributions were necessary in the kinetics model to obtain the good agreement shown in Figure 5.3.

The experimental procedure is similar to $O(^1D)+CH_4$, but with a different gas mixture: a quartz glass cell with the $OH/N_2O/H_2$ gas mixture (Table 3) is photolyzed in a vacuum chamber and expanded into a CRDS cavity for spectroscopic measurement of methane isotopologues. Figures 5.7A and 5.8C show linear regressions of the data for ^{13}C and D KIEs, respectively, for $OH+CH_4$ at four temperatures spanning 177-293 K. Different from the $O(^1D)+CH_4$ case, $OH+CH_4$ KIEs displays pronounced temperature dependences, particularly for ^{D}KIE. The fitted slopes are plotted in Figures 5.7B and 5.8D for better clarity of the temperature dependent trends. The data are fitted to an Arrhenius form $KIE(T)=Aexp[B/T]$ where A and B are fitted parameters. Both ^{13}C and D display a rising KIE effect at colder temperatures.

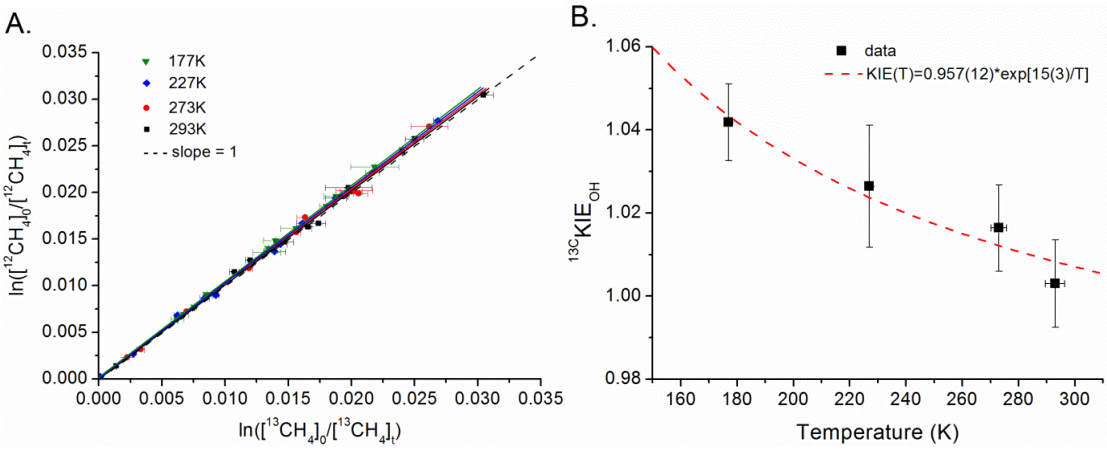

Figure 5.7: Temperature dependences of ^{13C}KIE for $OH+CH_4$. A) Raw data and linear regression of ^{13}C KIE for $OH+CH_4$ at four different temperatures. B) A plot of the KIE as a function of temperature displays an increasing slope as temperature decreases, indicating a temperature dependent KIE effect. Fits to an Arrhenius equation resulted in $KIE(T)=0.957(12)exp(15(3)/T)$ for $O(^1D)+CH_4$.

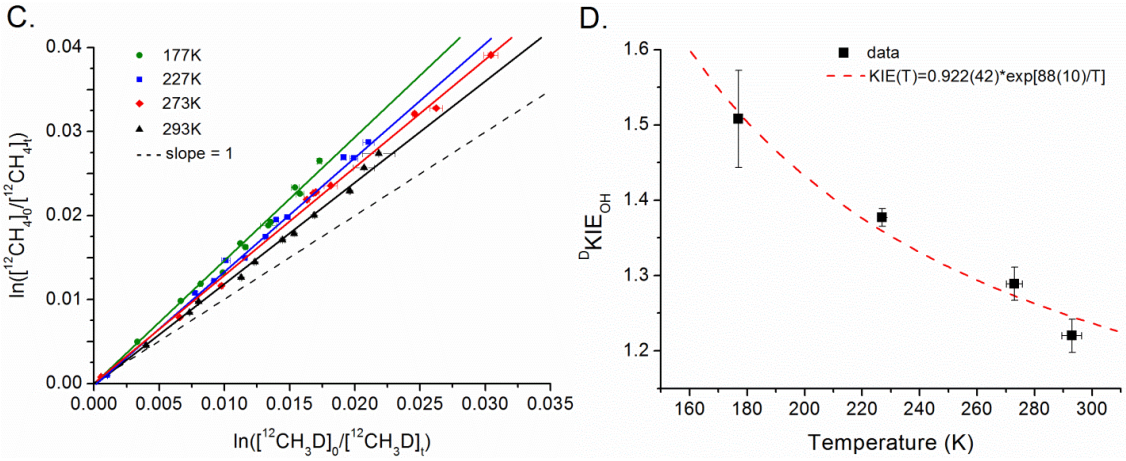

Figure 5.8: Temperature dependences of ^{D}KIE for OH+CH_4. C) Raw data and the linear regressions at four different temperatures. D) Plot of the $^{D}KIE_{OH}$ as a function of temperature. This reaction displays increasing KIE effects at lower temperatures. Fits to an Arrhenius equation resulted in KIE(*T*)=0.922(42)*exp*(88(10)/*T*) for OH+CH_4.

5.4.3 Literature Comparisons

The measured KIE temperature dependences for OH+CH_4 are compared to current experimental and theoretical literature data. Figure 5.9 compares all the available literature data for $^{13C}KIE_{OH}$. The data points and lines represent experiments and theory, respectively. The only experimental data available is from Cantrell et al.[12], who determined that the $^{13C}KIE_{OH}$ is independent of temperature from 273-353 K. Rust & Stevens[10], Davidson et al.[11], Saueressig et al.[15] all reported single temperature $^{3C}KIE_{OH}$. Our results and fit are shown in the black circles and solid lines, respectively. While the error bars are larger, our room temperature measurement agrees with the others.

In contrast to the Cantrell et al.[12], we measured a noticeable trend for an increasing $^{13C}KIE_{OH}$ as a function of temperature from 177-293 K. While previously unobserved in experimental work, theory has predicted this increasing behavior. Initial

early attempts by Lasaga and Gibbs[30] and Gupta et al.[34] used conventional transition state theory (CTST) and one dimensional tunneling corrections to predict a flat temperature dependence for $^{13C}KIE_{OH}$. Melissas and Truhlar[31] utilized variation transition state theory with multidimensional tunneling (MT) corrections (VTST/MT) and showed similar temperature independent results from 200-500 K. Lin et al.[32] improved upon VTST/MT calculations by using higher level electronic structure theory via hybrid functional theories (MPW1K, MC3MPW, MC3BB) to obtain more accurate potential energy surfaces (PES). Lin et al.'s treatment differed from previous theoretical methods in two ways: 1) torsional anharmonicity is better treated with an improved PES, 2) incorporation of multidimensional tunneling by the small curvature tunneling (SCT) method.[32] Consequently, all three levels of electronic structure theory predict an increasing KIE with decreasing temperature. This behavior comes out when MT was implemented, which accounted for reaction path curvature. Lin et al.[32] concluded that the deficiency of Melissas and Truhlar[31] was in the errors from the extrapolated frequencies along the reaction path from limited electronic structure data. These errors effectively canceled the temperature dependence from tunneling. Finally, recent work from Suleimanov and Espinosa-Garcia[33] used VTST/MT to compute $^{13C}KIE_{OH}$ using their new analytical PES for $OH+CH_4$, PES-2014. While their new results also display the same temperature dependent KIE trend at Lin et al.[32] and our work, they predicted a much larger value of $^{13C}KIE_{OH}$ 1.036 at 300 K.

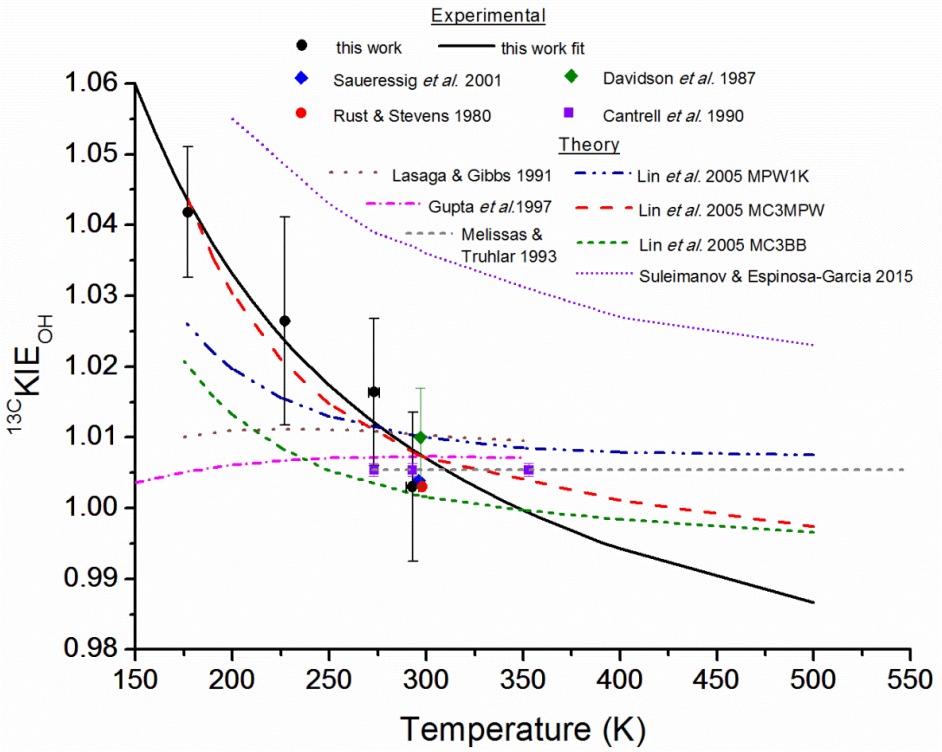

Figure 5.9: $^{13C}KIE_{OH}$ literature comparisons. Experimental data and theoretical results are represented by data points and lines, respectively. Data from this work are displayed as black circles and the extrapolated fits as a solid black line. Single temperature experimental values are reported by Rust and Stevens[10] (red circle), Davidson et al.[11] (green diamond, and Saueressig et al.[15] (blue diamond). Cantrell et al.[12] reported $^{13C}KIE_{OH}$ at three temperatures (purple square). A number of theoretical studies have been reported and plotted as dashed lines: Lasaga & Gibbs[30] (brown), Melissas & Truhlar[31] (gray), Gupta et al.[34] (pink), Lin et al.[32] (blue, red, green) and Suleimanov and Espinosa-Garcia[33] (purple).

For $^{D}KIE_{OH}$, both DeMore[13] (298-360 K) and Gierczak et al.[14] (250-420 K) experimentally observed temperature dependences of $^{D}KIE_{OH}$. Both studies provided Arrhenius parameters, which were used to plot the temperature dependent extrapolation curves in red and blue solid lines in Figure 5.10. The data for our work are in black squares, and the temperature dependent extrapolation is the solid black line. Saueressig et al.[15] reported $^{D}KIE_{OH}$ at a single temperature 296 K, plotted as a blue diamond. Our temperature dependent curvature looks most similar to DeMore[13], but the amplitude of the KIE is significantly different by about 100‰. Compared to values of Gierczak et al.[14], the qualitative behavior deviates from our results at both warm and cold

temperatures. Also, the discrepancies in the reported KIEs with our measurements become increasingly large as temperature decreases. Any attempts at atmospheric modeling will incur the corresponding rise in uncertainty due to temperature dependences.

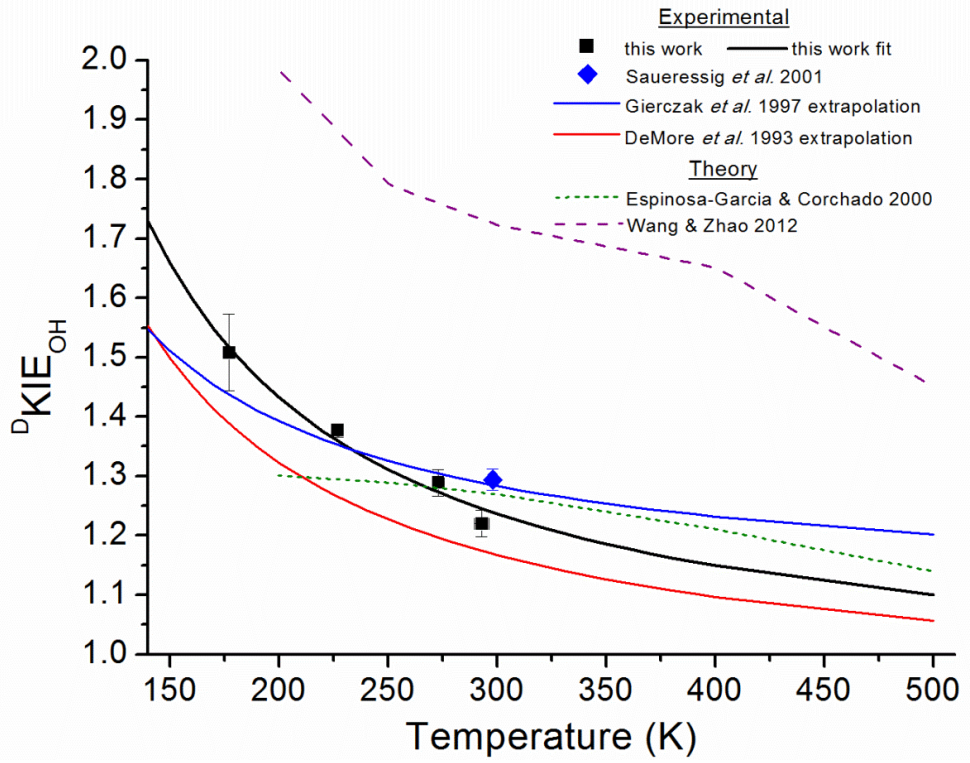

Figure 5.10: $^{D}KIE_{OH}$ literature comparisons. Data for our work is displayed as black squares, and the temperature extrapolation is the black solid line. Saueressig et al.[15] reported a single temperature $^{D}KIE_{OH}$ value at 296 K in blue diamond. Gierczak et al.[14] measured $^{D}KIE_{OH}$ from 250 to 420 K and the temperature extrapolation is in blue solid line. DeMore[13] measured $^{D}KIE_{OH}$ from 298 to 360 K and the extrapolation is the solid red line. Two theoretical reports are available from Espinosa-Garcia and Corchado[35] using VTST/μOMT in green dashed line and Wang and Zhao[36] using QI in purple dashed line.

Two theoretical studies have attempted to compute the $^{D}KIE_{OH}$ for $OH+CH_4$ from *ab initio* PES. Espinosa-Garcia and Corchado[35] performed VTST dynamical calculations on their constructed analytical PES for $OH+CH_4$. For tunneling contributions, the microcanonical optimized multidimensional tunneling (μOMT)[37] approach was implemented. The calculated results gave reasonable agreement with experimental data

from at temperatures higher than 300 K. Below 300 K, the calculated KIE appears to plateau, deviating from all reported experimental results. This suggests that the tunneling contribution is underestimated in their work. Subsequent theoretical work by Wang & Zhao[36] used the quantum instanton (QI)[38] dynamical theory to calculate $^{D}KIE_{OH}$ from the same analytical PES constructed by Espinosa-Garcia and Corchado[35]. QI improves upon treatment of tunneling by considering all tunneling paths and weighs each by the quantum Boltzmann factor. This approach provided qualitative behavior that agrees with our measured KIE trends at low and high temperatures, with the most interesting being the tunneling dominated cold regime. Nevertheless, QI appears to overestimate $^{D}KIE_{OH}$ as evident by the large offset in the amplitude of the computed and experiment results.

Finally, Table 5.4 compiles all the KIE values measured in this work along with all reported literature values at room temperature (296-298 K). The tabulated KIE values are corrected for O(^{1}D) and OH contributions determined from kinetics modeling (Figure 5.4) by applying eq. 7.

T=296-298 K	**OH ^{D}KIE**	**OH ^{13}CKIE**	**O(^{1}D) ^{13}CKIE**	**O(^{1}D) ^{D}KIE**
This work	1.251(44)	1.007(20)	1.042(18)	1.129(51)
Saueressig et al. *2001*[15]	1.294(18)	1.0039(4)	1.013	1.06
Gierczak et al. *1997*[14]	1.25(14)	N/A	N/A	N/A
DeMore 1993[13]	1.169	N/A	N/A	N/A
Davidson et al. *1987*[11]	N/A	1.010(7)	1.001	N/A
Cantrell et al. *1990*[12]	N/A	1.0054(9)	N/A	N/A
Rust & Stevens 1980[10]	N/A	1.003	N/A	N/A

Table 5.4: Tabulated literature measurements of KIEs for O(^{1}D) and OH+CH_4 reactions at T=296-298 K. The 2σ uncertainties are denoted within parentheses. The KIEs from our work are corrected values from considering interfering contributions from both O(^{1}D) and OH to the observed value (eq. 7).

5.5 Conclusion

Temperature dependent (177-293 K) KIE laboratory measurements of ^{13}C and D kinetic isotope effects for both $O(^1D)+CH_4$ and $OH+CH_4$ show elevated KIEs at colder temperatures for only the $OH+CH_4$ reaction. Our observed temperature dependences for $^{D}KIE_{OH}$ display increasing discrepancies with published results by both Gierczak et al.[14] and DeMore[13] as temperature decreases, which presents significant concerns for using published data for extrapolating to colder temperature. In the case of $^{13C}KIE_{OH}$, a temperature dependent trend is observed, which contrasted the only experimental report by Cantrell et al.[12] who did not observed any temperature dependencies. Moreover, theoretical studies by both Lin et al.[32] and Suleimanov and Espinosa-Garcia[33] have predicted this temperature dependent rise in $^{13C}KIE_{OH}$ with decreasing temperature. We expect that these new reports for temperature dependencies of $OH+CH_4$ will be important for modeling methane oxidation from Earth's upper atmosphere and the Martian atmosphere down to 177 K, which will hopefully reduce errors due to extrapolation from data at warmer temperatures.

5.6 Acknowledgements

This work was supported by the NASA Mars Fundamental Research Grant NNX12AI01G. T. Q. B. was supported by a NASA Earth and Space Sciences Fellowship and the NASA Mars Fundamental Research Grant NNX12AI01G. L.S. was supported by a NASA Earth and Space Sciences Fellowship.

5.7 References

1. C. R. Webster, P. R. Mahaffy, S. K. Atreya, G. J. Flesch, M. A. Mischna, P.-Y. Meslin, K. A. Farley, P. G. Conrad, L. E. Christensen, A. A. Pavlov, J. Martin-Torres, M.-P. Zorzano, T. H. McConnochie, T. Owen, J. L. Eigenbrode, D. P. Glavin, A. Steele, C. A. Malespin, P. D. Archer, Jr., B. Sutter, P. Coll, C. Freissinet, C. P. McKay, J. E. Moores, S. P. Schwenzer, J. C. Bridges, R. Navarro-Gonzalez, R. Gellert, M. T. Lemmon and M. S. L. S. Team, Science **347** (6220), 415-417 (2015).

2. S. K. Atreya, P. R. Mahaffy and A.-S. Wong, Planetary and Space Science **55** (3), 358-369 (2007).

3. V. A. Krashnopolsky, J. P. Maillard and T. C. Owen, Icarus **172** (2), 537-547 (2004).

4. F. Forget, F. Montmessin, J. L. Bertaux, F. Gonzalez-Galindo, S. Lebonnois, E. Quemerais, A. Reberac, E. Dimarellis and M. A. Lopez-Valverde, J. Geophys. Res.-Planets **114**, 19 (2009).

5. J. Seinfeld and S. Pandis, *Atmospheric Chemistry and Physics: From Air Pollution to Climate Change*. (John Wiley & Sons, 1996).

6. J. Lelieveld, P. J. Crutzen and F. J. Dentener, Tellus Ser. B-Chem. Phys. Meteorol. **50** (2), 128-150 (1998).

7. S. C. Tyler, J. Geophys. Res.-Atmos. **91** (D12), 3232-3238 (1986).

8. A. R. Ravishankara, Annu. Rev. Phys. Chem. **39**, 367-394 (1988).

9. M. Whiticar, Atmospheric Methane: Its Role in the Global Environment, Khalil M.A.K., ed., Berlin: Springer-Verlag (2000).

10. F. E. Rust and C. M. Stevens, Int. J. Chem. Kinet. **12**, 371-377 (1980).

11. J. A. Davidson, C. A. Cantrell, S. C. Tyler, R. E. Shetter, R. J. Cicerone and J. G. Calvert, J. Geophys. Res.-Atmos. **92** (D2), 2195-2199 (1987).

12. C. A. Cantrell, R. E. Shetter, A. H. McDaniel, J. G. Calvert, J. A. Davidson, D. C. Lowe, S. C. Tyler, R. J. Cicerone and J. P. Greenberg, J. Geophys. Res.-Atmos. **95** (D13), 22455-22462 (1990).

13. W. B. Demore, J. Phys. Chem. **97** (33), 8564-8566 (1993).

14. T. Gierczak, R. K. Talukdar, S. C. Herndon, G. L. Vaghjiani and A. R. Ravishankara, J. Phys. Chem. A **101** (17), 3125-3134 (1997).

15. G. Saueressig, J. N. Crowley, P. Bergamaschi, C. Bruhl, C. A. M. Brenninkmeijer and H. Fischer, J. Geophys. Res.-Atmos. **106** (D19), 23127-23138 (2001).

16. T. B. Bui, L. Shen, P. Chen and M. Okumura.
17. L. Galatry, Phys. Rev. **122** (4), 1218 (1961).

18. J. C. Ianni, *A comparison of the Bader-Deuflhard and the Cash-Karp Runge-Kutta integrators for the GRI-MECH 3.0 model based on the chemical kinetics code Kintecus*. (2003).

19. L. L. Springsteen, S. Satyapal, Y. Matsumi, L. M. Dobeck and P. L. Houston, J. Phys. Chem. **97** (28), 7239-7241 (1993).

20. H. B. Chen, W. D. Thweatt, J. J. Wang, G. P. Glass and R. F. Curl, J. Phys. Chem. A **109** (10), 2207-2216 (2005).

21. G. Blyth, A. A. Clifford, P. Gray and J. I. Waddicor, Journal of the Chemical Society-Faraday Transactions I **83**, 751-757 (1987).

22. N. L. Arthur, I. A. Cooper and Y. M. Gershenzon, Journal of the Chemical Society-Faraday Transactions **93** (19), 3485-3490 (1997).

23. B. S. Wang, H. Hou, L. M. Yoder, J. T. Muckerman and C. Fockenberg, J. Phys. Chem. A **107** (51), 11414-11426 (2003).

24. M. Brouard, M. T. Macpherson, M. J. Pilling, J. M. Tulloch and A. P. Williamson, Chem. Phys. Lett. **113** (5), 413-418 (1985).

25. S. P. Sander, J. P. D. Abbatt, J. R. Barker, J. B. Burkholder, R. R. Friedl, D. M. Golden, R. E. Huie, K. C.E., M. J. Kurylo, G. K. Moortgat, V. L. Orkin and P. H. Wine, JPL Publication 10-6, Jet Propulsion Laboratory, Pasadena, http://jpldataeval.jpl.nasa.gov (2011).

26. Y. L. Huang, Y. K. Gu, C. S. Liu, X. F. Yang and Y. S. Tao, Chem. Phys. Lett. **127** (5), 432-437 (1986).

27. S. G. Cheskis, A. A. Iogansen, P. V. Kulakov, I. Y. Razuvaev, O. M. Sarkisov and A. A. Titov, Chem. Phys. Lett. **155** (1), 37-42 (1989).

28. K. Yamasaki, A. Watanabe, T. Kakuda, N. Ichikawa and I. Tokue, J. Phys. Chem. A **103** (4), 451-459 (1999).

29. G. C. Light and J. H. Matsumoto, Chem. Phys. Lett. **58**, 578 (1978).

30. A. C. Lasaga and G. V. Gibbs, Geophysical Research Letters **18** (7), 1217-1220 (1991).

31. V. S. Melissas and D. G. Truhlar, J. Chem. Phys. **99** (5), 3542-3552 (1993).

32. H. Lin, Y. Zhao, B. A. Ellingson, J. Z. Pu and D. G. Truhlar, J. Am. Chem. Soc. **127** (9), 2830-2831 (2005).

33. Y. V. Suleimanov and J. Espinosa-Garcia, Journal of Physical Chemistry B (2015).

34. M. L. Gupta, M. P. McGrath, R. J. Cicerone, F. S. Rowland and M. Wolfsberg, Geophysical Research Letters **24** (22), 2761-2764 (1997).

35. J. Espinosa-Garcia and J. C. Corchado, J. Chem. Phys. **112** (13), 5731-5739 (2000).

36. W. J. Wang and Y. Zhao, J. Chem. Phys. **137** (21), 10 (2012).

37. Y. P. Liu, D. H. Lu, A. Gonzalezlafont, D. G. Truhlar and B. C. Garrett, J. Am. Chem. Soc. **115** (17), 7806-7817 (1993).

38. W. H. Miller, Y. Zhao, M. Ceotto and S. Yang, J. Chem. Phys. **119** (3), 1329-1342 (2003).

39. P. W. Seakins and S. R. Leone, J. Phys. Chem. **96** (11), 4478-4485 (1992).

40. S. Vranckx, J. Peeters and S. A. Carl, Atmos. Chem. Phys. **8** (20), 6261-6272 (2008).

41. J. A. Davidson, H. I. Schiff, T. J. Brown and C. J. Howard, J. Chem. Phys. **69** (3), 1216-1217 (1978).

42. J. C. Shi and J. R. Barker, Int. J. Chem. Kinet. **22** (12), 1283-1301 (1990).

43. R. F. Heidner and D. Husain, Int. J. Chem. Kinet. **6** (1), 77-87 (1974).

5.8 Appendices

5.8.1 Reactions for Chemical Kinetics Model

k(298 K)	A	E/R	Reactions	Reference
$O(^1D)$ Chemistry				
7.96E-15	8.00E-12	2060	$O(^3P)+O_3 \Rightarrow O_2+O_2$	JPL Publication 10-6[157]
1.20E-10	1.20E-10	0	$O(^1D)+ O_3 \Rightarrow O_2+ O_2$	JPL Publication 10-6
3.36E-11	3.36E-11	0	$O(^1D)+H_2 \Rightarrow OH(v=0)+H$	Huang Y. et al. 1986[158]
2.64E-11	2.64E-11	0	$O(^1D)+ H_2 \Rightarrow OH(v=1)+H$	Huang Y. et al. 1986[158]
2.64E-11	2.64E-11	0	$O(^1D)+ H_2 \Rightarrow OH(v=2)+H$	Huang Y. et al. 1986[158]
2.28E-11	2.28E-11	0	$O(^1D)+ H_2 \Rightarrow OH(v=3)+H$	Huang Y. et al. 1986[158]
1.08E-11	1.08E-11	0	$O(^1D)+ H_2 \Rightarrow OH(v=4)+H$	Huang Y. et al. 1986[158]
1.99E-10	1.63E-10	-60	$O(^1D)+H_2O \Rightarrow 2OH(v=0)$	JPL Publication 10-6
7.75E-11	7.25E-11	-20	$O(^1D)+N_2O \Rightarrow NO+NO$	JPL Publication 10-6
1.21E-10	1.21E-10	0	$O(^1D)+CH_4 \Rightarrow CH_3+ OH(v=0)$	JPL Publication 10-6
3.50E-11	3.50E-11	0	$O(^1D)+CH_4 \Rightarrow CH_3O+H$	JPL Publication 10-6
9.00E-12	9.00E-12	0	$O(^1D)+CH_4 \Rightarrow CH_2O+H_2$	JPL Publication 10-6
4.05E-18	4.05E-18	0	$H+N_2O \Rightarrow OH(v=0)+N_2$	Arthur et al. 1997[154]
HOx Chemistry				
3.29E-11	1.80E-11	-180	$O(^3P)+ OH(v=0) \Rightarrow O_2+H$	JPL Publication 10-6
5.87E-11	3.00E-11	-200	$O(^3P)+HO_2 \Rightarrow OH(v=0)+O_2$	JPL Publication 10-6
1.70E-15	1.40E-12	2000	$O(^3P)+H_2O_2 \Rightarrow OH(v=0)+HO_2$	JPL Publication 10-6
5.48E-14	5.48E-14	0	$H+O_2 \Rightarrow HO_2$	JPL Publication 10-6
2.89E-11	1.40E-10	470	$H+O_3 \Rightarrow OH(v=0)+O_2$	JPL Publication 10-6
7.20E-11	7.20E-11	0	$H+HO_2 \Rightarrow 2OH(v=0)$	JPL Publication 10-6
1.60E-12	1.60E-12	0	$H+ HO_2 \Rightarrow O+H_2O$	JPL Publication 10-6
6.90E-12	6.90E-12	0	$H+ HO_2 \Rightarrow H_2+O_2$	JPL Publication 10-6
7.25E-14	1.70E-12	940	$OH(v=0)+O_3 \Rightarrow HO_2+O_2$	JPL Publication 10-6
6.67E-15	2.80E-12	1800	$OH(v=0)+H_2 \Rightarrow H_2O+H$	JPL Publication 10-6
1.80E-12	1.80E-12	0	$OH(v=0)+ OH(v=0) \Rightarrow H_2O+O$	JPL Publication 10-6
7.39E-13	7.39E-13	0	$OH(v=0)+ OH(v=0) \Rightarrow H_2O_2$	JPL Publication 10-6
1.11E-10	4.80E-11	-250	$OH(v=0)+HO_2 \Rightarrow H_2O+O_2$	JPL Publication 10-6
1.80E-12	1.80E-12	0	$OH(v=0)+H_2O_2 \Rightarrow H_2O+HO_2$	JPL Publication 10-6
1.93E-15	1.00E-14	490	$HO_2+O_3 \Rightarrow OH(v=0)+2O_2$	JPL Publication 10-6
1.40E-12	3.00E-13	-460	$HO_2+HO_2 \Rightarrow H_2O_2+O_2$	JPL Publication 10-6
5.96E-14	2.72E-15	-920	$HO_2+HO_2 \Rightarrow H_2O_2+O_2$	JPL Publication 10-6
NOx Chemistry				

1.09E-13	1.09E-13	0	$O(^3P)+NO==> NO_2$	JPL Publication 10-6
1.03E-11	5.10E-12	-210	$O(^3P)+NO_2==>NO+O2$	JPL Publication 10-6
2.87E-13	2.87E-13	0	$O(^3P)+ NO_2==>NO_3$	JPL Publication 10-6
1.00E-11	1.00E-11	0	$O(^3P)+ NO_3==>O_2+ NO_2$	JPL Publication 10-6
1.28E-10	4.00E-10	340	$H+ NO_2==> OH(v=0)+NO$	JPL Publication 10-6
7.79E-13	7.79E-13	0	$OH(v=0)+NO==>HONO$	JPL Publication 10-6
1.73E-12	1.73E-12	0	$OH(v=0)+NO_2==>HNO_3$	JPL Publication 10-6
1.13E-13	1.13E-13	0	$OH(v=0)+NO_2==>HOONO$	JPL Publication 10-6
4.86E-12	1.80E-11	390	$OH(v=0)+HONO==>H_2O+NO_2$	JPL Publication 10-6
1.40E-13	1.40E-13	0	$OH(v=0)+HNO_3==>H_2O+NO_3$	JPL Publication 10-6
8.17E-12	3.30E-12	-270	$HO_2+NO==> NO_2+OH(v=0)$	JPL Publication 10-6
1.90E-13	1.90E-13	0	$HO_2+NO_2==>HO_2NO_2$	JPL Publication 10-6
3.50E-12	3.50E-12	0	$HO_2+NO_3==> OH(v=0)+NO_2+O_2$	JPL Publication 10-6
1.95E-14	3.00E-12	1500	$NO+NO_3==> 2NO_2$	JPL Publication 10-6
Organic Compound Reactions				
9.40e-11	9.40e-11	0	$O(^3P)+CH_3==>CH_2O+H$	Seakins & Leone 1992[171]
1.99E-11	3.40E-11	160	$O(^3P)+CH_2O==>OH(v=0)+HCO$	JPL Publication 10-6
2.00E-12	2.00E-12	0	$O_2+HOCO==>HO_2+CO_2$	JPL Publication 10-6
7.00E-15	7.00E-15	0	$OH(v=0)+CO==>HOCO$	JPL Publication 10-6
9.23E-14	9.23E-14	0	$OH(v=0)+CO==>H+CO_2$	JPL Publication 10-6
8.60E-12	8.60E-12	0	$OH(v=4)+CH_4==> OH(v=3)+CH_4$	Yamasaki et al. 1999[160]
4.80E-12	4.80E-12	0	$OH(v=3)+CH_4==> OH(v=2)+CH_4$	Yamasaki et al. 1999[160]
1.10E-12	1.10E-12	0	$OH(v=2)+CH_4==> OH(v=1)+CH_4$	Yamasaki et al. 1999[160]
3.50E-13	3.50E-13	0	$OH(v=1)+CH_4==> OH(v=0)+CH_4$	Yamasaki et al. 1999[160]
6.34E-15	2.45E-12	1775	$OH(v=0)+CH_4==>CH_3+H_2O$	JPL Publication 10-6
5.44E-16	2.10E-13	1775	$OH(v=1)+CH_4==>CH_3+H_2O$	Yamasaki et al. 1999[160]
2.33E-15	9.00E-13	1775	$OH(v=2)+CH_4==>CH_3+H_2O$	Yamasaki et al. 1999[160]
4.68E-16	1.81E-13	1775	$OH(v=3)+CH_4==>CH_3+H_2O$	Yamasaki et al. 1999[160]
7.61E-16	2.94E-13	1775	$OH(v=4)+CH_4==>CH_3+H_2O$	Yamasaki et al. 1999[160]
6.00E-13	6.00E-13	0	$OH(v=1)+H_2==>OH(v=0)+H_2$	Light & Matsumoto, 1978[161]
8.37E-12	5.50E-12	-125	$OH(v=0)+CH_2O==>H_2O+HCO$	JPL Publication 10-6
9.11E-13	2.90E-12	345	$OH(v=0)+CH_3OH==>CH_2OH+H_2O$	JPL Publication 10-6
2.50E-13	7.66E-12	1020	$OH(v=0)+C_2H_6==>H_2O+C_2H_5$	JPL Publication 10-6
2.33E-13	2.33E-13	0	$CH_3+O_2==>CH_3O_2$	JPL Publication 10-6
1.90E-12	1.90E-12	0	$CH_3+H==>CH_4$	Brouard et al. 1985[156]
4.80E-11	4.80E-11	0	$CH_3+CH_3==>C_2H_6$	Wang et al. 2003[155]
5.20E-12	5.20E-12	0	$HCO+O_2==>CO+HO_2$	JPL Publication 10-6
9.10E-12	9.10E-12	0	$CH_2OH+O_2==>CH_2O+HO_2$	JPL Publication 10-6
1.90E-15	3.90E-14	900	$CH_3O+O_2==>CH_2O+HO_2$	JPL Publication 10-6

8.00E-12	**8.00E-12**	**0**	**$CH_3O+NO==>CH_2O+HNO$**	**JPL Publication 10-6**
1.02E-11	**1.02E-11**	**0**	**$CH_3O+NO==>CH_3ONO$**	**JPL Publication 10-6**
1.96E-13	**1.10E-11**	**1200**	**$CH_3O+NO_2==>CH_2O+HONO$**	**JPL Publication 10-6**
1.03E-11	**1.03E-11**	**0**	**$CH_3O+NO_2==>CH_3ONO_2$**	**JPL Publication 10-6**
6.46E-12	**6.46E-12**	**0**	**$C_2H_5+O_2==>C_2H_5O_2$**	**JPL Publication 10-6**
$O(^1D)$ Quenching Reactions				
5.48E-12	**5.48E-12**	**0**	**$O(^1D)+N_2O==>O(^3P)+N_2O$**	**Vranckx et al. 2008[172]**
3.11E-11	**2.15E-11**	**-110**	**$O(^1D)+N_2==>O(^3P)+N_2$**	**JPL Publication 10-6**
6.22E-22	**6.22E-22**	**0**	**$O(^1D)+CO==>O(^3P)+CO$**	**Davidson et al. 1978[173]**
4.95E-11	**4.63E-11**	**-20**	**$O(^1D)+N_2O==>N_2+O_2$**	**JPL Publication 10-6**
3.97E-11	**3.30E-11**	**-55**	**$O(^1D)+O_2==>O(^3P)+O_2$**	**JPL Publication 10-6**
1.10E-10	**7.50E-11**	**-115**	**$O(^1D)+CO_2==>O(^3P)+CO_2$**	**Shi & Barker 1990[174]**
7.00E-16	**7.00E-16**	**0**	**$O(^1D)+He==>O(^3P)+He$**	**Heidner & Husain 1974[175]**

5.8.2 Matlab code for simulating a repetitive pulsed photolysis experiment

```
% Summary: This code runs Kintecus from Matlab. The code simulates a multi-pulse photochemical
experiment for kinetic isotope effect measurements of methane oxidation by O(1D) and OH reactions. The
molecular species used in this simulation is based on our specific kinetics model.


clear all; % clear all data previously generated from Matlab

cd ('C:\Kintecus'); %set the location of the Kintecus executable and required “species.dat” and
“CONC.TXT” files.

%Read in “SPECIES.DAT” and “CONC.TXT” files.
species_workbook = fopen('SPECIES.DAT', 'r');
species_content = textscan(species_workbook, '%s %s %s %s %s %s %s %s', 'Delimiter','\t'); %do not
change these delimiters
fclose(species_workbook);
[~,species_ncols] = size(species_content);
species_nrows = length(species_content{1});
concentration = importdata('CONC.TXT');
conc_data = concentration.data;

%initial_conc_row = conc_data(1,:);

N_pulse = 250;  % number of pulses
conc_matrix = zeros(N_pulse,49);

% Start of loop to perform iterations for the number of excimer pulses, N_pulse

for M = 1:N_pulse

   disp(M);

concentration = importdata('CONC.TXT'); %Read in “CONC.TXT”
conc_data = concentration.data;
conc_matrix(M,:) = conc_data(end,:);

%This following section imports the last row (in this case, row 45) from the Kintecus ‘CONC.TXT’. Row
45 here contains concentrations for all species at the last time step of the kinetics simulation. Matlab
generates an array with these values, which will be re-written back into the “species.dat” file to set a new
initial condition for the next simulation. The next simulation is the next excimer pulse.

conc_row = 45;
k=1;  %index to start counting

CH4 = conc_data(conc_row,k+1);
N2O = conc_data(conc_row,k+2);
O1D = conc_data(conc_row,k+3);
H2 = conc_data(conc_row,k+4);
O = conc_data(conc_row,k+5);
CO2 = conc_data(conc_row,k+6);
CO = conc_data(conc_row,k+7);
CH3OH = conc_data(conc_row,k+8);
```

```
CH2O = conc_data(conc_row,k+9);
O2= conc_data(conc_row,k+10);
H2O = conc_data(conc_row,k+11);
NO = conc_data(conc_row,k+12);
H2O2 = conc_data(conc_row,k+13);
NO2 = conc_data(conc_row,k+14);
NO3 = conc_data(conc_row,k+15);
C2H6 = conc_data(conc_row,k+16);
N2 = conc_data(conc_row,k+17);
HONO = conc_data(conc_row,k+18);
O3 = conc_data(conc_row,k+19);
H = conc_data(conc_row,k+20);
CH3 = conc_data(conc_row,k+21);
CH3O = conc_data(conc_row,k+22);
HO2 = conc_data(conc_row,k+23);
HNO3 = conc_data(conc_row,k+24);
He = conc_data(conc_row,k+25);
HOONO = conc_data(conc_row,k+26);
HO2NO2 = conc_data(conc_row,k+27);
N2O5 = conc_data(conc_row,k+28);
HCO = conc_data(conc_row,k+29);
HOCO = conc_data(conc_row,k+30);
CH2OH = conc_data(conc_row,k+31);
C2H5 = conc_data(conc_row,k+32);
HO2CH2O = conc_data(conc_row,k+33);
CH3O2 = conc_data(conc_row,k+34);
CH3OOH = conc_data(conc_row,k+35);
C2H5O2 = conc_data(conc_row,k+36);
C2H5OOH = conc_data(conc_row,k+37);
HNO = conc_data(conc_row,k+38);
CH3ONO = conc_data(conc_row,k+39);
CH3ONO2 = conc_data(conc_row,k+40);
CH3O2NO2 = conc_data(conc_row,k+41);
CH3NO = conc_data(conc_row,k+42);
OH_0 = conc_data(conc_row,k+43);
OH_1 = conc_data(conc_row,k+44);
OH_2 = conc_data(conc_row,k+45);
OH_4 = conc_data(conc_row,k+47);
OH_3 = conc_data(conc_row,k+46);
CH2 = conc_data(conc_row,k+48);

%Photolysis Calculations

E = 70; %excimer pulse energy mJ
A = 1.784; %beam area cm^2
sigma_N2O = 8.76e-20; % N2O 193nm photolysis cross-section
sigma_H2O2 = 8.1823e-19; % H2O2 193nm photolysis cross-section
sigma_HONO = 1.5e-18; % HONO 193nm photolysis cross-section

%calculate concentrations for one excimer pulse to input into Kintecus “SPECIES.DAT” for use as initial
conditions for simulation

N2O_initial = E./A.*0.9.*5.03069e12.*193.*(A./11.4).*sigma_N2O.*N2O;
H2O2_initial = E./A.*0.9.*5.03069e12.*193.*(A./11.4).*sigma_H2O2.*H2O2;
HONO_initial = E./A.*0.9.*5.03069e12.*193.*(A./11.4).*sigma_HONO.*HONO;
```

```
O1D_initial = O1D+N2O_initial;
N2_initial = N2+N2O_initial;
N2O_input = N2O - N2O_initial;
H2O2_input = H2O2 + H2O2_initial;
HONO_input = HONO + HONO_initial;

  % Sets new concentrations. Keep 15 digits in num2str.
   formatSpec = '%10.15e';
   species_content{1,3}{4,1} = num2str(CH4,formatSpec);
   species_content{1,3}{5,1} = num2str(N2O_input,formatSpec);
   species_content{1,3}{6,1} = num2str(O1D_initial,formatSpec);
   species_content{1,3}{7,1} = num2str(H2,formatSpec);
   species_content{1,3}{8,1} = num2str(O,formatSpec);
   species_content{1,3}{9,1} = num2str(CO2,formatSpec);
   species_content{1,3}{10,1} = num2str(CO,formatSpec);
   species_content{1,3}{11,1} = num2str(CH3OH,formatSpec);
   species_content{1,3}{12,1} = num2str(CH2O,formatSpec);
   species_content{1,3}{13,1} = num2str(O2,formatSpec);
   species_content{1,3}{14,1} = num2str(H2O,formatSpec);
   species_content{1,3}{15,1} = num2str(NO,formatSpec);
   species_content{1,3}{16,1} = num2str(H2O2_input,formatSpec);
   species_content{1,3}{17,1} = num2str(NO2,formatSpec);
   species_content{1,3}{18,1} = num2str(NO3,formatSpec);
   species_content{1,3}{19,1} = num2str(C2H6,formatSpec);
   species_content{1,3}{20,1} = num2str(N2_initial,formatSpec);
   species_content{1,3}{21,1} = num2str(HONO_input,formatSpec);
   species_content{1,3}{22,1} = num2str(O3,formatSpec);
   species_content{1,3}{23,1} = num2str(H,formatSpec);
   species_content{1,3}{24,1} = num2str(CH3,formatSpec);
   species_content{1,3}{25,1} = num2str(CH3O,formatSpec);
   species_content{1,3}{26,1} = num2str(HO2,formatSpec);
   species_content{1,3}{27,1} = num2str(HNO3,formatSpec);
   species_content{1,3}{28,1} = num2str(He,formatSpec);
   species_content{1,3}{29,1} = num2str(HOONO,formatSpec);
   species_content{1,3}{30,1} = num2str(HO2NO2,formatSpec);
   species_content{1,3}{31,1} = num2str(N2O5,formatSpec);
   species_content{1,3}{32,1} = num2str(HCO,formatSpec);
   species_content{1,3}{33,1} = num2str(HOCO,formatSpec);
   species_content{1,3}{34,1} = num2str(CH2OH,formatSpec);
   species_content{1,3}{35,1} = num2str(C2H5,formatSpec);
   species_content{1,3}{36,1} = num2str(HO2CH2O,formatSpec);
   species_content{1,3}{37,1} = num2str(CH3O2,formatSpec);
   species_content{1,3}{38,1} = num2str(CH3OOH,formatSpec);
   species_content{1,3}{39,1} = num2str(C2H5O2,formatSpec);
   species_content{1,3}{40,1} = num2str(C2H5OOH,formatSpec);
   species_content{1,3}{41,1} = num2str(HNO,formatSpec);
   species_content{1,3}{42,1} = num2str(CH3ONO,formatSpec);
   species_content{1,3}{43,1} = num2str(CH3ONO2,formatSpec);
   species_content{1,3}{44,1} = num2str(CH3O2NO2,formatSpec);
   species_content{1,3}{45,1} = num2str(CH3NO,formatSpec);
   species_content{1,3}{46,1} = num2str(OH_0,formatSpec);
   species_content{1,3}{47,1} = num2str(OH_1,formatSpec);
   species_content{1,3}{48,1} = num2str(OH_2,formatSpec);
   species_content{1,3}{49,1} = num2str(OH_3,formatSpec);
   species_content{1,3}{50,1} = num2str(OH_4,formatSpec);
   species_content{1,3}{51,1} = num2str(CH2,formatSpec);
```

```
    % Rewrite the SPECIES.DAT file with new concentrations
   species_workbook = fopen('SPECIES.DAT', 'r+');
   for species_row = 1:species_nrows
      for species_col = 1:species_ncols
         fprintf(species_workbook, '%s\t', species_content{1,species_col}{species_row,1});
      end
      fprintf(species_workbook, '\r\n');
   end
   fclose(species_workbook);

   % Run the Kintecus program. Some initial setup is required. Running the
   % Kintecus program independently (through the Excel workbook) once
   % before running the full program guarantees your settings (i.e.
   % populates the SPECIES.DAT, MODEL.DAT, and PARM.DAT files with your
   % specific model and settings).
   stringKintecus = 'Kintecus.exe';
   evalc('system(stringKintecus);');
   % Use of 'evalc' suppresses the command line output that Kintecus
   % generates. This is useful because if it is not suppressed, the Matlab
   % Command Window is filled with Kintecus information.



  % Save the concentration file as a new file
%     destination = ['CONC.TXT'];
%     copyfile('CONC.txt',destination);

%     % Reports to the user the Kintecus run has ended.
%     Report = rem(photolysis_iterations,61);
%     if Report == 0
%        fprintf('runKintecus iteration is complete.\r');
%     else
%     end

end

% Plot percent depletions
% total_conc_matrix = cat(1, initial_conc_row, conc_matrix);
% Methane percent depletion
%x = 1:size(total_conc_matrix, 1);

x = 1:size(conc_matrix, 1);

for k = 1:size(conc_matrix,1)
   percent_CH4(k) = abs(100*(conc_matrix(k,2)-conc_matrix(1,2))/(conc_matrix(1,2)));
end

P_CH4 = polyfit(x, percent_CH4, 1);
y_fit_CH4 = P_CH4(1)*x+P_CH4(2);

% N2O percent depletion
```

```
for l = 1:size(conc_matrix,1)
   percent_N2O(l) = abs(100*(conc_matrix(l,3)-conc_matrix(1,3))/(conc_matrix(1,3)));
end

P_N2O = polyfit(x, percent_N2O, 1);
y_fit_N2O = P_N2O(1)*x+P_N2O(2);

plot(x, percent_CH4, 'ro', x, y_fit_CH4, 'r');
gtext(['y = ', num2str(P_CH4(1)), 'x+', num2str(P_CH4(2))])
hold on
plot(x,  percent_N2O, 'b*',x, y_fit_N2O, 'b');
gtext(['y = ', num2str(P_N2O(1)), 'x+', num2str(P_N2O(2))])
cd('C:\Users\novicebeing_home');
```

Chapter 6: Mid-Infrared Time-Resolved Frequency Comb Spectroscopy of Transient Free Radicals

This chapter was published as:

A.J. Fleisher, B.J. Bjork, T.Q. Bui, K.C. Cossel, M. Okumura, and J. Ye. *J. Phys. Chem. Lett.*, 2014, 5 (13), pp 2241–2246.

6.1 Abstract

We demonstrate time-resolved frequency comb spectroscopy (TRFCS), a new broadband absorption spectroscopy technique for the study of trace free radicals on the microsecond timescale. We apply TRFCS to study the time-resolved, mid-infrared absorption of the deuterated hydroxyformyl radical *trans*-DOCO, an important short-lived intermediate along the OD + CO reaction path. Directly after photolysis of the chemical precursor acrylic acid-d1, we measure absolute *trans*-DOCO product concentrations with a sensitivity of 5×10^{10} cm^{-3} and observe its subsequent loss with a time resolution of 25 μs. The multiplexed nature of TRFCS allows us to detect simultaneously the time-dependent concentration of several other photoproducts and thus unravel primary and secondary chemical reaction pathways.

6.2 Text

Norrish and Porter's seminal work on flash photolysis heralded the beginning of quantitative studies in gas-phase free-radical chemistry.[1] There have been remarkable experimental advances since then in the time-resolved detection of transient free radicals to directly measure product spectra, concentrations, branching ratios, or reaction rate coefficients. However, acquiring truly multiplexed spectral data regarding several species in a fast chemical reaction with high-frequency resolution and fast time resolution over a broad spectral bandwidth remains a technical challenge. Ultrasensitive single-species detection limits can be achieved using continuous-wave (cw) laser absorption techniques with narrow single wavelength detection, but this approach requires relatively slow scans to cover wide spectral ranges. Traditional multiplexed techniques such as time-resolved mid-infrared (mid-IR) spectroscopy use a step-scan Fourier transform approach, and newer cavity-enhanced methods using light-emitting diodes provide the desired microsecond (or better) time resolution and broad bandwidth but normally with an incoherent light source and thus long total acquisition times to achieve high sensitivity.[2,3] Techniques that improve upon these state-of-the-art methods would have wide-ranging applications such as direct measurements of carbonyl oxides formed during the ozonolysis of alkenes,[4−7] understanding unexplained OH radical concentrations in the atmosphere,[8,9] and verification of nuclear-spin selection rules in reactions of polyatomics.[10]

Mid-IR frequency combs generated using coherent, high-powered femtosecond fiber lasers have recently been developed that unify these three desired traits: high

detection sensitivity, large spectral bandwidth, and fast time resolution.[11] The advent of the phase-stabilized femtosecond optical frequency comb merged the seemingly divergent fields of ultrafast spectroscopy performed with temporally short laser pulses and the ultraprecise measurement of optical frequencies using stable cw lasers.[12] The optical frequency comb has proven to be an invaluable tool for the transfer of precise microwave frequency standards into the optical domain, allowing for the direct interrogation of atomic eigenstates with unprecedented precision while also probing time-dependent quantum coherence effects.[13] Because of their broad spectral bandwidth but inherently high resolution, frequency combs have found applications as sources for trace-gas detection and broadband survey spectroscopy.[11, 14-17] Here we make use of these remarkable advances in optical physics and laser stabilization to address current problems in free-radical trace detection and chemical kinetics. Our technique, named time-resolved frequency comb spectroscopy (TRFCS), enables transient molecular absorption spectroscopy on the microsecond time scale with rovibrational state resolution (0.03 cm^{-1}) simultaneously over a 65 cm^{-1} spectral bandwidth. TRFCS, demonstrated here in the important mid-IR spectral region, allows for the reactivity of several species to be observed in a single spectrum with noise-equivalent absorption (NEA) sensitivity of 1×10^{-9} cm^{-1} $Hz^{-1/2}$ per spectral element. The ability to measure multiple species simultaneously can then rapidly provide precise rate coefficients and branching ratios for multiple reactions.

For this initial demonstration of TRFCS, we studied the time-resolved absorption of a deuterated analogue of the HOCO radical, an important short-lived intermediate in the OH+ CO → H+CO_2 reaction. Throughout Earth's lower atmosphere, this reaction

recycles hydroxyl (OH) radical to hydroperoxy (HO_2) radical and is important in radical reaction cycles that determine ozone concentrations.[18] This reaction also serves as the primary oxidation pathway for carbon monoxide (CO) to form carbon dioxide (CO_2), therefore regulating the global concentrations of both species.[19] In addition, OH + CO → H+ CO2 is critical in the combustion of fossil fuels, where it is also the primary route for converting CO to CO_2 and accounts for a major fraction of the heat released.[20] The kinetics of OH + CO is complicated by an anomalous temperature dependence; near room temperature, the reaction rate coefficient deviates significantly from a simple Arrhenius expression due to formation of the HOCO intermediate. Two structures have been identified, the *cis* and *trans* conformers of HOCO,[21,22] with the *trans*-HOCO conformer more stable by ∼7 kJ mol^{-1}. Although this reaction has been studied extensively, quantitative yields of HOCO would provide a direct test of statistical rate models and tunneling effects.[25]

As a first step toward this goal, we demonstrate the applicability of TRFCS for detecting trace transient HOCO intermediates by measuring the absolute concentration and subsequent reaction rate of deuterated *trans*-HOCO (*trans*-DOCO) following laser photolysis of acrylic acid-d1 ($H_2CCHCOOD$, AA-d_1, 90% isotopic purity) via detection of the *trans*-DOCO OD fundamental stretch.[26] The photodissociation of AA/AA-d_1, an α-unsaturated acid, is a well-known source of HOCO/DOCO. The broadband capability of TRFCS allows us not only to detect the prompt *trans*-DOCO products but also to observe the depletion of parent AA-d_1 and to observe other primary and secondary photochemical products.

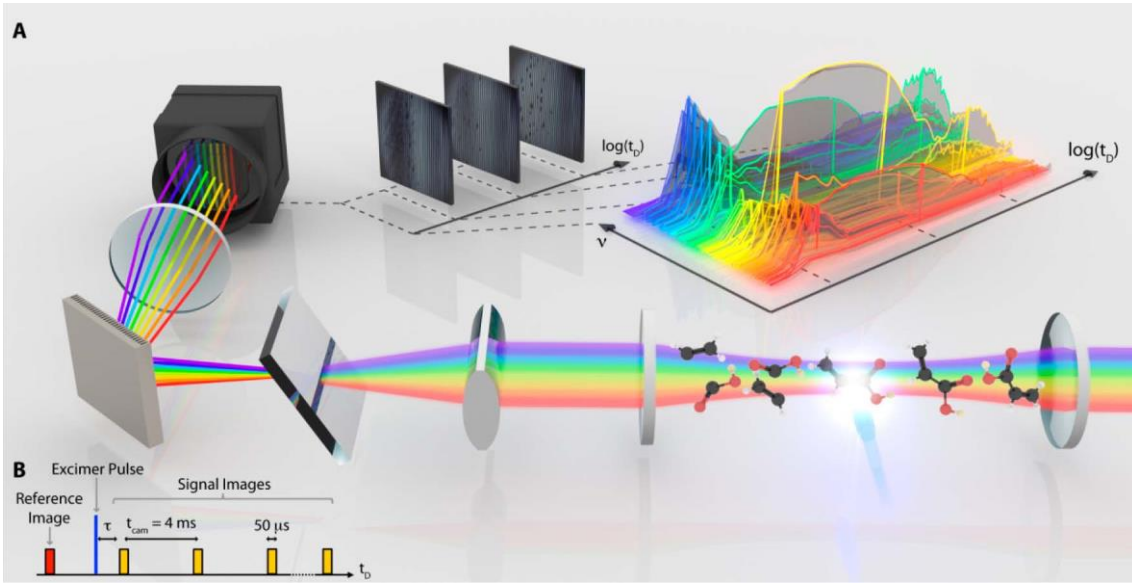

Figure 6.1. (A) Illustration of time-resolved frequency comb spectroscopy (TRFCS) performed with a high-finesse optical cavity coupled to a reaction flow cell. The time delay between photolysis and spectral acquisition provides microsecond time resolution over a broad spectral bandwidth of 65 cm^{-1} in the mid-infrared (mid-IR). (B) Block diagram of the data acquisition scheme, where time zero (t_D=0 µs) is defined by the photolysis pulse (blue).

An illustration of the experimental apparatus is shown in Figure 1A. A mid-IR frequency comb with its output spectrum centered at 2680 cm^{-1} (3.73 µm) was coupled to a high-finesse enhancement cavity (finesse of 1250) that also functioned as a reaction flow cell for photolysis experiments.[27,28] In the frequency domain, the frequency comb teeth correspond to unique frequencies $f_m = mf_{rep} + f_{ceo}$, where m is the comb tooth index (on the order of 10^5), f_{rep} is the repetition rate of the mode-locked laser, and f_{ceo} corresponds to the carrier-envelope offset within the individual ultrashort laser pulses.[12] By dithering the femtosecond pump laser cavity length, we dither f_{rep} at a rate of 50 kHz, causing the individual frequency comb teeth to be swept through their respective enhancement cavity modes (separated by the free spectral range (FSR) of the external cavity). This results in a large peak in cavity transmission because many frequency comb modes are simultaneously resonant with the cavity. A small portion of the total power

contained in these large cavity transmission peaks was used to generate a feedback signal for fast f_{ceo} stabilization (via the OPO cavity length) and slow enhancement cavity length stabilization (via a PZT mounted on the second enhancement cavity mirror), thus ensuring maximum cavity-comb coupling at the center of each dither half-period.[15] The majority of the broadband frequency comb light transmitted through the cavity (~150 cm^{-1} bandwidth) was spatially dispersed using a cross-dispersed virtually imaged phased array (VIPA) spectrometer with 1 GHz (0.03 cm^{-1}) resolution,[29] which set the resolution of the spectra measured here. This spectrometer mapped individual optical frequencies to points on an image plane, allowing for the simultaneous multiplexed detection of differential cavity transmission on time scales limited ultimately by molecular decoherence.[13] The size of the detector array limited our instantaneous spectral bandwidth to 65 cm^{-1}, which was resolved into 1930 elements (7072 comb teeth). A mixture of AA-d_1, CO_2, and N_2 (1.60 kPa total pressure and 21 °C) flowed continuously through the central 12 cm of the cavity, refreshing gas in the photolysis region on a <1 s time scale. High flows of purge gas were introduced to keep the mirrors clean. Typical final concentrations of AA-d_1 in the cell were on the order of 4×10^{14} cm^{-3}. A 10 ns, 193 nm laser pulse from an ArF excimer laser (~5 mJ per pulse within a 3 cm × 1 cm photolysis region) was used to initiate photolysis[30] and defined time zero (t_D=0 μs) for subsequent DOCO kinetics. Images from the VIPA spectrometer were recorded before and after the excimer pulse with integration times of either 25 or 50 μs. The excimer laser repetition rate was 0.2 Hz, allowing for the high-finesse flow cell to be replenished with fresh AA-d_1 sample before each subsequent photolysis experiment. In a typical experimental cycle,

a sequence of 200 transient absorption spectra was recorded, each delayed by a total time relative to the single 193 nm photolysis pulse of $t_D=(n-1)t_{cam}+\tau$, where n is the signal image number (1 to 200), t_{cam} is the constant delay between successive camera images (4 ms) limited by the camera frame rate, and τ is a variable μs time delay. (See Figure 1B.) Several sections of the 1-D absorption spectra constructed from these images[31] are shown in Figure 2. Each spectrum is the average over 950 cycles with an integration time of 50 μs for individual camera images. Slow baseline fluctuations, periodic oscillations, and the AA-d_1 photodepletion spectrum have been subtracted from the experimental traces. Figure 2A shows the experimental spectrum recorded at a time delay of tD=0 μs, that is, within the first 50 μs after photolysis. Simulations of the individual molecular contributions to the spectral fit are shown, inverted and offset for clarity.

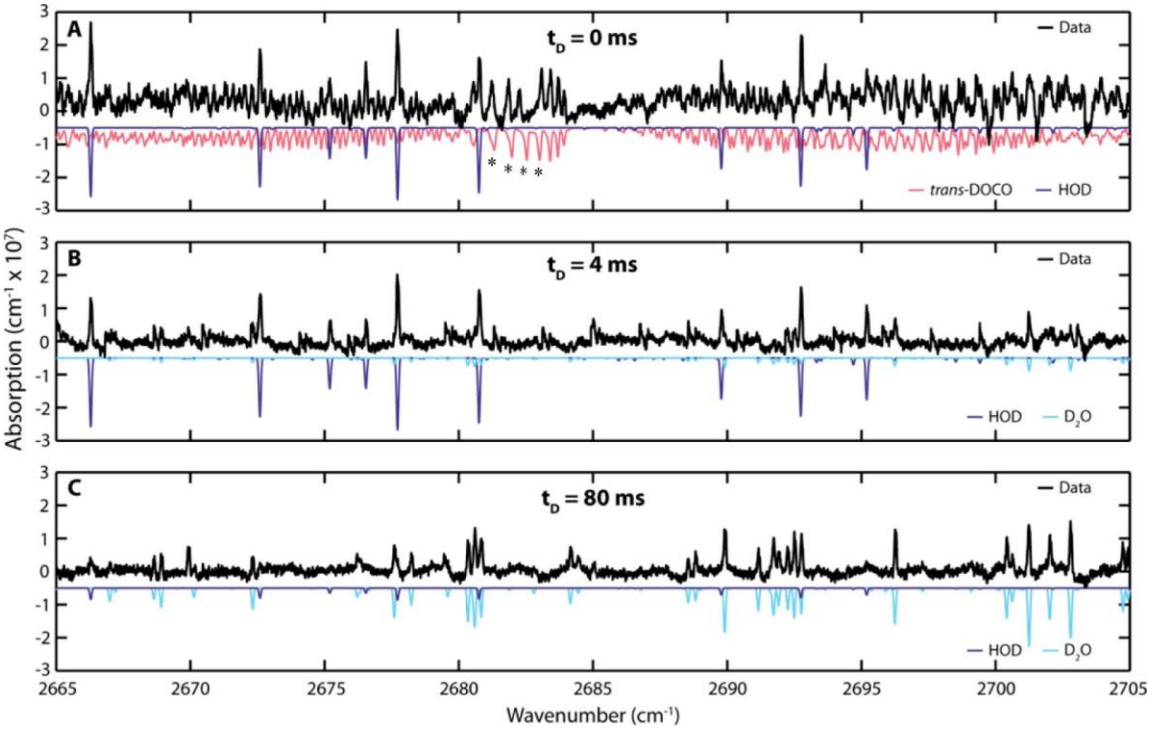

Figure 6.2. Transient absorption following the photolysis of acrylic acid-d_1 (AA-d_1). (A) Experimental spectrum recorded immediately following photolysis (t_D=0 μs) is shown in black, along with fitted simulations of *trans*-DOCO (red) and HOD (dark blue) spectra, which are inverted and offset (by 0.5×10^{-7} cm^{-1}) for clarity. The four transitions marked with an asterisk (*) are known to be perturbed by a Coriolis or Fermi interaction[26] and therefore were not included in any fits of *trans*-DOCO concentration. (B) Experimental trace at t_D = 4 ms, where the concentration of *trans*-DOCO has decayed below our detection limits. Spectral fits at t_D = 4 ms (HOD in dark blue, D_2O in light blue) are again inverted and offset. (C) Experimental trace at t_D = 80 ms with inverted and offset spectral fits (HOD in dark blue, D_2O in light blue).

At t_D=0 μs, rovibrational features of *trans*-DOCO could be unambiguously assigned using previously determined spectroscopic parameters and calculated intensities.[26,32,33] By fitting the observed spectral features to the simulated spectrum, we measured the absolute molecular concentration of *trans*-DOCO within this 50 μs integration window to be 3.1×10^{12} cm^{-3} ± 0.5×10^{12} cm^{-3} (1σ total experimental uncertainty; see Supporting Information). The statistical uncertainty in the spectral fitof *trans*-DOCO molecules was 5×10^{10} cm^{-3}, a direct result of the multiline fitting routines possible when performing broadband spectroscopy.[27] We also observed a prompt (within

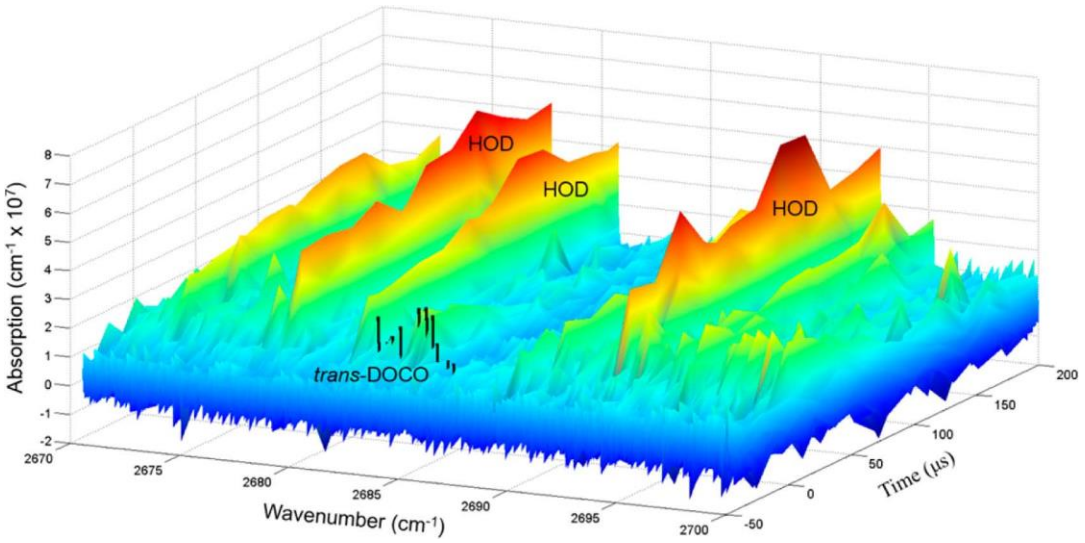

Figure 6.3: *trans*-DOCO absorption and decay measured in the first 200 μs following photolysis of AA-d_1. The strong *trans*-DOCO Q-branch lines are outlined in black. Increasing absorption from HOD product is also visible.

50 μs) formation of HOD within this spectral window. At t_D = 4 ms (Figure 2B), the absolute concentration of *trans*-DOCO had dropped below our detection limit, leaving only strong absorption features from HOD, along with new, weaker features from D2O arising from isotopic exchange reactions with AA-d_1. At a longer time delay of t_D =80 ms (Figure 2C), the HOD had mostly decayed, and strong absorptions from D_2O dominated the spectral window, indicating that the flow system has been fully passivated with deuterium and that there is little or no contamination by H_2O.

To investigate the submillisecond decay of *trans*-DOCO, we obtained a set of interleaved time-series spectra by stepping the time delay τ in 20 μs increments. These spectra were recorded with a camera-limited integration time of 25 μs, beginning 40 μs before the photolysis pulse (t_D= −40 μs). In total, we use 13 different values of τ over the range −40 μs ≤ τ ≤ 200 μs, acquiring 200 spectra at the camera frame rate at each unique value of τ. These interleaved time-series spectra were averaged 50 times and are shown for t_D ≤ 200 μs in Figure 3 as a 3-D surface. The strongest *trans*-DOCO Q-branch

transitions, ~2684 cm^{-1}, are outlined in black; they decayed much faster than the overall rise in surrounding HOD absorption. From spectral fits to the data shown in Figures 2 and 3 as well as that shown in the Supporting Information,[33] we obtained time-dependent absolute concentrations of *trans*-DOCO, HOD, and D_2O (Figure 4). In addition to these three species, we also detected (in a different spectral region) the immediate formation of C_2HD following photolysis;[33] its time-dependent concentration is plotted in Figure 4. Within the time integration window immediately after excimer photolysis, HOD, C_2HD, and *trans*-DOCO were all formed instantaneously after the first photolysis laser shot and after all subsequent duty cycles (Figure 4B,C).

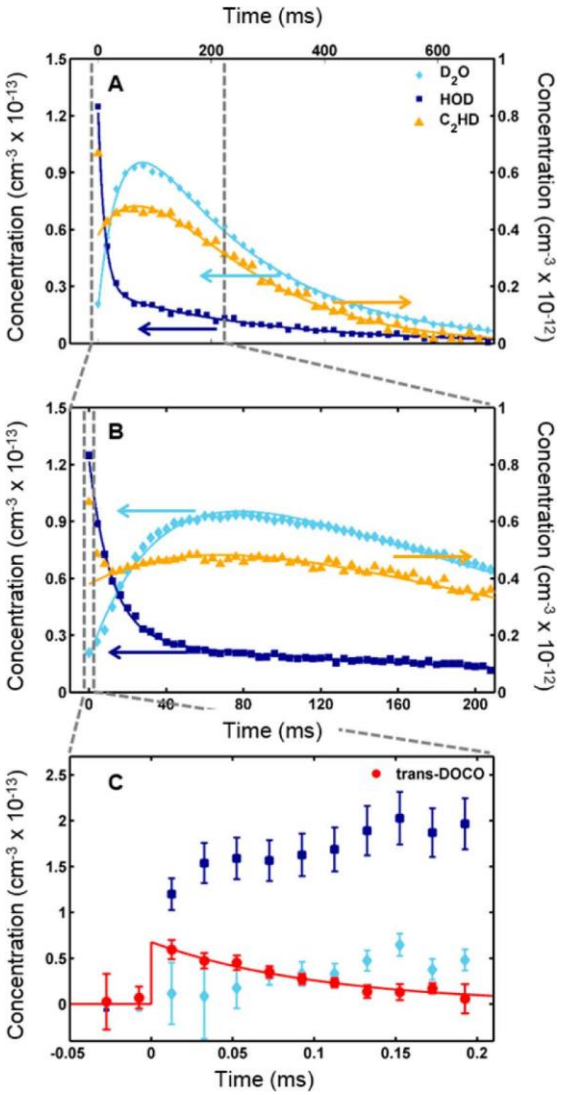

Figure 6.4: (A) Measured absolute concentrations of HOD (dark-blue squares), D_2O (light-blue diamonds), and C_2HD (orange triangles) with a 50 μs integration time and ~0.05 s of averaging. For clarity, only every fourth data point is shown. Empirical fits to bi-exponential functions are plotted as solid lines of the appropriate color for each observed molecular signal. The data plotted here are influenced by two types of instrument response: diffusion of primary photoproducts out of the comb probe beam on short time scales and net flow out of the cell due to continuous pumping on longer times. (B) Zoom from 0 to 200 ms of the data in panel A, now showing all data points. In both panels A and B, the concentration axis for HOD and D_2O is on the left, whereas the concentration of C_2HD (smaller in scale by an order of magnitude) is shown on the right. (C) Measured absolute concentrations of HOD, D_2O, and *trans*-DOCO (red circles) at times ≤200 μs (25 μs integration time). Experimental error bars are shown at 1σ. The decay of *trans*-DOCO was empirically fit to an effective first-order loss with a coefficient $k'_{tDOCO,eff} = 9.6 \times 10^{3}\ s^{-1} \pm 0.9 \times 10^{3}\ s^{-1}$ (solid red line).

Immediately after photolysis, within the first 25 μs for *trans*-DOCO and HOD and the first 50 μs for C_2HD, we measure concentrations of $6.0 \times 10^{12}\ cm^{-3} \pm 0.5 \times 10^{12}\ cm^{-3}$,

1.20×10^{13} cm^{-3} ± 0.07×10^{13} cm^{-3}, and 7×10^{11} cm^{-3} ± 3×10^{11} cm^{-3}, respectively. Of these products, only *trans*-DOCO has been reported previously.[30] At our low partial pressures of AAd_1(~1 Pa), no secondary reactions were possible within the first 50 μs, diffusion to/from walls is too slow, and we therefore deduce that these products were not formed by subsequent radical chemistry. Over the subsequent 200 μs after photolysis, we observed a rapid decay in trans-DOCO and a slight rise in the concentration of HOD on time scales consistent with bimolecular reactions. The effective first-order rate coefficient, $k'_{t\mathrm{DOCO,eff}}$ = 9.6×10^{3} s^{-1} ± 0.9×10^{3} s^{-1}, is similar to HOCO loss rates observed by Petty, Harrison, and Moore under similar conditions, which they attribute to fast bimolecular reactions with radical intermediates,[34] for example, the vinyl radical or DOCO. At longer times (>200 μs), D_2O grows in as HOD decays, likely due to isotope exchange reactions HOD + HOD and HOD + AA-d_1. While OH products have been observed by laser-induced fluorescence, the yield has not been measured.[35,36] Our detection limit for OD absorption within our probe wavelength range is ~5×10^{12} cm^{-3}, and we find no evidence of OD production above this minimum detectable level.[33] This observation is consistent with those of Osborne, Li, and Smith, who have reported that CO (and implicitly OH) is formed in nearly equal concentrations with HOCO following AA photolysis under similar experimental conditions.[37]

Our observation of prompt HOD and C_2HD products is unexpected, and we speculate that these may be formed from the unimolecular decomposition of AA-d_1, which possess 620 kJ mol^{-1} of internal energy. These could be coproducts from the previously observed decarboxylation or decarbonylation channels,[37] resulting from

hydrogen migration or abstraction pathways[38] similar to mechanisms seen in the 193 nm photolysis of propene.[39] In molecular beam experiments, Kitchen et al. find that 193 nm photodissociation leads to only two prompt channels, C−C bond fission (HOCO + C_2H_3) and C−O bond fission (OH + C_2H_3CO) under collisionless conditions,[30] although in the bulk gas, other products could be formed by collisional dissociation of vibrationally hot intermediates or relaxation to long-lived, electronically excited AA* with alternate unimolecular pathways. However, acrylic acid forms strong hydrogen bonds and is known to be "sticky", and our current experiments do not allow us to definitively eliminate alternative explanations (artifacts such as wall contamination or photochemistry, H_2O impurities, photolysis of AA-dimers or AA-water clusters). Further experiments are needed to test the validity of the above hypothesis.[33]

Our results on acrylic acid photodissociation highlight how the high molecular sensitivity (10^{10} cm^{-3}) and broad spectral coverage (65 cm^{-1}) of mid-IR time-resolved frequency comb spectroscopy enable the identification and characterization of multiple transient species simultaneously (including, under more carefully controlled experimental conditions, their respective photolysis yields and branching ratios), while the high time resolution can give precise information about the subsequent reaction rates. The coherent nature of TRFCS provides its high sensitivity, as laser phase stabilization results in the concentration of optical power into narrow, discrete frequencies (that is, comb teeth). In this initial implementation, we demonstrate sensitive detection of *trans*-DOCO in the mid-IR toward the study of DOCO produced in the OD + CO reaction. Time-resolved spectroscopy of this and many other fast radical reactions would benefit from the unique characteristics of highly coherent ultrafast lasers, which now provide frequency combs

from the mid-IR to the extreme ultraviolet.[40]

6.3 Acknowledgements

We thank Keeyoon Sung of the National Aeronautics and Space Administration (NASA) Jet Propulsion Laboratory (JPL) for providing a list of D2O mid-IR line positions and intensities measured by Robert A. Toth of JPL. We are grateful to Scott A. Diddams of the National Institute of Standards and Technology (NIST) and Tim Dinneen of Precision Photonics for providing the mid-IR VIPA etalon used in this work. We also thank Brad Baxley for artistic contributions to Figure 1 and acknowledge financial support from NIST, NSF, NASA, AFOSR, and DTRA. Adam J. Fleisher was supported by a National Research Council postdoctoral fellowship and Thinh Bui by a NASA Earth and Space Science Fellowship.

6.4 References

1. Porter, G. In The Chemical Bond: Structure and Dynamics; Zewail, A. H., Ed.; Academic Press: Boston, 1992; pp 113−148.

2. Toscano, J. P. In *Reviews of Reactive Intermediate Chemistry*; Platz, M. S., Moss, R. A., Jones, M., Jr., Eds.; Wiley: Hoboken, NJ, 2007; pp 183−205.

3. Ball, S. M.; Povey, I. M.; Norton, E. G.; Jones, R. L. Broadband Cavity Ringdown Spectroscopy of the NO_3 Radical. Chem. Phys. Lett. 2001, 342, 113−120.

4. Welz, O.; Savee, J. D.; Osborn, D. L.; Vasu, S. S.; Percival, C. J.; Shallcross, D. E.; Taatjes, C. A. Direct Kinetic Measurements of Criegee Intermediate (CH_2OO) Formed by Reaction of CH_2I with O_2. *Science* **2012**, *355*, 204-207.

5. Su, Y. -T.; Huang, Y. -H.; Witek, H. A.; Lee, Y. -P. Infrared Absorption Spectrum of the Simplest Criegee Intermediate CH_2OO. *Science* **2013**, *340*, 174-176.

6. Taatjes, C. A.; Welz, O.; Eskola, A. J.; Savee, J. D.; Scheer, A. M.; Shallcross, D. E.; Rotavera, B.; Lee, E. P. F.; Dyke, J. M.; Mok, D. K. W.; Osborn, D. L.; Percival, C. J. Direct Measurements of Conformer-Dependent Reactivity of the Criegee Intermediate CH_3CHOO. *Science* **2013**, *340*, 177-180.

7. Su, Y.-T.; Lin, H.-Y.; Putikam, R.; Matsui, H.; Lin, M. C.; Lee, Y.- P. Extremely Rapid Self-Reaction of the Simplest Criegee Intermediate CH_2OO and its Implications in Atmospheric Chemistry. Nat. Chem. 2014, 6, 477−483.

8. Levieveld, J.; Butler, T. M.; Crowley, J. N.; Dillon, T. J.; Fischer, H.; Ganzeveld, L.; Harder, H.; Lawrence, M. G.; Martinez, M.; Taraborreli, D; Williams, J. Atmospheric oxidation capacity sustained by a tropical forest. *Nature* **2008**, *452*, 737-740.

9. Mauldin III, R. L.; Berndt, T.; Sipilä, M.; Paasonen, P.; Petäjä, T.; Kim, S.; Kurtén, T; Stratmann, F.; Kerminen, V. -M.; Kulmala, M. A new atmospherically relevant oxidant of sulphur dioxide. *Nature* **2012**, *488*, 193-197.

10. Oka, T. Nuclear spin selection rules in chemical reactions by angular momentum algebra. *J. Mol. Spectrosc.* **2004**, *228*, 636-639.

11. Schliesser, A.; Picqué, N.; Hänsch, T. W. Mid-Infrared Frequency Combs. Nat. Photonics 2012, 6, 440−449.

12. Cundiff, S. T.; Ye, J. Colloquium: Femtosecond optical frequency combs. *Rev. Mod. Phys*. **2003**, *75*, 325-342.

13. Marian, A.; Stowe, M. C.; Lawall, J. R.; Felinto, D.; Ye, J. United Time-Frequency Spectroscopy for Dynamics and Global Structure. *Science* **2004**, *306*, 2063–2068.

14. Thorpe, M. J.; Moll, K. D.; Jones, R. J.; Safdi, B.; Ye, J. Broadband Cavity Ringdown Spectroscopy for Sensitive and Rapid Molecular Detection. *Science* **2006**, *311*, 1595–1599.

15. Adler, F.; Thorpe, M. J.; Cossel, K. C.; Ye, J. Cavity-Enhanced Direct Frequency Comb Spectroscopy: Technology and Applications. *Annu. Rev. Anal. Chem*. **2010**, *3*, 175–205.

16. Newbury, N. R. Searching for applications with a fine-tooth comb. *Nature Photon*. **2011**, *5*, 186-188.

17. Gilli, R.; Méjean, G.; Kassi, S.; Ventrillard, I.; Abd-Alrahman, C.; Romanini, D. Frequency Comb Based Spectrometer for *in Situ* and Real Time Measurements of IO, BrO, NO_2, and H_2CO at pptv and ppqv Levels. *Environ. Sci. Technol*. **2012**, *46*, 10704-10710.

18. Crutzen, P. J. in *Low-Temperature Chemistry of the Atmosphere*, Moortgat, G. K., Barnes, A. J., Le Bras, G., Sodeau, J. R., Eds.; Springer-Verlag: Berlin Heidelberg, 1994; pp. 465-498.

19. Wayne, R. P. *Chemistry of Atmospheres*; Oxford Univ. Press: New York, 2000; ed. 3, pp. 24, 330-334.

20. Glassman, I.; Yetter, R. A. *Combustion*; Academic Press: New York, 2008; ed 4., pp. 117-119.

21. Francisco, J. S.; Muckermann, J. T.; Yu, H. -G. HOCO Radical Chemistry. *Acc. Chem. Res*. **2010**, *43*, 1519-1526.

22. Oyama, T.; Funato, W.; Sumiyoshi, Y; Endo, Y. Observation of the pure rotational spectra of *trans*- and *cis*-HOCO. *J. Chem. Phys*. **2011**, *134*, 174303.

23. Nguyen, T. L.; Xue, B. C.; Weston, R. E.; Barker, J. R.; Stanton, J. F. Reaction of HO with CO: Tunneling Is Indeed Important. *J. Phys. Chem. Lett*. **2012**, *3*, 1549–1553.

24. Weston, R. E., Jr.; Nguyen, T. L.; Stanton, J. F.; Barker, J. R. HO + CO Reaction Rates and H/D Kinetic Isotope Effects: Master Equation Models with ab initio SCTST Rate Constants. J. Phys. Chem. A 2013, 117, 821−835.

25. Guo, H. Quantum Dynamics of Complex-Forming Bimolecular Reactions. Int. Rev. Phys. Chem. 2012, 31, 1−68.

26. Petty, J. T.; Moore, C. B. Transient infrared absorption spectrum of the ν_1 fundamental of *trans*-DOCO. *J. Chem. Phys*. **1993**, *99*, 47-55.

27. Adler, F.; Masłowski, P.; Foltynowicz, A.; Cossel, K. C.; Briles, T. C.; Hartl, I.; Ye, J. Mid-infrared Fourier transform spectroscopy with a broadband frequency comb. *Opt. Express* **2010**, *18*, 21861–21872.

28. Mollner, A. K.; Valluvadasan, S.; Feng, L.; Sprague, M. K.; Okumura, M.; Milligan, D. B.; Bloss, W. J.; Sander, S. P.; Martien, P. T.; Harley, R. A.; McCoy, A. B.; Carter, W. P. L. Rate of Gas Phase Association of Hydroxyl Radical and Nitrogen Dioxide. *Science* **2010**, *330*, 646–649.

29. Nugent-Glandorf, L.; Neely, T.; Adler, F.; Fleisher, A. J.; Cossel, K. C.; Bjork, B. J.; Dinneen, T.; Ye, J.; Diddams, S. A. Mid-infrared virtually imaged phased array spectrometer for rapid and broadband trace gas detection. *Opt. Lett*. **2012**, *37*, 3285–3287.

30. Kitchen, D. C.; Forde, N. R.; Butler, L. J. Photodissociation of Acrylic Acid at 193 nm. *J. Phys. Chem. A* **1997**, *101*, 6603–6610.

31. Diddams, S. A.; Hollberg, L.; Mbele, V. Molecular fingerprinting with the resolved modes of a femtosecond laser frequency comb. *Nature* **2007**, *445*, 627–630.

32. Huang, X.; Fortenberry, R. C.; Wang, Y.; Francisco, J. S.; Crawford, T. D.; Bowman, J. M. Dipole Surface and Infrared Intensities for the *cis*- and *trans*-HOCO and DOCO Radicals. *J. Phys. Chem. A* **2013**, *117*, 6932-6939.

33. See the Supporting Information.

34. Petty, J. T.; Harrison, J. A.; Moore, C. B. Reactions of *trans*-HOCO studied by infrared spectroscopy. *J. Phys. Chem*. **1993**, *97*, 11194-11198.

35. Upadhyaya, H. P.; Kumar, A.; Naik, P. D.; Sapre, A. V.; Mittal, J. P. Dynamics of OH Formation in the Dissociation of Acrylic Acid in its (n,π*) and (π,π*) Transitions Excited at 248 and 193 nm. J. Chem. Phys. 2002, 117, 10097.

36. Zhang, R.-R.; Qin, C.-C.; Long, J.-Y.; Yang, M.-H.; Zhang, B. Ultrafast Predissociation Dynamics of Excited State of Acrylic Acid. Acta Phys.-Chim. Sin. 2012, 28, 522−527.

37. Osborne, M. C.; Li, Q.; Smith I. W. M. Products of the ultraviolet photodissociation of trifluoroacetic acid and acrylic acid. *Phys. Chem. Chem. Phys*. **1999**, *1*, 1447-1454.

38. Clark, J. M.; Nimlos, M. R.; Robichaud, D. J. Comparison of unimolecular decomposition pathwyas for carboxylic acids of relevance to biofuel. *J. Phys. Chem. A* **2014**, *118*, 260-274.

39. Zhao, Y.-L.; Laufer, A. H.; Halpern, J. B.; Fahr, A. Hydrogen Migration and Vinylidene Pathway for Formation of Methane in the 193 nm Photodissociation of Propene: CH3CH=CH2 and CD3CD=CD2. J. Phys. Chem. A 2007, 111, 8330−8335.

40. Cingoz, A.; Yost, D. C.; Allison, T. K.; Ruehl, A.; Fermann, M. E.; Hartl, I.; Ye, J. Direct Frequency Comb Spectroscopy in the Extreme Ultraviolet. Nature 2012, 482, 68−71.

6.5 Supporting Materials and Methods

The photolysis experiments described here were conducted in a flow cell coupled to a high-finesse optical cavity similar to that described in the Supplementary Material for Ref. 28 of the main text and illustrated in Fig. S1. The gas flow rates of three different inlets (two purge, one sample) were set such that the pressure in the photolysis region of the cavity was maintained at 1.60 kPa ± 0.02 kPa. The N_2 purge inlets located near each high-reflectivity mirror were set at a total flow of 400 sccm (200 sccm through each) as controlled by a fine needle valve.

Mono-deuterated acrylic acid, AA-d_1, was synthesized by mixing D_2O with commercial acrylic acid (Sigma Aldrich, 99% purity) for several hours; the sample was extracted with methylene chloride and purified by roto-evaporation as outlined by Petty and Moore in Ref. 26 of the main text. Care was taken to exclude water (H_2O) from the

liquid AA-d_1 precursor during synthesis. The AA-d_1 sample was confirmed by both proton and deuterium NMR to have been synthesized with 90% isotopic efficiency, and no resonances originating from water were observed. We found a very small amount of hydrocarbon contamination at low NMR shifts (~0.85 and 1.3 ppm in $CDCL_3$). These resonances, not present in the commercial undeuterated AA sample, can be attributed to a small amount of vacuum grease.

The same research grade N_2 was supplied to a temperature-controlled bubbler (20.00 °C ± 0.07 °C) containing AA-d_1 at a rate of 10 sccm. Bubbling was slowed to a rate of tens of fine bubbles per second using a valve located between the AA-d_1 liquid bubbler and the flow cell while maintaining constant flow rates. Just before expansion into the flow cell, the N_2/AA-d_1 sample was mixed in a stainless steel tee of diameter 0.635 cm with 80 sccm of research grade CO_2 in order to increase vibrational cooling of hot DOCO formed during photolysis. For the current experiments, to minimize contamination of the high reflectivity mirrors, we used purge flows (400 sccm) that were substantially higher than the flow of reagent and carrier gas introduced through the central inlet (90 sccm). This arrangement led to further dilution of the AA-d_1 and may have resulted in a gradient along the probe axis, with AA-d_1 concentration highest in the center of the cell, by the inlet.

The ArF excimer that initiated acrylic acid-d_1 (AA-d_1) photolysis was operated at an output power of 10 mJ/pulse and a repetition rate of 0.2 Hz. The beam was steered using two highly-reflective mirrors coated for 193 nm. Together, these two mirrors had a reflection coefficient of 77%. The photolysis laser window through which the 193 nm pulse entered the high-finesse cavity flow cell was an uncoated UV fused silica plate ≈1

mm thick, with a measured transmission coefficient of 62%. Consequently, only 4.8 mJ per photolysis pulse reached the molecules within the flow cell. The entire photolysis beam cross-sectional area was 3 cm × 1 cm at the photolysis laser window, with the 3 cm width aligned parallel to the mid-infrared (mid-IR) optical axis. The vertical beam profile possessed a roughly Gaussian shape with a full width at half maximum of 5.4 mm ± 0.2 mm measured with a knife edge and power meter. The photolysis windows were carefully cleaned and dried under vacuum for several hours before a series of single-photolysis-pulse experiments were performed. An illustration of the flow cell coupled to a high finesse optical cavity is shown in Fig. S1.

The mid-IR frequency comb was operated with an average power of 500 mW before entering the high-finesse cavity, and had a full width at half maximum (FWHM) bandwidth of 150 cm^{-1}. For detection of *trans*-DOCO, HOD, D_2O, and AA-d_1, the center wavelength was 3.73 μm. The comb repetition rate (f_{rep}) was 136.5 MHz, which is equal to one-half the high-finesse cavity free spectral range (FSR). This condition, where $2f_{rep}$ = FSR, results in half the mid-IR frequency comb teeth being rejected by the optical cavity, and the comb mode spacing observed by the VIPA spectrometer is 273 MHz, well below its measured resolving power at a 15° tilt angle of 1.0 GHz ± 0.1 GHz. Over the 64.4 cm^{-1} simultaneous bandwidth recorded by the VIPA spectrometer, 7072 frequency comb teeth are incident on the VIPA following transmission through the high-finesse cavity. The VIPA resolution therefore limits the number of resolvable spectral elements to 1930. All elements spanning the 64.4 cm^{-1} bandwidth are recorded in as little as 25 μs.

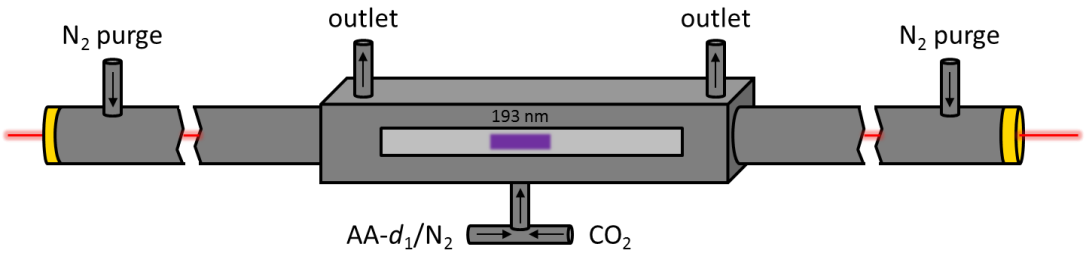

Fig. S1. Mass flow cell coupled to a high-finesse optical cavity (length not drawn to scale, as indicated by the breaks in each cylindrical purge arm). Arrows on the inlet/outlet ports indicate the direction of mass flow. The distance between the two highly-reflective low-loss optics (gold color above) is the optical cavity length, L_{cav} = 54.88 cm. The photolysis pathlength, L_{phot}, is equivalent to the width of the 193 nm excimer pulse (purple, traveling in and out of the page) shown irradiating the photolysis laser window (light gray). The mid-infrared frequency comb is shown in red, traveling perpendicular to the photolysis pulse.

The C_2HD spectrum was observed in a separate spectral window, centered at 3.93 μm (2545 cm^{-1}). In order to record time-resolved spectra from a different portion of the cavity-transmitted mid-IR frequency comb, we simply tuned the ruled diffraction grating located at the output of the tilted VIPA etalon. More details on the entire 2-D dispersive spectrometer are available in Ref. 29 of the main text (and references therein).

Supporting Text:

Fitting Procedure: In direct absorption spectroscopy, the measured absorption coefficient $\alpha(\tilde{\nu})$ is related to the absolute concentration of the absorbing species via (ES1),

$$\alpha(\tilde{\nu}) = SNg(\tilde{\nu} - \tilde{\nu}_0) \qquad \text{(ES1)}$$

where S is the molecular line strength in cm per molecule, N is the molecular density of absorbers in cm^{-3} (normalized to 101.325 kPa), and $g(\tilde{\nu} - \tilde{\nu}_0)$ is the normalized lineshape function in cm.

The molecular line strengths S for HOD mid-IR transitions are available in the HITRAN database (*S1*). The line strengths for D_2O infrared transitions were measured by Robert A. Toth at Caltech/JPL, and generously provided through private communication with Keeyoon Sung of JPL (line positions available in Ref. *S2*). Line strengths for the ν_1 band of *trans*-DOCO, however, have not been reported. In order to generate a line list for the ν_1 band at 2684 cm^{-1}, the previously measured rotational parameters in the ground and excited vibrational states from Ref. 26 of the main text were used in combination with a calculated total band intensity available in Ref. 32 of the main text and simulated in PGOPHER at a rotational temperature of 295 K (*S3*).

Each molecular line list containing center frequencies and line strengths were broadened using a single Gaussian normalized lineshape function $g(\tilde{\nu} - \tilde{\nu}_0)$, with a fixed FWHM of 1.0 GHz. The VIPA spectrometer-limited FWHM was measured independently using known methane (CH_4) infrared lines and confirmed by the presence of low residuals following the subtraction of molecular fits. Since these CH_4 lines were not measured contemporaneously in the current experiment, there is some minor discrepancy between certain simulated widths and fitted peak heights. Since we employ a global fit of all peaks within our spectral bandwidth, the uncertainty in the absolute frequency axis (<1 GHz) is directly related to our uncertainty in the integrated area of all peaks belonging to a single molecular species, and therefore makes an implicit contribution to our reported molecular sensitivities.

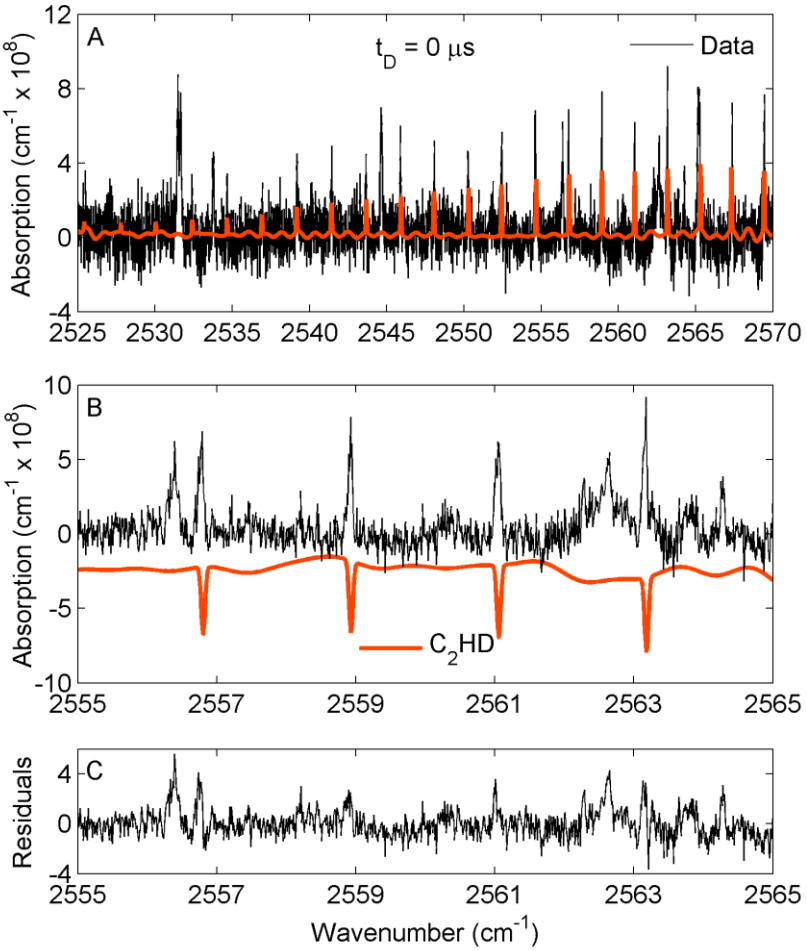

Fig. S2. Absorption spectrum of C_2HD at a time delay of t_D = 0 μs following 193 nm laser photolysis of acrylic acid-d_1. (**A**) The data (black) is the result of 1000 averages at an individual camera integration time of 50 μs. The fit C_2HD absorption spectrum is shown superimposed in orange on the black experimental data. (**B**) A zoom of the experimental data show in (**A**) with the fit C_2HD spectrum (orange) inverted and offset (by 2×10^{-8} cm^{-1}) for clarity. A 5th order polynomial baseline function and the intensities of about ten periodic baseline oscillations were also included in the fit. (**C**) Fit residuals. Absorption features in (**A-C**) not assigned to C_2HD are only present at t_D = 0 μs, whereas C_2HD persists until the flow cell is refreshed (see Fig. S6).

We determined the absolute time-dependent concentrations of HOD, D_2O, and *trans*-DOCO by fitting their experimental spectra (in units of $\alpha(\tilde{\nu})$), recorded at varying time delays following photolysis. We fit intensities of all lines of each molecular spectrum simultaneously to a broadened model line spectrum, along with a 5^{th} order polynomial baseline function and the amplitudes of about ten periodic baseline functions (both *sine* and *cosine* components) of fixed frequencies extracted from a Fourier transform of the one-dimensional absorption spectra. In Figs. 2-3 of the main text, the baseline polynomial, periodic oscillations, and the AA-d_1 photo-depletion spectrum have been subtracted from the experimental traces, leaving only the molecular contributions and high-frequency noise.

A majority of the C_2HD ν_3 *P*-branch can be seen in Fig. S2, with the TRFCS spectral window centered at 2545 cm^{-1} (near the calculated ν_1 band center of *cis*-DOCO reported in Ref. 32 of the main text). For spectral fitting, a C_2HD line list was generated in PGOHPER (*S3*) at a rotational temperature of 295 K using previously measured rotational parameters from Ref. *S4* and a calculated fundamental band intensity of 20.6 km/mol. In order to obtain the unknown band intensity, the optimized geometry and fundamental vibrational frequencies and intensities (including anharmonic corrections calculated using second order vibrational perturbation theory VPT2) of C_2HD were calculated at the CCSD(T)/aug-pVDZ level using the CFOUR program (*S5*).

Total Experimental Uncertainty: For the linear fitting of molecular spectra described above, a theoretical spectrum of concentration *C* was simulated for each species and fit to a linear scaling factor *N*. The fit concentration *NC* was then converted from units of μmol/mol to molecular concentration units (cm^{-3}) using the Loschmidt constant (N_L) at

experimental pressure and temperature. In addition, the difference in total optical cavity length (L_{cav}) and photolysis pathlength (L_{phot}) was taken into account when reporting photoproduct concentrations. The final expression for photoproduct molecular concentration in cm^{-3} is shown below.

$$C_f = NCN_L \frac{L_{cav}}{L_{phot}} \tag{ES2}$$

Each quantity in Eq. ES2 has an associated experimental uncertainty. The uncertainty in N is extracted as described in Ref. 27 of the main text using known multiline fitting procedures. For the band intensity of *trans*-DOCO, we estimate the uncertainty in C to be $\sigma_C = 0.1 \times C$ (10% uncertainty), which we postulate entirely from the calculated intensity reported by Huang et al. (Ref. 32 of the main text). The uncertainty in N_L is related to the uncertainty in our measurement of intracavity pressure, which was done using a pressure gauge with an observed precision of 1% ($\sigma_{NL} = 0.01 \times N_L$). The optical cavity length is known to much higher precision, and was monitored continuously by recording the eight harmonic of the repetition rate of the mode-locked OPO pump laser during the experiment. Its uncertainty is not considered to play a significant role compared to other sources. The photolysis pathlength, however, has an estimated uncertainty of 0.3 cm, or 10% of the measured excimer beam width at the flow cell. Finally, the experimental uncertainty in C_f is calculated using Eq. ES3 below.

$$\sigma_{C_f}^2 = \left(\frac{\partial C_f}{\partial N}\right)^2 \sigma_N^2 + \left(\frac{\partial C_f}{\partial C}\right)^2 \sigma_C^2 + \left(\frac{\partial C_f}{\partial N_L}\right)^2 \sigma_{N_L}^2 + \left(\frac{\partial C_f}{\partial L_{phot}}\right)^2 \sigma_{L_{phot}}^2 \tag{ES3}$$

There may be gradients in concentrations along the probe beam axis, due to the flow conditions. While we measure the column densities accurately, our computed

concentrations should be considered an average value over the appropriate effective cavity length (L_{phot}, L_{cav}, etc). The gradient, however, should not otherwise affect the results reported here, since we are not measuring bimolecular rate constants in the current experiment. The potential for unwanted gradients will be greatly reduced in future experiments by decreasing the purge flow to a value commensurate with the sample inlet flow.

For *trans*-DOCO, the following parameters were used to determine C_f and σ_{Cf}: N = 0.43, C = 1.0 μmol/mol, $N_L = 3.94\times10^{17}$ cm^{-3}, L_{cav} = 54.88 cm, L_{phot} = 3.0 cm, σ_N = 0.02, σ_C = 0.1 μmol/mol, $\sigma_{NL} = 4 \times 10^{15}$ cm^{-3}, and σ_{Lphot} = 0.3 cm. Therefore, we report in the main text, as measured in a typical run, a *trans*-DOCO molecular concentration of $C_f = 3.1\times10^{12}$ cm^{-3} ± 0.5×10^{12} cm^{-3} for t_D = 0 μs with an integration time of 50 μs and 950 averages. It is worth noting that the contribution to σ_{Cf} that arises solely from spectral fitting and observed signal-to-noise (σ_N) is an order of magnitude better than the overall experimental uncertainty reported here. Thus, we report a *trans*-DOCO sensitivity of 5×10^{10} cm^{-3}.

Time-Resolved Frequency Comb Spectroscopy Performance: The figure-of-merit used in comparison with other direct absorption techniques is the noise-equivalent absorption (NEA) normalized to 1 s of averaging time. In time-resolved frequency comb spectroscopy (TRFCS) we have the unique ability to recorded hundreds of broadband absorption spectra in rapid succession. An illustration of our data acquisition scheme is shown in Fig. S3.

For comparison with continuous-wave (cw) absorption techniques we calculate a bandwidth normalized NEA, known as NEA per spectral element, since many spectral

elements are resolved simultaneously in a single TRFCS experiment. This can be expressed as

$$NEA = \sigma_{noise} \frac{\pi}{FL_{phot}} \sqrt{\frac{T}{M}} \tag{ES4}$$

where σ_{noise} is the standard deviation of the noise in absorbance (absorbance $A = 1 - I/I_0$, where I is the light acquired in each VIPA image in the presence of photolysis products and I_0 is the reference light acquired in VIPA images recorder prior to photolysis), F is the measured cavity finesse, L_{phot} is the optical pathlength over which photolysis can occur, T is the total camera integration time required to record two images (one reference and one signal), and M is the number of resolvable spectral elements per image. A representative set of experimental conditions are as follows: $\sigma_{noise} = 6\times10^{-3}$, F = 1250 at 2684 cm^{-1}, L_{phot} = 3 cm, T = 2×50 μs = 100 μs, and M = 1930 elements. Therefore, in this initial demonstration of mid-IR TRFCS, we measure NEA = 1.1×10^{-9} cm^{-1} $Hz^{-1/2}$ per spectral element.

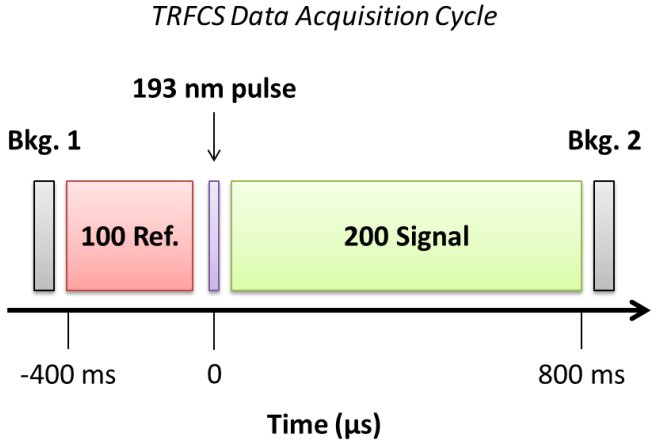

Fig. S3. Illustration of TRFCS data acquisition scheme. The time axis and blocks are not drawn to scale. The individual VIPA images that comprise the reference (abbreviated Ref. above) and signal blocks above were acquired at a camera-limited frame rate of 250 Hz. The 100 reference images are averaged and used as a single reference for the 200 time-resolved signal images recorded following photolysis. The integration time for each individual image was either 25 μs (camera-limited) or 50 μs. Camera background images recorded with the mid-infrared frequency comb blocked (Bkg. 1 and 2) were taken before and after a single TRFCS cycle in order to subtract camera dark counts.

We use the above observed absorption noise, measured finesse, and cavity length to estimate our OD sensitivity within this spectral region of the mid-IR. Looking at the line list reported in Abrams et al. (*S6*), the *R*1(1.5) lines of the 1←0 vibrational band of OD should appear at 2676.7 cm^{-1}, near the center of the broadband spectral window shown in Fig. 2 of the main text. We estimate the line strength of these transitions to be equal to the line strength of the same *R*1(1.5) transitions in OH, but scaled by the ratio of the OD fundamental vibration band origin to that of OH. Therefore, $S_{OD} \approx 3.5\times10^{-20}$ cm/molecule. Taking the maximum of a Gaussian lineshape function of 1 GHz FWHM, we calculate our single-line minimum detectable concentration for OD to be 5×10^{12} cm^{-3} (without averaging).

Osborne, Li, and Smith have reported in Ref. 37 of the main text nearly equivalent AA photolysis yields for HOCO, CO_2, and CO under similar experimental conditions. Assuming all photolysis reactions that lead to CO formation also promptly form OH as an upper bound, we can estimate an upper-bound for the expected formation of OD in our experiment to be [OD] = [*trans*-DOCO] = 3×10^{12} cm^{-3}. Therefore, we do not expect significant absorption features from OD in our current TRFCS experiments. On the μs

timescale, when both *trans*-DOCO and HOD are also present, spectroscopic interferences could also limit our realistic ability to spectroscopically identify OD, since only a handful of OD features exist even within our broad spectral window.

Initial AA-d_1 Concentration and Gas Residence Time: We could directly observe AA-d_1 by its fundamental ν_1 band (OD stretch) absorption spectrum. An absorption spectrum of the precursor mixture N_2/CO_2/AA-d_1 recorded under typical flow conditions is shown in Fig. S4. The observed spectrum (blue) matches well with the OH-stretch absorption band of undeuterated acrylic acid recorded at a temperature of 50 °C and a pressure of 101.325 kPa (1 atmosphere) from Ref. *S7*, shown in red. The red trace is obtained by shifting the origin of the known undeuterated AA spectrum (PNNL database) and scaling the overall intensity to match the observed band. The origin frequency (and overall intensity) was scaled by a factor of approximately $\approx 1/\sqrt{2}$, consistent with deuteration. We observe additional structure in the AA-d_1 OD-stretch absorption spectrum due to the presence of periodic baseline functions.

We could use the known cross sections of the undeuterated OH-stretch spectrum to estimate the concentration of AA-d_1 monomers. We can correct for the effect of deuteration using a density functional theory calculation (*S8,S9*) at the B3LYP/6-311++G level, which suggests that the integrated intensity of the OD-stretch of AA-d_1 is approximately 20% lower than that of the OH stretch intensity in AA. From the spectrum shown in Fig. S4, recorded under typical flow conditions, we estimate a partial pressure of AA-d_1 monomers to be on the order of 10^{14} cm^{-3} ($p_{AA} \approx 2$ Pa). This value is roughly consistent with calculations based on the flow conditions, though we find that the latter consistently underestimates the AA-d_1 concentration, most likely due to unsaturated

bubbler conditions and inhomogeneous mixing within the outlet-to-outlet region of the flow cell of the low flow of precursor mixture from the inlet with the much higher purge flow of N_2. Given the uncertainties in flow conditions, the spectrum thus provides a more direct and reliable estimate of AA-d_1 concentrations. We found that AA-d_1 concentrations varied with flow settings, most likely due to incomplete saturation in the bubbler and to limitations of the current flow meters. Since our primary goal of the current experiment was to detect DOCO radicals and determine the sensitivity of the TRFCS technique, we did not record AA-d_1 spectra prior to every run and hence cannot report absolute quantum yields.

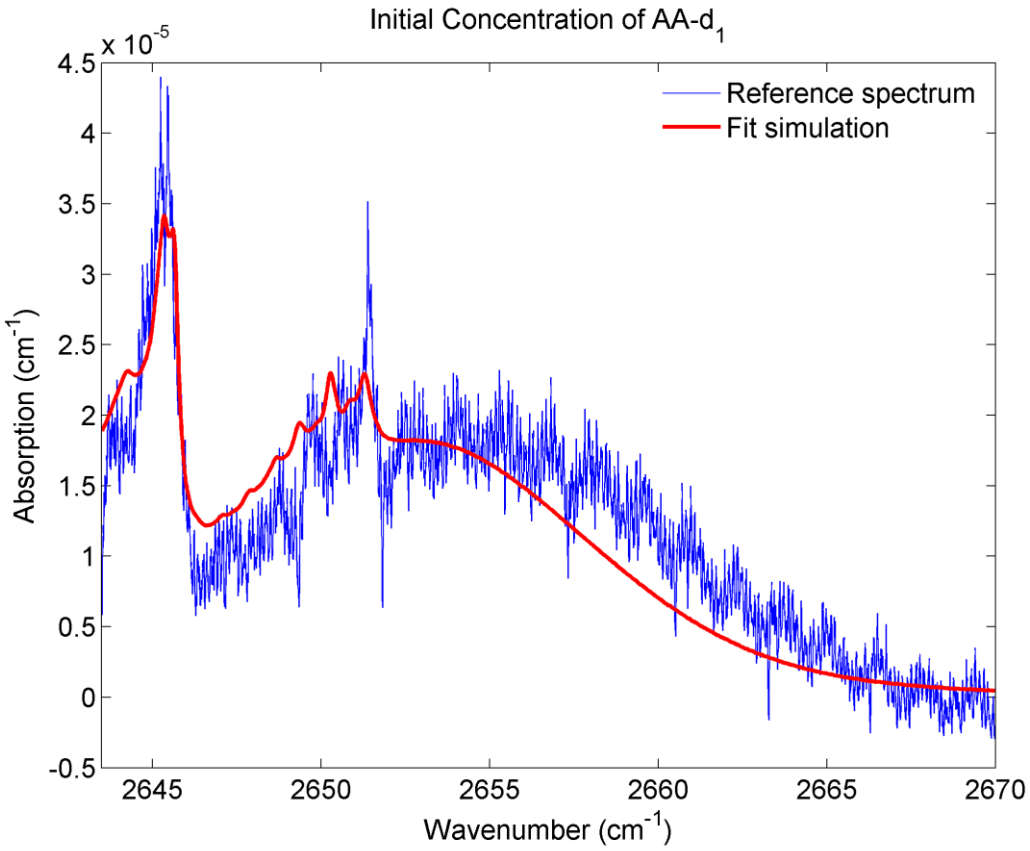

Fig. S4. Typical broadband absorption spectrum of acrylic acid-d_1 (AA-d_1) in blue, averaging 950 spectra. A shifted spectrum of undeuterated acrylic acid (AA) taken from

the PNNL database (*S7*) is shown in red. Fine structure that appears in the blue trace is due to periodic baseline oscillations and not highly resolved ro-vibrational features of the AA-d_1 band. The average initial AA-d_1 molecular concentration is estimated above from the shifted and scaled AA band intensity to be $\approx 4\times10^{14}$ cm^{-3} over the entire 12 cm central region of the flow cell (outlet-to-outlet, see Fig. S1), assuming even mixing within this high-flow region.

In Fig. S5, we show the recovery of the AA-d_1 depletion as the gas in the photolyzed volume in pumped away and refreshed. At each delay time t_D, the spectrum (a representative spectrum is shown as the blue trace shown in Fig. S4) was smoothed using a low pas filter function and integrated to determine the percent depletion of AA-d_1 following photolysis. After a single 193 nm pulse (time zero), the initial AA-d_1 concentration is depleted by ≈1.6% (extrapolated to a delay of t_D = 0 ms) relative to the typical initial spectrum shown in Fig. S4. The blue curve in Fig. S5 is a fit to an exponential decay, with an amplitude of 1.61% ± 0.04% and a decay coefficient k_{pump} = 3.0 s^{-1} ± 0.1 s^{-1} (1σ statistical uncertainty from the fit). This value agrees well with the decay constant at long times of ≈3 s^{-1} of the HOD concentration.

The photodepletion of AA-d_1 at t_D = 0 μs provides the AA-d_1 absorption cross section σ_{AA}

$$\frac{[AA]}{[AA]_0} = 1 - \exp(-\sigma_{AA}\Phi H), \qquad \text{(ES5)}$$

where Φ is the photodissociation quantum yield and H is the laser fluence divided by the photon energy (photon cm^{-2}). Assuming Φ = 1 and a laser fluence calculated from the excimer parameters, we estimate $\sigma_{AA} = 1\times10^{-17}$ cm^2 at 193 nm, in good agreement with that reported in Fig. 1 of Ref. *S10* and noted in Ref. 34 of the main text.

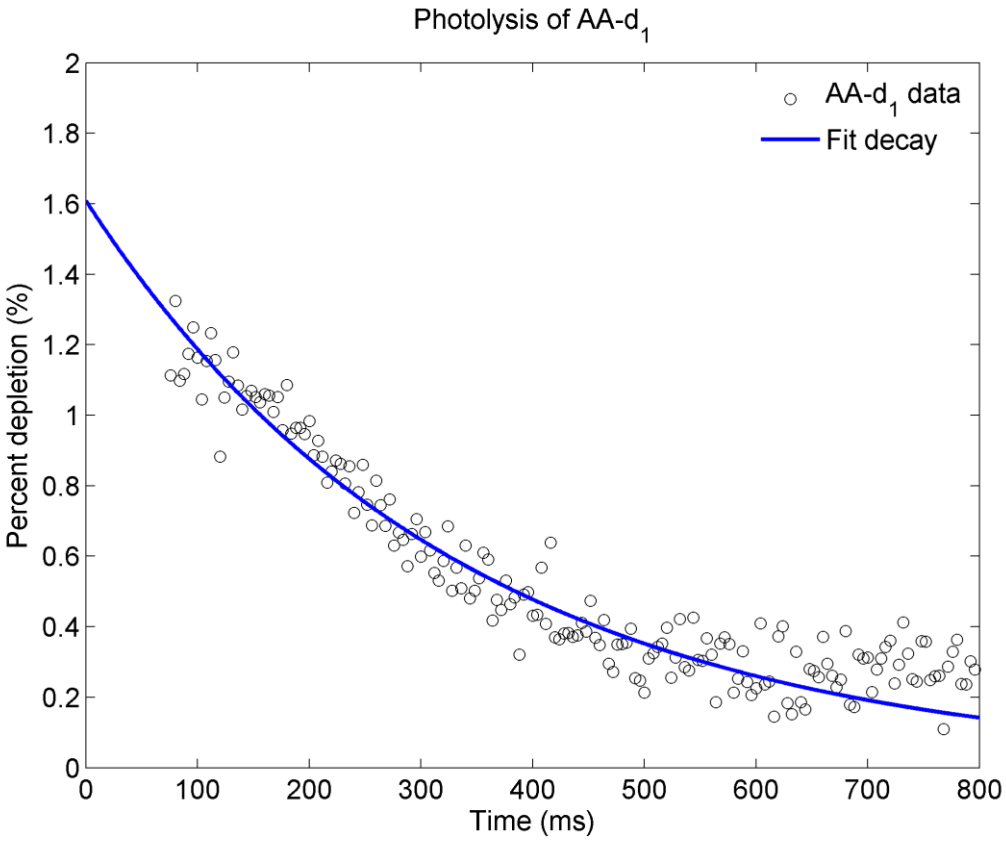

Fig. S5. Percent depletion of the integrated AA-d_1 band intensity as a function of time after the 193 nm photolysis pulse. Each data point in Fig. S5 is an average of 950 duty cycles at an integration time of 50 μs. The fit decay curve is a measure of the gas residence time within the high-finesse cavity flow cell. The fit decay constant is k_{pump} = 3.0 ± 0.1 s^{-1}.

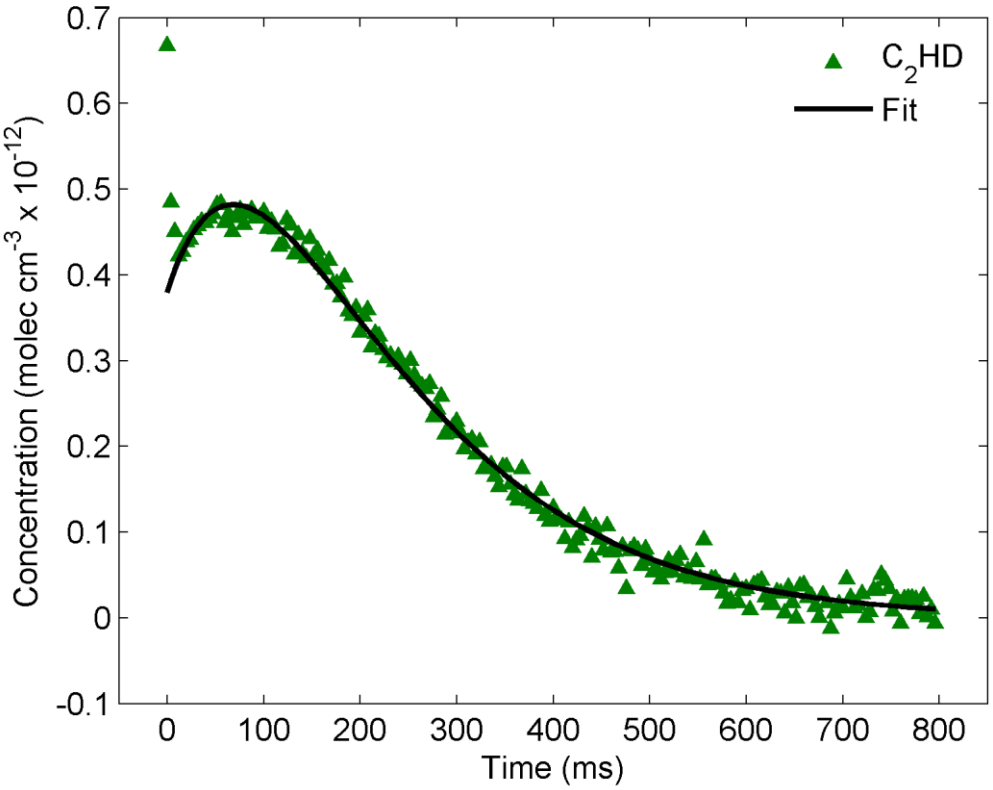

Fig. S6. Unobscured plot of the measured C_2HD concentration versus time following the photolysis of AA-d_1. Note that C_2HD is formed immediately ($t_D = 0$), therefore making it a direct product of AA-d_1 photodissociation. The biexponential fit (black) excludes data measured at times $t_D \leq 12$ ms (the first three data points).

Time-dependent Acetylene-d_1 concentration: The measured time-dependent absolute concentration of C_2HD is plotted in Fig. S6, as well as in Fig. 4 of the main text. The initial molecular concentration of C_2HD in the 50 μs immediately following photolysis was 7×10^{11} cm^{-3} with an experimental uncertainty of $\pm3\times10^{11}$ cm^{-3}. We observe an initial decay of C_2HD of approximately 30% in the first 4 ms. Since, following initial formation, C_2HD does not undergo subsequent reactions, we attribute this decay to fast local diffusion of primary photoproducts out of the probe volume (1.2 mm cavity waist at the

center of the flow cell). This arises from both the non-uniform illumination of the sample by the excimer beam and any inhomogeneous distribution of reagent AA-d_1 within the flow cell caused by the high purge flows. Diffusion must also be partially responsible for a small fraction of the initial 4 ms decay of HOD (panels A and B of Fig. 4 of the main text), but isotope exchange reactions must contribute to most of the decay, especially after 4 ms. The magnitude of HOD loss due to exchange reactions can be seen in the concomitant rise of D_2O products (panels A and B, Fig. 4), which is not formed as a primary photoproduct. Again, roughly 30% of the HOD loss, occurring in the first 4 ms, cannot be accounted for by reaction and is consistent with early diffusional loss. The *trans*-DOCO reacts too rapidly to be affected by diffusion. As was the case for HOD and D_2O, the C_2HD concentration at t_D > 100 ms is dominated by the gas residence time within the flow cell.

***Short Time Diffusional Loss*:** The transient decays in C_2HD and HOD products in the first few milliseconds arise from diffusion out of the prove volume, in the direction transverse to the cavity optical axis. Along this direction, the excimer laser responsible for photolysis is only about a factor of 5 larger in beam waist than the cavity probe beam. The photolysis volume has a cross-sectional area of 3 cm × 1 cm, whereas the probe volume is defined by the cavity waist radius of ≈1.2 mm. While the photolysis volume is much larger than the probe, the excimer laser power is not evenly distributed throughout the photolysis volume. We have made knife edge measurements of the vertical (1 cm) excimer beam profile which indicate a roughly Gaussian power distribution, whereas the horizontal (3 cm) beam profile appears to have a more complicated shape. As the measured absorption is integrated over the horizontal beam profile, diffusion in this

dimension should play a smaller role than diffusion in the vertical. We have modeled the diffusion as a one-dimensional problem involving a Gaussian distribution of photoproducts with a FWHM = 0.54 cm. Under our experimental conditions (T = 21 °C, P =1.6 kPa, average molecular diameter of $d \approx 300$ pm), we calculate the diffusion coefficient of C_2HD in N_2 to be $D_{C2HD} = 20$ cm^2 s^{-1}. We find that the modeled decay is in good agreement with the initial decay observed for C_2HD. We obtain similar results for HOD.

***Possible Sources of Photoproducts HOD and C_2HD*:** We observe HOD and C_2HD products that are formed, within the first 25-50 μs, prior to any secondary chemistry. We hypothesize that these are formed from the unimolecular photodissociation of acrylic acid, but we acknowledge that we cannot yet exclude all other explanations without further experiments. Among the possible alternatives, we consider below issues related to cluster formation, H_2O contamination and wall effects.

Acrylic acid is well known to form dimers or larger clusters at room temperature. The new photoproducts could in principle arise from the photolysis of clusters. However, we estimate the fraction of dimers to be <1%, based on the dimerization equilibrium constant of K_p = 2.6 Torr (estimated by Osborne et al. in Ref. 37 of the main text) and the average partial pressure of AA-d_1 determined spectroscopically. This suggests that AA-d_1 clusters do not play a significant role in the observed photochemsitry. However, in our current configuration, the AA-d_1 concentration is potentially inhomogeneous in the photolyzed volume, and is significantly higher as the precursor gas flow expands into the cell. We can exclude neither the possibility that some clusters are present in some regions of the cell, nor that there could a non-equilibrium concentrations of clusters

It is difficult to quantify potential H_2O contamination on the walls of the flow cell, including the excimer windows. As described above, care was taken to ensure the isotopic purity of the synthesized AA-d_1 sample. Clean and dry excimer windows were installed prior to photolysis experiments, and a series of dry nitrogen flow and vacuum pumping cycles were conducted before AA-d_1 was introduced. We used research grade N_2 and CO_2, and AA-d_1 was bubbled through the flow cell under experimental conditions for several minutes prior to the acquisition of photolysis data. Although the flow cell was not baked out at high temperature prior to photolysis experiments, the flow/pump cycles and AA-d_1 purging is expected to significantly reduce hydrogen contamination on the wall of the flow cell to a minimum. These details regarding sample cell preparation are available earlier in the Supporting Information.

Experimentally, we always observed that D_2O formation dominates the absorption spectra at long times (>80 ms), while the HOD signal simultaneously decreases (see Figs. 4A and 4B). We concluded that HOD is being converted to D_2O, secondary chemistry is dominated by deuteration, thus indicating that H_2O concentration must be low, and that the system is well passivated for deuterium over hydrogen.

It is possible that the excimer radiation initiates photochemistry of acrylic acid deposited on the laser windows; AA* + AA reactions could give rise to the products observed. The excimer windows are located approximately 1.27 cm from the probe beam. Photoproducts would need to be ejected into the central probe axis (central 1.2 mm beam waist) within the first 25-50 μs. It is less likely that the H in HOD comes from OH groups on the window. Given the 90% isotopic composition of the AA-d_1 precursor and

complete reaction of HOD to D_2O, we expect species adsorbed on the excimer windows to be heavily depleted in reactive hydrogen.

References

(*S1*) Rothman, L. S.; Gordon, I. E.; Barbe, A.; Benner, D. C.; Bernath, P. F.; Birk, M.; Boudon, V.; Brown, L. R.; Campargue, A.; Champion, J. -P.; Chance, K.; Coudert, L. H.; Dana, V.; Devi, V. M.; Fally, S.; Flaud, J. -M.; Gamache, R. R.; Goldman, A.; Jacquemart, D.; Kleiner, I.; Lacome, N.; Lafferty, W. J.; Mandin, J. -Y.; Massie, S. T.; Mikhailenko, S. N.; Miller, C. E.; Moazzen-Ahmadi, N.; Naumenko, O. V.; Nikitin, A. V.; Orphal, J.; Perevalov, V. I.; Perrin, A.; Predoi-Cross, A.; Rinsland, C. P.; Rotger, M.; Šimečková, M.; Smith, M. A. H.; Sung, K.; Tashkun, S. A.; Tennyson, J.; Toth, R. A.; Vandaele, A. C.; Vander Auwera, J. The *HITRAN* 2008 Molecular Spectroscopic Database, *J. Quant. Spectrosc. Radiat. Transf*. **2009**, *110*, 533-572.

(*S2*) Toth, R. A.; HDO and D_2O Low Pressure, Long Path Spectra in the 600-3100 cm^{-1} Region. *J. Mol. Spectrosc*. **1999**, *195*, 73-97.

(*S3*) PGOPHER, a Program for Simulating Rotational Structure, C. M. Western, University of Bristol, http://pgopher.chm.bris.ac.uk.

(*S4*) Baldacci, A.; Ghersetti, S.; Hurlock, S. C.; Rao, K. N. Infrared Bands of $^{12}C_2HD$. *J. Mol. Spectrosc*. **1976**, *59*, 116-125.

(*S5*) CFOUR, a quantum chemical program package written by Stanton, J. F.; Gauss, J.; Harding, M. E.; Szalay P. G.; with contributions from Auer, A. A.; Bartlett, R. J.; Benedikt, U.; Berger, C.; Bernholdt, D. E.; Bomble, Y. J.; Christiansen, O.; Heckert, M.;

Heun, O.; Huber, C.; Jagau, T. -C.; Jonsson, D.; Jusélius, J.; Klein, K.; Lauderdale, W. J.; Matthews, D. A.; Metzroth, T.; O'Neill, D. P.; Price, D. R.; Prochnow, E.; Ruud, K.; Schiffmann, F.; Stopkowicz, S.; Tajti, A.; Vázquez, J.; Wang, F.; Watts, J. D. and the integral packages MOLECULE (Almlöf J.; Taylor, P.R.), PROPS (Taylor, P. R.), ABACUS (Helgaker, T.; Aa. Jensen, H. J.; Jørgensen, P.; Olsen, J.), and ECP routines by Mitin, A. V.; van Wüllen, C. For the current version, see http://www.cfour.de.

(*S6*) Abrams, M. C.; Davis, S. P.; Rao, M. L. P.; Engleman, Jr., R. High-Resolution Fourier Transform Spectroscopy of the Vibration-Rotation Spectrum of the OD Radical. *J. Mol. Spectrosc*. **1994**, *165*, 57-74.

(*S7*) The acrylic acid spectrum was recorded at Pacific Northwest National Lab (PNNL) on March 19, 2010 and accessed from the PNNL database by Adam J. Fleisher at JILA on April 20, 2013. The original database reference is: Sharpe, S. W.; Johnson, T. J.; Sams, R. L.; Chu, P. M.; Rhoderick, G. C.; Johnson, P. A. Gas-Phase Databases for Quantitative Infrared Spectroscopy. *Appl. Spectrosc*. **2004**, *58*, 1452-146.

(*S8*) Gaussian 09, Revision B.01, Frisch, M. J.; Trucks, G. W.; Schlegel, H. B.; Scuseria, G. E.; Robb, M. A.; Cheeseman, J. R.; Scalmani, G.; Barone, V.; Mennucci, B.; Petersson, G. A.; Nakatsuji, H.; Caricato, M.; Li, X.; Hratchian, H. P.; Izmaylov, A. F.; Bloino, J.; Zheng, G.; Sonnenberg, J. L.; Hada, M.; Ehara, M.; Toyota, K.; Fukuda, R.; Hasegawa, J.; Ishida, M.; Nakajima, T.; Honda, Y.; Kitao, O.; Nakai, H.; Vreven, T.; Montgomery, J. A., Jr.; Peralta, J. E.; Ogliaro, F.; Bearpark, M.; Heyd, J. J.; Brothers, E.; Kudin, K. N.; Staroverov, V. N.; Kobayashi, R.; Normand, J.; Raghavachari, K.; Rendell, A.; Burant, J. C.; Iyengar, S. S.; Tomasi, J.; Cossi, M.; Rega, N.; Millam, N. J.; Klene, M.; Knox, J. E.; Cross, J. B.; Bakken, V.; Adamo, C.; Jaramillo, J.; Gomperts, R.;

Stratmann, R. E.; Yazyev, O.; Austin, A. J.; Cammi, R.; Pomelli, C.; Ochterski, J. W.; Martin, R. L.; Morokuma, K.; Zakrzewski, V. G.; Voth, G. A.; Salvador, P.; Dannenberg, J. J.; Dapprich, S.; Daniels, A. D.; Farkas, Ö.; Foresman, J. B.; Ortiz, J. V.; Cioslowski, J.; Fox, D. J. Gaussian, Inc., Wallingford CT, 2009.

(*S9*) Certain commercial equipment, instruments, or materials are identified in this paper in order to specify the experimental procedure adequately. Such identification is not intended to imply recommendation or endorsement by the National Institute of Standards and Technology, nor is it intended to imply that the materials or equipment identified are necessarily the best available for the purpose.

(*S10*) Morita, H.; Fuke, K.; Nagakura, S. Electronic Structure and Spectra of Acrylic Acid in the Vapor and Condensed Phases. *Bull. Chem. Soc. Jpn.* **1976**, *49*, 922-928. In Figure 1 of the online edition of this article, the *y*-axis is missing decimal points which appear in the original paper copy. The reported gas phase molar absorptivity of acrylic acid at 193 nm (51.8×10^{3} cm^{-1}) is $\approx4.5\times10^{3}$ dm^{3} mol^{-1} cm^{-1}, which yields $\sigma_{AA} \approx 7.5\times10^{-18}$ cm^{2}.